

A.I.Ch.E. JOURNAL

CHEMICAL ENGINEERING RESEARCH AND DEVELOPMENT /

DECEMBER 1958

CONTENTS

Liquid-Phase Adsorption Equilibria
Edward B. Stuart and James Coull

A General Index of Fractional Distillation Power for Hydrocarbon Mixtures
R. L. Geddes

Turbulent Heat Transfer Inside Tubes and the Analogy Among Heat, Mass, and Momentum Transfer
W. L. Friend and A. B. Metzner

Gas-Solid Contacting with Ozone Decomposition Reaction
C. G. Frye, W. C. Lake, and H. C. Eckstrom

Wetting Effects on Boiling Heat Transfer: The Cooper-Stearic Acid System
W. B. Harrison and Zelvin Levine

Condensation of Vapor in the Presence of Noncondensing Gas
Ferdinand Votta, Jr., and Charles A. Walker

Dissolution Rates of Solids in Mercury and Aqueous Liquids: The Development of a New Type of Rotating Dissolution Cell
J. A. R. Bennett and J. B. Lewis

Surface Dynamics of Fluidized Beds and Quality of Fluidization
W. J. Rice and R. H. Wilhelm

Volumetric Properties of Nonpolar Gaseous Mixtures
J. M. Prausnitz and R. D. Gunn

Kinetics of Steady State Phase Transitions
Kenneth A. Wilde

On Phase Equilibrium at the Gas-Liquid Interface During Absorption
L. E. Scriven and R. L. Pigford

Characteristics of Gas Pockets in Fluidized Beds
George Yasui and L. N. Johanson

Extraction of Sugar from Beets
H. H. Yang and J. C. Brier

Radial Porosity Variations in Packed Beds
L. H. S. Roblee, R. M. Baird, and J. W. Tierney

Perforated Plate Efficiency: Effect of Design and Operating Variables
J. D. Hellums, C. J. Braulick, C. D. Lyda, and Mathew Van Winkle

A Theoretical-Empirical Approach to the Mechanism of Particle Entrainment from Fluidized Beds
F. A. Zenz and N. A. Weil

Density: Reduced-State Correlations for the Inert Gases
Charles E. Hamrin, Jr., and George Thodos

Flow Patterns of Liquids in Agitated Vessels
Shuichi Aiba

UNIVERSITY
OF MICHIGAN

JAN 13 1959

ENGINEERING
LIBRARY

YORKMESH[®] DEMISTERS

will improve
**PROCESS VESSEL
PERFORMANCE**

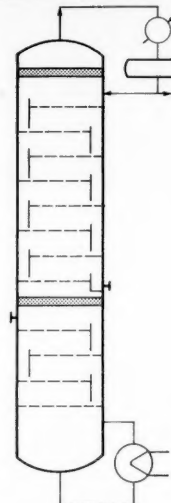
It will pay you to investigate YORKMESH DEMISTERS if your process vessels need a lift in efficiency. The versatile knitted wire-mesh pads are being used more and more throughout industry to *stop* liquid entrainment and improve the performance of:

Vacuum Towers, Distillation Equipment, Gas Absorbers, Scrubbers, Evaporators, Knock-Out Drums, Steam Drums and many others.

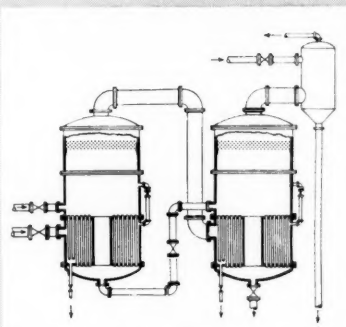
Here is what happens when YORKMESH DEMISTERS are installed:

1. As vapor disengages from liquid it carries with it fine liquid droplets.
2. When the vapor stream passes thru the fine wire mesh, the liquid droplets impinge on the wire surfaces, coalesce into large drops, and fall.
3. The vapor is now dry and free from entrained liquid.

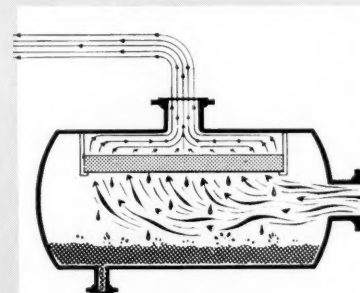
Send us details on your type of process vessel or operation, vapor flow rate, pressure, temperature, and density or molecular weight; approximate amount of entrained liquid, viscosity, and specific gravity . . . for existing equipment advise dimensions, indicate vertical or horizontal vessel and material of construction required for mesh and grids. Complete details will make it possible for us to present our recommendations and quotation.



The efficiency of separation and throughput capacity of distillation equipment can be significantly improved by the use of YORKMESH DEMISTERS.



YORKMESH DEMISTERS installed in evaporators avoid product loss and provide clean condensate.



YORKMESH DEMISTERS installed in Knock-Out Drums result in high separation efficiency at low pressure drop.



OTTO H. YORK CO., INC.
6 CENTRAL AVE. • WEST ORANGE, N.J.

A.I.Ch.E. JOURNAL

DECEMBER 1958 • VOL. 4, NO. 4

PUBLISHER

F. J. Van Antwerpen

EDITOR

Harding Bliss

ADVERTISING MANAGER

L. T. Dupree

ADVISORY BOARD

C. M. Cooper, O. E. Dwyer, W. C. Edmister, E. R. Gilliland, A. N. Hixson,

H. F. Johnstone, W. R. Marshall, Jr., R. H. Newton, R. L. Pigford,

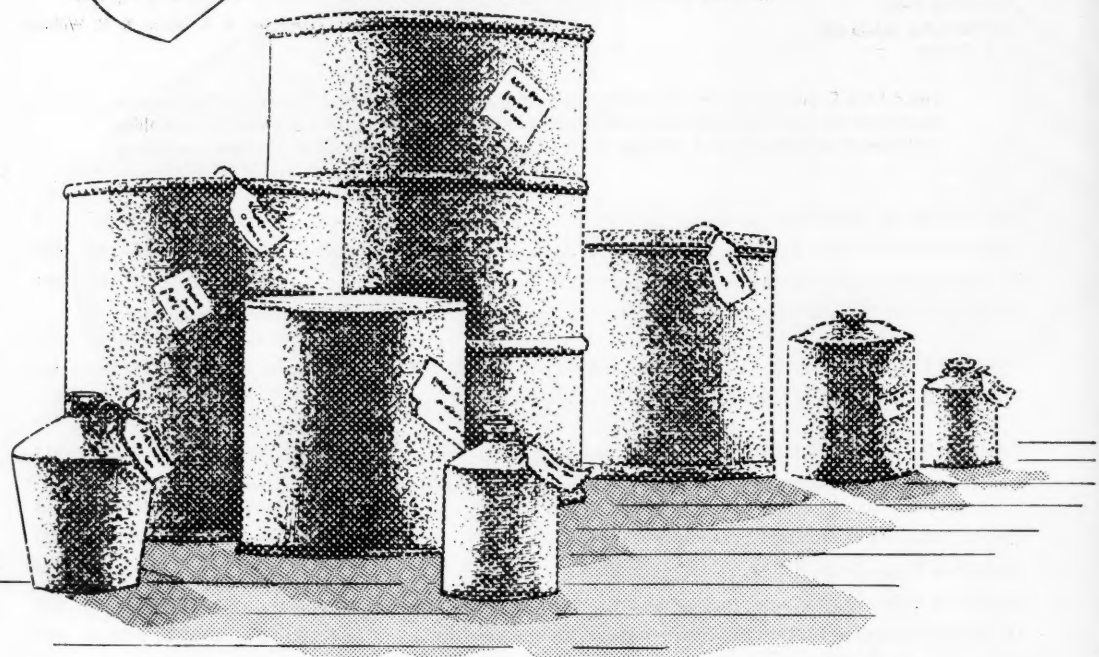
E. L. Piret, J. M. Smith, Theodore Vermeulen, R. R. White, R. H. Wilhelm

The A.I.Ch.E. Journal, an official publication of the American Institute of Chemical Engineers, is devoted in the main to theoretical developments and research in chemical engineering and allied branches of engineering and science. Manuscripts should be submitted to the New York office.

Opportunities for Engineers	7
Liquid-Phase Adsorption Equilibria	Edward B. Stuart and James Coull 383
A General Index of Fractional Distillation Power for Hydrocarbon Mixtures	R. L. Geddes 389
Turbulent Heat Transfer Inside Tubes and the Analogy Among Heat, Mass, and Momentum Transfer	W. L. Friend and A. B. Metzner 393
Gas-Solid Contacting with Ozone Decomposition Reaction	C. G. Frye, W. C. Lake, and H. C. Eckstrom 403
Wetting Effects on Boiling Heat Transfer: the Copper-Stearic Acid System	W. B. Harrison and Zelvin Levine 409
Condensation of Vapor in the Presence of Noncondensing Gas	Ferdinand Votta, Jr., and Charles A. Walker 413
Dissolution Rates of Solids in Mercury and Aqueous Liquids: The Development of a New Type of Rotating Dissolution Cell	J. A. R. Bennett and J. B. Lewis 418
Surface Dynamics of Fluidized Beds and Quality of Fluidization	W. J. Rice and R. H. Wilhelm 423
Volumetric Properties of Nonpolar Gaseous Mixtures	J. M. Prausnitz and R. D. Gunn 430
Kinetics of Steady State Phase Transitions	Kenneth A. Wilde 436
On Phase Equilibrium at the Gas-Liquid Interface During Absorption	L. E. Scriven and R. L. Pigford 439
Characteristics of Gas Pockets in Fluidized Beds	George Yasui and L. N. Johanson 445
Extraction of Sugar from Beets	H. H. Yang and J. C. Brier 453
Radial Porosity Variations in Packed Beds	L. H. S. Roblee, R. M. Baird, and J. W. Tierney 460
Perforated Plate Efficiency: Effect of Design and Operating Variables	J. D. Hellums, C. J. Braulick, C. D. Lyda, and Mathew Van Winkle 465
A Theoretical-Empirical Approach to the Mechanism of Particle Entrainment from Fluidized Beds	F. A. Zenz and N. A. Weil 472
Density: Reduced State Correlations for the Inert Gases	Charles E. Hamrin, Jr., and George Thodos 480
Flow Patterns of Liquids in Agitated Vessels	Shuichi Aiba 485
Index	490
Communications to the Editor	
Pseudocritical Constants from Volumetric Data for Gas Mixtures	J. M. Prausnitz and R. D. Gunn 494
Note on the Analogy Between Momentum Transfer and Heat or Mass Transfer for a Homogeneous Isotropic Turbulent Field	Thomas J. Hanratty 495
The Derivation of an Equation for Predicting Minimum Spouting Velocity	L. A. Madonna and R. F. Lama 497
A New Type of Countercurrent Column for the Zirconium-Hafnium Separation	Nadine Isaac and R. De Witte 498
Steady State Absorption of a Sparingly Soluble Gas in an Agitated Tank with Simultaneous Irreversible First-Order Reaction	E. N. Lightfoot 499
Books	500

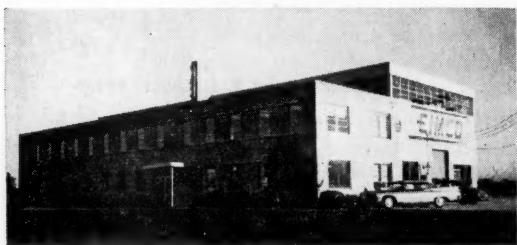
Publication Office, Richmond, Virginia. Published quarterly in March, June, September, and December by the American Institute of Chemical Engineers, 25 West 45 Street, New York 36 New York. Manuscripts and other communications should be sent to the New York office. Correspondence with the editor may be addressed to him at Yale University, 225 Prospect Street, New Haven 11, Connecticut. Statements and opinions in the *A.I.Ch.E. Journal* are those of the contributors, and the American Institute of Chemical Engineers assumes no responsibility for them. Subscriptions: one year, member \$4.50, nonmember \$9.00; two years, member \$7.50, nonmember \$15.00; additional yearly postage, Canada 50 cents, Pan American Union \$1.50, other foreign \$2.00 (foreign subscriptions payable in advance). Single copies: \$3.00. Second-class mail. Postage paid at Richmond, Virginia. Copyright 1958 by the American Institute of Chemical Engineers. National headquarters of A.I.Ch.E. is concerned about nondelivery of copies of the *A.I.Ch.E. Journal* and urgently requests subscribers to give prompt notification of any change of address. Sixty days must be allowed for changes to be made in the records.

STUBBORN PROCESS PROBLEMS INSIDE



DELIVER TO EIMCO FILTRATION "TROUBLE SHOOTERS"

When you "package" your filtration troubles and present them to Eimco for study, you're moving in the right direction. Stay on that route and you'll wind up with a modern, labor-saving plant designed to give you the best results for every phase of your flow sheet handling liquid-solids separation.



OUR MODERN RESEARCH AND DEVELOPMENT CENTER AND PILOT PLANT AT PALATINE, ILL. VISITORS ARE WELCOME.

Here's what you get when Eimco goes to work for you:

1. Experience of trained, competent engineers at our Research and Development Center.
2. Facilities of a modern, completely equipped pilot plant.
3. A detailed, comprehensive written report containing verified test data.
4. Honest equipment recommendations to fit your requirements . . . based on dependable answers.

Eimco skills, experience and facilities that have won widespread client confidence are at your disposal. Prepare to use them, today!

THE EIMCO CORPORATION
Salt Lake City, Utah—U.S.A. • Export Offices: Eimco Bldg., 52 South St., New York City
Research and Development Center—Palatine, Ill.

New York, N.Y. Chicago, Ill. San Mateo, Calif. El Paso, Texas Birmingham, Ala. Duluth, Minn. Kellogg, Ida. Baltimore, Md. Pittsburgh, Pa. Seattle, Wash.
Cleveland, Ohio Houston, Texas Vancouver, B.C. London, England Gateshead, England Paris, France Milan, Italy Johannesburg, South Africa



B-298

ADSORPTION IS A BASIC CHEMICAL ENGINEERING PROCESS

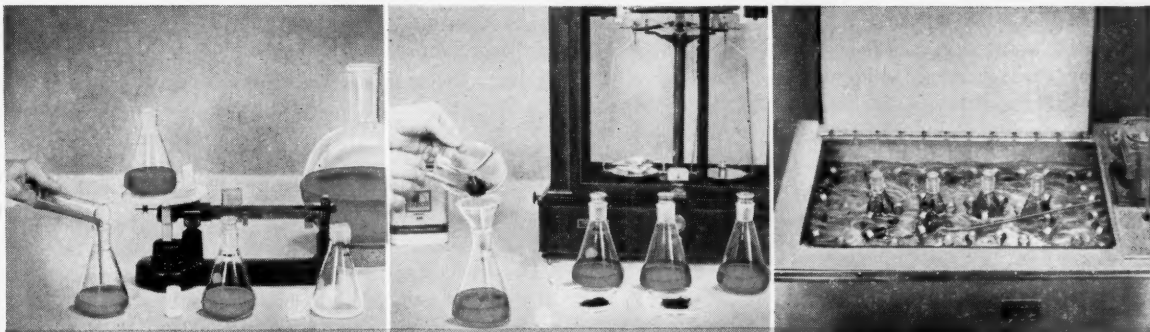


REG. U. S. PAT. OFF.

DARCO *Digest*

CHEMICALS DIVISION, ATLAS POWDER COMPANY, WILMINGTON 99, DELAWARE • Atlas Powder Company, Canada, Ltd., Brantford, Ontario, Canada

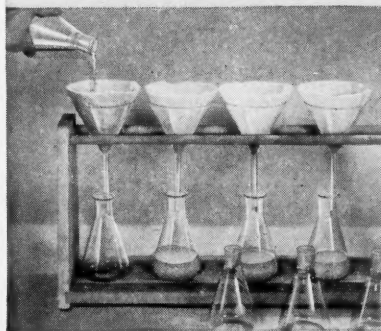
Simple tests in your lab determine dosage of DARCO activated carbon to solve your purification problem



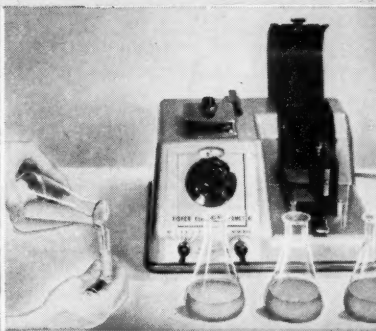
1 Measure out four equal (100-gm or 100-ml.) samples of liquid to be purified . . . to establish 3 points on adsorption curve for your liquid.

2 Add 0.5, 1.0 and 1.5 grams of DARCO activated carbon to samples 1, 2 and 3 respectively. The number 4 sample is your untreated control.

3 Agitate all samples for one-half hour in water bath at a safe temperature for your liquid. Motor-driven agitator assures uniform shaking.



4 Filter out carbon from samples 1, 2 and 3. Collect sample only after filtrate becomes clear. For viscous liquids you may need to apply suction.



5 Measure residual color of all samples with a colorimeter. For other purification uses, measure desired characteristic (% impurity, for instance).



6 Plot color adsorption vs. carbon dosage on a Darcograph. Read off the dosage of DARCO needed to get the residual color you require.

You can make these tests easily in your own laboratory, using equipment which you have on hand. By varying temperatures, contact time and dosage ranges, you can establish optimum treatment conditions. Write to Atlas for a Darcograph, instructions on its

use, and samples of Darco for your evaluation. Give us the details of your specific problem, and we can recommend the most effective Darco grade for your particular use . . . and thus save you testing grades that our experience indicates are less suitable.

PROCESS SIMULATION

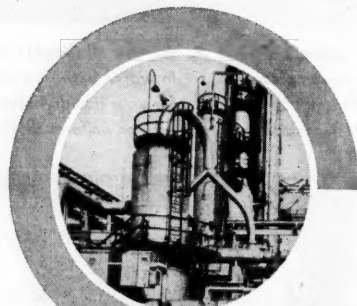
What is it?

Process Simulation is a technique of equating electronically the operation of a given process whether chemical or petroleum.

Essentially it involves the use of analog computing equipment whose components can operate on d-c voltages in the same manner that a refinery operates on the material which it is processing.

Process Simulation, applied to a process design problem, provides the engineer with a miniature process plant at his fingertips, one which can be quickly and conveniently manipulated to operate in any way he chooses, either as it should, or even as it shouldn't.

The desirability of applying Process Simulation to your design problems can be quickly and economically explored at Electronic Associates, Inc. computation centers in Princeton, New Jersey; Los Angeles, California; and Brussels, Belgium.



PROCESS SIMULATION COMES OF AGE



Detailed information can be obtained by mail, wire or telephone :

Electronic Associates, Inc.

Manufacturers of **PACE** *Precision Analog Computing Equipment*

LONG BRANCH, NEW JERSEY Dept. AI-12

Tel. Capital 9-1100

Opportunities for Engineers

Certain relatively recent developments seem to point to a future demand for engineers which may be greatly in excess of any figures based on a simple extrapolation of past trends with allowances for normal growth. We may be heading into a greatly changed condition in which the required number of capable engineers must rise by an order of magnitude rather than by a simple arithmetic amount.

In the immediate past most engineers have been corporation or government employees with a relatively small number in private practice and in teaching. It is to be expected, of course, that these occupations will grow normally with the population.

Consider, however, these challenges and opportunities, which are recent in origin or in increased importance:

- Rockets and missiles
- Conservation of natural resources
- Food requirements
- Assistance to the relatively undeveloped nations

There is very little in the past which can help us to estimate the need for engineers in these fields in the future, but certainly such need will be acute.

Rockets and missiles must not be considered solely as matters of defense and war or as the domain of "Buck Rogers." In the future there will be peaceful, economically sound applications of these devices which will be of great value when we have the engineering manpower to develop and perfect them. Also such developments always breed by-products of wide utility; in this case one may visualize new special power sources, control instruments, and materials of construction.

Our natural resources are becoming more and more strained to maintain our present living standards for our growing population. Population pressure, known elsewhere for a long time, is coming to this country.

In some cases we, as a nation, are in considerable danger. Water is one item about which we may be in a grave situation sooner than one might think. Our profligate use of water must be restrained, and engineers must be concerned more and more with preservation of water supplies, proper reuse of water, reduction of pollution, and demineralization of sea and brackish waters. It should be noted that a very effective beginning has been made on the demineralization of sea water but only as a result of a concentration of engineering effort on the problem.

At the moment one can hardly become unduly disturbed at the possibility of a shortage of food in this great country, but water shortages, population growth, upsetting of nature's balance by the destruction of trees for housing and highways, and the gradual reduction of trace elements in our soils could combine to bring trouble here sooner rather than later. Food shortages in other parts of the world are, of course, of long duration.

Assistance to less-favored nations is often essentially a matter of engineering alone. Their problems of food, water, transportation, communication, power, and development of industries will be solved by engineers and not by politicians, economists, or bankers. It is up to us to help them; if we do not, we may well imagine that engineers of another nation will do so. It is also worthy of note that engineering assistance is not at all costly when compared with blind outpourings of money for temporary relief.

All these problems can be solved; the scientific principles are well known. It is the solution of them in a manner which we can afford to pay for which is required. The best process, combined with the optimum use of capital and of equipment, must be found. This is engineering, pure and simple. The opportunity for competent engineers seems limitless.

H.B.



Millions of tiny pores like these make Davison Silica Gel "vapor-thirsty"!

THEY STRONGLY ATTRACT CONDENSABLE VAPORS, HOLD THEM AS LIQUIDS

it any wonder that Davison Silica Gel is ideally suited for air and gas dehydration?

One cubic inch of this high capacity adsorbent and desiccant contains pores having a surface area of about 90,000 square feet (roughly the same surface area as the flight decks of two aircraft carriers). Davison Silica Gel can adsorb up to 40% of its weight of moisture at

100% relative humidity. Even when saturated, it remains dry and free flowing.

Davison Silica Gel is specially treated to give optimum resistance to attrition, and promotes rapid dehydration because of its granular shape. High purity (99.70% SiO_2) and chemical inertness contribute to its resistance to fouling.

A variety of particle sizes, densities and adsorptive capacities are available. Each has been developed to meet specific application demands. There is one to suit yours.

W.R. GRACE & CO.
DAVISON CHEMICAL DIVISION
BALTIMORE 5, MARYLAND



A
temp
ascrib
deriv
tratio
data
syste
20.7

Ec
the
sorpti
soluti
comp
of ex
of co
as de
great
equil

Ka
desig
chron
on th
immor
conce
static
in a
hydro
ford
has
efflu
tion o
alum

Ea
equili
arom
that
be tr
the o
separ
simila
used
um

EFFECT
AND S

Fro

Ads
t

91
92
70
22-08

6

SA-

(a)
(b)

Vol.

Liquid-phase Adsorption Equilibria

EDWARD B. STUART and JAMES COULL, University of Pittsburgh, Pittsburgh, Pennsylvania

A correlating equation for liquid-phase adsorption equilibria, including the effects of temperature and pore diameter, is presented, together with a derivation of the equation ascribing the equilibration process of physical adsorption to van der Waal's forces. The derivation is based on the effect of temperature and surface configuration on the concentration of adsorbate at the surface. The correlating equation was tested with experimental data for the benzene-cyclohexane-silica-gel system and the toluene-isoctane-silica-gel system. Temperatures ranged between 23.9° and 99°C. and the pore diameters between 20.7 and 149.5 Å.

Equilibrium data are unimportant in the design of percolation or contact adsorption equipment, and in decolorizing solutions the low concentration of the component to be removed allows the use of excess adsorbent, but with the advent of countercurrent liquid-phase contacting as described by Eagle and Scott (9), a greater need exists for more liquid-phase equilibrium data.

Karnofsky (18) has suggested that the design of an adsorption percolation or chromatographic column may be based on the concentrations in the pores or immobile phase as a function of liquid concentrations. Mair (23) has correlated static equilibrium data with kinetic data in a packed column for a number of hydrocarbon binary solutions. Weatherford (30), using static equilibrium data, has predicted the concentrations of effluents in the chromatographic separation of a benzene-cyclohexane mixture on alumina.

Eagle and Scott (10), reporting on equilibrium data used on a mixture of aromatic and kerosene distillates, found that this polycomponent system could be treated as a simple binary system, in the design of adsorption columns for separating aromatics from nonaromatics, similar to the key-component method used in polycomponent-distillation-column design.

EFFECT OF TEMPERATURE AND SURFACE CONFIGURATION

From a chemical engineering viewpoint,

fundamental theories on phase equilibria are useful in that they reduce the amount of experimental data needed for design calculations. It is sufficient but not necessary that the theory describe the mechanism of equilibration. A contribution to engineering adsorption theory could be made if the effect of one or more of the variables could be correlated for liquid-phase selective adsorption.

The Brunauer-Emmett-Teller equation has been very successful in representing the adsorption of single gases and vapors (5). Lewis and others (20) have correlated vapor-phase adsorption capacities for a binary system with the adsorption capacities of the pure components, and a correlation of liquid-phase adsorption capacity with nitrogen or butane surface areas has been presented by Rescorla (29) and Mair (22). The latter work, which was intended to facilitate surface-area measurements, is based on a single temperature and a constant concentration of the starting binary solution.

To aid in the design of fractionation equipment, it would be desirable to be able to estimate the effect of the operating variables of temperature, pressure, and adsorbent properties. The intrinsic pressures in a liquid are very large compared with the operating-pressure variation; consequently the effect of pressure was not studied. The two variables chosen were surface configuration and temperature.

Silica gel was chosen as the adsorbent because its high adsorption capacity and industrial importance (9, 10, 15, 21, 23)

increases the usefulness of equilibrium data based on it. Three commercial types of silica gel were studied: Davison 912, 922, and 70. Gels 912 and 922 differed only in their particular size range; gel 70 had a larger average pore diameter.

The choice of a liquid binary was based partially on industrial interest in aromatic-nonaromatic separation (9, 10, 15, 23). The benzene-cyclohexane system has the additional advantage of having similar molecular dimensions, which decreases the problem of selectivity by a screening effect alone.

Since the range of data was limited, the correlating equation presented here was checked by supplementary data from the literature. The experimental data were taken at three temperatures, 33°, 52.6°, and 77°C., three different silica gels with two average pore diameters being used, for the complete concentration range of a benzene-cyclohexane binary solution. The literature data used included four isotherms from 23.9° to 99°C., two additional silica gels and a silica-alumina gel, and the toluene-isoctane system.

PRESENT THEORIES ON ADSORPTION

The adsorption of a vapor increases with pressure at constant temperature, and at a high temperature the volume adsorbed is small since the adsorption process is exothermic. When both the adsorbed volume and pressure are low, an equation analogous to Henry's Law will represent the data, and so

$$G' = kp \quad (1)$$

At higher adsorption capacities the volume adsorbed is a power function of the pressure and is expressed as

TABLE I
SUMMARY OF ADSORBENT PROPERTIES AND CORRELATING CONSTANTS

Adsorbent type	Adsorbent source	Pore Volume cc./g.	Surface Area sq. m./g.	Pore Diam., D Å	Mesh Size	ξ	d Å	k °K	ψ °K	Lit. cited
Benzene-cyclohexane system										
912	Davison	0.429	698.8	24.6	28-200	5.92	14.5	54.2	77.5	This Work
922	Davison	0.429	698.8	24.6	-200	5.92	14.5	54.2	77.5	This Work
70	Davison	1.088	290	149.5	24-250	1.22	14.5	54.2	77.5	This Work
22-08 (a)	Davison	0.43	700	24	-200	6.39	14.5	54.2	77.5	23
1 (b)	Davison	0.350	630	22.2	28-200	8.32	14.5	54.2	77.5	10
Toluene-isoctane system										
61 (b)	California Res.	0.304	587	20.7	10-14	11.15	14.5	54.2	31.0	10
1 (b)	Davison	0.350	630	22.2	28-200	8.32	14.5	54.2	31.0	10
SA-4 (b)	Socony	0.395	388	40.7	6-10	2.41	14.5	54.2	31.0	10

(a) This gel is equivalent to Davison No. 922.

(b) Pore volumes and surface areas originally obtained from butane isotherms are corrected to nitrogen values to correspond to gels 922, 912, and 70.

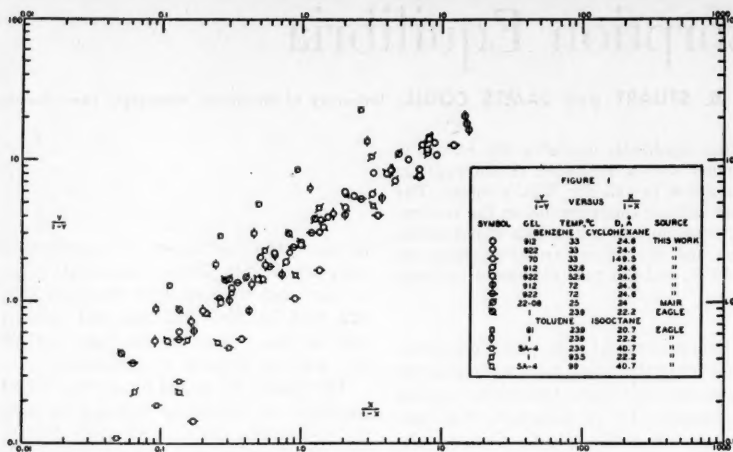


Fig. 1—Experimental data showing mole ratio in adsorbed phase vs. mole ratio in bulk phase.

$$G' = k' p^{1/n} \quad (2)$$

where n is greater than 1. Equation (2) was developed by Freundlich (14, 25) and when obeyed by the system is quite useful for engineering calculations because of its simplicity. It can be used to correlate data from a liquid-phase adsorption process when used in the following form

$$G = k' x^{1/n} \quad (3)$$

Zeldowitsch (32) added flexibility to the vapor-phase Freundlich Equation (2) by empirically representing the constants k' and n as functions of temperature:

$$\frac{1}{n} = \frac{T}{T_F} : \log k' = b_1 T + b_2 \quad (4)$$

where T is the temperature of adsorption and T_F a limiting temperature. Above T_F

$$\frac{1}{n} = 1 : \log k' = b_3 + \frac{b_4}{T} \quad (5)$$

Polanyi, who advanced a theory based on the assumption that adsorption was a physical process and that the adsorbed phase was many layers thick (24), defined the adsorption potential as the work done by the adsorption forces in bringing a molecule to a point in the adsorbed state;

$$\epsilon_i = \int_{b_s}^{b_i} v dp \quad (6)$$

Polanyi assumed that an equation of state that describes the effect of temperature and pressure of the gas could be used for the adsorbate. The potential theory also assumes that the potential does not change with temperature, and so

$$\frac{d\epsilon_i}{dT} = 0 \quad (7)$$

Berenyi, calculating ϵ_i as a function of the volume adsorbed, assumed as a first approximation that the vapor behaved as

an ideal gas and that the liquid was incompressible. Berenyi's equation is as follows:

$$\epsilon_i = \int_{p_s}^{p_i} \frac{RT}{p} dp = RT \ln \frac{p_0}{p_s} \quad (8)$$

Although the Polanyi potential theory does not offer an expression for an adsorption isotherm, the potential theory using a three-dimensional equation of state for the adsorbed phase can account for the temperature dependency of adsorption. Polanyi and Berenyi (27) also found empirically that the maximum adsorption potential ϵ_0 was related to the van der Waal's constant a for a single adsorbent as follows:

$$\epsilon_0 = k \sqrt{a} \quad (9)$$

Equation (9) is similar to the expression $(\sqrt{a_a} \sqrt{a_b})$ for attractive potential between two molecules as proposed by Berthelot (4).

In the determination of the selective adsorption capacity, or the quantity of more strongly adsorbed component per unit weight of adsorbent, it is assumed that only one component is adsorbed. Experimentally, the adsorbent is added to a binary of known composition. The change in composition of the liquid is recorded and the selective adsorptive capacity is defined as

$$G' = \frac{v}{m} \left[\frac{X_0 - X}{1 - X} \right] \quad (10)$$

where G' is the selective adsorptive capacity in volume of adsorbate per unit weight of adsorbent, v is the volume of the initial solution, m is the weight of adsorbent, and X_0 and X are the initial and final volume fraction of adsorbate respectively.

If the adsorbed phase can be distinctly separated from the equilibrium liquid, it is assumed that the immobile liquid, or

liquid in the pore space, constitutes a pseudoadsorbed phase (11, 30). For process-design calculations, the equilibrium data are more useful in the form of an $x-y$ diagram (10, 18). The adsorbed-phase concentration may be calculated by the following equation:

$$Y = \frac{G' + (V_p - G')X}{V_p} \quad (11)$$

where Y is the volume fraction of strongly adsorbed component in the pore volume, V_p is the pore volume, and G' and X are defined in Equation (10). By use of the liquid densities the equilibrium data may be presented by either weight or mole fractions.

The relative adsorbability α is defined as follows (23)

$$\left(\frac{y}{1-y} \right) = \alpha \left(\frac{x}{1-x} \right) \quad (12)$$

where y is the mole fraction of more strongly adsorbed component in the adsorbed phase or pore space, and x is the mole fraction of the same component in the equilibrium liquid.

This definition of α in Equation (12) is analogous to the relative volatility in vapor-liquid equilibrium calculations. It is of interest to note that Eagle (10) using Equation (12), correlated benzene cyclohexane data essentially assuming a constant relative adsorbability, while Main (28) records the variation in α with concentration for the same system.

Equation (12) is plotted as in $y/1-y$ vs. in $x/1-x$ should give a straight line with a slope of one and, an intercept equal to $\ln \alpha$ if α is a constant over the experimental range.

Corrigan and Koble (7, 19) have suggested an equation primarily for chemical adsorption but including physical adsorption. By the use of the methods of Hougen and Watson (17) Equation (13) is derived relating the concentration of one component on a solid surface to the partial pressures of the binary and the equilibrium constants for the individual adsorption reactions.

$$C_{a1} = \frac{K_a p_a}{(1 + K_a p_a + K_b p_b)} \quad (13)$$

By extending Corrigan's discussion to include a concentration ratio of the two adsorbed components, one obtains,

$$\frac{C_{a1}}{C_{b1}} = \frac{K_a p_a}{K_b p_b} \quad (14)$$

The temperature dependency of K is given by,

$$\ln K = \frac{-\Delta H^0}{RT} + \frac{\Delta S^0}{R} \quad (15)$$

If liquid concentrations are used instead of gas partial pressures in Equation (14) and with logarithms,

$$\frac{1}{RT} \int_{P_y}^{P_x} v_i dp \quad (24)$$

$$= \left[\ln \frac{RT}{v_i - b} - \frac{b}{v_i - b} - \frac{2a}{RTv_i} \right]_{v_i y}^{v_i x}$$

Equation (21) may be written in the form of mole ratios for a binary solution as,

$$\frac{y}{1-y} = \frac{x}{1-x} \quad (25)$$

where v_a and v_b are volumes of component A and B at the conditions in each phase.

Using Equation (24) in (25) and taking logarithms of both sides of the resulting equation give the following:

$$\ln \frac{\frac{y}{1-y}}{\frac{x}{1-x}} = \ln \left[\frac{v_b - b_b}{v_a - b_b} \right] \quad (26)$$

$$+ \frac{b_b(v_b - b_b)}{b_b(v_a - b_b)} + \frac{2a_b}{RTv_b} - \frac{2a_a}{RTv_a} \right]_{v_y}^{v_x}$$

It is assumed that constants a and b are functions of composition since the proper representation of the volume of each component at the pressure of each phase should include a variation of attractive force per unit area represented by a , and minimum volume represented by b . The free volume for the liquid is given approximately by the equation

$$(v - b) = v_f \quad (27)$$

where b is the van der Waal's constant in Equation (23). As stated in the previous section, the free volumes for liquids having the same entropy of vaporization should be equal (12, 13).

Since most nonpolar compounds follow Trouton's rule, $\Delta H_{LV}/T = \Delta S_{LV} = \text{constant}$ and for nonpolar liquids Equation (26) reduces to,

$$\ln \left(\frac{y}{1-y} \right) \left(\frac{1-x}{x} \right) - \left[\frac{b_{ax}}{b_{bx}} - \frac{b_{ay}}{b_{by}} \right. \\ \left. - \frac{2}{RT} \left(\frac{a_{ax}}{v_{ax}} - \frac{a_{bx}}{v_{bx}} + \frac{a_{by}}{v_{by}} - \frac{a_{ay}}{v_{ay}} \right) \right] \quad (28)$$

the interaction constants for both components will be the same so that Equation (28) becomes,

$$\ln \left(\frac{y}{1-y} \right) \left(\frac{1-x}{x} \right) \quad (29)$$

$$= \frac{2}{RT} \left[a_y \left(\frac{1}{v_{ay}} - \frac{1}{v_{by}} \right) - a_x \left(\frac{1}{v_{ax}} - \frac{1}{v_{bx}} \right) \right]$$

The attractive force constant in the adsorbed phase, a_y , is dependent on the attractive force of the solid surface and of the liquid.

Comparing the thermodynamic equation of state,

$$P + T \left(\frac{\partial P}{\partial T} \right)_v - \left(\frac{\partial E}{\partial v} \right)_T \quad (30)$$

with Equation (23)

$$\left(\frac{\partial E}{\partial v} \right)_T = \frac{a}{v^2} \quad (31)$$

where the cohesive energy is defined as,

$$E = -\frac{a}{v} \quad (32)$$

If the attractive potential energy between the adsorbate and the surface, ϕ is divided by the effective volume, v_e ,

$$\frac{\phi}{v_e} = -\frac{a}{v_e^2} \quad (33)$$

the result is a potential-energy density term having the dimensions of force per unit area.

To account for varying pore or capillary curvature, the attractive force per unit area may be referred to a plane surface equivalent.

With the assumption of an effective distance, d , from the surface of the adsorbent, the attractive force per unit of surface area for a flat plane is,

$$\frac{a_y}{v_{ep}^2} = \frac{a_y}{d^2} \quad (34)$$

The attractive force per unit area in a capillary of radius r is,

$$\frac{a_0}{v_{ec}^2} = \left(\frac{a_0}{d^2} \right) \left(\frac{2r}{2r-d} \right)^2 \quad (35)$$

Equating the terms for attractive force per unit area and solving for a_y result in:

$$a_y = a_0 \left(\frac{2r}{2r-d} \right)^2 = a_0 \left(\frac{D}{D-d} \right)^2 \quad (36)$$

where a_0 is a measure of the attractive force between the binary liquid at composition y and the adsorbent corrected to zero curvature.

Substitution of Equation (36) in Equation (29) gives the following

$$\ln \left(\frac{y}{1-y} \right) \left(\frac{1-x}{x} \right) \quad (37)$$

$$= \frac{2}{RT} \left[\left(\frac{D}{D-d} \right)^2 a_0 \Delta \rho_y - a_x \Delta \rho_x \right]$$

where $\Delta \rho_y$ and $\Delta \rho_x$ are the density differences of the adsorbed components and liquid components, respectively.

The attractive force constant, a_0 , in the adsorbed phase will be a function of y . Since the solid has a constant volume fraction in the combination of adsorbed binary and surface, a_0 should not vary greatly with composition.

The constant a_x shows a variation of approximately 10% over the composition range studied for the system benzene-cyclohexane (31). Assuming a_x to be constant with composition leads to an equation of the following form,

$$\ln \left(\frac{y}{1-y} \right) = \ln \left(\frac{x}{1-x} \right) + M \quad (38)$$

where

$$M = \frac{2}{RT} \left[\left(\frac{D}{D-d} \right)^2 a_0 \Delta \rho_y - a_x \Delta \rho_x \right]$$

Equation (38) indicates that a plot of $\ln(y/1-y)$ vs. $\ln(x/1-x)$ at a constant temperature would give a straight line with a slope of plus one and an intercept equal to M . Figure 1 shows that the isotherms have slopes less than one, and the slope does not correlate with the pore radius. If a_x is a weak function of $\ln(x/1-x)$, Equation (38) may be written as,

$$\ln \left(\frac{y}{1-y} \right) = \ln \left(\frac{x}{1-x} \right) \cdot \left[1 - \frac{\psi}{T} \right] + \frac{\xi}{T} \quad (39)$$

where

$$\psi = \frac{2a_x \Delta \rho_x}{R \ln \left(\frac{x}{1-x} \right)}$$

$$\xi = \left(\frac{2r}{2r-d} \right)^2 = \left(\frac{D}{D-d} \right)^2$$

$$k = \frac{2a_0 \Delta \rho_y}{R}$$

In exponential form Equation (39) becomes

$$\left(\frac{y}{1-y} \right) = e^{\xi k/T} \left(\frac{x}{1-x} \right)^{1-\psi/T} \quad (40)$$

Equation (40) indicates that liquid-phase data may be correlated by obtaining constants k , ψ , and d for the binary system on an adsorbent which has an average pore diameter D .

To calculate the constants for a system, a log-log plot of equilibrium data can be made at a minimum of two temperatures or pore diameters, from which the slope and intercept can then be determined. The log of the intercept is called C and the slope M , then the constants are,

$$C = \frac{\xi k}{T} \quad (41)$$

$$M = 1 - \frac{\psi}{T} \quad (42)$$

A plot of M vs. $1/T$ gives ψ since

$$C = \frac{\left(\frac{D}{D-d} \right)^2 k}{T} \quad (43)$$

rearranging

$$\left(\frac{CT}{k} \right)^{1/2} = \frac{D}{D-d} \quad (44)$$

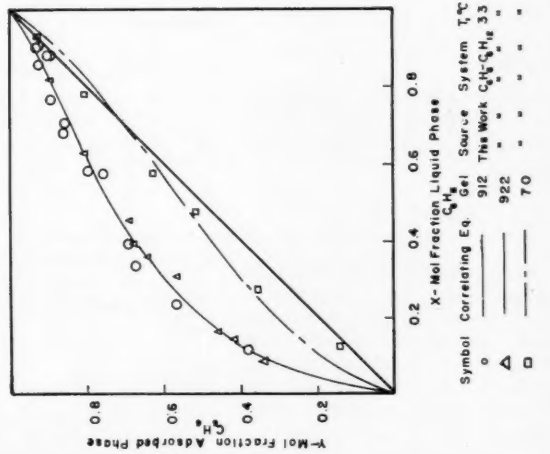
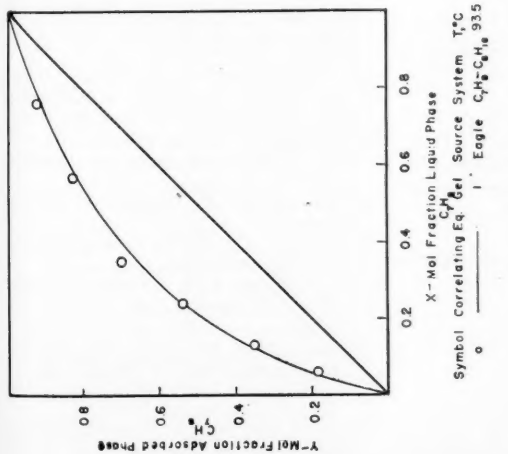
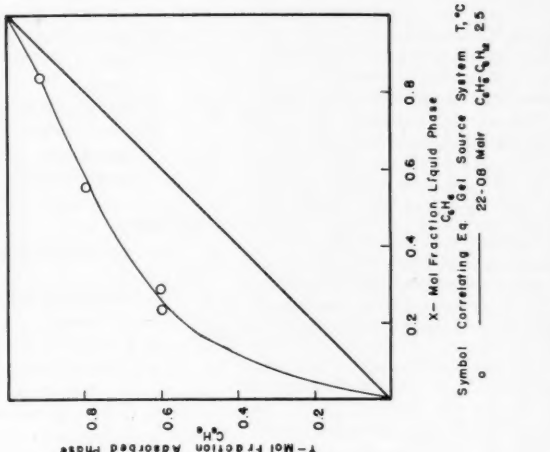
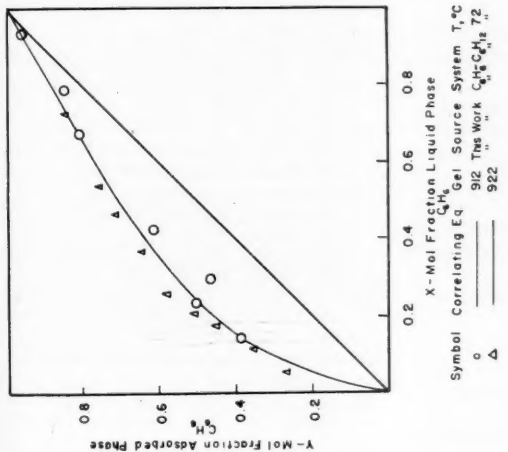
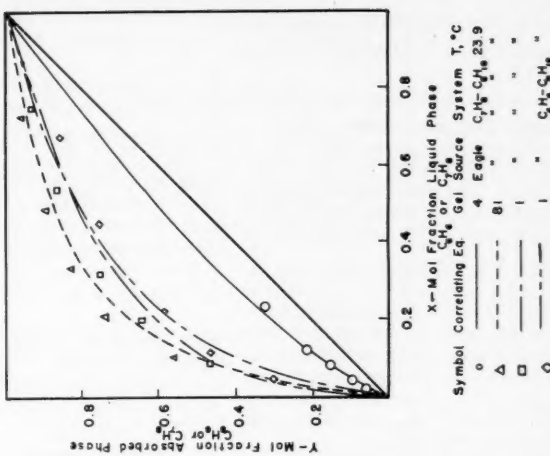
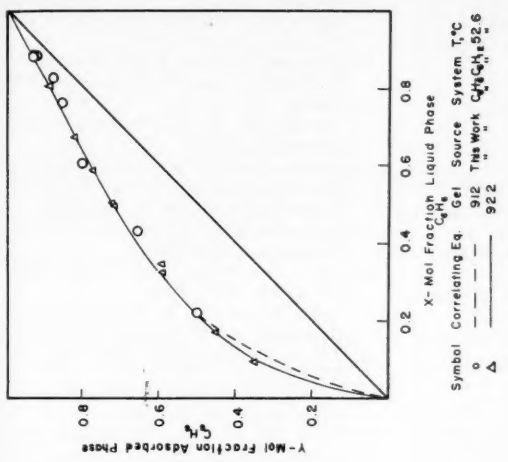


Fig. 3. Mole-fraction curves comparing experimental and predicted equilibrium data.

A General Index of Fractional Distillation Power for Hydrocarbon Mixtures

R. L. GEDDES

Stone and Webster Engineering Corporation, Boston, Massachusetts

Results from precise calculations for fractionation of multicomponent hydrocarbon mixtures show that the relative separations between components are rationalized in a simple manner in terms of the relative volatilities. A quantitative criterion for sharpness of fractionation with complex mixtures, the Fractionation Index, is suggested. This function is useful for general correlation purposes. It also enables prediction of the detailed compositions of the products from a proposed fractionation and thereby simplifies the computation procedures.

With regard to computation of power of fractionation needed in separations of complex hydrocarbon mixtures, relatively little has been contributed in the past twenty-five years on one important problem: Given the required separation to be achieved between two selected feed components, how can an engineer predict the consistent distributions of all other components to distillate and bottoms before making detailed column computations to establish the number of plates and reflux needed to accomplish the specified fractionation? The literature is almost devoid of data which would give a reliable basis for speculations. The present paper will examine this question and present information which gives considerable clarification.

The derivations and the data presented refer to hydrocarbon mixtures for which the vapor-liquid equilibria are reconciled by the laws of ideal solutions. The conditions under which the conclusions are applicable to some other mixtures should become evident during the developments.

LIMITING CASES IN FRACTIONATION

An orientation can be obtained by considering the mathematical relations for two limiting cases in fractionation. The simplest, least powerful continuous fractionation is the equilibrium flash distillation. For each constituent the ratio of its concentration in the vapor to the concentration in the liquid is by definition $y_i/x_i = k_i$. Taking logarithms of both sides, one gets

$$\log(y_i/x_i) = \log(k_i) \\ = \log \alpha_i + \log k_0 \quad (1)$$

where k_0 refers to one of the constituents taken as a reference component and is a constant in the equation. By the definitions used, $\alpha_0 = 1.0$. Any component in the mixture may be taken as the reference component, or the reference component may be a hypothetical one having a volatility intermediate between those of two real components.

The significance of Equation (1) is that plots of $\log(y_i/x_i)$ vs. $\log \alpha_i$ for

flash vaporizations are straight lines having unit slopes. In other words, a fundamental characteristic for this least powerful fractionation is that the logarithmic plots have the slope of 1.0; this is independent of the composition and of the ideality or nonideality of the mixture.

For the case of the fractionator operating at total reflux or infinite reflux ratio, the Fenske-Underwood equation (2, 6)

$$n \log \alpha_i = \log \frac{(x_d/x_w)_i}{(x_d/x_w)_0} \quad (2)$$

relates the terminal composition ratios for any pair of constituents to the relative volatilities and the number of theoretical stages in the fractionator. This may be rearranged to

$$\log(x_d/x_w)_i = n \log \alpha_i \\ + \log(x_d/x_w)_0 \quad (3)$$

and shows that a plot of $\log(x_d/x_w)_i$ vs. $\log \alpha_i$ will give a straight line having a slope equal numerically to the number of theoretical stages. The absolute values of $\log(x_d/x_w)_i$ depend upon the arbitrary value assigned to the reference component, identified in Equation (3) by the subscript zero. Any constituent in the mixture may be taken for reference, but there are advantages in using a constituent for which $x_d/x_w = 1$, and hence $\log(x_d/x_w)_0 = 0$; the reference component may be a hypothetical one having a volatility intermediate between those of two real components.

TABLE 1. CONDITIONS FOR COLUMN COMPUTATIONS FOR WIDE-BOILING-RANGE HYDROCARBON MIXTURE

Case	Theoretical plates		Bottom temperature,* °F.	Molal flows		
	Rectifying	Stripping		D/W	Top L/V	Bottom V/L
A	7	0	440	3.6	0.48	
B	4	3	455	4.2	0.53	0.89
C	2	5	458	4.3	0.42	0.86
D	4	3	410	2.8	0.023	0.54
E	2	2	445	3.8	0.52	0.86
F		7	460	4.4		Total reflux
G	2	2	400	2.8	0.033	0.45
H	2	5	420	3.0	0.044	0.60

*Top temperature is 322°F. in all cases.

The relationships indicated by Equations (1) and (3) are illustrated graphically in Figure 6, with the reference constituents selected such that the lines pass through the origin. The straight line at a 45-deg. angle, having unit slope, defines the terminal composition ratios x_d/x_w as a function of relative volatilities for all single-stage equilibrium vaporizations, at zero reflux or at infinite reflux. Lines are shown having slopes of 2, 3, 4, and 10, corresponding to increasingly sharper fractionation; these slopes are equal numerically to the number of theoretical plates used at infinite reflux ratio. The vertical line having infinite slope indicates the limiting condition for the most powerful fractionation obtainable by using infinite plates and infinite reflux ratio; it represents the hypothetical condition of completely sharp separation between constituents.

When the relative fractionations between components for a given feed composition are defined by equations such as (1) or (3), or by other means, there is but one over-all material balance that will satisfy a given set of x_d/x_w values. The quantities and compositions of distillate and bottoms are determined by the over-all balance equations

$$\left\{ \frac{Fx_f}{(D/W)(x_d/x_w) + 1} \right\}_i = (Wx_w)_i \quad (4)$$

$$D = F - W = F - \sum (Wx_w)_i \quad (5)$$

$$D/W \text{ (calculated)}$$

$$= \{F - \sum (Wx_w)_i\} / \sum (Wx_w)_i \quad (6)$$

$$(Dx_d)_i = (Fx_f)_i - (Wx_w)_i \quad (7)$$

Equations (4) and (6) are solved by using various assumed values for D/W until a value of D/W is found which gives a consistent value for the calculated W .

Equation (4) is derived from Equation (7) and will be recognized as one form of the equations commonly used for evaluating flash vaporizations. In general, Equations (7) and (4) are the over-all material balance equations which apply to all fractionation problems.

EFFECT OF REFLUX RATIO AND FEED-PLATE LOCATION

In contrast with the simplicity of the variables for the single-stage equilibrium separation or the total reflux fractionation, the separations in the practical fractionator involve the effects of variable plates and variable reflux ratios in both rectifying and stripping sections. Both theory and experience show that the degree of removal of light components from the bottoms depends primarily upon the fractionating power in the stripping section and is influenced little by the power in the rectifying section, and that the degree of removal of heavy components from the distillate is dependent basically on the power in the rectifying section and but little on the power in the stripping section.

Some indication of the general relationships between the component distribution ratios for the practical fractionator is given by the distributions from a computation study cited by Thiele and Geddes (5). This case is of interest as it involved the fractionation of gasoline from a wide-boiling-range feed containing components boiling as high as 550°F. by use of a low-powered column having a reboiler and one theoretical plate in the stripping section and only two theoretical plates in the rectifying section. Hence there were wide overlappings of components appearing in both the distillate and bottoms in appreciable quantities. The distillate quantity corresponded to a molar D/F ratio of about 0.75; the top L/V ratio was 0.26, and the bottom V/L ratio was 0.85. The calculated top and bottom temperatures were 322° and 435°F. for operation at atmospheric pressure.

The calculated x_d/x_w ratios for all nineteen components are shown in Figure 1 which is plotted as a function of the relative volatilities taken at 380°F., approximately the mean of the column terminal temperatures. The component boiling at 393°F., for which x_d/x_w equaled 0.75, was taken as the reference component. The relative volatilities were calculated as the ratios of vapor pressures for the pure components.

Figure 1 shows that the curve reconciling the data points consists basically of two intersecting straight lines on the log-log plot, with some deviation of the points from the straight lines in the region near the intersection. The fractionating power of this column of four theoretical plates should be less than that for a four plate column operating at infinite reflux ratio and greater than the power for a single-plate equilibrium vaporization. The lines on Figure 1 have slopes consistent with these limiting con-

ditions. The upper data points fall on a straight line having a slope of 1.95, this slope being related to the fractionating power in the column stripping section. The lower points fall on a line of slope 3.40, related to power in the rectifying section.

Both these lines have slopes intermediate to the values 1.0 and 4.0 corresponding to the theoretical limiting values from Equation (3).

As there are no other published data having enough range and accuracy for the present purposes, some additional cases will be presented taken from computation work done at the same time as that on which Figure 1 is based. The feed composition and methods of computation were the same; cases were calculated for fractionators containing a reboiler plus either three or six theoretical plates, and various reflux ratios and feed plate locations were used. The important conditions are tabulated in Table 1, and the calculated distribution ratios are graphed in Figures 2, 3 and 4 as functions of the relative volatilities of the components. The relative volatilities were taken as the ratios of the vapor pressures of the pure hydrocarbons at average temperatures corresponding to the means of the column terminal temperatures; in each of the cases the selected reference component was that constituent for which x_d/x_w most closely approached unity.

On Figure 2 are shown the distribution ratios calculated for the case of infinite reflux fractionation of the wide boiling range mixture in a column consisting of a reboiler plus six theoretical plates and operating with terminal temperatures of 322° and 460°F. at atmospheric pressure. The relative volatilities were calculated at 390°F., the mean of the terminal temperatures. The x_d/x_w values for all components fall on the straight line F in accordance with the Fenske-Underwood relation [Equation (3)], the correlation line having a slope of 6.8 compared to the theoretical value of 7.0 for seven stages.

Plots of the distribution ratios for cases A, B, C, and D are given in Figure 3; these exhibit the same general characteristics as the case covered in Figure 1. The locus of points for each case consists of two intersecting straight lines, with some departure of the points in the transition region. Curves A and B bend downward, indicating relatively greater power in the rectifying sections than in the stripping sections; curves C and D bend upward, indicating relatively greater power in the stripping sections. The slopes of all straight line segments lie between the value 1.0 for a single stage equilibrium separation and 4.0 to 7.0 corresponding to operation of four or seven theoretical plates at infinite reflux ratio. Case A refers to a seven plate column having no stripping section, the feed being introduced directly to the reboiler; the upper characteristic line on Figure 2 for the stripping section has a slope only slightly greater than 1.0 corresponding to equilibrium solubility of distillate components in the heavier hydrocarbon bottoms.

Both theory and experience show that a definite fractionating power in a rectifying or stripping section may be obtained by means of various combinations of reflux ratio and number of plates and that the power in either section can be modified by appropriate changes in reflux ratio, number of plates, or both. This is illustrated well by the slopes of the curves in Figure 4 for cases E, G, and H. Reference to Table 1 will show that quite low L/V ratios were used in the rectifying sections for cases G

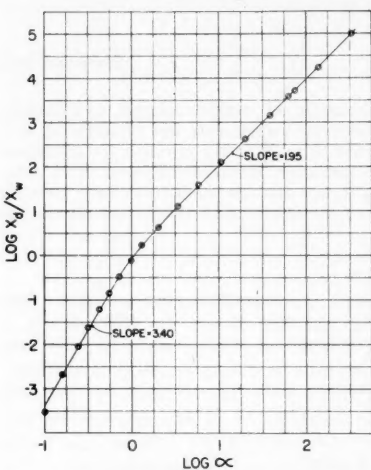


Fig. 1. Component distribution ratios for case given in reference (5).

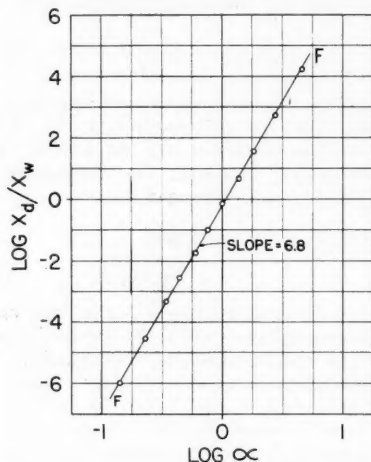


Fig. 2. Component distribution ratios for infinite reflux ratio fractionation.

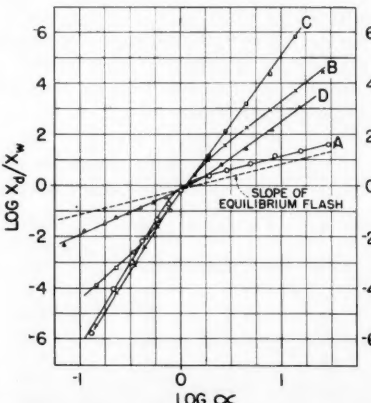


Fig. 3. Component distribution ratios obtained under various fractionation conditions (Table 1).

and
sub-
heat
of the
Ca-
two
with
the e-
and
cati-
case
slope
resul-
with
segm-
plate
incre-
the v-
Fig-
pone-
debu-
made-
Ged-
enter-
plus
theor-
temp-
lb./sc-
were
at 25-
termi-
lation
the f-
and n-
Th-
that
the r-
comp-
hydr-
only
termi-
butio-
becor-
linear
to 5.
tions
which
inde-
must
relati-
impor-
Mu-
befor-
impli-
logica-
chara-
point
1, 3,
of a
exten-
temp-
are ts-
The
relati-
mate-
temp-
For ex-
for th-
show-
straig-
pare-
seven
lines a-

and H ; the stripping V/L ratios remained substantial, however, owing to the reboiler heat needed to complete the vaporization of the net distillate.

Case E on Figure 4 involved the use of two rectifying and two stripping stages with a top L/V ratio of 0.52; the slopes for the curve were 3.3 and 2.3 for the rectifying and stripping sections, respectively, indicating the greater power in the rectifying section. Reducing the top L/V to 0.033 in case G caused more reduction in rectifying slope than in stripping slope; this almost resulted in a single straight correlation line with slopes of 1.6 and 1.8 for the curve segments. For case H three added stripping plates were used, resulting in the marked increase for the stripping section slope to the value 4.7.

Figure 5 is a plot of the calculated component distribution ratios for a gasoline debutanizer tower taken from computations made by the procedure of Thiele and Geddes. The partially vaporized feed entered a column consisting of a reboiler plus four stripping and ten rectifying theoretical plates operating with terminal temperatures of 150° and 340°F. at 100 lb./sq. in. gauge. The relative volatilities were taken as the ratios of the y/x values at 250°F., approximately the average of the terminal temperatures. The straight correlation line indicates a good balance between the fractionating powers in the stripping and rectifying sections.

These examples are sufficient to show that there is a simple, orderly pattern for the relative separations achieved between components in a complex mixture of hydrocarbons. When the distributions of only a few selected components to the terminal products are known, the distributions of all the other components become definite, conforming with the linear relations illustrated in Figures 1 to 5. In other words there are interrelations in the complex fractionation process which reduce markedly the number of independent composition variables which must be considered; these simplifying relations are associated closely with the important fundamental variable, the relative volatilities of the components.

Much more data must become available before all the secondary questions and implications can be settled. It seems logical that the intersection of a pair of characteristic lines should occur near the point where x_d/x_w equals unity (Figures 1, 3, and 4). It is evident that the slope of a characteristic line depends to some extent upon the arbitrary selection of the temperature at which relative volatilities are taken.

The present examination indicates that relative volatilities evaluated at approximately the mean of the column terminal temperatures have the most significance. For example the component distributions for the infinite reflux ratio fractionation shown in Figure 2 conform to a single straight line having a slope of 6.8 compared to the theoretical value of 7.0 for seven plates. Single straight correlation lines also were obtained when the relative

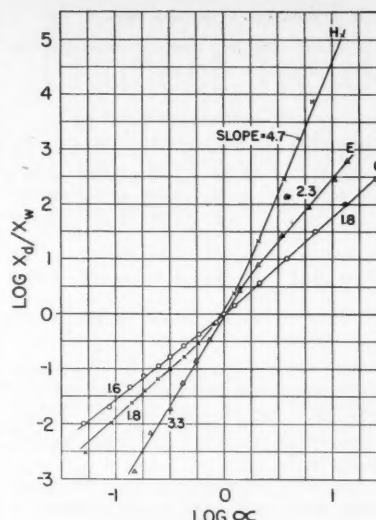


Fig. 4. Effect of changes in number of plates and reflux ratios (Table 1).

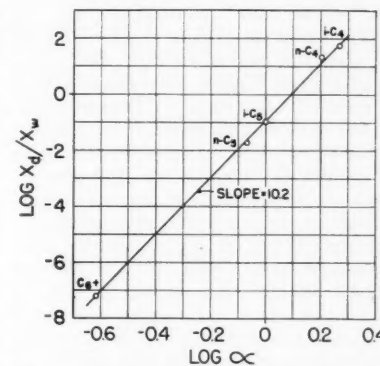


Fig. 5. Component distribution ratios for gasoline debutanizer.

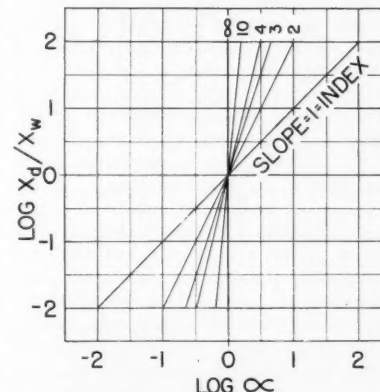


Fig. 6. Component distribution ratio vs. relative volatilities, fractionation index.

volatilities were taken at the terminal temperatures of 322° or 460°F., but the slopes were 5.9 and 7.7, respectively.

On theoretical grounds one might speculate that it would be more sound to take relative volatilities for the light constituents at the bottoms temperature and relative volatilities for the heavy

constituents at the top temperature or to use the average temperatures in the stripping and in the rectifying sections. For the cases cited in the present paper, pairs of straight correlation lines still result. The slopes of the straight lines vary with the changes in relative volatilities of constituents at different temperature levels.

GENERAL INDEX OF FRACTIONATION POWER

The data presented indicate that the characteristic straight lines obtained from plots of $\log x_d/x_w$ vs. $\log \alpha$ give simple identifications for the manner in which multicomponent mixtures separate in fractional distillation. The slopes of these lines also provide a rational criterion for power of fractionation in distillation systems. In view of the fundamental nature and the usefulness of the slope function it is proposed that the natural descriptive term *fractionation index* be used to designate the logarithmic slopes of the straight characteristic lines.

Figure 6 gives the graphical definition of the fractionation index with separate lines shown for index numbers of one, two, three, four, ten, and infinity. The plot is based on the use of Equation (3), with the constant term $\log (x_d/x_w)_0$ for the reference component taken equal to zero (i.e., $x_d/x_w = 1.0$). This reference component can be a normal component, a trace component, or a hypothetical component.

PRACTICAL USES

The concept of the fractionation index is useful in condensing the results of computation studies, since it is a means of conveying much information in a brief way. For a fractionator having balanced power in the stripping and rectifying sections a single value of the index plus one x_d/x_w value for a reference component fully define the yields and detailed compositions of distillate and bottoms from a given feed stock. If the known separation is characterized by a pair of intersecting straight lines, only the two values of the Index plus the value of x_d/x_w at the point of intersection are required. In other words in each case there is but one yield and composition of distillate which will satisfy these conditions and the over-all component balances defined by Equations (4) to (7). Cataloguing this way should be helpful in comparing new fractionation problems with ones that have been evaluated previously.

The calculation of a fractionator by plate to plate methods can be done more conveniently by making use of the fractionation index, whether the computations are carried out by the Lewis-Matheson (4) or the Thiele-Geddes (5) procedure. Persons familiar with the Thiele-Geddes method will recognize that the characteristic slopes of the index lines are fairly well established after the first trial solutions, and that these slopes

TABLE 2. DEVELOPMENT OF PRODUCT YIELDS AND COMPOSITIONS

Assumed: Index = 6.0 in rectifying section, 2.0 in stripping section; index lines to intersect at $\log x_d/x_w = 0$

1	2	3	4	5	6	7	8	9	10
Component	Feed, Fx_f	Log α	Log x_d/x_w	x_d/x_w	Dx_d/Wx_w	Wx_w	Dx_d	x_w	x_d
1	15	0.5	1.0	10	10.3	1.33	13.67	0.027	0.270
2	20	0.3	0.6	3.98	4.10	3.92	16.08	0.079	0.317
3	25	0.1	0.2	1.59	1.63	9.50	15.50	0.193	0.306
(reference) Trace	0	0	1.0						
4	25	-0.1	-0.6	0.252	0.259	19.82	5.18	0.403	0.102
5	15	-0.3	-1.8	0.0159	0.0164	14.75	0.25	0.298	0.005
						49.32	50.68	1.000	1.000

generally do not change substantially with further trial solutions. The first index lines often enable estimation of the final compositions of the product streams without the need to complete the plate to plate computations rigorously.

The use of the fractionation index has a distinct value in the computation of a column by the Lewis-Matheson procedure. In the common problem, where a balanced fractionator is desired, a single value of the index plus a value of x_d/x_w for one component will define precisely the relative separations of components and the concentrations of every component in the products; this enables plate to plate calculations to be made from each end of the column with the minimum of trial and error work continued until composition matches indicate that the feed plate has been reached.

The setting of the component distributions by use of a single, straight index line is consistent with the most efficient usage of plates and leads to the simplest column computation procedures. In effect this was the distribution Hengstebeck (3) used for reduction of a multicomponent feed to an equivalent binary mixture in the application of his graphical computation procedure.

There are conditions however where the engineer has practical justification for the design of an unbalanced fractionator. The predetermination of consistent product compositions and yields can be done by a calculating procedure similar to that used in the case of a single, straight index line. This will be illustrated by considering the case of a fractionation to be accomplished in a column where the rectifying section would have three times as much fractionating power as that of the stripping section. Table 2 gives the premises and derivations of product yields and compositions. It was arbitrarily assumed that the feed would be split so that a hypothetical constituent (or a trace component) having a relative volatility midway between those for components three and four would appear in distillate and bottoms in equal concentrations, or $x_d/x_w = 1.0$. It was also assumed that a fractionation index of 2.0 would be used for the stripping section and of 6.0 for the rectifying section, with intersection of the

index lines at $\log x_d/x_w = 0$. The consequent composition ratios based on the relative volatilities of column 3 are tabulated in columns 4 and 5 and plotted in Figure 7.

Equation (4) was then used to determine the yields and compositions of products consistent with the assumed composition ratios in column 5 by using trial values for D/W . Columns 6 to 10 summarize the calculations for the correct trial value $D/W = 1.03$. Column 6 gives the product of D/W and x_d/x_w , and column 7 gives the values of Wx_w evaluated by means of Equation (4). The component quantities in the distillate Dx_d were calculated by difference, with Equation (7) used, and are tabulated in column 8. The derived compositions of distillate and bottoms are given in columns 9 and 10. These terminal compositions then could be the starting point for the Lewis-Matheson type of plate to plate calculations by using reflux ratios greater than the minimum reflux ratio required for this separation.

Years ago Docksey (1) gave an ingenious algebraic solution for the plate to plate enrichment equations in terms of the relative volatilities of the components, thus avoiding the trial and error methods of Lewis and Matheson for reconciling vapor-liquid equilibria and temperature on successive plates. The practical use never developed however since it was necessary to know accurately the concentration of every component in the products from a proposed fractionator to start the computations. With the means available for estimating these rather accurately engineers should find the Docksey equations particularly helpful for some computation studies. Docksey's solution is similar to that developed by Underwood (6), but it is somewhat simpler in execution.

While the present study has been concerned with hydrocarbon mixtures, the conclusions are applicable to mixtures of other organic molecules where the departures from the laws of ideal solutions are small; they should apply also to some nonideal mixtures in special cases where the activity coefficients of the components change only moderately over the concentration ranges existing within a fractionator.

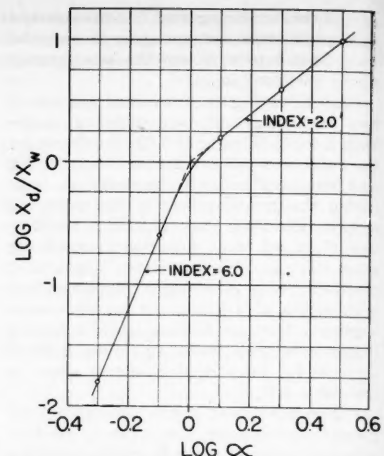


Fig. 7. Component distribution ratios for unbalanced fractionator problem (Table 2).

ACKNOWLEDGMENT

The Standard Oil Company (Indiana) gave helpful cooperation by making available the results of fractionation computation studies carried out many years ago.

NOTATION

F = total moles of feed
 D = total moles of distillate
 W = total moles of bottoms
 L = moles of liquid overflow within column
 V = moles vapor flowing within column
 n = number of theoretical plates
 x = mole fraction of a constituent in the liquid (x_d in distillate, x_w in bottoms)
 y = mole fraction of a constituent in the vapor
 k = y/x

Greek Letters

α = relative volatility of a constituent ($\alpha_i = k_i/k_0$)
 Σ = summation

Subscripts

0 = reference constituent
 i = constituent i
 d = distillate from column
 w = bottoms from column
 f = feed

LITERATURE CITED

1. Docksey, P., *J. Inst. Petroleum Technol.*, **23**, 316 (1937).
2. Fenske, M. R., *Ind. Eng. Chem.*, **24**, 482 (1932).
3. Hengstebeck, R. J., *Trans. Am. Inst. Chem. Engrs.*, **42**, 309 (1946).
4. Lewis, W. K., and G. L. Matheson, *Ind. Eng. Chem.*, **24**, 494 (1932).
5. Thiele, E. W., and R. L. Geddes, *Ind. Eng. Chem.*, **25**, 289 (1933).
6. Underwood, A. J. V., *Trans. Inst. Chem. Engrs. (London)*, **10**, 130 (1932).

Manuscript received May 14, 1958; revision received July 7, 1958; paper accepted July 7, 1958.

*Equation prediction which is to be obtained between words, is unfindable, dependent on the fluid correction in viscosity. Recent data in which 2 to 14 w. McAdam account f.

W. L. New York

Vol. 4

Turbulent Heat Transfer Inside Tubes and the Analogy Among Heat, Mass, and Momentum Transfer

W. L. FRIEND and A. B. METZNER

University of Delaware, Newark, Delaware

The effect of fluid physical properties on the rates of convective heat transfer (or mass transfer) to Newtonian fluids flowing turbulently inside tubes has been studied extensively but never resolved for a wide range of variables. In the absence of precise experimental data the conflicting predictions of the many semitheoretical approaches developed during the last two decades have served to confuse rather than to clarify the basic question. To extend the range of the available data an experimental heat transfer study of the heretofore undefined region of high Prandtl number was performed. Fluid properties, determined experimentally, represented a variation in Prandtl number from 50 to 600.

For final correlation all the available data for heat transfer with moderate temperature differences except those on liquid metals were considered. The effect of the Prandtl number for the range of the data (N_{Pr} of 0.50 to 600) was not well represented by any of the generally accepted theories or empirical equations, although a semitheoretical correlation was deduced from the data with Reichardt's general formulation of the analogy between heat and momentum transfer. The resulting equation fits all the available data with a standard deviation of 9.4%. The applicability of the correlation to turbulent mass transfer in tubes is demonstrated for Schmidt numbers up to 3,000.

At the present time empirical design equations are normally employed for prediction of the heat transfer rates to fluids flowing turbulently inside tubes, and there is no clear choice of one in preference to another. The familiar equations of Colburn (4), Dittus and Boelter (7), Drexel and McAdams (9), and Sieder and Tate (31) are all of the form

$$N_{Nu} = c_1 (N_{Re})^{c_2} (N_{Pr})^{c_3} \quad (1)$$

but significant differences in the numerical values of c_1 , c_2 , and c_3 are reported.*

McAdams (24) noted these discrepancies and commented appropriately, "It is clear that equations of the form of the products of the powers of the three dimensionless groups, each with a constant exponent, are inadequate."

The theory of turbulent transport and the analogy between heat, mass, and momentum transfer have been advanced considerably during the past two decades, enabling quantitative prediction of heat or mass transfer rates in equipment of

simple geometry for low and moderate values of the Prandtl group ($N_{Pr} < 20$). For viscous liquids however, for which the Prandtl number is large, the assumptions employed in the theoretical developments are subjected to a more critical test, and experimental verification is largely lacking. For extremely viscous liquids ($N_{Pr} > 100$) the literature is entirely void of any complete and accurate* experimental work, as turbulence is difficult to obtain with such fluids and they often do not conform to simple Newtonian flow behavior. Preliminary studies with viscous non-Newtonian fluids under turbulent conditions have been reported (26), and further work is in progress. Complete interpretation and correlation of these results in terms of fundamental arguments has not been achieved however partially owing to the undefined effect of the Prandtl number over as wide a range as may be encountered, approximately 1 to 1,000.

The ultimate goal of this investigation was to represent the rate of the heat transfer process to fluids flowing turbulently in smooth, round tubes for a broad range of fluid properties or Prandtl number, excluding from consideration only molten metals ($N_{Pr} < 0.10$) and strongly nonisothermal flow. To extend

the range of the available data an experimental study of the heretofore undefined region of high Prandtl number was performed. Fluid physical properties, often only estimated by previous investigators but imperative for successful interpretation of the results, were determined experimentally. With this extension of the experimental evidence to higher values of the Prandtl number, the prior art was critically reviewed and analyzed, from the standpoint of both the theoretical mechanics of turbulent transport and the more precise and extensive data currently available. The analogy between heat, mass, and momentum transfer was examined in detail for the corresponding regions of high Schmidt and Prandtl numbers.

THEORY

The effect of the tube aspect ratio L/D has been clearly defined (13) and is present only in short tubes ($L/D < 20$) in which entrance effects persist over an appreciable portion of the tube length. These will be excluded from consideration here.

McAdams (24a) has presented the basic equations for the rates of heat (or mass) and momentum transfer and has reviewed the early theoretical attempts to obtain solutions to these equations. Experimental data on heat (or mass) transfer to fluids of high Prandtl (or Schmidt) numbers however indicate transfer rates which are much higher than those predicted by the theories. It

*Equation (1) is rigorously applicable only for prediction of the isothermal heat transfer coefficient, which is defined as that limiting value which would be obtained with a zero temperature difference between the tube wall and the flowing fluid. In other words, it is that coefficient which is completely uninfluenced by complications due to the temperature dependence of the relevant physical properties of the fluid. Sieder and Tate (31) added an empirical correction, $(\mu_b/\mu_w)^{0.14}$, to account for radial variations in viscosity due to the radial temperature gradient. Recent data for heating aniline and *n*-butanol (19) in which the viscosity ratio μ_b/μ_w was varied from 2 to 14 were correlated with the correction $(\mu_b/\mu_w)^{0.10}$. McAdams (24) reviews the other attempts to account for deviations from this isothermal coefficient.

W. L. Friend is with The Lummus Company, New York, New York.

*The few data available in this region are confused by the fact that high temperature differences were employed. Accordingly the resultant heat transfer coefficients are affected perhaps more strongly by complications due to the radial variation of physical properties than by the other physical properties which normally completely determine the heat transfer rates.

has been suggested (6, 22, 30, 34) that this failure of the theoretical solutions may be due to the assumption of an entirely laminar sublayer of fluid adjacent to the wall. Unfortunately the usual experimental methods for obtaining turbulent velocities and their fluctuations break down as one approaches the tube wall, and no direct experimental confirmation of the existence of turbulence, as defined by a finite value of the eddy diffusivity, is available for the so-called "laminar" sublayer.

Several authors (6, 22, 30, 34) have assumed arbitrary relationships to describe the variation of eddy diffusivity with distance from the tube wall, within this nearly laminar region close to the wall. As there is no check whatever available on such a detailed distribution, but only on its integrated effect in the over-all correlation, this practice cannot be claimed to give a necessarily correct picture of the variations in turbulence with distance from the wall. However Reichardt (30) deduced the general form of the correlation prior to the introduction of any such hypothetical assumptions:

$$N_{st} = \frac{f/2(\phi_m/\theta_m)}{1 + (N_{Pr} - 1)(\phi_m) \sqrt{f/2(b)}} \quad (2)$$

where

$$b = \int_0^{U/u^*} \frac{du^+}{1 + N_{Pr} E_m / \nu} = \int_0^{U/u^*} \frac{q_{mo}}{q} du^+ \quad (3)$$

The development of these equations is presented in another paper (25), where the assumptions required are discussed in detail. Briefly, they are

1. The shear stress and heat flux are both linear functions of radial position within the tube.

2. The eddy diffusivities for heat (or mass) transfer and momentum transfer are equal.

The ratio of the mean to maximum velocities ϕ_m is nearly constant at a value of about 1/1.2 under turbulent-flow conditions (24, 25). The ratio of the mean to maximum temperature differences between the fluid and the tube wall θ_m is also nearly constant, provided one is dealing with Prandtl numbers greater than about unity. Therefore, by excluding the low-Prandtl-number region (that is, heat transfer to liquid metals) from consideration here, evaluation of Equation (2) is reduced to determining the value of the Reichardt b function defined by Equation (3).

Since the integrand q_{mo}/q in Equation (3) represents the fraction of the total heat transferred which is conducted by molecular motion, its value must be unity at the tube wall itself, where turbulence must be completely absent.

As one moves away from the wall into the turbulent core, the ratio q_{mo}/q will decrease at a rate dependent on the Prandtl number. If one again excludes the region of very low Prandtl numbers, the numerical value of this ratio will be significant only near the wall, and the b function as a whole will be determined only by the flow conditions close to the tube wall. A detailed analysis (12, 25) shows that under these conditions b will be a function only of the Prandtl number, if the following criterion is met

$$(N_{Pr})(N_{Re})^2(f) > 5 \times 10^5$$

A similar analysis by Reichardt, using a less severe restriction, yielded

$$N_{Pr} N_{Re} > 2500$$

These analyses limit the theoretical development to Prandtl numbers above 0.60 and 0.25, respectively, at a Reynolds number of 10,000.

Inserting these considerations into Equation (2) one obtains as the final result

$$N_{st} = \frac{f/2}{1.20 + (N_{Pr} - 1)b \sqrt{f/2}} \quad (4)$$

where the term b is a function only of the Prandtl number and is to be determined empirically in the absence of eddy-diffusivity data close to the tube wall.

EXPERIMENTAL APPARATUS AND PROCEDURE

Heat Transfer Rates

A schematic flow diagram of the apparatus is presented in Figure 1.* The test fluid was contained in a 160-gal. stainless steel tank equipped with low- and high-speed propeller agitators and a copper coil for steam heating or water cooling. A gravity-fed Moyno progressing cavity type of pump with a Reeves variable-speed drive discharged the fluid into a length of $\frac{3}{4}$ -in.-nominal-diameter extra-strong brass pipe, the first 10 ft. of which were insulated and served as a calming section. The following 9.90 ft. were the heated section and were insulated longitudinally from the remainder of the tube with $\frac{1}{4}$ -in.-wide Bakelite rings. The wall temperature was measured by seven thermocouples distributed along the length of the heated section; the thermocouples were embedded in grooves cut deeply within the circumference of the tube. Calibrated copper-constantan thermocouple wire was used throughout. The fluid was discharged from the heated section into a series of orifice mixers equipped with a thermocouple well for measurement of the exit temperature.

The volumetric flow rate was measured with a Foxboro magnetic flowmeter and two-range dynalow recorder incorporated in the $2\frac{1}{2}$ -in. return line. After leaving the

*Figures 1 through 6 have been deposited as document 5765 with the American Documentation Institute, Photoduplication Service, Library of Congress, Washington 25, D. C., and may be obtained for \$2.50 for photoprints or \$1.75 for 35-mm. microfilm.

flowmeter the fluid passed through a double-pipe cooler, with water in the annular space, and then was returned to storage. The heater for the test section was a double-wall concentric jacket consisting of a 3-in. pipe serving as a steam jacket and a 5-in. pipe acting as a heated insulator. Slightly superheated low-pressure steam was introduced into the outer pipe and flowed into the 3-in. jacket through narrow slots cut in its surface. Cover baffles prevented condensate from dripping into the inner jacket. The inner heating jacket was provided with a small line and helical cooling coil for the removal and subcooling of condensate; the outer jacket was continuously purged from two vents, one located on the underside for condensate drainage. The heating medium was obtained by expanding a 100 lb./sq. in.-gauge line steam to about 5 lb./sq. in.-gauge, a part of the flow being diverted through a standard throttling steam calorimeter. The enthalpy change across the exchanger was determined by the calorimeter reading and the exit condensate temperature, measured prior to subcooling.

When the apparatus was running, steady-state was considered reached when both the inlet- and exit-fluid temperatures were essentially constant for a 20-min. interval. All thermocouple voltages, referred to an ice junction, were then determined with a Leeds and Northrop type-8662 portable precision potentiometer. The volumetric flow and system pressures were recorded, as well as the time required to collect between 1,000 and 2,000 cc. of condensate.

In all cases the heat transfer coefficient was based on the heat flux measured by the rate of steam condensation. Owing to the small temperature rise of the fluid through the test section, often less than 1°F., the heat flux determined by the rate of heating of the fluid was far less accurate. Even with this limitation, however, the average deviation in the two heat fluxes for the eighty experimental runs was only 9%.

The wall temperature was taken as the arithmetic average of the individual thermocouple readings. Only for the data taken with high ΔT did any one thermocouple reading differ from this average by more than 2°F., the agreement for the bulk of the data obtained with small temperature differences usually being about a few tenths of a degree.

At several times during the course of the investigation data were obtained with water ($N_{Pr} = 2.2-2.5$) as the test fluid. These data compared favorably with the Colburn equation, as shown in Figure 2,* over the entire range of Reynolds numbers which could be covered (from 30,000 to 420,000). This was deemed to represent excellent proof of the reliability of the experimental technique. The Colburn equation represents one of the accepted standard equations for use with fluids of low Prandtl number. Therefore its use for proving the reliability of experimental techniques may be justified on this basis (provided one uses a fluid of low Prandtl number), even though it will be shown in a later section of this paper that it and other similar equations are appreciably in error when extrapolated for use at high Prandtl numbers.

*See footnote in column 2.

Fluid
Molas
MA
MB
MC
Corn
SA
SB
SC
SD

Fluid
capillary
Metzger
water
therm
measur
describ
ton (2
chamber
(24) w
determ
earlier
The
with a
permitt
trated
strong
wise a
employ

EXPERI
Fluids
The
phases
trated
genera
of high
accom
flow b
variab
easily
origin
employ
estima
refined
solids
trine,
approx
origin
thereof
chased
menta
temper
variatio
to 600.

Small
copper
matte
to in
sample
was ke
expose
polyeth
stabilit
fluid w

TABLE 1. SUMMARY OF FLUID PROPERTIES

Fluid	Percentage of solids	Density, lb./cu. ft.	Viscosity, centipoise	Thermal conductivity, B.t.u./hr.(sq. ft.)(°F.)	Specific heat, B.t.u./lb.(°F.)	Prandtl number, dimensionless
Molasses: properties estimated at 180°F.						
MA	80	82.5	37	0.16	0.62	350
MB	72	81.9	15	0.17	0.64	140
MC	64	79.8	7.4	0.22	0.66	50
Corn syrup: properties estimated at 195°F.						
SA	73	83.1	60	0.14	0.59	600
SB	69	82.8	37	0.15	0.61	370
SC	65	81.7	19	0.17	0.63	180
SD	62	79.8	12	0.21	0.67	90

Fluid Physical Properties

Fluid viscosity was measured with a capillary-tube viscometer described by Metzner and Otto (26) and calibrated with water and a traveling microscope. The thermal conductivity of the fluids was measured by the steady state method described by Metzner, Vaughn, and Houghton (26). Data obtained with water in both chambers agreed with the published values (24) within 3%. Heat capacities were also determined in an apparatus described earlier (26).

The density of the fluids was measured with a hydrometer when surface properties permitted (the surface of the more concentrated fluids tended to scum and adhere strongly to the hydrometer stem); otherwise a modified pyrometric method was employed.

EXPERIMENTAL RESULTS

Fluids Studied

The fluids selected for the experimental phase of this investigation were concentrated aqueous sugar solutions, which generally exhibit the desired properties of high viscosity or high Prandtl number accompanied by perfectly Newtonian flow behavior. The Prandtl number, the variable of principal interest, could be easily changed by merely diluting the original fluid stock. The base fluids employed were a blackstrap molasses estimated as 80% sucrose and a highly refined corn syrup analyzed at 80% solids and consisting of dextrose, dextrose, maltose, and higher sugars in approximately equal proportions. The original molasses and two dilutions thereof and four dilutions of the purchased corn syrup were studied experimentally. These seven fluids, at the temperatures employed, represented a variation in the Prandtl number of 50 to 600.

Small amounts of sodium benzoate and copper nitrate were added in approximately equal proportion (total of 0.1%) to inhibit degradation of the fluid samples by fermentation. Evaporation was kept to a minimum by covering the exposed areas of the mixing tank with polyethylene film. To ensure further the stability of the fluids the data for a given fluid were obtained in the course of only

a few days. Samples for the determination of physical properties were withdrawn during the runs and processed immediately thereafter. The data for the molasses-based fluids were obtained in the initial phase of the investigation, whereas the syrup-derived systems were studied with a perfected experimental technique and with smaller temperature differences; therefore they are believed to be somewhat more precise, although the agreement between the results for the two fluid groups is good.

Physical Properties

Table 1 gives a summary of the relevant properties of the seven fluids studied. The properties are estimated at approximately the bulk temperatures employed, although for the actual correlations more accurate values were estimated at the precise bulk temperature for each run from the smooth curves representing the experimental results as functions of temperature (Figures 3 to 6*). All the fluids proved to be perfectly Newtonian, with the exception of the original molasses, which exhibited slightly pseudoplastic behavior below 150°F.; at higher temperatures however it also appeared to be Newtonian.

With the exception of specific heat, fluid physical properties were measured experimentally at several temperatures. The specific heats of the molasses fluids were determined by extrapolation of data reported in *The International Critical Tables* for aqueous sucrose solutions at 68°F. as a function of composition. The specific heats of the syrups were measured experimentally at approximately 100°F. and assumed invariant with temperature. The use of these values is supported by the agreement of the heat fluxes computed independently from the rate of steam condensation and the rate of heating of the fluid, particularly for those runs in which the temperature rise of the fluid was sufficiently large to be measured precisely ($\Delta T > 2^{\circ}\text{F}$).

Fluid viscosity and density, although strongly temperature dependent, posed no particular problem, as the experimental

techniques employed permitted measurement of these properties over the entire temperature range of interest. Smooth curves were drawn through the experimental results for interpolation.

Owing to limitations in the experimental procedure thermal conductivities could be measured only within the region of 90° to 150°F.,* and extrapolation of the data to the higher temperatures of interest was necessary. The data which could be obtained were of sufficient variation however to establish adequately the relatively large negative temperature coefficient of thermal conductivity exhibited by all of the fluids studied. The extrapolation to higher temperatures could therefore be performed with a fair degree of accuracy. In anticipation of possible criticism that the measured heat transfer rates are too high, compared with conventional correlations for less viscous fluids, it may be pointed out that the extrapolation was, in all cases, conservative, the curvature of the thermal conductivity-temperature curves favoring high values of the thermal conductivity. Furthermore, possible error introduced by this extrapolation is diminished in the final dimensionless correlations, as the thermal conductivity enters only to a fractional power of approximately $\frac{2}{3}$. It is estimated that the maximum possible error in the correlation which may be attributed to thermal conductivity was always less than 10%.

Heat Transfer Rates

To avoid serious nonisothermal complications, small temperature driving forces were maintained, 14° to 19°F., for the syrup runs and 20° to 35°F. with the molasses and its dilutions. The experimental Nusselt numbers are plotted against the Reynolds numbers for the syrup and molasses runs (Figures 7 and 8 respectively). Since the bulk of the data are in the transition and early turbulent regions and the temperature potentials are small, all properties are evaluated at the average bulk temperature.

The indicated curves in the transition region, which extends to a Reynolds number certainly no greater than 10^4 , are merely smooth curves through the data. For the more viscous fluids, where the experimental results terminate in the transition region, the curves have been extrapolated to $N_{Re} = 10^4$ to permit later comparison of all the data at this Reynolds number. Extrapolation of these curves was greatly facilitated by following the form established by the experimental results for the more dilute systems.

In the fully turbulent region, defined conservatively by $N_{Re} > 10^4$, all the lines shown were drawn with a slope of 0.90. This represents approximately the

* A reported value for the thermal conductivity at 150°F. actually represents a mean value over the approximate region of 110° to 190°F.; at 90°F. the range of temperature is about 65° to 115°F.

*See footnote on page 394.

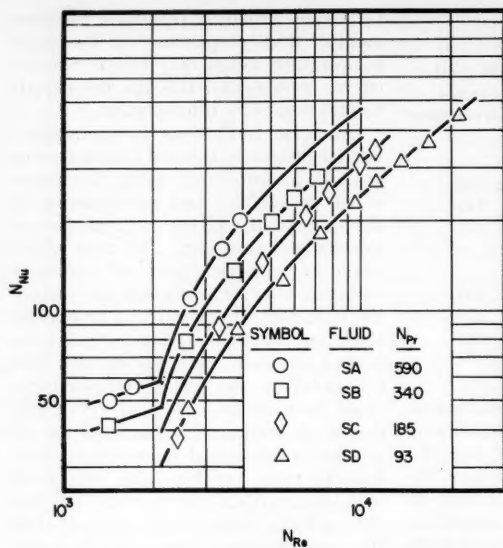


Fig. 7. Heating corn syrup (low temperature difference).

behavior predicted by Equation (4): for a high Prandtl number N_{st} is proportional to $\sqrt{f/2}$, or approximately to $(N_{Re})^{-0.10}$. The Nusselt number is then proportional to $\sqrt{f/2(N_{Re})}$, or approximately to $(N_{Re})^{0.90}$. The equation predicts the conventional 0.80 Reynolds number exponent only for fluids with a Prandtl number in the vicinity of unity. The agreement of the data with this predicted effect of the Reynolds number is remarkably good. However *MC* is the only fluid for which the Reynolds number range covered is broad enough to permit a truly critical distinction. Because of unperfected technique in the earliest part of the work the average temperature and thus the Prandtl number was allowed to decrease as the flow rate and Reynolds number was increased from run to run. In this respect the earlier molasses data, fluids *MA* and *MB*, are inferior to the other results and must be described by a small range of Prandtl number for each series; whereas the data obtained with *MC* and the syrups are each adequately represented by a single value. The important conclusion to be drawn from this discussion and from Figure 7 is that the curves which were extrapolated to Reynolds numbers of 10,000 correctly portray the Nusselt group to within a few per cent. This, it will be seen later, is sufficiently accurate to define the correlation up to Prandtl numbers of 600.

Effect of the Temperature Difference

To approach the isothermal heat transfer coefficient as closely as possible heat transfer rates were measured with small temperature-driving forces, as small as could be maintained without destroying the accuracy of the measurement. The viscous fluids studied were still

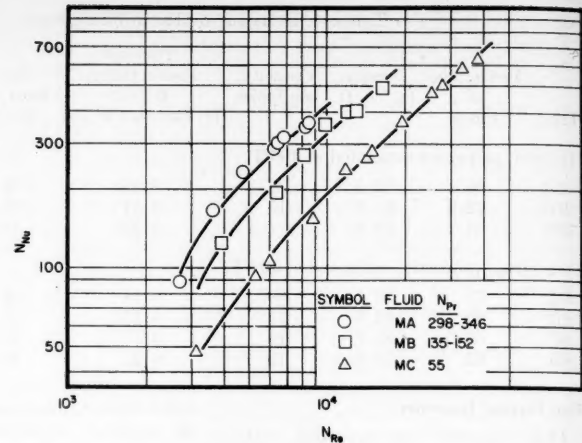


Fig. 8. Heating molasses.

of the Prandtl number was assumed to be given by the low ΔT data for the four syrup fluids studied.

The data indicate a good correlation between the results obtained with high and low temperature differences. The high ΔT Nusselt numbers are consistently slightly smaller than the behavior indicated by the low ΔT correlation, but the difference is only 5% at the maximum temperature difference. This result may be attributed to the compensating effects of the radial variations in viscosity and thermal conductivity, as shown by the following illustrative calculation for run SD-17 (*12*):

$$N_{Re} = 6,290 \quad T_b = 149.0^\circ\text{F}.$$

$$N_{Pr} = 201 \quad T_w = 199.5^\circ\text{F}.$$

$$N_{Nu} = 199 \quad T_m = 50.5^\circ\text{F}.$$

$$\frac{\mu_b}{\mu_w} = \frac{0.0200}{0.0073} = 2.74$$

$$\frac{k_w}{k_b} = \frac{0.205}{0.240} = 0.854$$

The influence of the viscosity gradient may be estimated by the Sieder-Tate (*31*) factor $(\mu_b/\mu_w)^{0.14} = 1.15$ or by the correction recommended by Kreith and Summerfield (*19*) $(\mu_b/\mu_w)^{0.10} = 1.10$. The slope of the low ΔT correlation between the Nusselt and Prandtl numbers indicated by Figure 10 is 0.35. The heat transfer coefficient is therefore approximately proportional to $(k)^{0.65}$. When one assumes that the conductivity should be evaluated precisely at the wall, then the correction for its variation is approximately $(k_w/k_b)^{0.65} = 0.90$. The effects of thermal conductivity and viscosity are therefore of the same order of magnitude and should be approximately compensating as indicated by experiment.

In view of these considerations non-isothermal corrections were not applied to the data for final correlations, and all properties were retained at the main-

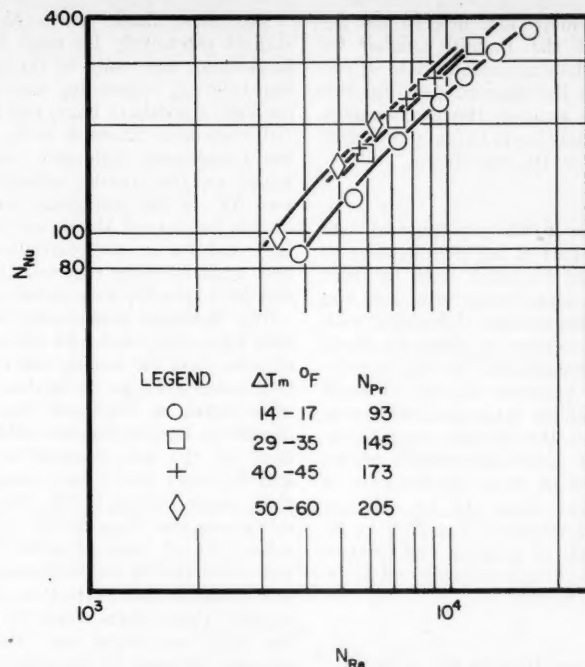


Fig. 9. Heating SD: (effect of the temperature difference).

stream temperature. Any small effects which are present are well within the accuracy of the data and cannot be formulated quantitatively.

CORRELATION

The Effect of the Reynolds Number

The final form of dimensionless correlations for the isothermal Nusselt or Stanton number involves both the Reynolds and Prandtl groups as independent variables. The theory developed earlier completely determines the effect of the Reynolds number, however, and it remains only to demonstrate the agreement of experiment with theory on this point. The final simplified theoretical result was

$$N_{St} = \frac{f/2}{1.20 + (N_{Pr} - 1) \sqrt{f/2}} \quad (4)$$

or for the Nusselt number

$$N_{Nu} = \frac{(f/2)(N_{Re}N_{Pr})}{1.20 + (N_{Pr} - 1) \sqrt{f/2}} \quad (5)$$

Since f is approximately proportional to $(N_{Re})^{-0.20}$, Equation (5) predicts that for low Prandtl numbers in the neighborhood of unity the Nusselt number varies with the 0.80 power of the Reynolds number, whereas for high Prandtl number the variance is with the 0.90 power of N_{Re} . For low and moderate N_{Pr} , the 0.80 exponent has long been well established by experiment. [See, for example, reference (24).] For high Prandtl numbers the present experimental results for heating

molasses and corn syrup confirm the predicted variation. Kern (17) also has observed that the data of Morris and Whitman (28) for gas straw oils (Prandtl numbers of 35 to 100) are best correlated with the 0.90 power of the Reynolds number. Further the data of Bernardo and Eian (1), which cover a much wider range of Reynolds numbers than either

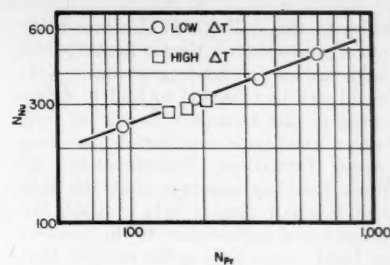


Fig. 10. Heating corn syrup, $N_{Re} = 10^4$

of previously mentioned references, show a consistent increase in the value of the exponent on the Reynolds number as the Prandtl number is increased. In fact from a Prandtl number of 3 to one of 25 the value of the exponent increased by 0.10, although all the exponents were abnormally low. On the other hand the excellent mass transfer data of Eisenberg, Tobias, and Wilke (11), covering a thousandfold range of Reynolds numbers at extremely high Schmidt numbers, predict a variation of N_{St} (or N_{Nu}) with f rather than with \sqrt{f} . These investigators, however, studied rotating cylinders rather than flow inside round tubes. While a detailed recent study (16) revealed that the temperature fields close to a heated rotating cylinder appeared similar to those next to the hot wall of a round tube through which a fluid is flowing, the differences under consideration in high Prandtl or Schmidt number systems would quite possibly be too small to measure or might be too

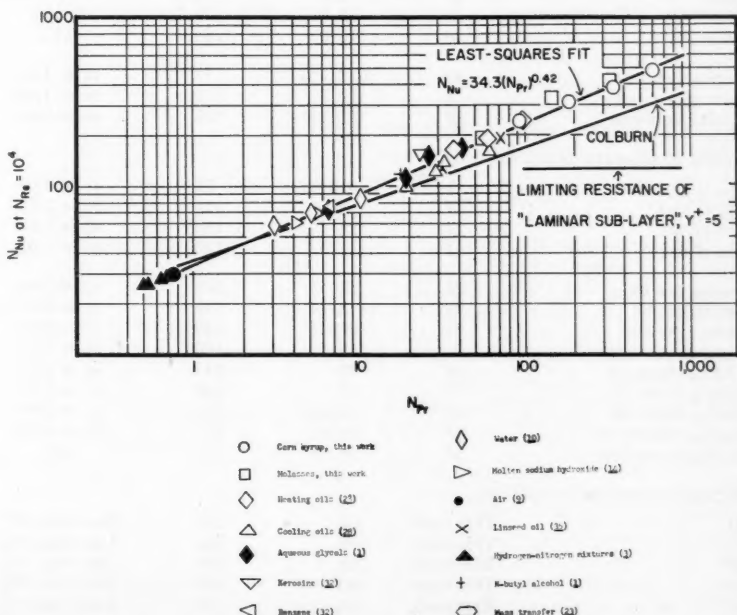


Fig. 11. Effect of the Prandtl number.

close to the wall itself. The possibility of the presence of vortices in the turbulent field around a rotating cylinder (15) could well be expected to lead to differences in the boundary layers as well, under conditions conductive to such vortex formations. Unfortunately one must therefore conclude that the best high Schmidt number data available are of unproved applicability to the problem at hand; while it is quite possible that the work is directly relevant, this would not be so under all conditions. Since by comparison the heat transfer data cover only modest ranges of Reynolds numbers, the predicted variation of heat and mass transfer rates with Reynolds number, over wide ranges, requires further study. Fortunately, highly viscous systems, which are the only ones for which the heat transfer rate variations are still in doubt, probably are seldom processed in regions far removed from those of Figures 7 and 8. Therefore the remaining problem is of importance primarily in the transfer of mass rather than heat.

Analysis may now proceed to the influence of the Prandtl number by examining the experimental data at one value of the Reynolds number. For this purpose the smallest Reynolds number which definitely lies in the fully turbulent region, $N_{Re} = 10^4$, was chosen.

Data Selected

In addition to the experimental data obtained as part of this investigation all the available literature data for heat transfer in long tubes with low and moderate temperature differences with the single exception of those for liquid metals were assembled for final correlation. The variation in the Prandtl number for all the data considered is over more than a three-decade range, from 0.50 to 600. Especially notable among the more recent work are the data of Bernardo and Eian (1) for ethylene glycol-water mixtures, N_{Pr} , of 6 to 40, and the study of Coglan and Colburn (3) with hydrogen-nitrogen mixtures, N_{Pr} , of 0.46 to 0.69.

For those fluids which have been studied extensively by more than one investigator the results of the investigation believed outstanding were selected: for water the data of Eagle and Ferguson (10) were used, inasmuch as the effect of the temperature difference was determined and the results extrapolated to zero ΔT , or the isothermal coefficient; for oils the data of Morris and Whitman (28); and for air the correlation of the best available data reported by Drexel and McAdams (9) were chosen.

The literature is markedly devoid of data for cooling, and with the exception of some data for cooling oils all of the results examined are for heating, usually with steam or electrical energy. The deviations from isothermal behavior are large for the data reported by Morris and Whitman; hence only those runs in their paper obtained with temperature differences less than 100°F. were considered. In all cases physical properties were evaluated at the bulk temperature, and nonisothermal corrections were not applied; these effects, small for most of the data considered, are within the accuracy of many of the measurements.

In the treatment of the data the experimental Nusselt numbers were plotted against the Reynolds number for a series of runs with an approximately constant Prandtl number, and smooth curves were drawn through the points. The ordinates of these curves at $N_{Re} = 10^4$ are the data considered. A summary of all the results obtained in this manner is given in Table 2, including complete references and comments pertaining to the nonisothermal conditions. For those cases in which only the viscosity varies appreciably with temperature the Sieder-Tate viscosity correction (μ_b/μ_w)^{0.14}, denoted in the table as vc , has been tabulated as a first estimate of this effect. This correction was not employed for correlation however and is intended only to illustrate the approximate magnitude of the effect.

Empirical Correlation

The Nusselt numbers at $N_{Re} = 10^4$ are shown in Figure 11 as a function of the Prandtl number for all of the data considered. The empirical equations of Colburn and Sieder and Tate, employing the $\frac{1}{3}$ power of the Prandtl number, are not representative of the data at all, being only fair approximations over a small range of Prandtl numbers.* A horizontal line, representing the maximum value

TABLE 2. SUMMARY OF EXPERIMENTAL AND LITERATURE DATA AT $N_{Re} = 10^4$

System	Reference	N_{Pr}	N_{Nu}	Temperature effects
Heating hydrogen-nitrogen mixtures				
55.0% Hydrogen	3	0.46	24.8	Inestimable,
37.0% Hydrogen	3	0.50	26.0	believed
28.6% Hydrogen	3	0.53	26.5	very
8.9% Hydrogen	3	0.63	28.5	small
Pure nitrogen	3	0.69	29.0	
Air, correlation	9	0.74	30.0	Not considered in correlation
Heating molten				
Sodium hydroxide	14	4.2	60.3	ΔT_m less than 30°F.
Water	10	3.0	58.4	Extrapolated
Water	10	5.0	70.7	to zero
Water	10	10.0	84.5	ΔT_m
Heating benzene	32	5.7-7.3	77	$vc = 1.03$
Heating <i>n</i> -butanol	1	17.7	115	$vc = 1.04$
Heating kerosene	32	21-25	155	$vc = 1.05$
Heating glycol-water mixtures				
30% Glycol	1	6.3-6.4	72	$vc = 1.03$
70% Glycol	1	18.6	115	$vc = 1.03$
Pure glycol	1	25.3	150	$vc = 1.04$
Pure glycol	1	41.0	170	$vc = 1.02$
Heating gas oil	28	37	165	$vc = 1.09$
Cooling gas oil	28	18.2-19.9	110	$vc = 0.91$
Cooling gas oil	28	27-31	120	$vc = 0.91$
Heating straw oil	28	58.5	193	$vc = 1.07$
Heating straw oil	28	95	245	$vc = 1.13$
Cooling straw oil	28	32	140	$vc = 0.90$
Cooling straw oil	28	55-65	160	$vc = 0.86$
Heating linseed oil	35	31.6	127	About 60°F.
Heating linseed oil	35	70.3	189	ΔT_m
Heating molasses and corn syrup				
SD	This work	93	245	Less than 5%
SC	This work	185	315	Less than 5%
SB	This work	340	380	Less than 5%
SA	This work	590	480	Less than 5%
MC	This work	55	195	Less than 5%
MB	This work	135-152	330	Less than 5%
MA	This work	298-346	420	Less than 5%

*The range from 0.50 to 20 in which the Colburn equation fits approximately is the range of variables for which Colburn claimed the equation to be useful. However common usage of this and similar empirical equations which have an exponent of approximate $\frac{1}{3}$ on the Prandtl numbers has not been restricted accordingly. Comparison with the Dittus-Boelter equation is not made, since neither form of their equation was intended to apply to isothermal coefficients; hence any agreement with the data of Figure 11 would be fortuitous. It may be noted in passing, however, that the heating form of their equation would closely approximate the trend shown by the experimental data.

been
one
investi-
gated:
Gus-
son
set of
deter-
mined
to
cient;
tman
of the
rexel

aid of
option
of the
equally
The
ar are
orris
ns in
ature
con-
erties
ture,
e not
ost of
the
ents.
ere
were
er for
ately
smooth
points.
 R_e =
primary
anner
plete
ing to
those
aries
eder-
, de-
lated
This
rela-
ly to
de of

$N_{Re} = 10^4$
on of
data
ns of
oying
er, are
being
small
ontal
value

colburn
ables
to be
similar
ent of
as not
th the
neither
ply to
with
t may
form
te the

$$N_{Nu} = 0.022(N_{Re})^{0.80}(N_{Pr})^{0.42} \quad (7)$$

Semitheoretical Correlation

Values of the Reichardt b function were computed by Equation (4) for each of the data points. The correlation of Drew,* Koo, and McAdams (8) was used to determine the friction factor

$$N_{Nu} = 34.3(N_{Pr})^{0.42} \quad (6)$$

$$f = 0.00140 + 0.125(N_{Re})^{-0.32} \quad (8)$$

*Over a small range of Reynolds numbers the Blasius equation (9) could also have been used.

To complete this conventional form of correlation by including the effect of the Reynolds number as a simple exponential function is impossible, inasmuch as the exponent probably varies with the Prandtl number. If as a first crude approximation the exponent is taken constant as 0.80, then

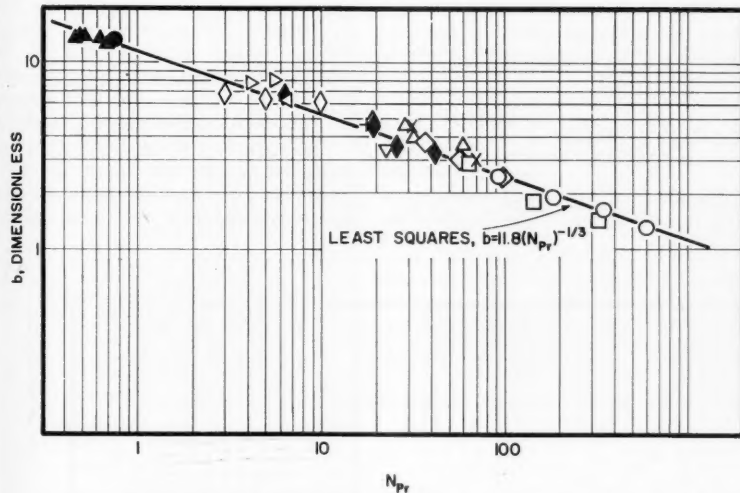


Fig. 12. Evaluation of the Reichardt b function. (See Figure 11 for legend.)

The experimental values of b are plotted vs. the Prandtl number on logarithmic coordinates in Figure 12. The data appear to be well represented by a linear relation on these coordinates, so a simple empirical exponential form $b = B(N_{Pr})^m$ was assumed. The equation of the least-squares line through the data is

$$b = 11.8(N_{Pr})^{-1/3} \quad (9)$$

The final semitheoretical correlation for the heat transfer is then

$$N_{St} = \frac{f/2}{1.20 + 11.8\sqrt{f/2(N_{Pr}) - 1}(N_{Pr})^{-1/3}} \quad (10)$$

Stanton numbers computed from the correlating equation are plotted vs. the Prandtl number for a Reynolds number of 10^4 in Figure 13. The Colburn equation is shown for comparison, and a design chart based on the correlation is presented in Figure 14.

The experimental results at $N_{Re} = 10^4$ are correlated with a standard deviation of 9.4%, 74% of the data falling within this limit. The maximum deviation is 22%. The correlation is believed to be a good approximation of the isothermal coefficient, inasmuch as the maximum deviations are for those data for which nonisothermal effects are strongest. Inclusion of the Sieder-Tate viscosity correction reduced the standard deviation to 6.5% and the maximum deviation to 15%. This by no means represents a general solution to the nonisothermal problem, however, and use of this correction is recommended only as an estimate of nonisothermal deviations for heat transfer with high temperature differences and fluids for which only viscosity varies appreciably with temperature.

The curves of the Stanton number vs. the Prandtl number shown in Figures 13 and 14 exhibit a point of inflection at a Prandtl number of approximately two. This representation has no theoretical significance of course; it is merely a consequence of the simple empirical form chosen for b , and the approximate treatment of the second-order effects θ_m and ϕ_m , which become increasingly important for low Prandtl numbers. Fortunately, within the range of applicability of the equation ($N_{Pr} > 0.50$) the change in slope is very slow, and the correlating equation deviates from a smooth extension of the curve at a higher Prandtl number by a maximum of only about 3%.

Application to Homogeneous Mass Transfer

Since the theoretical developments apply equally well to the turbulent diffusion of mass in a homogeneous phase, if the eddy diffusivity for mass is assumed equal to the eddy diffusivity for heat and momentum, one may write as the correlating equation for turbulent mass transfer in tubes

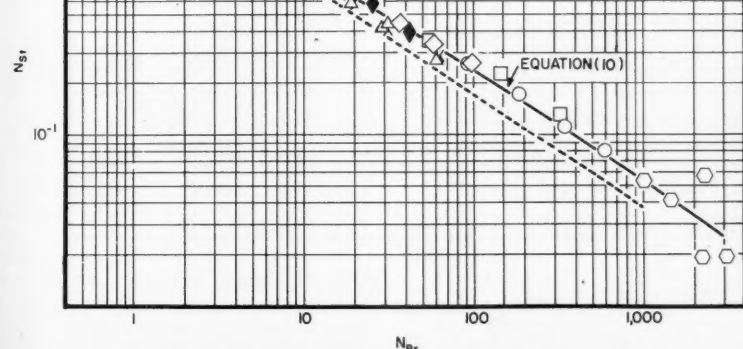


Fig. 13. Semitheoretical correlation. (See Figure 11 for legend.)

$$\left(\frac{k_L}{V}\right) = \frac{f/2}{1.20 + 11.8 \sqrt{f/2(N_{Sc} - 1)(N_{Sc})^{-1/3}}} \quad (11)$$

The excellent agreement between heat and mass transfer data for low and moderate values of the Schmidt and Prandtl numbers (0.50 to 20) is well known (6, 33). There is little point therefore in an extensive review of this data; rather, attention was directed exclusively to the undefined region of very high Schmidt numbers for which two important investigations have been reported.

Linton and Sherwood (23) measured rates of solution of various organic salts coated on the inside wall of a tube. The Schmidt number was varied from 1,000 to 3,000. Their data were considered here in the same manner as the heat transfer results, and the smooth values of (k_L/V) at $N_{Re} = 10^4$ are plotted against the Schmidt number in Figure 13. The data scatter appreciably but generally tend to support the proposed correlation. This agreement is especially important, as it constitutes support of the correlation beyond the range of the heat transfer data upon which it was based and permits an approximate extension of the range of applicability of the results to Prandtl numbers as great as 3,000.

A more recent study of a similar problem was performed by Lin and coworkers at the University of Washington (21). This work is of particular interest, as the results are quoted by Deissler (6) and Lin, Moulton, and Putnam (22) in support of their analogies. Mass transfer coefficients were measured for the diffusion of ions in a diffusion-controlled electrolytic system. The solutions flowed through an annular space ($D_2/D_1 = 2$) between two concentric electrodes. The data for the laminar region are reported as agreeing with the "Leveque (20) approximation,"

$$\frac{k_L D_e}{D_L} = 1.62 \left(\frac{GD_e^2}{\rho D_L L} \right)^{1/3} \quad (12)$$

while the turbulent data for Schmidt numbers of 300 to 3,000 fit the Colburn equation

$$\frac{k_L}{V} (N_{Sc})^{2/3} = 0.023 \left(\frac{D_e V \rho}{\mu} \right)^{-0.20} \quad (13)$$

The results in the turbulent region agree with the correlation presented here as

to the effect of the Schmidt number for high values of this group, but they are about 30% lower than those predicted by Equation (11). In view of the apparent disagreement between these widely quoted mass transfer data and the proposed correlation, the results of the investigation of Lin et al. (21) will be discussed in further detail.

Generally one should not assume that transport phenomena in annuli may be represented by the same equations for flow in tubes by merely replacing the tube diameter with the equivalent diameter D_e ($= D_2 - D_1$). From a purely dimensional viewpoint the pi theorem requires that the consideration of an additional variable in the dimensional analysis of a problem without including an additional dimension be offset by the inclusion of an additional dimensionless group—for flow in an annulus (D_2/D_1). The theoretical equation for laminar friction factors (18) as well as the empirical equations for turbulent friction (5, 37) and for turbulent heat transfer (27) all contain functions of this group.

Although Leveque's result for flow inside tubes does not apply, the basic principle of the Leveque approximation under laminar flow conditions should

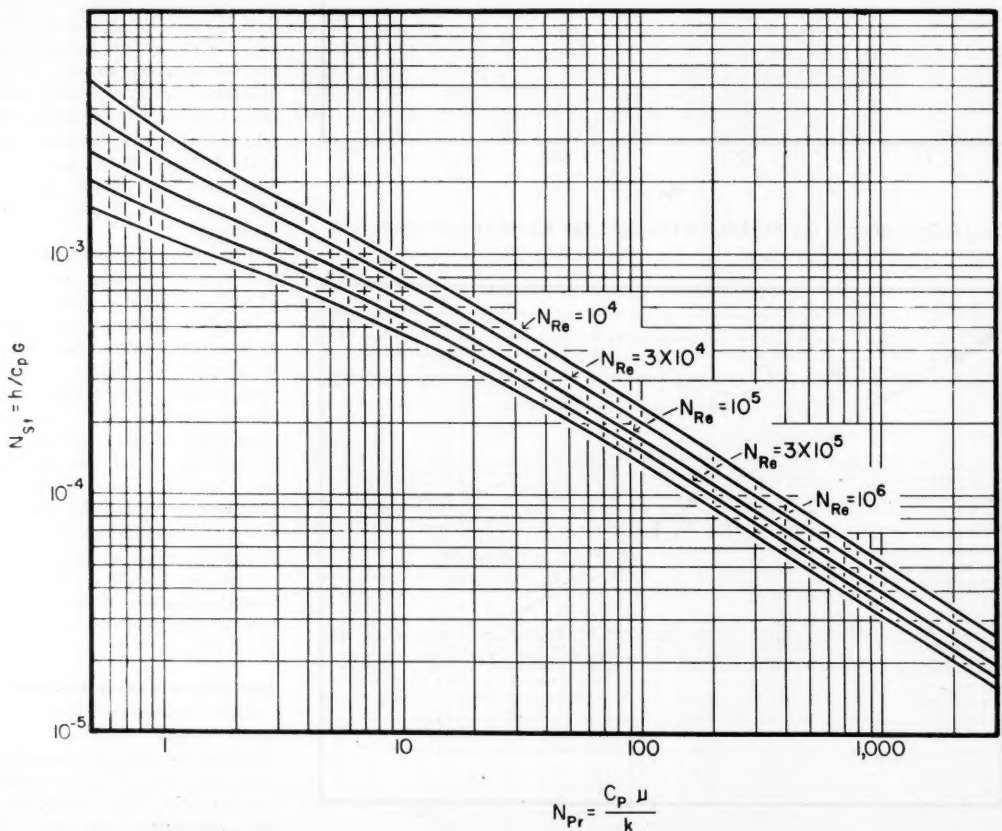


Fig. 14. Design chart.

apply to annular flow for the conditions of high mass flow rates through short tubes. The difference in the final result arises from the difference in the laminar-velocity distributions for the two distinct geometrical configurations. The appropriate derivation* has been performed (12), and the final result is

$$\frac{k_L D_1}{D_L} = 1.75 \left(\frac{w}{\rho D_L L} \right)^{1/3} [F(D_1/D_2)]^{1/3} \quad (14)$$

where $F(D_1/D_2)$ is given by

$$F(D_1/D_2) = \frac{(D_1/D_2)^2}{1 - (D_1/D_2)^2} \quad (15)$$

$$\left[0.50 - \left\{ \frac{(D_1/D_2)^2}{1 - (D_1/D_2)^2} \right\} \ln \frac{D_2}{D_1} \right] \quad (15)$$

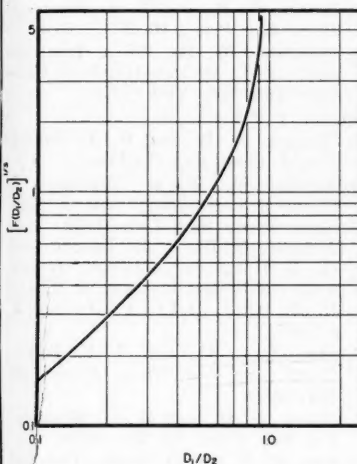


Fig. 15. $F(D_1/D_2)$ -Leveque approximation for annuli.

To aid the use of these theoretical results they are shown graphically in Figure 15. For $D_1/D_2 = 0.50$ the theory predicts

$$\frac{k_L D_1}{D_L} = 1.46 \left(\frac{w}{\rho D_L L} \right)^{1/3} \quad (16)$$

whereas the data in question are corrected by

$$\frac{k_L D_1}{D_L} = 1.24 \left(\frac{w}{\rho D_L L} \right)^{1/3} \quad (17)$$

The experimental results of Lin et al. are thus approximately 15% lower than the proper theoretical relation in the laminar region, and they are 22% lower than the best empirical relation (27) in

*A similar approach with some empirical corrections for natural convection was used by Rao (29) to correlate laminar heat transfer data for water in annulus.

the turbulent region. Clearly the use of these data cannot be recommended.

In the absence of further data for mass transfer the agreement of the data of Linton and Sherwood for high Schmidt number as well as the bulk of the data for low and moderate Schmidt number are accepted as confirmation of the proposed correlation. The analogies of Deissler and of Lin, Moulton, and Putnam which fit the disputed annular data of Lin et al. are believed to predict coefficients which are too low in the high Prandtl or Schmidt range. The difference between their coefficients and those predicted by the present work is about 30% in the range of Prandtl numbers between 1,000 and 3,000 when based on the present coefficient or 45% when based on values given by the earlier correlations.

conservative, as the exponent on the Reynolds number appears to increase toward 0.90. A design chart, based on the precise relationship, is given in Figure 14.

3. The theoretical solution indicated by the analogy between heat and momentum transfer, with the exception of the region of extremely low Prandtl number, is of the form

$$N_{st} = \frac{f/2}{1.20 + \sqrt{f/2}(N_{Pr} - 1)} \quad (b)$$

where the Reichardt b function is determined exclusively by the Prandtl number if $(N_{Pr})(N_{Re})^2(f) > 5 \times 10^6$.

4. The Reichardt b function is given empirically for a Prandtl number range of 0.50 to 600 by $b = 11.8 (N_{Pr})^{-1/3}$. The final semitheoretical correlation

$$N_{st} = \frac{f/2}{1.20 + 11.8 \sqrt{f/2}(N_{Pr} - 1)(N_{Pr})^{-1/3}} \quad (18)$$

CONCLUSIONS AND RECOMMENDED DESIGN EQUATIONS

1. The generally accepted empirical correlations and the semitheoretical analogies between heat and momentum transfer derived with experimental data for low and moderate Prandtl number are not representative of heat transfer in high Prandtl-number systems. In par-

representing all the available data for heat transfer with low and moderate temperature differences with a standard deviation of 9.4%. Nonisothermal deviations may arise from strong radial variations in both viscosity and thermal conductivity. If only viscosity varies appreciably with temperature, these may be approximately estimated with the correction $(\mu_w/\mu_n)^{0.14}$ or $(\mu_b/\mu_w)^{0.10}$.

5. The corresponding result for liquid-phase mass transfer in tubes

$$\left(\frac{k_L}{V} \right) = \frac{f/2}{1.20 + 11.8 \sqrt{f/2}(N_{Sc} - 1)(N_{Sc})^{-1/3}} \quad (19)$$

ticular the model of a perfectly laminar wall layer is clearly refuted. The modified analogies of Deissler (6), Lin, Moulton, and Putnam (22), and Rannie (34), although significant improvements, predict coefficients which are still appreciably too small in the high Prandtl or Schmidt number regions.

2. The best empirical equation for the turbulent heat transfer of the simple exponential form at $N_{Re} = 10^4$ is

$$N_{Nu} = 34.4 (N_{Pr})^{0.42}$$

This relation was found to correlate heat transfer data over a range of Prandtl numbers from 0.50 to 600 and is extended by approximate mass transfer data to Prandtl numbers of 3,000. If, as a first approximation, the conventional 0.80 exponent of the Reynolds number is assumed for the entire range of Prandtl numbers, then

$$N_{Nu} = 0.022 (N_{Re})^{0.80} (N_{Pr})^{0.42}$$

However for fluids with high Prandtl numbers this empirical equation becomes

is supported by the bulk of the available data for low and moderate Schmidt numbers and the data of Linton and Sherwood (23) for Schmidt numbers of 1,000 to 3,000. The widely quoted annular flow data of Lin et al. (21) are not directly applicable to pipe flow, and furthermore they consistently deviate by approximately 15 and 22% from the proper theoretical relation in the laminar region and the best empirical equation in the turbulent region, respectively.

RECOMMENDATIONS FOR FURTHER WORK

The final semitheoretical correlation presented in this work is believed to be a satisfactory representation of the limiting or isothermal coefficient of heat transfer. Nonisothermal deviations may be only crudely estimated with the present state of the art, however, and future studies of strongly nonisothermal flow should prove enlightening. Extremely precise experimental techniques would be required, and of first interest would be a fluid for which only viscosity varies with temperature. Studies with gases for which the specific heat and density

change relatively rapidly with temperature would also be of fundamental interest.

The problem of non-Newtonian heat transfer appears amenable to a theoretical approach similar to that used herein. If a suitable expression for the molecular shear such as the empirical power-law model is incorporated in the momentum transfer equation, manipulation of the equations for the fluxes of heat and momentum to indicate the form of the final solution for the heat transfer should be possible. Empirical representation of the unknown functions or, if possible, theoretical computation from basic turbulent flow measurements would then complete the solution.

ACKNOWLEDGMENT

This work was supported by the Office of Ordnance Research, U. S. Army. The interest and the very helpful suggestions of D. C. Bogue, D. W. Dodge, and R. L. Pigford are greatly appreciated.

NOTATION

Any consistent set of units may be employed. Those listed are merely illustrative.

b = Reichardt b function defined by Equation (3) and given experimentally by $11.8 (N_{Pr})^{-1/3}$, dimensionless
 c_1, c_2, c_3 = empirical constants, dimensionless
 C_p = specific heat, B.t.u. / (lb.-mass) ($^{\circ}\text{F}$)
 d = differential operator
 D = tube diameter, ft.
 D_1 = outside diameter of inner tube in concentric annulus, ft.
 D_2 = inside diameter of outer tube in concentric annulus, ft.
 D_e = equivalent diameter, ft.
 D_L = liquid molecular diffusion coefficient, sq. ft./hr.
 E_m = eddy diffusivity for momentum, sq. ft./hr.
 f = fanning friction factor, dimensionless
 F = function of (D_1/D_2) in equation for laminar heat or mass transfer in annuli
 g_c = conversion factor 32.17 (lb. $_{m}$ / ft.) / (lb. $_{f}$) (sec. 2)
 G = mass velocity, lb.-mass / (hr.) (sq. ft.)
 h = film coefficient of heat transfer, B.t.u. / (hr.) (sq. ft.) ($^{\circ}\text{F}$)
 k = thermal conductivity, B.t.u. / (hr.) (ft.) ($^{\circ}\text{F}$)
 k_L = liquid phase mass transfer coefficient, moles / (sec.) (sq. ft.) (moles / cu. ft.)
 L = tube length, ft.
 q = heat flux, B.t.u. / (hr.) (sq. ft.)
 T = temperature, $^{\circ}\text{F}$.

ΔT = temperature difference or temperature rise, $^{\circ}\text{F}$.
 u = time average point velocity in x direction, ft./sec.
 u^* = friction velocity, $\sqrt{g_c \tau / \rho}$, ft./sec.
 u^+ = generalized velocity parameter, u/u^* , dimensionless
 U = maximum linear velocity at center line, ft./sec.
 V = mean linear flow velocity, ft./sec.
 w = mass flow, lb.-mass/hr.

Greek Letters

θ = dimensionless temperature difference, $T - T_0/T_e - T_0$
 θ_m = ratio of mean to maximum temperature differences
 μ = viscosity, lb.-mass/ft. sec. or lb.-mass/(ft.) (hr.)
 ν = kinematic viscosity, sq. ft./hr.
 ρ = fluid density, lb.-mass/cu. ft.
 τ = shear stress, lb.-force/sq. ft.
 ϕ = dimensionless velocity, u/U
 ϕ_m = ratio of mean to maximum velocities, V/U

Subscripts

b = bulk average
 c = center line
 mo = molecular
 w = wall

Dimensionless Numbers

$N_{Nu} = (hD/k)$ Nusselt number
 $N_{Pr} = (C_p \mu / k)$ Prandtl number
 $N_{Re} = (DG/\mu)$ Reynolds number
 $N_{Sc} = (\mu / \rho D_L)$ Schmidt number
 $N_{Sh} = (k_L/V)$ Sherwood number
 $N_{St} = (h/C_p G)$ Stanton number

LITERATURE CITED

- Bernardo, Everett, and C. S. Eian, *Nat. Advisory Comm. Aeronaut.*, ARR No. E5F07 (1945).
- Blasius, H., *Forsch. Arb. Ing. Wes.*, **131** (1913).
- Coglan, Charles, M.Ch.E. thesis, Univ. of Delaware, Newark (1940).
- Colburn, A. P., *Trans. Am. Inst. Chem. Engr.*, **29**, 174 (1933).
- Davis, E. S., *Trans. Am. Soc. Mech. Engrs.*, **65**, 755 (1943).
- Deissler, R. G., *Nat. Advisory Comm. Aeronaut.*, Report 1210 (1955).
- Dittus, P. W., and L. M. K. Boelter, *Univ. of Calif. Engr. Publ.* **2**, 443 (1930). [Through reference 24].
- Drew, T. B., E. C. Koo, and W. H. McAdams, *Trans. Am. Inst. Chem. Engrs.*, **28**, 56 (1933).
- Drexel, R. E., and W. H. McAdams, *Nat. Advisory Comm. Aeronaut.*, ARR. No. 4F28, also Wartime report 108 (1945).
- Eagle, Albert, and R. M. Ferguson, *Proc. Roy. Soc. London*, **A127**, 540 (1930).
- Eisenberg, Morris, C. W. Tobias, and C. R. Wilke, *Chem. Eng. Progr. Symposium Series* No. 16, **51**, 1 (1955).
- Friend, W. L., M.Ch.E. thesis, Univ. of Delaware, Newark (1957).
- Hartnett, J. P., *Trans. Am. Soc. Mech. Engrs.*, **77**, 1211 (1955); Deissler, R. G., *ibid.*, p. 1221; and Kays, W. M., *ibid.*, p. 1265.
- Hoffman, H. W., paper presented at 1953 Heat Transfer and Fluid Mechanics Institute, Univ. of S. Calif. (1953).
- Kay, Joseph and E. C. Elgar, *Trans. Am. Soc. Mech. Engrs.*, **80**, 753 (1958).
- Kays, W. M. and I. S. Bjorklund, *ibid.*, **80**, 70 (1958).
- Kern, D. Q., "Process Heat Transfer," p. 46, McGraw-Hill Book Company, Inc., New York (1950).
- Knudsen, J. G., and D. L. Katz, "Fluid Dynamics and Heat Transfer," Eng. Res. Inst., Univ. of Mich. (1954).
- Kreith, Frank, and Martin Summerfield, *Trans. Am. Soc. Mech. Engrs.*, **72**, 869 (1950).
- Leveque, M. A., *Ann. mines*, **13**, 201 (1928).
- Lin, C. S., E. B. Denton, H. S. Gaskell, and G. L. Putnam, *Ind. Eng. Chem.*, **43**, 2136 (1951).
- Lin, C. S., R. W. Moulton, and G. L. Putnam, *ibid.*, **45**, 636 (1953).
- Linton, W. H., and T. K. Sherwood, *Chem. Eng. Progr.*, **46**, 258 (1950).
- McAdams, W. H., "Heat Transmission," 3 ed., McGraw-Hill Book Company, Inc., New York (1954).
- Metzner, A. B., *Ibid.*, p. 208.
- Metzner, A. B. and W. L. Friend, *Can. J. Chem. Eng.* (In Press).
- Metzner, A. B., in "Advances in Chemical Engineering," vol. I, Academic Press, New York (1956). Also Metzner, A. B., R. D. Vaughn, and G. L. Houghton, *A.I.Ch.E. Journal*, **3**, 92 (1957); and Metzner, A. B., and R. E. Otto, *A.I.Ch.E. Journal*, **3**, 3 (1957).
- Monrad, C. C., and J. F. Pelton, *Trans. Am. Inst. Chem. Engrs.*, **38**, 593 (1942).
- Morris, F. H., and W. G. Whitman, *Ind. Eng. Chem.*, **20**, 234 (1928).
- Rao, C. V., Ph.D. thesis, Univ. of Delaware, Newark (1949).
- Reichardt, H., "Fundamentals of Turbulent Heat Transfer," trans. from *Arch. ges. Warmtech.*, No. 6/7 (1951), *Nat. Advisory Comm. Aeronaut.*, TM-1408 (1957), and N-41947 (1956).
- Sieder, E. N., and G. E. Tate, *Ind. Eng. Chem.*, **28**, 1429 (1936).
- Sherwood, T. K., and J. M. Petrie, *ibid.*, **24**, 736 (1932).
- Sherwood, T. K., and R. L. Pigford, "Absorption and Extraction," McGraw-Hill Book Company, Inc., New York (1952).
- Summerfield, Martin, Heat Transfer Symposium, Eng. Res. Inst., Univ. of Mich., 151 (1953) [through reference 6].
- Ullock, D. S., and W. L. Badger, *Ind. Eng. Chem.*, **29**, 905 (1937).
- von Karman, Theodore, *Trans. Am. Soc. Mech. Engrs.*, **61**, 705 (1939).
- Walker, J. E., G. A. Whan, and R. R. Rothfus, *A.I.Ch.E. Journal*, **3**, 484 (1957).

Manuscript submitted January 6, 1958; revision received August 14, 1958; paper accepted August 26, 1958.

Gas-Solid Contacting with Ozone Decomposition Reaction

C. G. FRYE, W. C. LAKE, and H. C. ECKSTROM

Pan American Petroleum Corporation, Tulsa, Oklahoma

Fluidized catalyst beds have advantages in catalyst handling and heat transfer when compared with fixed beds. At a given space velocity, however, the conversion in fluidized beds is lower than that observed in fixed beds, owing to less efficient gas-solid contacting. Since the performance of fluid-bed reactors depends upon gas-catalyst contacting, their design benefits from a knowledge of the variables affecting contacting. Contacting mechanisms for fluidized beds have been proposed and tested by several investigators: Shen and Johnstone (1) studied the kinetics of decomposition of nitrous oxide over an impregnated alumina catalyst in fixed and fluid beds, and in a more recent paper Mathis and Watson (2) studied the effect of fluidization on the kinetics of catalytic cumene dealkylation in fixed and fluid beds. Both papers were concerned primarily with developing a mechanism of fluid-bed contacting by applying fluid-bed kinetic data to proposed models of fluid-bed behavior. These papers indicate that current knowledge of the contacting mechanism is insufficient to develop generalized correlations for reactor design; therefore the design of large-scale fluid-bed reactors depends upon empirical correlations developed from fluid-bed kinetic data. Unfortunately, as the number of fluid-bed parameters that may influence gas-catalyst contacting is large, experiments performed to obtain these design data with most industrial reactions are expensive and time consuming.

To reduce the expense and time

required to obtain these fluid-bed kinetic data a substitute reaction may be used which has the following characteristics: low concentrations of reactant; rapid and accurate analysis by simple, well-established methods; and measurable reaction rates at low pressures and temperatures. In addition to these characteristics the substitute reaction must be rate controlled in the same way and by the same catalyst as the reaction for which it is to be substituted.

Hydrocarbon synthesis on mill-scale catalyst is a reaction for which a substitute is desirable to obtain reactor design data, and ozone decomposition was found to possess the requirements of a satisfactory substitute for this reaction.

EXPERIMENTAL PROCEDURE

The experimental procedures used to study fluid-bed gas-solid contacting with the ozone decomposition reaction in 2-, 8-, and 30-in.-diam. metal reactors are described under Pilot Plant Procedure. The small-diameter (11 and 22 mm.) glass-reactor experimental procedures (for both fixed and fluid beds) are described under Laboratory Procedure.

The catalyst used in these studies was rod mill scale obtained from the Bethlehem Steel Corporation plant at Sparrows Point, Maryland. The catalyst was ground to a particle size of -40 mesh, washed with boiling water twice, and air dried. Bulk settled density of the catalyst varied from 165 to 200 lb./cu. ft. and particle specific gravity from 4.5 to 5.0. Average properties for the catalysts, indicated as fine grind and coarse grind, are as follows:

SCREEN ANALYSIS, WT. %

(U. S. National Bureau of Standards)

Sieve Sizes

	Average settled catalyst density lb./cu. ft.	-40 +60	-60 +80	-80 +100	-100 +140	-140 +200	-200 +325	-325	Minimum fluidization velocity ft./sec.
Fine	165	—	—	2.6	37.8	28.4	22.0	9.2	0.05
Coarse	197	11.8	18.1	15.1	21.4	12.7	12.8	8.1	0.13

The ozone decomposition reaction was used in 2-, 8-, and 30-in.-diam. metal reactors to obtain data for predicting fluid-bed reactor performance. In addition experiments were performed in small glass fixed- and fluid-bed reactors to investigate the mechanism of fluid-bed gas-catalyst contacting. The purpose of this paper is to discuss the results of these experiments.

The minimum fluidization velocity was determined in separate small-scale equipment by use of nitrogen at room temperature and atmospheric pressure.

Pilot Plant Procedure

A flow diagram of the 30-in. reactor used in the pilot plant is shown in Figure 1. The 2- and 8-in. fluid units were operated with the same gas-supply system as the 30-in. unit.

Compressed air was passed through a knockout drum, felt oil filter, and charcoal adsorber to remove contaminants. Water concentration in the reactor feed was controlled by saturating the air with water at a measured pressure and temperature (usually 85 lb./sq. in. gauge and 85°F.) in a small packed tower. A portion of the air stream from the saturator was mixed with the ozone-oxygen stream in a Venturi tube, the purpose of which was to eliminate surges in the ozone-oxygen stream by absorbing the pressure changes in the main feed line to the reactor grid.

Ozone was made in a Welsbach type C ozone generator from bottled oxygen. A low nitrogen concentration was essential to avoid poisoning the catalyst with nitrogen oxides formed in the ozone generator. All valves, piping, and equipment from the ozone-generator exit to the Venturi were constructed of stainless steel.

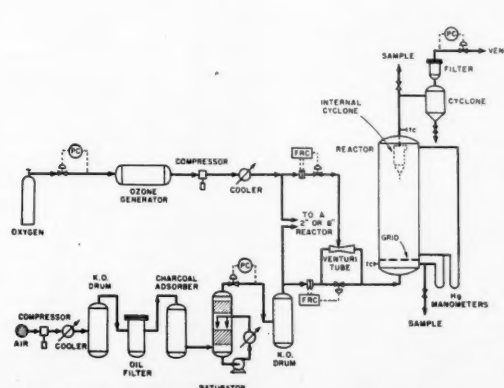


Fig. 1. Flow diagram of pilot plant experimental equipment.

The combined feed stream was preheated to 85°F. before entering the reactor through a multiholed flat plate grid. The reactor was insulated and electrically heated to maintain a constant temperature. Sample lines of Tygon tubing were connected to stainless steel valves just below the grid and between the reactor and external cyclone on the vent line for the 30-in.-diam. unit. For the 2- and 8-in.-diam. units sampling ports were located below the grid, on the vent line, and about 11 ft. above the grid. All three reactors were about 20 ft. long.

Air and ozone-oxygen flow rates were measured by orifice meters, static pressures by mercury manometers or pressure gauges, and temperatures by thermocouples. Most of the pilot plant experiments were conducted with atmospheric pressure at the reactor vent, although a few runs were made with about 45 lb./sq. in. gauge back pressure.

Since the comparison of the efficiencies of gas-solid contacting in different reactor systems requires a catalyst of constant activity, periodic activity checks were performed in the 8-in.-diam. unit. Before any of the reactors were loaded with catalyst, a blank run was made to measure the amount of ozone conversion due to the walls of the reactor. The ozone conversion on the walls of the 8-in. unit slowly increased with time. Instead of the reactor being replaced a new sheet-metal liner was inserted in the unit to provide a less active surface whenever the empty unit conversion became too large.

During loading of the reactors an air flow of about 0.1 ft./sec. was maintained. Ozone

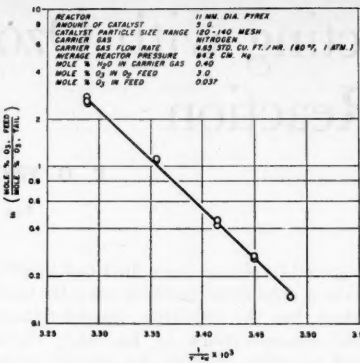


Fig. 4. Arrhenius plot for activation energy of ozone decomposition reaction.

concentration was adjusted to 0.03 ± 0.005 mole % ozone in the total feed. After steady state conditions had been attained, two or three samples each of the reactor feed and vent gas streams were analyzed for ozone concentration by either a chemical or an optical method.

A catalyst inventory was maintained and samples taken during unloading for particle size determination. Catalyst fines were retained in the 30-in. reactor by an internal cyclone, while the fines from an external cyclone were returned at the end of each run.

The catalyst bed height (settled) was calculated from the catalyst inventory, bulk settled density, and open cross-sectional area of the reactor. Superficial gas velocity

through Drierite and the ozone generator before entering the mixing chamber. A constant fraction of the mixed stream was continuously withdrawn for feed gas analysis. The remainder of the mixed stream was passed through the glass preheater and through the reactor. The reactor effluent stream was analyzed chemically, and a wet test meter measured the total tail gas rate. All pressures were measured with open-end mercury manometers; temperatures were measured by mercury thermometers with 0.1°C. graduations.

An 11 mm. diam. pyrex glass reactor was used for fixed bed experiments. Downflow operation was used with the catalyst supported by a coarse fritted glass disk. A similarly constructed 22-mm. Pyrex glass reactor was used for the fluid-bed experiments. The usual catalyst charge to the 11- and 22-mm. diam. reactors was 5 and 20 g., respectively.

Analytical Procedure

Chemical Method

Ozone was determined volumetrically by the iodide method (3) which depends upon the reaction



Optical Method

Ozone was determined by its ultraviolet absorption using $255 \text{ m}\mu$ as the analytical wave length. A Beckman recording ultraviolet spectrophotometer with a 10-cm. absorption cell was used and calibrated with the iodide method.

RESULTS AND DISCUSSION

Fixed-Bed Kinetics of the Ozone Decomposition Reaction

A characteristic of a substitute reaction for fluidization studies is similar reaction kinetics. Consequently the kinetics of ozone decomposition over mill scale were determined in small fixed-bed glass reactors for comparison with hydrocarbon synthesis data.

Order of Reaction

To determine the order of the ozone decomposition reaction the mole fraction of ozone was varied from about 0.02 to

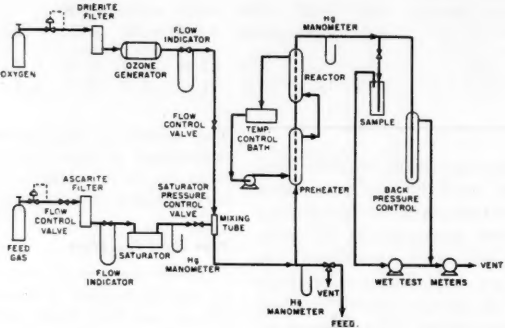


Fig. 2. Flow diagram of laboratory experimental equipment.

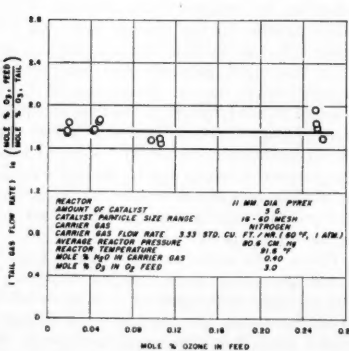


Fig. 3. Order of ozone decomposition reaction.

was calculated at the conditions in the top of the reactor. Experimental results were obtained at constant reactor temperature (generally 85°F. \pm 0.5°) to eliminate the need for temperature corrections.

Laboratory Procedure

A flow diagram of the experimental equipment used with the glass reactors is shown in Figure 2. Various gases were used instead of air as the carrier gas in this system. The carrier gas stream was passed through an ascarite trap to remove small amounts of carbon dioxide and then saturated with water vapor at a controlled temperature and pressure before being throttled into the mixing tube. In a single experiment it was observed that carbon dioxide as the carrier gas poisoned the catalyst. The oxygen stream was passed

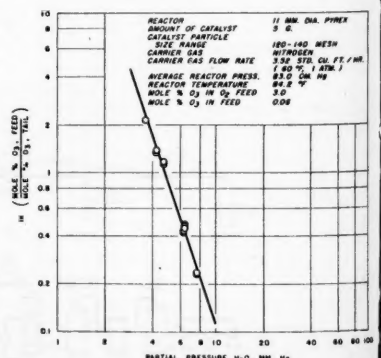


Fig. 5. Effect of water partial pressure on ozone decomposition reaction.

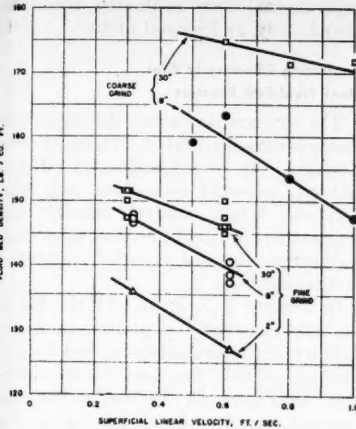


Fig. 6. Effect of linear velocity on fluid-bed density.

0.26 with all other variables held constant. The data from this experiment are shown in Figure 3. Since the product (total gas flow rate) $[\ln(\text{mole \% ozone, feed}/\text{mole \% ozone, tail})]$ is constant over about a tenfold change in feed ozone concentration, it has been concluded that the reaction is first order with respect to ozone concentration. Data from similar experiments with the hydrocarbon synthesis reaction show this reaction to be first order also, as confirmed by data appearing in the literature (4).

Activation Energy

Activation energy of the reaction was evaluated over the temperature range from 57° to 88°F. The data are presented in Figure 4 as a plot of $\log[\ln(\text{mole \% } o_3, \text{ feed}/\text{mole \% } o_3, \text{ tail})]$ vs. $1/T$. An activation energy of about 29 kcal./g. mole was calculated from the slope of this curve. Since the magnitude of this energy of activation is consistent with a surface rate-controlled reaction, it was assumed that the ozone decomposition reaction is surface rate controlled. Data from similar experiments with the hydrocarbon synthesis reaction indicate that this reaction is also surface rate controlled (4).

Effect of Water Partial Pressure

To determine the effect of water upon the ozone decomposition reaction water partial pressure was varied from 3.5 to 7.5 mm. mercury holding all other variables constant, including a pressure of 1 atm. Data from this experiment are shown in Figure 5 as a plot of $\log[\ln(\text{mole \% ozone, feed}/\text{mole \% ozone, tail})]$ vs. \log partial pressure of water in millimeters of mercury. Since the slope of the correlating line is approximately minus 3, it has been concluded that over the range investigated the reaction is reciprocal third order with respect to water vapor concentration.

Derivation and Evaluation of Reaction Rate Constants

Derivation

From the fixed-bed data discussed, rate of ozone decomposition per unit mass catalyst is equal to $k(p_{o_3}/p_{H_2O})$. In a differential length of reactor of cross section area, the mass of catalyst is equal to $\eta A dl$. Thus, rate of ozone decomposition in reactor segment dl is equal to $kA\eta(p_{o_3}/p_{H_2O}) dl$. Under steady state conditions the moles of ozone decomposed per unit time are equal to the moles of ozone entering reactor segment dl per unit time (n_{o_3}) minus the moles of ozone leaving reactor segment dl per unit time ($n_{o_3} + dn_{o_3}$). Thus rate of ozone decomposition in reactor segment dl becomes

$$-dn_{o_3} = kA\eta \frac{p_{o_3}}{p_{H_2O}} dl$$

This may be rewritten

$$\frac{-d(N_{o_3}y_{o_3})}{y_{o_3}} = \frac{kA\eta}{y_{H_2O}} \frac{dl}{\pi^2} \quad (1)$$

When the total pressure varies linearly with the length of the reactor, $\pi = a - b\eta l$. With η assumed constant, $d\pi = -b\eta dl$. Equation (1) may now be written

$$\frac{d(N_{o_3}y_{o_3})}{y_{o_3}} = \frac{kA}{by_{H_2O}} \frac{d\pi}{\pi^2} \quad (2)$$

For the case in which the change in total moles of gas is negligible (moles total gas \gg moles ozone), and temperature and mole fraction water are constant, this equation may be integrated over the length of a fixed bed and solved for k to yield

$$k = by_{H_2O}^3 \left(\frac{N_{o_3}}{A} \right) \left(\frac{1}{\frac{1}{\pi_T} - \frac{1}{\pi_B}} \right) \ln \left(\frac{(y_{o_3})_B}{(y_{o_3})_T} \right) \quad (3)$$

Although Equation (3) has been derived for fixed catalyst beds, it has been used in this paper as a measure of the activity of fluid catalyst beds. For fluid

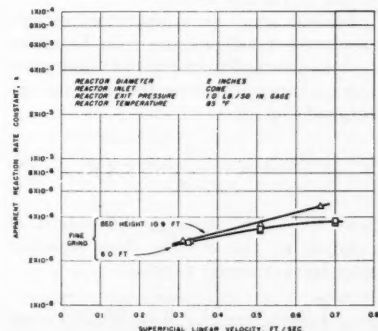


Fig. 7. Apparent reaction rate constant vs. linear velocity and bed height for 2-in. reactor.

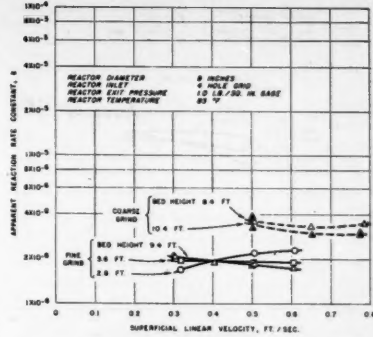


Fig. 8. Apparent reaction-rate constant vs. linear velocity, bed height, and catalyst particle size for 8-in. reactor.

beds, when π is expressed in pounds per square foot and η in pounds per cubic foot, $b = 1$. Since the reaction rate constant in Equation (3) is a direct measure of fluid-bed reactor performance, this equation offers a convenient means of correlating ozone conversion data from a fluid bed. Use of Equation (3) for fluid bed data correlation purposes does not necessarily suggest any particular contacting mechanism in fluid beds.

Corrections for Ozone Conversion on Reactor Walls

Since the sampling point for the reactor tail gas was generally several feet above the top of the fluid bed, ozone was decomposed by the reactor walls above the bed before the gas was sampled and analyzed. Thus the ozone concentration at the top of the fluid bed in Equation (3) was unknown. To obtain this concentration blank runs were made without catalyst before and after each set of experiments with catalyst present. These data are sufficient to calculate the ozone concentration at the top of the fluid bed if the following assumptions are made: Rate equation (1) developed for reaction within the bed is applicable to reaction on the walls; activity of the exposed wall surface is constant; and pressure change in the empty reactor is negligible.

With these assumptions Equation (1) can be integrated from the bottom of the reactor to the top sampling point to yield the result

$$\ln \frac{(y_{o_3})_{B_1}}{(y_{o_3})_{T_1}} = \frac{k' l_{RE}}{y_{H_2O}^3 \pi_{avg}^2 N_{o_3}} \quad (4)$$

Similarly Equation (1) can be integrated from the top of the fluid bed to the top sampling point to yield

$$\ln \frac{(y_{o_3})_T}{(y_{o_3})_{T_0}} = \frac{k' (l_{RCAT} - l_{BED})}{y_{H_2O}^3 \pi_{avg}^2 N_{o_3}} \quad (5)$$

Elimination of k' from Equations (4) and (5), rearranging them, and subtracting $\ln(y_{o_3})_B$ from both sides of the final equation yields the desired expression

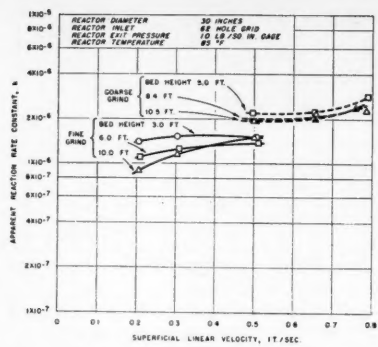


Fig. 9. Apparent reaction-rate constant vs. linear velocity, bed height, and catalyst particle size for 30-in. reactor.

to substitute in Equation (3), which then becomes

$$k = y_{H_2O}^3 (N_G/A) \left[\ln \frac{(y_{o_3})_{T_0}}{(y_{o_3})_B} + B \frac{(l_{RCAT} - l_{BED})}{(l_{RE})} \ln \frac{(y_{o_3})_{B_1}}{(y_{o_3})_{T_0}} \left[\frac{1}{\frac{1}{\pi_B} - \frac{1}{\pi_{T_0}}} \right] \right] \quad (6)$$

where

$$B = \frac{[y_{H_2O}^3 \pi_{avg}^2 (N_G/A)]_E}{[y_{H_2O}^3 \pi_{avg}^2 (N_G/A)]_{CAT}} \quad (7)$$

and the subscripts *E* and *CAT* indicate that these quantities be evaluated at conditions used in the runs without catalyst and with catalyst, respectively. All ozone mole fractions on the right side of Equation (6) were measured.

Corrections for the ozone conversion above the bed were not greater than 10% of the apparent reaction rate constant.

Since ozone was found to be decomposed on contact with the reactor walls above the top of the fluid bed, some decomposition is also possible on the reactor wall below the top of the fluid bed. No correction for this conversion has been made, since the data are insufficient to calculate its extent. However it is likely to be insignificant compared to the total ozone conversion because the average actual velocity of gas within the bed is high compared to the velocity above the fluid bed, and the concentration of ozone in the dense phase of the fluid bed and therefore in contact with the reactor wall is low.

Under constant experimental conditions the precision of the data was determined, and the calculated reaction rate constant *k* found to deviate by a maximum of about 5%. Other experiments were performed to determine the validity of the corrections for ozone conversion on the reactor wall above the fluidized-catalyst bed. In these experiments reaction rate constants were

evaluated from analyses of tail gas samples taken rapidly from the top of the reactor and from a special sample port near the top of the fluid bed. The percentage of deviation in these *k* values was significantly smaller than the 5% error in precision already noted.

Evaluation

Height of the fluid bed was calculated by dividing the catalyst inventory, pounds, by the cross-sectional area, square feet, and by a constant settled catalyst density, 165 lb./cu. ft., and multiplying by a constant expansion factor for fluid beds of 1.20. Pressure at the top of the bed was assumed equal to the measured pressure at the reactor exit. Pressure at the bottom of the bed was calculated by adding the bed pressure drop (measured by a mercury manometer) to the pressure at the top of the bed.

In the expression $(y_{H_2O}^3 \pi_{avg}^2 (N_G/A))_{CAT}$, the term π_{avg} lb./sq. ft. abs. was assumed to be the measured pressure at the top sampling point. In Equation (6) the following expression was evaluated from an average of data taken in the empty reactor before and after each set of experiments with catalyst present

$$\left[\ln \frac{(y_{o_3})_{B_1}}{(y_{o_3})_{T_0}} \right] \left[\frac{[y_{H_2O}^3 \pi_{avg}^2 (N_G/A)]_E}{l_{RE}} \right]$$

The term π_{avg} lb./sq. ft. abs. was assumed equal to the measured pressure at the top sampling point.

It should be noted that the corrections for conversion above the catalyst bed were made by using estimated fluid-bed heights. For convenience the same settled-bed density and fluid-bed expansion factor were used in all calculations. In general the corrections to the *k* values for ozone conversions above the catalyst bed were less than 5% of the *k* value. Use of actual fluid-bed heights would not significantly affect this correction for conversion above the fluid bed. Figure 6 is a plot of fluid-bed density vs. superficial linear velocity for the three reactors with coarse and fine catalysts. These data can be used to calculate actual fluid-bed heights from the settled-bed heights shown in Figures 7 to 11.

For the small-scale laboratory experiments the total pressure π in Equation (1) was assumed to be constant and equal to π_{avg} . Integration over the length of the catalyst bed gives

$$N_G \ln \frac{(y_{o_3})_F}{(y_{o_3})_T} = \frac{k}{y_{H_2O}^3 \pi_{avg}^2} (A \eta l_{BED}) \quad (8)$$

Since $W_{CAT} = A \eta l_{BED}$, the weight of catalyst in the reactor, this equation may be rearranged to read

$$k = \left[\frac{y_{H_2O}^3 \pi_{avg}^2 N_G}{W_{CAT}} \right] \left[\ln \frac{(y_{o_3})_F}{(y_{o_3})_T} \right] \quad (9)$$

The apparent reaction-rate constants for both pilot plant and laboratory

experiments were evaluated by using pound, foot, and second units.

Contacting Efficiency in Pilot Plant Fluid-Bed Reactors

The apparent ozone decomposition reaction-rate constant, *k*, evaluated from Equation (6), is a function of catalyst activity, gas-solid contacting, and temperature. When catalyst activity and temperature are held constant, *k* becomes a direct measure of gas-solid contacting in fluidized beds.

In Figures 7, 8, 9, and 11 the log of the rate constant *k* is plotted vs. linear velocity with parameters of bed height, catalyst particle size, and reactor diameter. In Figure 10 the log of the rate constant is plotted vs. the log of the reactor diameter with bed height as a parameter. Superficial linear velocities were calculated at the top of each reactor, and the bed heights (settled) were calculated from the catalyst inventory, reactor cross-sectional area, and average settled catalyst density for each grind.

Saturation temperature and pressure (which determined water concentration in the feed gas) were held constant at 85°F. and 85 lb./sq. in. gauge for the experiments shown in Figures 7 to 10; saturator temperature was increased to 90°F. for the experiments of Figure 11. All other experimental conditions are stated on the figures.

Figures 7, 8, and 9 show the effect on *k* of linear velocity, bed height, and particle size for reactor diameters of 2, 8, and 30 in. No coarse-grind data were available for the 2-in. reactor.

According to these three figures *k* appears to increase slightly as the linear velocity is increased, except for bed heights above 5.6 ft. in the 8-in. unit. Over most of the range of linear velocities studied *k* is shown to decrease with increased bed heights, with the exception of the 2-in. data. The most pronounced effect on *k*, shown by Figures 8 and 9, is due to increased particle size of the catalyst. At 0.5 ft./sec. linear velocity *k* increased 75% in the 8-in. unit and 40% in the 30-in. unit when the particle size

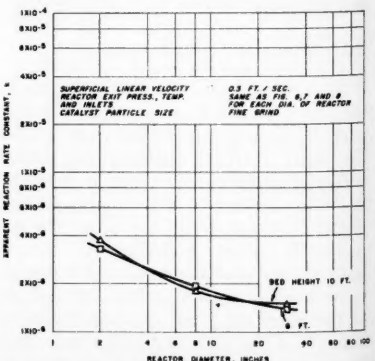


Fig. 10. Apparent reaction-rate constant vs. reactor diameter and bed height.

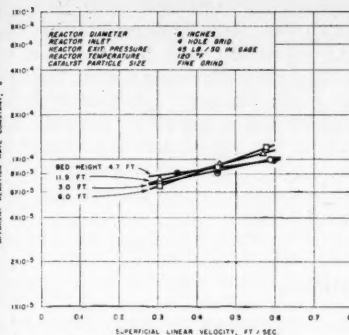
position
from
catalyst
temperature
and
comes
actinglog of
linear
height,
diam-
rate
of the
as a
plicities
actor,
were
atory,
verage
ind.
pressure
ration
nt at
or the
o 10;
ed to
re 11.
s areect on
and
of 2, 8,
wereres k
linear
bed
unit.
cencies
with
option
duced
nd 9,
of the
city k
40%
e size10 FT.
80 60 40
ant vs.

Fig. 11. Apparent reaction-rate constant vs. linear velocity and bed height for 8-in. reactor at 45 lb./sq. in. pressure.

was changed from fine to coarse grind.

Figure 10 shows the effect of reactor diameter on k with all other parameters held constant. At a bed height of 10.0 ft. and a linear velocity of 0.5 ft./sec., the ratio of k values for a 2-in. to an 8-in. reactor is 2.1 for a fine grind. This ratio, obtained with ozone decomposition, can be compared to a value of 2.3 for the ratio of 2- to 8-in. reactor performance from the hydrocarbon synthesis reaction over an iron catalyst in fluidized beds. Another comparison of the ozone decomposition with hydrocarbon synthesis can be made by using the ratios for fixed bed to 8-in. reactor performance. For these reactors the ratios are about 15 to 1 to 20 to 1 for ozone or hydrocarbon synthesis, depending on the experimental conditions. These data suggest that the ozone decomposition reaction can be used to simulate the gas-solid contacting process occurring in a hydrocarbon synthesis fluid-bed reactor. In addition these data also suggest that the ozone decomposition reaction may be used for studying gas-solid contacting in fluid beds for other first order reactions.

Figure 11 illustrates how increased reactor pressure (4 atm.) in an 8-in. reactor affects the shape of the linear-velocity-bed-height curves (Figure 8) obtained at 1-atm. pressure. At the higher pressure the effect of linear velocity appears about the same, with the bed-height effect slightly reduced. An absolute comparison between Figures 8 and 11 is complicated, since the reactor temperature was increased from 85° to 120°F. to obtain measurable ozone conversions at the higher pressure.

Preliminary Investigation of Fluid Bed Contacting Mechanism

In the preceding paragraphs no consideration has been given to the mechanism of the actual contacting process. The purpose of the experimental work discussed was to use the ozone decomposition reaction for determining the effects on gas-solid contacting of changes in certain operation variables in fluidized-bed reactors. These data suggest that

ozone decomposition data may be used to develop empirical correlations for fluid-bed hydrocarbon-synthesis reactor design. However to develop generalized correlations for reactor design an understanding of the actual mechanism of gas-solid contacting is necessary.

Experiments have been performed in small glass fixed- and fluid-bed reactors by using the ozone decomposition reaction to investigate the actual contact mechanism. Such an investigation requires examination of the variables affecting gas-catalyst contacting over much wider ranges than is required for empirical reactor design. In addition parameters, which were held constant in reactor design studies, for example, catalyst activity, were varied in these preliminary mechanism studies.

This investigation began with experiments designed to determine whether the contacting process taking place in the small glass reactors is the same as that in the larger, for example, 8-in. diameter reactors. The data obtained from this preliminary study show no contradiction of an assumption that the contacting processes are the same. Two tests were made that indicated that the contacting processes were similar.

One such test was the variation of apparent reaction rate constant with temperature. In Figure 12 the quantity $\ln(\text{mole \% } O_3 \text{ feed}/\text{mole \% } O_3 \text{ tail})$ is plotted against reciprocal temperature for a typical 22-mm.-glass-reactor experiment and for a variable-temperature run made in the 8-in.-diameter fluid reactor. The glass reactor was operated at slightly above atmospheric pressure at a gas linear velocity of about 0.44 ft./sec. and contained 20 g. of catalyst. The 8-in. reactor contained 312 lb. of catalyst and was operated at an exit pressure of 45 lb./sq. in. gauge and a linear velocity of about 0.20 ft./sec. No correction was made for empty unit conversion in the 8-in.-diameter unit. Although the conditions of operation were somewhat different (1 and 4 atm.), it is evident that the change in conversion with temperature is qualitatively similar in the two systems; thus the data suggest that the contacting process is similar in the two systems.

The other test was to investigate the effect of gas linear velocity upon gas-solid contacting. Experiments were performed in the 22-mm.-diameter reactor with nitrogen at variable flow rates as the fluidizing gas. Data from these runs are presented in Figure 13 together with similar data from a fixed-bed run with the same 120- to 140-mesh mill-scale catalyst. Each separate fluid-bed run was made with the same 20 g. of catalyst by adjusting linear velocity to a constant value and observing the change in ozone conversion with changes in temperature. Thus fluidization conditions for each run were constant. Changes in conversion

were thus obtained as a function of temperature only. (Changes in linear velocity, gas density, and viscosity were small over the 30°F. temperature range used.)

Examination of Figure 13 indicates that all the fluid-bed data are correlated by a single line, although the four sets of fluid-bed data were obtained at different linear velocities. These data indicate that the effect of linear velocity is directly correlated for this particular catalyst particle size and reactor system by the first order reaction rate constant values. The data obtained with coarse catalyst in the larger diameter fluid reactor (Figures 8 and 9) also show little or no variation in k value with linear velocity, suggesting again that the contacting process in the small glass reactors is similar to that in the larger units. The corresponding data from the 2-, 8-, and 30-in.-diameter reactors, Figures 7, 8 and 9, with fine-grind catalyst (for which there are no comparable glass-reactor data) show an increase in apparent activity with linear velocity. These data suggest that the gas-catalyst contacting process may not be the same with the smaller particle-size catalyst.

Comparison of the fluid-bed with the corresponding fixed-bed activity values in Figure 13 indicates that at low conversions (about 20%) the fixed-bed activity is about 2.2 times the value for the fluid bed at the same temperature ($1/T \times 10^3 = 3.48$). The difference between the two sets of values increases with increased conversion, and so at high conversion (about 80 to 90%) the fixed-bed activity is about 5.5 times the value for the fluid bed ($1/T \times 10^3 = 3.29$). With the larger 8-in.-diameter reactor the fixed-bed value at high conversion is about fifteen to twenty times that of the fluid bed. Thus these data are consistent with the trend toward lower activity of the 8-in.-diameter reactor, compared with that of the 2-in.-diameter reactor (Figures 7 and 8).

To determine the effect of gas density upon gas-solid contacting experiments

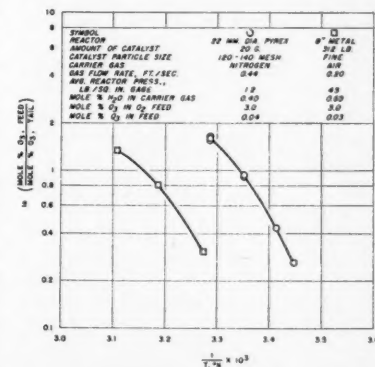


Fig. 12. Comparison of temperature effect on conversion between pilot plant and laboratory fluid-bed reactors.

were performed with helium used as the fluidizing gas. The experiments were performed in the same manner as those with nitrogen, with the same catalyst and covering the same linear velocity range. The results from these runs, which are shown in Figure 14, are not significantly different from the corresponding data with nitrogen used as the carrier gas. Since the viscosity of nitrogen and that of helium are approximately the same and the densities differ by a factor of seven, gas density is not an important factor in the gas-solid contacting process with this particular system.

The over-all kinetics of the fluidization process were determined in 11- and 22-mm.-diameter reactors. With all other variables held constant, feed-gas ozone concentration was approximately doubled. Ozone conversion in both experiments initially was 70%, and no change in percentage of conversion was observed after the feed-gas concentration had been increased. Thus it appears that under constant fluidization conditions the total conversion process is first order with respect to ozone concentration.

To determine the effect of catalyst particle size upon gas-solid contacting, experiments were performed with 60- to 100-mesh catalyst. These experiments were performed with nitrogen used as the fluidizing gas in the same manner as were the series of experiments with 120- to 140-mesh mill-scale catalyst. The data from these runs are shown in Figure 15. As in the case of the 120- to 140-mesh catalyst a single correlating line has been drawn through all the different sets of data at constant linear velocities. Close examination of Figure 15 indicates a trend toward increased k values at higher linear velocities. As in the case with the pilot plant experiments, however, this change is small.

Comparison of the fluid-bed with the corresponding fixed-bed data with the 60- to 100-mesh catalyst (Figure 15) shows that the differences are much smaller than those observed with the 120- to 140-mesh catalyst (Figure 13). At low conversions (about 20%) with 60- to 100-mesh catalyst the fixed-bed activity is about 1.4 times the values for the fluid bed at the same temperature ($1/T \times 10^3 = 3.40$). The corresponding comparison with 120 to 140-mesh catalyst was 2.2 times. At high conversions (about 80%) the fixed-bed activity is about 2.4 times the value for the fluid bed with 60 to 100 mesh catalyst ($1/T \times 10^3 = 3.25$) compared to 5.5 times with 120- to 140-mesh catalyst. Since for a fixed-temperature and catalyst-particle-size comparison of data from fixed with those from fluid beds constitutes a comparison of the effectiveness of catalyst utilization or gas-catalyst contacting, the data in Figures 13 and 15 may be interpreted to mean that the gas-solid contacting in the fluid bed with the 60- to

100-mesh catalyst is better than with the 120 to 140-mesh catalyst. In addition, since the minimum fluidization velocities for the 120- to 140-mesh catalyst and for the 60- to 100-mesh

catalyst are 0.10 and 0.22 ft./sec., respectively, the improvement in gas-solid contacting may be attributed to the larger fraction of gas flowing through the dense phase of the coarser grind catalyst. Since gas flow through the voids in the dense phase is probably in the viscous range, gas viscosity should also be a variable in the gas-solid contacting mechanism.

NOTATION

A	= cross-section area of reactor
$b\eta$	= constant characteristic of catalyst bed
k	= reaction rate constant per unit mass catalyst
k'	= reaction rate constant per unit length
N_A	= total gas flow per unit time
p_{H_2O}	= partial pressure H_2O
p_{O_3}	= partial pressure O_3
y_{H_2O}	= mole fraction H_2O
y_{O_3}	= mole fraction O_3
$(y_{O_3})_B$	= mole fraction O_3 at bottom of catalyst bed
$(y_{O_3})_E$	= ozone mole fraction at inlet for empty reactor
$(y_{O_3})_F$	= mole fraction of ozone in feed
$(y_{O_3})_T$	= mole fraction O_3 at top of catalyst bed
$(y_{O_3})_{T_e}$	= ozone mole fraction at top sampling point for empty reactor
$(y_{O_3})_{T_c}$	= ozone mole fraction at top sampling point with catalyst present
l_{BED}	= height of fluid bed, ft.
l_{RCAT}	= height of top sampling point above inlet with catalyst present, ft.
l_{RE}	= height of top sampling point above inlet for empty reactor, ft.

Greek Letters

η	= catalyst density
π	$= p_{O_3}/y_{O_3} = p_{H_2O}/y_{H_2O}$ = total pressure
π_T	= total pressure at top of catalyst bed, lb./sq. ft. abs.
π_B	= total pressure at bottom of catalyst bed, lb./sq. ft. abs.

LITERATURE CITED

1. Shen, C. Y., and H. F. Johnstone, *A.I.Ch.E. Journal*, 1, 349 (1955).
2. Mathis, J. F., and C. C. Watson, *ibid.*, 2, 518 (1956).
3. Scott, W. W., "Scott's Standard Methods of Chemical Analysis," 5th ed., Volume 2, p. 2370, D. Van Nostrand Co., New York (1939).
4. Storch, H. H., Norma Golumbic, and R. B. Anderson, "The Fischer-Tropsch and Related Syntheses," p. 535, John Wiley & Sons, New York (1951).

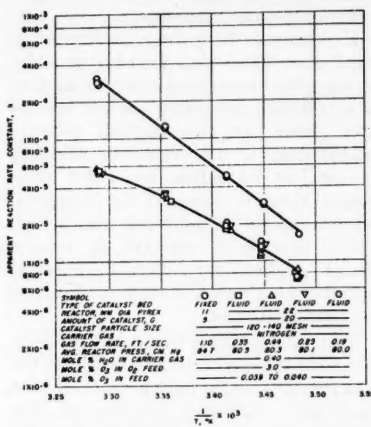


Fig. 13. Comparison of temperature effect on apparent reaction-rate constant between laboratory fixed- and fluid-bed reactors.

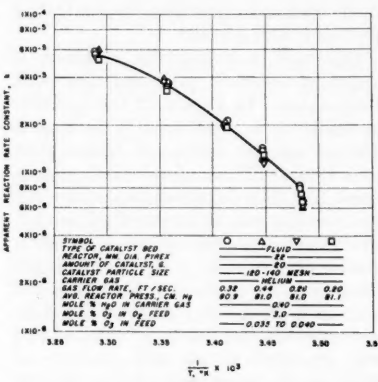


Fig. 14. Temperature effect on apparent reaction-rate constant in laboratory fluid-bed reactors.

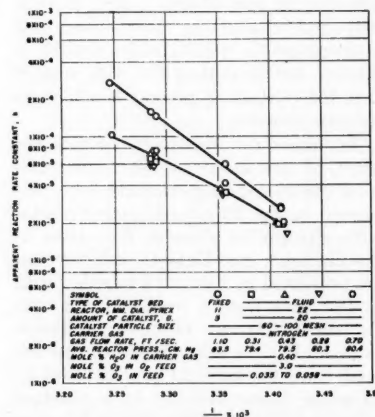


Fig. 15. Comparison of temperature effect on apparent reaction-rate constant between laboratory fixed- and fluid-bed reactors.

Presented at A.I.Ch.E. Chicago Meeting. Manuscript received December 3, 1957; revision received April 21, 1958; manuscript accepted April 21, 1958.

W
th

stea
One
wett
prim
temp
flux,
reve
wett
In
of 1
temp
to 1
(hr.)

has
prod
influ
met
is th
liqui
int
surf
addi
mech
cond
vapo
mov

M
poi
effe
In b
used
tens
conv
of so
ordi
diffe
used
steel
whic
tive
effec
The
stain
ured
elect
int
liqui
in a
wett
repo
non
follo

1.
alte
2.
film

3.
mat

Ze

and

Wetting Effects on Boiling Heat Transfer: the Copper-Stearic Acid System

W. B. HARRISON and ZELVIN LEVINE

Georgia Institute of Technology,
Atlanta, Georgia

In order to study effects of wetting on heat transfer in the nucleate boiling regime, stearic acid was boiled in contact with different crystal planes of single crystals of copper. One crystal plane being wetted by the acid more completely than the other, they are called *wetted* and *nonwetted* surfaces. In the region of low heat flux, where heat transfer is primarily nonboiling natural convection, the nonwetted crystal required higher values of temperature difference than the wetted crystal for the same flux. At high values of heat flux, though not in the vicinity of the critical temperature difference, the situation was reversed; that is, the nonwetted surface required lower temperature difference than the wetted surface.

In the present studies, stearic acid was boiled at about 465°F, corresponding to a pressure of 17 mm. of mercury. Heat flux ranged from 3,450 to 63,300 B.t.u./hr.(sq. ft.), and temperature difference between the copper crystal and the stearic acid ranged from 38° to 132°F. The corresponding range of heat transfer coefficient was from 91 to 510 B.t.u./hr.(sq. ft.)(°F.).

An influence of wetting on heat transfer has long been recognized in the boiling processes (1, 2, 3), and recently an influence of wetting has been suspected in convective studies with certain liquid metals such as mercury (4 to 7). The idea is that, if a surface is not wetted by a liquid, the thermal resistance across the interface would be greater than if the surface is wetted by the liquid. An additional consideration in the boiling mechanism is the influence that this condition has on the ease with which a vapor bubble may be formed and removed from the interface.

McAdams (3) and Jakob (2) have pointed out some of the qualitative effects of wetting on boiling heat transfer. In boiling studies, some observers have used detergents to change the surface tension of the liquid (8). In nonboiling convective heat transfer, small additions of sodium have been made to mercury in order to promote wetting (4, 6), and different surface materials have been used with mercury, such as stainless steel, which is not wetted, and copper, which is wetted (7). Nonboiling convective heat transfer to liquid sodium has also shown some evidence of wetting effects at a heat transfer surface (9). Thermal resistances across a sodium-stainless steel interface have been measured (10, 11), and measurements of electrical resistance across liquid-solid interfaces have also been made with liquid mercury and liquid sodium (12, 13) in an effort to learn more about the wetting mechanism. In these cases reported in the literature, *wetting* and *nonwetting* are achieved by one of the following methods:

1. Addition of agents to the liquid to alter its surface tension or increase wetting.
2. Coating of the solid surface with a film to change the nature of the interface.
3. Alternate use of differing solid materials with the same liquid.

Zelvin Levine is at present with the Babcock and Wilcox Company, Lynchburg, Virginia.

4. Alternate use of differing liquids with the same solid surface.

Another method has been employed in the present work, based on observations of Gwathmey, Leidheiser, and Smith (14), who, examining the chemical action of oils on single copper crystals, found that, under certain conditions, the degree of wetting of a solid by a liquid depended on the orientation of the crystal lattice at the liquid-solid interface. In particular, they found that at 200°C. only the 110° faces of a crystal were wetted by stearic acid in air, and that the 100° faces were not. These observations suggest the mode of approach for the present experiments: to use the same material (copper) in contact with the same liquid (stearic acid) but to achieve different degrees of wetting by having different crystal faces in contact with the liquid at the interface.

MECHANISM OF BOILING HEAT TRANSFER

Various general descriptions of the boiling process may be found in the work of such writers as Bosworth (1), and McAdams (3), and Jakob (2). Hawkins (15) prepared an extensive review of the literature on boiling heat transfer up to 1950. Since that time many papers on boiling have appeared, some of which seem to be pertinent to the present problem.

The process involving formation of discrete bubbles at the interface is referred to as *nucleate* boiling. The term implies the existence of *vaporization nuclei* which promote formation of individual bubbles. The exact nature of the nuclei is somewhat in doubt, but it may be that they are gas molecules adsorbed at the solid surface, gas molecules absorbed in the liquid, gas molecules generated by chemical reaction between the solid and liquid, or small solid particles suspended in the liquid. However, the nuclei may be nothing more than cavities or roughness elements in the surface which favor the formation of bubbles or differing force

fields arising from differing atomic lattice orientations at the surface.

Corty and Foust (16), investigating the influence of *degree of wetting* and *surface roughness* on nucleate boiling, concluded that the size and shape distribution of roughness elements on the surface and the contact angle of the bubble influenced the temperature difference required to achieve a particular heat flux, as well as the number of *active* centers (locations on the surface which favor repeated bubble formations). It might be pointed out here that there is a connection between contact-angle measurements and surface roughness. Wenzel (17) has proposed that the important aspect of roughness as it pertains to wetting is the ratio of actual surface area to projected area, rather than the mean height of roughness elements which is determined from surface profiles. He refers to findings of Bikerman which indicated the same contact angle for stainless steel plates having heights of roughness elements differing by a factor of over a hundred. The possibility also exists that actual force fields are on a microscopic scale but that contact angles must be on a much larger scale and hence may not faithfully reflect the important atomic or molecular interaction.

It may well be that the true effect of surface roughness is related to the atomic population density of the surface material. In a polycrystalline surface with random crystal orientations, if force field can be related to the number of atoms/unit of surface area, it is apparent that different crystal faces may have different attractive forces for the same liquid. Thus, the *active* center may be merely the location at which crystal-lattice orientation provides the least attraction for the liquid. Roughness may serve the function of providing only more of such crystal faces for a unit of projected area (though perhaps no more for a unit of actual area). Later in the report is a description of an effort to learn more about this effect of crystal orientation.

Jakob (2) has reported data on the frequency of formation of discrete bubbles at particular spots on a solid surface. Apparently the formation process is cyclic and the frequency is related to the ultimate size attained by the bubble just before it leaves the surface. The *leaving* size of the bubble is believed to be related to the interfacial attraction between the liquid and solid, the surface tension of the liquid, the buoyant force arising from the

*Miller indexes.

difference in density of the liquid and vapor, and perhaps other factors.

Some of the most penetrating comments on the boiling mechanism have been presented by Larson (18, 19), summarizing his earlier investigations (20) and expanding his concept of an *ebullator* theory. In developing this theory, Larson has taken into account attractive or Van der Waals' forces, repulsive forces related to overlap of atomic or molecular electron orbits, and relative atomic spacing of the solid and liquid. He suggested further that the influence of wettability would show in a family of curves, with the maximum flux and the corresponding temperature difference both increasing as wettability increases. It may be that experimental data on maximum heat flux obtained in nucleate boiling in geometrically similar systems can be used to estimate the degree of wettability.

THE WETTING OF COPPER BY STEARIC ACID

Before proceeding further in the discussion of wetting effects, one should define what is meant by the term *wetting* and the associated concept of *contact angle*. *Wetting* is considered to represent closeness of contact between a solid and a liquid. Three typical shapes of water-vapor bubbles on a heated surface are indicated by Jakob (2) to describe non-wetting, partial wetting, and wetting of the solid by the liquid. Spreading of a liquid drop on a solid is also indicative of wetting. If the drop spreads out over the surface, the surface is said to be wet. If the drop remains as a spheroid on the surface, the surface is not wet. At the solid-liquid-vapor interface the degree of wetting is ordinarily related to the angle (measured through the liquid) which the liquid-vapor interface makes with the solid-liquid interface at the intersection with the solid-vapor interface. A contact angle of zero implies complete wetting of the solid by the liquid, 180 deg. implies complete nonwetting, and any intermediate angle would describe degree of partial wetting. Gregg (21) and a number of other writers have extensively discussed wetting and contact angles.

As mentioned previously, the objective of the present work is to study wetting effects on boiling. The intent is to perform boiling heat transfer studies wherein changes in the degree of wetting are affected between the same solid and liquid. In the study of Gwathmey, Leidheiser, and Smith (14) on the chemical action of oils on single metal crystals, it was found that stearic acid would preferentially wet 110 planes on a spherical single crystal of copper, provided that the crystal had been alternately immersed in stearic acid and exposed to air for a certain period of time. In an atmosphere of hydrogen, this effect was not exhibited, an indication that the presence of oxygen as an oxide layer or complex was essential

in the mechanism. They also observed differences in rates of oxidation at different crystal planes as evidenced by the rate of change in color patterns on surfaces. The 100 planes apparently were the most active with respect to oxidation. Immersed in stearic acid, the crystal showed etch patterns which caused striated roughness at the 110 planes and smooth regions at the 100 and 111 planes. With respect to roughness as a factor in the wetting studies, they concluded that it had an influence but not a controlling one. One of their reports includes a detailed discussion of their results with respect to the present theory of the influence of crystal plane on surface reactions (22) and should be consulted for a more complete understanding of the status of the problem. Briefly, it

difference in roughness alone, one should expect a difference in wetting of copper by stearic acid at different crystal faces.

Figure 1 shows crystallographic details of the copper single crystal which pertain to the present study. Copper has a face-centered cubic structure, as indicated, and the 110 and 100 planes are identified. It may be seen that the population density of atoms is significantly different on the two crystal planes under consideration. The dimensions for the lattice are given by Seitz (24) and others.

Though the exact mechanism by which the preferential wetting occurs is not understood, there is some evidence to support the hypothesis that a monolayer of cuprous oxide is adsorbed at the copper surface, after which an oriented layer of stearic acid is formed. It is further postulated that stearic acid will not wet the oriented layer of itself. Since the 100 planes are more active than 110 planes for oxidation, and since 110 planes are etched more by stearic acid than the other planes, it appears that both facts suggest a breakdown of the cuprous-oxide-stearic-acid layer at the 110 planes to give wetting. Evidence that the monolayer of stearic acid may exist has been reported by Brummage (25). Polar liquids, which are unable to wet their own adsorbed films, have been called *autophobic*, and a number have already been identified by Hare and Zisman (26).

Whatever the mechanism is, it seems reasonable that the effect can exist at a polycrystalline surface, wherein *degree of wetting* becomes a highly localized concept with each crystal in the structure having its own degree of wetting. Indeed this may be the essence of *vaporization nuclei* or *active centers* in the boiling process.

PREPARATION AND PRELIMINARY STUDIES OF COPPER SURFACES

Simultaneous with the design and construction of the system to study effects on boiling heat transfer, studies were initiated on methods of preparing the surfaces to be used in the boiling experiments. Two cylindrical copper single crystals, 1-in. in diameter and 1-in. long, were purchased for these studies. They were oriented so that one had the flat ends parallel to the 110 planes and the other had flat ends parallel to the 100 planes. For purpose of identification, they will be referred to as the 110 crystal and the 100 crystal. Both of the single crystals were mechanically polished with abrasive papers down to 0000 grit size and, then electropolished and microphotographed.

An article by Jacquet (27) concerning principles involved in electrolytic polishing of copper in phosphoric acid was very helpful in formulating a polishing procedure for the present studies.

Gwathmey, *et al.* (14), had observed that a conditioning process was required

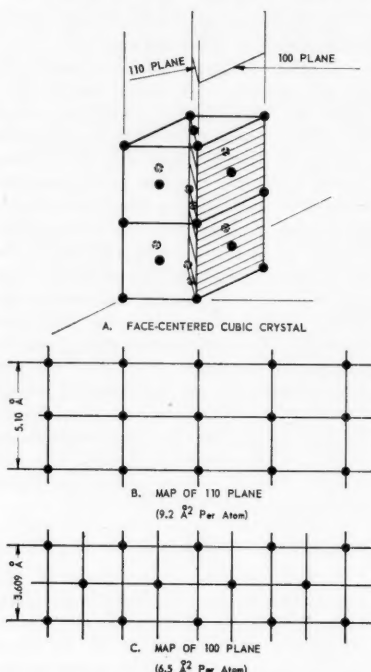


Fig. 1. Details of copper single crystal.

appears that arrangement of the atoms at the surface, including the number/unit area (population density), plays an important part in controlling reaction rates. Theoretical studies did not enable predictions for rates of oxidation, and simple energy concepts based on spacing of the atoms appeared to be of little value for such predictions.

The coexistence of differing roughness and differing wetting at differing crystal planes confuses the picture by preventing a separation of the variables. With respect to the influence of roughness on wetting, there are some interesting studies by Ray and Bartell (23) which show that contact angles are influenced by microroughness of extremely fine structure, perhaps even molecular in size. One might conclude that, from the dif-

before
obser
altern
stearic
mecha
so tha
imm
min.
bath
the d
Bel
starte
and
obser
angle
acid
of ea
were p
at a
micro
each
that a
ured.
angle
slight
dunkin
cryste
during
crysta
the ac
off be
merse
neith
appea
One
was t
micro
film o
surfac
the he
were n
the s
oxide
cylind
the n
micro
of the
acid w
than
copper
that
forma
molec
washe
angle
remov
return
Kru
of Gv
they
prefer
betwe
an ex
in co
made
200°C
differ
faces.
the ob
by W
wettin
vario

before the preferential wetting could be observed. This conditioning consisted of alternately exposing the surface to hot stearic acid and air. For this purpose, a mechanical dunking device was arranged so that the cylinders might be alternately immersed at a frequency of 20 cycles/min. The temperature of the stearic acid bath was kept at about 170°C. during the dunking operation.

Before the initial immersion period was started, periodically during the dunking, and after completion of the dunking, observations were made of contact angles between a drop of molten stearic acid and the benzene-washed top surface of each of the cylinders. The cylinders were placed on a hot plate and maintained at a temperature of about 100°C. A micrograph was prepared that showed each drop on each surface in profile so that the contact angles might be measured. Differences between the contact angles on the clean surfaces were very slight, although, before completion of the dunking, it was noted that the 100 crystal no longer appeared to be wetted during the immersion cycle. After the crystal was withdrawn from the acid, the acid would draw up and mostly drain off before the cylinder was again immersed. This was a distinct change, and neither of the other cylinders gave this appearance.

One explanation of these observations was that the conditions under which the micrographs were made were such that a film of cuprous oxide was formed on the surfaces soon after their removal from the hot stearic acid. Even if some means were used to prevent this oxidation before the stearic acid was cleaned off, the oxide layer would be formed when the cylinders were heated to 100°C. before the micrographs were taken. Thus the micrographs were in each case a measure of the contact angle of molten stearic acid with a film of cuprous oxide rather than the particular crystal face of the copper. Another possible explanation is that nonwetting develops during the formation of an oriented monolayer of the molecules. When the surfaces were washed with benzene prior to contact-angle measurements, the monolayer was removed, and the wetted condition returned.

Kruger (28), in discussing the work of Gwathmey *et al.*, pointed out that they were able to observe only the preferential wetting at temperatures between 160° to 270°C. Perhaps that is an explanation for the lack of difference in contact angles at 100°C., but Kruger made contact-angle measurements at 200°C. and also found only slight differences between the 110 and 100 faces. There may be a connection between the observations of Gwathmey and tests by Winkler and Vandenburg (13) on wetting temperatures of molten sodium on various surfaces.

Optical micrographs of the faces of the various cylinders were prepared, and considerable change in appearance was noted when they were compared with freshly polished surfaces. There seemed to be a growth of size in the small irregularities on the surface.

DESCRIPTION OF APPARATUS

Figure 2 is a layout of the entire boiler and vacuum system. The vacuum system was provided so as to enable operation at pressures below atmospheric. The main objective in reducing the pressure was to reduce the saturation temperature of the stearic acid and thereby reduce decomposition of the acid. Markley (29) states that heating stearic acid for 6 hr. at 300°C. in the presence of the oxides of copper produces not more than 6 or 7% ketones. Operating at considerably lower temperature, it is believed, minimized such decomposition.

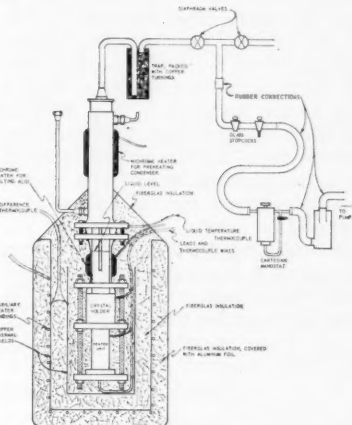


Fig. 2. Boiler and vacuum system.

The condenser section was an assembly of two concentric tubes, with boiling water in the annular space serving as an isothermal heat sink. The water vapor generated during experimental runs was vented to the atmosphere, and a small tube was provided for replacing water in the annulus as needed. The condenser was mounted vertically above, and concentric with, the boiler, into which the stearic acid condensate was permitted to return continuously.

The boiler was a 6-in. length of 1-in. Pyrex pipe surrounded with a Nichrome resistance-wire heater to melt the acid prior to boiling tests. The space in the boiler was equipped with a thermocouple well for liquid temperature measurement. The boiler was filled with liquid to within about 1-in. from the top during operation of the system.

The crystals and a polycrystalline sample used in the tests were 1 in. in diameter and 1 in. long. The crystal holder was constructed of brass, and a seal between the boiler and crystal holder was provided by a Teflon gasket. Leakage around the crystal itself was prevented by compressed asbestos packing. The holder and boiler were connected with tie bolts through flanges. The same tie bolts were extended through another flange which pushed the heater against the bottom face of the crystal in order to make good contact. The heater

was made of a solid copper core, insulated with a coating of Sauereisen cement and wound with a Nichrome resistance-wire heater. Radiation shields were provided, and the power input was controlled by a 0 to 270-volt variable transformer and measured by a Weston Model 310 precision wattmeter.

The entire heater and boiler assembly was surrounded with a double-jacketed thermal shield, as shown in Figure 2.

Temperatures were measured within each crystal and in the boiling liquid by means of No. 30 copper-constantan duplex thermocouples in connection with a Leeds and Northrup Type K-2 potentiometer and an optical beam-type galvanometer system. The crystal thermocouple was located in a thin protection tube inserted in a radial hole parallel to and about $\frac{1}{8}$ in. below the heat transfer surface. Corrections were made for the temperature drop between this thermocouple location and the heat transfer surface. The sensitivity of the temperature-measuring circuits was about 0.1°F., and the accuracy was believed to be within 0.5°F. All thermocouples were calibrated in comparison with a standard platinum, platinum-rhodium junction. The reference junction was maintained at the ice point, 32°F., in a Dewar flask.

EXPERIMENTAL PROCEDURE

Considerable effort was invested in the preparation of the sample and the system prior to operation. The system was first cleansed by boiling ethanol. The two single crystals and the polycrystal were mechanically polished and then electropolished, as described previously. All three samples were dunked simultaneously in stearic acid until preferential wetting was observed, after which the samples were left submerged until stearic acid solidified on the prepared surfaces. The sample with a protective layer of solid stearic acid was then installed in the crystal holder, which was then connected to the heater, and a thermocouple was passed into the center of the crystal. With the Teflon gasket in place, the crystal holder and heater assembly were connected to the Pyrex-pipe boiler section.

The boiler was next filled with stearic acid until the liquid was about 1 in. from the top of the tube (giving about 5 in. of liquid above the crystal surface). When this operation was completed, the boiler was connected to the condenser and the system was checked for leaks. The thermal shields were raised into position around the heater assembly, and the heater and boiler were further insulated with Fiberglas blanket and aluminum foil.

The test procedure involved the following steps:

1. The pressure was reduced to the desired level by means of the vacuum system and controlled by the Cartesian manostat.

2. The condenser section was preheated until steam was evolved from the jacket outlet.

3. The voltage on the heater was adjusted on the variable transformer so as to deliver the desired power (observed on the wattmeter).

4. After attainment of equilibrium, data were taken.

The data consisted of measured values of

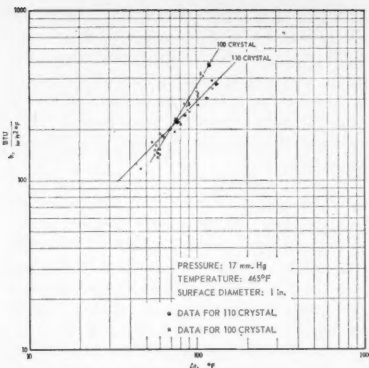


Fig. 3. Data for boiling stearic acid on copper single crystals.

power input, crystal temperature, and liquid temperature.

Data for boiling stearic acid at 17 mm. pressure are plotted on Figure 3 and summarized on Table 1.*

DISCUSSION OF RESULTS

Though at first glance it seems strange that the results from the two crystals cross as shown on Figure 3, this crossing may be explained in the following manner. At low values of heat flux, the heat exchange mechanism may be regarded as a simultaneous large contribution from nonboiling natural convection and, if there is boiling, a small contribution from the bubble formation. If the process is predominantly nonboiling natural convection, one would expect that the nonwetting interface would represent a larger thermal resistance than the wetted interface and that temperature difference would be higher for the nonwetted than for the wetted interface at the same value of heat flux. This idea is consistent with the results of the experimental studies, wherein the 100 crystal was not wetted as well as the 110 crystal and the temperature differences for the low range of heat flux were higher for the 100 crystal than for the 110 crystal.

As the heat flux increases, the rate of bubble formation increases, and the relative contribution of nonboiling natural convection is reduced. Hence, the influence of degree of wetting on ease of bubble formation assumes a more important role as heat flux increases in the nucleate boiling region. As mentioned previously, Larson (19), has proposed that the least wetted regions of a surface should ebullate first. This notion may be extended to postulate that the nonwetted surface requires less temperature difference than the wetted surface for the same heat flux. The data on Figure 3 tend to

confirm this line of reasoning. To extend his reasoning beyond the range of the present data, one can imagine the curve for the 110 crystal proceeding to a higher maximum flux and corresponding critical temperature difference than the curve for the 100 crystal. It is hoped that this can be confirmed by subsequent experimentation.

CONCLUSIONS AND RECOMMENDATIONS

It is concluded that nonwetting decreases the heat transfer coefficient in nonboiling natural convection but increases the heat transfer coefficient in nucleate boiling. It is further concluded that contact angles are not suitable criteria for establishing degree of wetting at least with respect to heat transfer studies; that is, surface conditions under which contact angles are measured do not necessarily reproduce the surface conditions existing during a heat transfer process. This conclusion results from the fact that no differences in contact angles were observed on clean surfaces, though the different nature of interaction between the solid and liquid was apparent from the manner in which liquid drained from the surfaces and the differences in heat transfer results.

It is recommended that additional effort be expended in developing systems for similar studies but involving liquid-solid combinations other than stearic acid and copper. There is still much need for an established theory of wetting as well as a method of measuring a meaningful degree of wetting.

ACKNOWLEDGMENT

The work described in this paper was sponsored by the Office of Ordnance Research under Contract DA-01-009-ORD-368. The details of the work are described more completely in other references (30, 31). Dr. A. T. Gwathmey, of the University of Virginia, made several suggestions on experimental technique and provided a single crystal of copper for initial studies. His assistance is gratefully acknowledged. LeRoy A. Woodward and Frank A. Thomas, Jr., also assisted in part of the experimental effort and their contributions to the project are greatly appreciated.

LITERATURE CITED

1. Bosworth, R. C. L., "Heat Transfer Phenomena," p. 136, John Wiley and Sons, New York (1952).
2. Jakob, Max, "Heat Transfer," Vol. I, Chap. 29, John Wiley and Sons, New York, (1949).
3. McAdams, W. H., "Heat Transmission," 3 ed., Chap. 14, McGraw-Hill Book Company, Inc., New York (1954).
4. Doody, T. C., and A. H. Younger, *Chem. Eng. Progr. Symposium Ser.* No. 5, **49**, 33 (1953).
5. McDonald, W. C., and R. C. Quittenton, *Chem. Eng. Progr. Symposium Ser.* No. 9, **50**, 59 (1954).
6. Stromquist, W. K., Ph.D. thesis, Univ. Tennessee, Knoxville (1953), published by U. S. Atomic Energy Commission, ORO-93.
7. Trefethen, Lloyd, *NP-1788*, Technical Information Service, U. S. Atomic Energy Comm., Oak Ridge, Tenn. (1950).
8. Morgan, A. I., L. A. Bromley, and C. R. Wilke, *Ind. Eng. Chem.*, **41**, 2767 (1949).
9. Harrison, W. B., Ph.D. thesis, Univ. Tennessee (1952), published by Oak Ridge National Laboratory, ORNL-915.
10. Moyer, J. W., and W. A. Rieman, *J. Appl. Phys.*, **25**, 400 (1954).
11. —, *KAPL-567*, Knolls Atomic Power Laboratory (June 1, 1951).
12. Droher, J. J., M.S. thesis, Univ. Tennessee (1952), published by U. S. Atomic Energy Commission, ORO-69.
13. Winkler, H. H., and L. B. Vandenburg, *KAPL-P-231*, Knolls Atomic Power Laboratory (Dec. 27, 1949).
14. Gwathmey, A. T., Henry Leidheiser, and G. P. Smith, *Tech. Note 982, Natl. Advisory Comm. Aeronaut.* (November, 1945).
15. Hawkins, G. A., "A Brief Review of the Literature on Boiling Heat Transfer," Univ. Calif., Los Angeles (June 1950).
16. Corty, Claude, and A. S. Foust, *Chem. Eng. Progr. Symposium Ser.* No. 17, **51**, 1 (1955).
17. Wenzel, Robert N., *J. Phys. Colloid Chem.*, **53**, 1466 (1949).
18. Larson, R. F., Oak Ridge National Laboratory, *Central Files No. 52-8-178* (Aug. 15, 1952).
19. —, *1953 Heat Transfer and Fluid Mechanics Institute*, Stanford Univ. Press, p. 163.
20. —, *Ind. Eng. Chem.*, **37**, 1004 (1945).
21. Gregg, S. J., "The Surface Chemistry of Solids," Reinhold Publishing Company, New York (1951).
22. Gwathmey, A. T., Henry Leidheiser, Jr., and G. P. Smith, *Tech. Note 1460, Nat. Advisory Comm. Aeronaut.* (June 1948).
23. Ray, B. R., and F. E. Bartell, *J. Colloid Sci.*, **8**, 214 (1953).
24. Seitz, Frederick, "The Modern Theory of Solids," McGraw-Hill Book Company, Inc., New York (1940).
25. Brummage, K. G., *Nature*, **164**, 244 (1949).
26. Hare, E. F., and W. A. Zisman, *J. Phys. Chem.*, **59**, 335 (1955).
27. Jacquet, Pierre A., *Metal Finishing*, **47**, 48 (May 1949).
28. Kruger, Jerome, Ph.D. thesis, Univ. Virginia, Charlottesville (1952).
29. Markley, K. S., "Fatty Acids," Interscience Publishing Company, New York (1947).
30. Harrison, W. B., Zelvin Levine, F. A. Thomas, Jr., and L. A. Woodward, *Eng. Exp. Sta., Proj. A-153*, Georgia Inst. Technol., Atlanta (May, 1955).
31. Levine, Zelvin, Ph.D. thesis, Georgia Inst. Technol., Atlanta (May 1956).

*Tabular material has been deposited as document 5713 with the American Documentation Institute, Photoduplication Service, Library of Congress, Washington 25, D. C., and may be obtained for \$1.25 for photoprints or \$1.25 for 35-mm. microfilm.

Manuscript received May 9, 1957; revised Jan. 5, 1958; accepted Feb. 1, 1958.

C
of

W
cold
rate
temp
vapo
ture
and
of th
sustai
vapo
to th
them
can b
theor

If a
conden
colde
partia
case l
an ac
heat
tube
theori
of the
a res
indica
throu
such a
diffusio
can b
latiatio
indivi
and t
mass
correla

(h_G)
 (cG)

The
design
by Co
The r
heat a
 $dq_T =$

The
partic
integra

To can
is nec
corres
 $h_{oi}(t_i$

Ferd
Rhode I

Vol. 4

Condensation of Vapor in the Presence of Noncondensing Gas

FERDINAND VOTTA, JR., and CHARLES A. WALKER,

Yale University, New Haven, Connecticut

When a pure vapor is passed over a cold surface, the vapor condenses at a rate which depends on the difference in temperature between the bulk of the vapor and the cold surface. The temperature at the interface between the vapor and liquid is assumed to be equal to that of the bulk of the vapor; thus the resistance to heat transfer between the vapor and the surface is due entirely to the layer of condensate separating them. The magnitude of this resistance can be estimated by methods such as the theoretical equations of Nusselt (13).

If a mixture of noncondensable gas and condensable vapor is passed over a surface colder than the dew point of the mixture, partial condensation will occur. In this case however it is necessary to consider an added resistance to the transfer of heat from the gas-vapor mixture to the tube wall. According to well-founded theories there exists between the bulk of the mixture and the condensate surface a resistance of such magnitude as to indicate that transfer of heat and mass through it occurs by very slow processes such as pure conduction and molecular diffusion. The magnitude of this resistance can be estimated from empirical correlations which provide a knowledge of the individual film coefficient of heat transfer and the individual film coefficient of mass transfer. An example of such a correlation is that of Colburn (7):

$$\begin{aligned} \left(\frac{h_g}{cG} \right) \left(\frac{c\mu}{k} \right)^{2/3} &= 0.023 \left(\frac{DG}{\mu} \right)^{-0.2} \\ &= \frac{k_g P_{nm} M}{G} \left(\frac{D_g \rho}{\mu} \right)^{-2/3} \end{aligned} \quad (1)$$

The method of using these ideas in the design of equipment was first proposed, by Colburn and Hougen (10), in 1934. The rate equation for transfer of sensible heat and latent heat may be written as

The heat transfer area required in a particular case is determined by graphical integration of the expression

To carry out this graphical integration it is necessary to determine values of t_i

$$h_{0i}(t_i - t_L) = h_g(t_v - t_i) \quad (4)$$

Ferdinand Votta, Jr. is with the University of Rhode Island, Kingston, Rhode Island.

The points (p_s, t_s) and (p_i, t_i) are assumed to be on the vapor-pressure curve of the condensing material; that is, it is assumed that the bulk of the vapor is saturated and that equilibrium exists at the interface. For given conditions of the inlet vapor composition and rate, selection of a value of p_s at a particular point will permit calculation of the amount of condensation which has occurred to this point. The value of t_L can be evaluated from a heat balance. Values of h_{oi} , h_{og} and k_g can be estimated from the flow rates and properties of the fluids. By using the vapor-pressure curve for the required second equation one can solve Equation (4) for p_i and t_i , usually by trial and error. However Bras (4) has recently proposed a method for carrying out this solution directly.

The method of Colburn and Hougher is in agreement with current methods of

calculation in the fields of heat and mass transfer, but is very tedious to apply; therefore several attempts have been made to arrive at simpler methods of calculation (1, 2, 3, 6, 12, 15) based on various assumptions. Until quite recently, however, there were available in the literature very few experimental results which would serve as a basis for testing the method of Colburn and Hougen and the simplified methods which have been proposed, only a few sets of data being available (5, 9, 16).

The research program described here was undertaken originally to provide a body of experimental data for such calculations. In the planning of the program it was considered essential that systems of widely varying characteristics be used: air-water, carbon dioxide-water, helium-water, and carbon dioxide-*n*-propyl alcohol. For each of these systems the effects of flow rate, temperature of the entering gas-vapor mixture, and cooling-water temperature were studied. Saturated mixtures of vapor and gas were cooled and condensed inside a single-tube vertical condenser, 1 in. I.D. and 42 in. long. All tests were made at atmospheric pressure with the vapor flowing downward inside the tube and countercurrent to the cooling water in the annular space. Data* are presented for a total of sixty-four experimental tests. The ranges of the variables covered in the investigation are given in Table 2. The interpretation of the data is presented in terms of a modified definition of a driving force involving the concept of availability of energy.

Fig. 1. Diagram of equipment

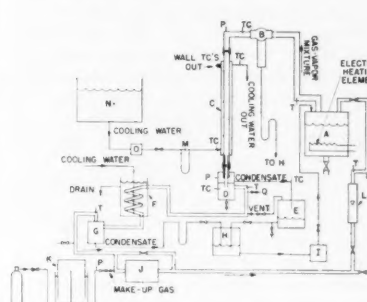


Fig. 1. Diagram of equipment

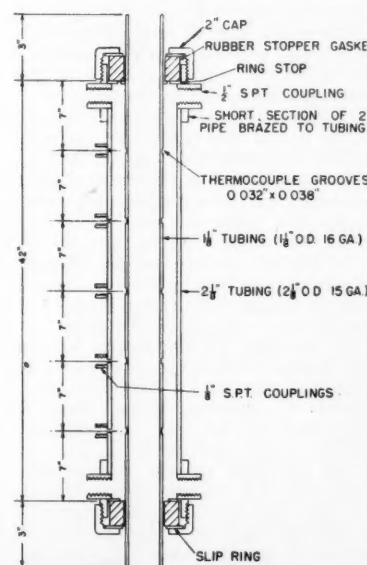


Fig. 2. Test condenser

TABLE 2. RANGE OF VARIABLES INVESTIGATED

Systems	Water-air, water-carbon dioxide, water-helium, <i>n</i> -propyl alcohol-carbon dioxide
Flow rate	Total inlet mass flow rate of 0.198 to 1.78 lb./sec./sq. ft., or average Reynolds number of 1,585 to 15,000.
Inlet-gas temperature	118° to 185°F.
Cooling-water temperature	51° to 100°F.

EXPERIMENTAL EQUIPMENT

Figure 1 shows a flow diagram of the equipment used. The vapor was produced in an electrically heated boiler (*A*) and mixed in the boiler with a measured stream

*Table 1 has been deposited as document 5766 with the American Documentation Institute, Photoduplication Service, Library of Congress, Washington 25, D. C., and may be obtained for \$1.25 for photoprints or \$1.25 for 35-mm. microfilm.

TABLE 3. TYPICAL WATER-AIR RUN
(Run A31)

Pressure in condenser	754.5 mm. Hg
Water flow rate	38.0 lb./min.
Water temperature in	69.6°F.
Water temperature out	70.6°F.
Water temperature rise (by differential thermocouple)	0.92°F.
Condensate flow rate	1.77 lb./hr.
Condensate tempera- ture	99.6°F.
Temperature of gas- vapor mixture enter- ing condenser	134.3°F.
Temperature of gas- vapor mixture leav- ing condenser	110.3°F.
Superheat of gas-vapor mixture leaving condenser	Negligible
Air flow rate	0.974 lb. mole/hr.
Wall temperatures	
7 in. from bottom of condenser	73.5°F.
14 in. from bottom of condenser	75.5
21 in. from bottom of condenser	77.0
28 in. from bottom of condenser	79.1

of noncondensing gas. The gas-vapor mixture then passed through a separator (*B*), where any condensate was removed before the stream entered the test condenser. The piping between the boiler and separator was left uninsulated, so that any superheat in the gas leaving the boiler would be removed before the mixture reached the separator. The mixture was cooled and condensed inside a single-tube vertical test condenser (*C*). The condensate was separated from the uncondensed gas-vapor mixture in the condensate separator (*D*) and collected in the condensate reservoir (*E*).

The uncondensed mixture was sent to the total condenser (*F*), where it was cooled somewhat below room temperature. Separation of this condensate from the noncondensing gas occurred in a separator (*G*) in the outlet of the total condenser. The combined condensate from condensers (*C*) and (*F*) was collected in a reservoir (*H*) and pumped back to the boiler by a small centrifugal pump (*I*). The noncondensable gas was recycled by a blower (*J*). A 4.5-cu. ft. gasometer (*K*) provided gas storage and pressure control.

The flow rate of gas to the boiler was measured by a rotameter (*L*); the cooling water flow was measured by a calibrated orifice (*M*) and checked by weighing for most runs. Temperature measurements were made by thermometers in the gas stream leaving the rotameter, in the gas-vapor mixture leaving the boiler, and in the exit streams from the separators (*D*, *G*). The temperatures of the gas-vapor mixtures entering and leaving the test condenser were measured by copper-constantan thermocouples (*TC*). Thermocouples were also installed in the inlet and exit cooling water and in the condensate leaving the test condenser. Pressure measurements (*P*) were made at the gasometer, at a point just beyond the rotameter, and at the inlet and outlet ends of the test condenser.

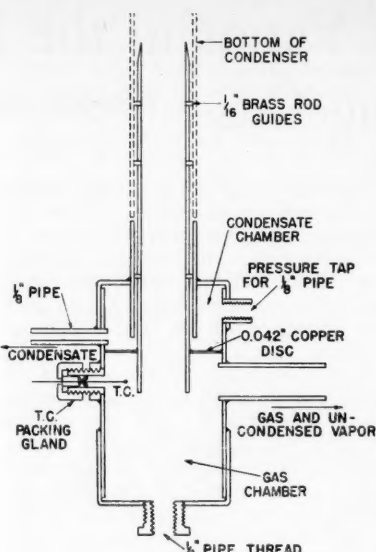


Fig. 3. Separator.

The piping from the boiler to the inlet separator was 1½-in. standard brass pipe, and from the inlet separator to the condensate separator the piping was 1½-in. O.D. copper tubing. All other gas-vapor lines in the recirculation system were constructed of 5/8-in. O.D. copper tubing. The test condenser and the separators (*B*) and (*D*) were thoroughly insulated.

Figure 2 shows a diagram of the test condenser consisting of a section of 1½-in. O.D. (0.995-in. I.D.) type-K copper tubing 48 in. long inside a section of 2½-in. O.D. (1.981-in. I.D.) type-L copper tubing. The actual heat transfer area was 0.912 sq. ft. (outside area of 1½-in. tube). Thermocouples were embedded in the wall of the inner tube at various locations in the condenser and also installed in the annular space midway between the two tubes in the cooling-water stream. (No use was made of the data from these cooling-water thermocouples, and the temperatures indicated by the wall thermocouples were used only to estimate the temperature of the condensate leaving the condenser.)

A tightly fitting rubber tube was used to join the butted ends of the test condenser and the interconnecting piping. A close fit between the ends of the copper tubing, resulting in minimum possible disturbance to the flow patterns, was effected by grinding. A length of 10 in., between the top of the test section and the adjacent elbow, was considered sufficient to ensure a fully developed flow pattern of the gas-vapor mixture entering the condenser.

The separator at the bottom of the condenser test section was constructed as shown in Figure 3. A 7/8-in. O.D. tube, centered by soldering 1/8-in. brass-rod guides, was inserted into the condenser tube, its tapered end coinciding with the end of the heat transfer section. The uncondensed gas mixture passed through the 7/8-in. tube, into the gas chamber of the separator, and thence through the exit line. The condensate flowed in the annular space between the two tubes, into the condensate chamber, and then to the

condensate receiver. (Another separator design was being used at the time the first twenty-two runs with the carbon dioxide-water system were being made. In that design the condensate and the exit gas-vapor mixture remained in contact for a relatively brief period after leaving the end of the condenser section. The heat exchange which occurred during this brief period was found to be appreciable. Although the magnitude of this exchange could be estimated from the data available, as was done in interpreting the data on the carbon dioxide-water runs, it was felt that a more satisfactory procedure would be to eliminate this heat exchange by the separator design already described.)

Cooling water maintained at a controlled uniform temperature was pumped from a 400-gal. mixing tank. A controller actuated a solenoid valve, which in turn regulated the flow of steam into the tank of well-stirred water. The temperature variation of the tank water was less than 0.3°F.

All thermocouples were checked against a Bureau of Standards calibrated thermometer in a water bath at room temperature and in a current of steam at atmospheric pressure. The steam temperature was calculated from the barometric pressure. In each case the cold junction was immersed in a water-ice bath. The thermocouples checked within 0.1°C. at both temperatures. The tube-wall thermocouples were calibrated in place against the water thermocouples. This was done first with cooling water flowing in the annular space and no flow in the condenser tube, that is, with no heat transfer, and then with steam flowing through both the annular space and the tube. The wall thermocouples checked within 0.05°C. of the water thermocouples.

The temperature rise of the cooling water in passing through the condenser was determined by a double differential thermocouple in the inlet and outlet water streams. This consisted of two thermocouples in each stream, all connected in series.

The electromotive force of the thermocouples was determined by a self-balancing electronic potentiometer with a sensitivity of 0.001 mv. (0.05°F.). Except for the differential thermocouple no attempt was made to read temperatures closer than 0.1°F. because of the occurrence of random variations in some of the temperatures. These were particularly noticeable in the case of high heat transfer rates, amounting to as much as 0.3° to 0.5°F. The temperature values recorded are averages.

EXPERIMENTAL PROCEDURES

The equipment was tested first by several runs involving simple heat transfer. Cooling water flowed in the annular space, and hot air or water through the inner tube. Heat transfer coefficients were determined from the results of these tests. The inside gas film coefficients were calculated for the air runs, and both the inside and outside coefficients for the water runs; this was possible because the tube-wall and cooling-water temperatures were measured at various points in the condenser.

The inside film coefficients of heat transfer for both air and water agreed within a few per cent with the values calculated by the Dittus-Boelter equation. The maximum deviation from the calculated values was

13.5% coefficient annual the e coefficient through high clients large the fl

A proce-
tion.
taken
was c
30-min
state

Wh
diox
gas w
gas in
In th
for ox
was c
the ga
was
and t
absor
No d
an in
above
For
the g
conden
bringin
with h
gas le
the wa
at wh
polish
with
gas le
since

EXPER
The
are su
total
the s
water
water
py al
The
are g
studie
turbu
tests
in a
those
the ca
the v
inside
annul
of the
tially
rates
for th
to 5,3
The
water
by usi
*See

13.5%. However the average heat transfer coefficient for the cooling water in the annular space was 50 to 70% higher than the expected value, and the instantaneous coefficient seemed to vary considerably through the length of the condenser. The high values of the outside transfer coefficients can be accounted for by the relatively large effect of the entrance turbulence on the flow pattern in the short condenser used.

A detailed description of the operating procedure is not essential to this presentation. It may be noted that the data were taken over 30-min. intervals. Each run was continued until the data on successive 30-min. intervals indicated that steady state conditions prevailed.

When a run was begun with carbon dioxide or helium, some of the recirculating gas was vented to the air until tests of the gas indicated that it was essentially pure. In the helium runs the gas was analyzed for oxygen, and the quantity of air present was calculated from this result. To analyze the gas for the carbon dioxide runs a sample was diluted with an equal volume of air and then analyzed for carbon dioxide by absorption in potassium hydroxide solution. No difficulty was encountered in reaching an indicated purity of the recirculating gas above 99%.

For many of the tests the dew point of the gas-vapor mixture leaving the test condenser was measured. This was done by bringing a polished dew-point cup filled with hot water in contact with some of the gas leaving the condensate separator. As the water in the cup cooled, the temperature at which condensation first occurred on the polished surface was noted. For comparison with the dew point the temperature of the gas leaving the separator was also measured, since this was usually slightly different from that in the separator.

EXPERIMENTAL DATA

The results of the experimental tests are summarized in Table 1.* Data on a total of sixty-four tests are presented for the systems water-air (fourteen tests), water-carbon dioxide (twenty-five tests), water-helium (fourteen tests), and *n*-propyl alcohol-carbon dioxide (eleven tests). The results of a typical water-air run are given in Table 3. The variables studied were flow rate, vapor concentration, and cooling-water temperature. The gas-vapor mixture was in transition or turbulent flow for the majority of the tests but approached the viscous range in a number of cases, particularly in those tests in which helium was used as the carrier gas. All tests were made with the vapor mixture flowing downward inside the condenser tube and with cooling water flowing upward in the annular space. In all cases the pressure of the gas-vapor mixture was substantially atmospheric. The cooling-water rates were such that the Reynolds number for the annular space ranged from 3,400 to 5,300.

The first twenty-two tests on the water-carbon dioxide system were made by using a condensate separator in which

there was appreciable heat transfer occurring between the gas-vapor mixture and the condensate beyond the bottom of the condenser. However, since the temperature of the condensate leaving the separator was measured, it was possible to calculate the magnitude of this effect and thus to estimate the condition of the gas-vapor mixture leaving the bottom of the condenser. This was done by making an enthalpy balance over the condensate separator and solving graphically for the temperature of the gas mixture leaving the condenser. For the purposes of this balance the temperature of the condensate leaving the condenser was assumed to be very close to the tube-wall temperature at this point, and the gas-vapor mixture was assumed to be saturated.

The flow rates of air and of carbon dioxide were determined by the rotameter and the manufacturer's calibration, corrected for the change in specific gravity. However in the case of the helium runs it was found that this procedure did not provide accurate values of the gas flow rates. The helium flow rates were therefore calculated from the quantity of condensate collected and the assumption of inlet and outlet saturation of the gas-vapor mixture. A subsequent partial calibration of the rotameter with helium at low flow rates, with a gasometer used as the primary standard, indicated that this procedure was quite satisfactory; it was further justified by the satisfactory nature of the material balances made on the other systems (by comparing the measured rate of condensate flow with the value calculated from data on the gas-vapor stream). The results of these material balances are shown in Table 1. The average ratio of the measured rate of condensate flow to the calculated rate was 1.01 for the air-water runs, 1.06 for the carbon dioxide-water runs, and 1.00 for the carbon dioxide-*n*-propyl alcohol runs. The higher value for the carbon dioxide-water system indicates that the mixture leaving the condenser was

slightly superheated. Dewpoint measurements confirm this for three of the tests, but these data were not available for the first twenty-two runs of this series.

The consistency of the data was further checked by means of heat balances. The quantity of heat absorbed by the cooling water was calculated from the measured flow rates and the readings of a differential thermocouple in the inlet and outlet water lines. The heat given up by the gas-vapor stream was calculated from the known inlet and outlet conditions of the gas-vapor stream together with the measured flow rate of the condensate and an estimated value of the temperature of the condensate leaving the bottom of the condenser. (The data include a measured condensate temperature, but this temperature was taken at the outlet of the separator and was different from the temperature of the condensate leaving the bottom of the condenser.) In this calculation the heat content of the condensate is small compared with that of the exit gas-vapor mixture. It was assumed that the condensate left the condenser at the temperature of the tube wall. The error introduced by this assumption is not more than 1% in the calculated quantity of heat transferred from the gas-vapor mixture. The results of these heat balances are shown in Table 1. The average ratio of heat absorbed by water to heat given up by the gas-vapor mixture is 1.00 for the air-water runs, 1.12 for the carbon dioxide-water runs, 1.07 for the helium-water runs, and 1.20 for the carbon dioxide-*n*-propyl alcohol runs. When the difficulty of measuring the small change in temperature of the water stream is considered, these results are satisfactory for the first three systems. No explanation has been found for the larger discrepancy in the last system.

INTERPRETATION OF DATA

Interpretation of the body of data presented in this work might be approached in several ways. The method

TABLE 4. EQUIVALENT TEMPERATURE DRIVING FORCE

Temperature	Saturated Gas-Vapor Mixtures				
	Reference temperature 492°R.				
	Total pressure 1 atm.	Values of Δ in °R. units			
32	0	0	0	0	0
40	14.4	12.8	17.0	11.9	41.7
50	40.2	34.6	48.9	30.5	87.7
60	64.9	55.8	79.1	52.8	145
80	144	120	180	113	279
100	280	230	357	210	450
120	497	404	632	352	669
140	841	689	1,052	550	894
160	1,367	1,146	1,648	803	1,130
170					1,270
180	2,145	1,880	2,480	1,095	
200	3,310	3,120	3,495		

*See footnote on page 413.

chosen here is based on the use of a driving force quite different from that ordinarily used. A method of correlating the data which employed a single driving force for the transfer of energy, similar to the one suggested by Colburn (8) and others, would be desirable. The success of the use of enthalpy as a potential for heat and mass transfer, even if limited to special cases, was encouraging; however enthalpy is not the correct driving force for mass transfer except for low concentrations of water vapor in air.

The resistance of a gas film to both heat and mass transfer is determined by the flow conditions and the physical properties of the system. The heat and the mass transfer coefficient are related, and most factors which affect one also affect the other. The question might then be asked, Is there a measure of driving force other than temperature, partial pressure, or enthalpy which could be used to measure the tendency for both heat and mass transfer? It seemed conceivable that such a driving force might exist, and the correlation of the data here is an attempt to find it.

Since any spontaneous process tends to result in a decrease in the availability of energy, the availability function was investigated as a possible driving force for both heat and mass transfer. It was assumed that the driving force was the difference in some function of the availability of energy between the main gas stream and the interface:

$$dq_T/dA = C[f(B) - f(B_i)] \quad (5)$$

The coefficient C would be expected to be a function of the physical properties of the stream, the geometry of the flow channel, and the mass flow rate.

The simplest function of availability is the availability itself. Interpretation of the data based on the availability of energy as a driving force was attempted first. In the case of air-water runs it was noted that the values of C calculated for runs in which dry air was used (heat transfer by convection only) were very

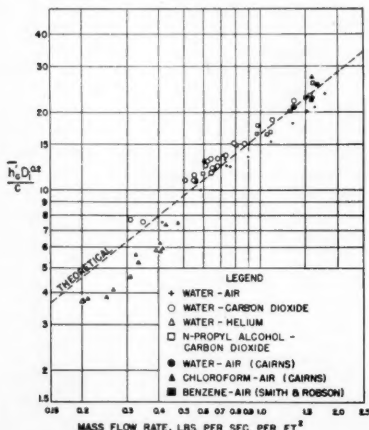


Fig. 4. Correlation of data.

TABLE 5. COMPARISON OF COLBURN AND HOUGEN AND EQUIVALENT-TEMPERATURE METHODS

Gas temperature, °F.	t_i , °F.	Colburn and Hougen		This Work	
		dq_T/dA , B.t.u. (hr.)(sq. ft.)	ΔA , sq. ft.	t_i , °F.	dq_T/dA , B.t.u. (hr.)(sq. ft.)
203	200.5	18,550	0	195.8	17,600
199.5	194.0	22,700	139.3	187.6	20,200
194	183.8	23,500	87.1	179.0	18,860
185	163.4	20,700	81.0	159.0	19,440
167	130.0	13,280	85.4	131.0	17,780
149	107.6	7,800	69.5	107.6	8,750
131	94.3	4,510	64.6	95.7	4,980
113	85.2	2,400	100.4	87.1	2,610
104	82.2	1,710	67.7	82.7	1,790
Total				695.0	698.0

nearly the same numerically as those calculated for runs in which condensation was occurring, provided comparisons were made at like conditions of flow rate and temperature level. To eliminate this effect of temperature level it was decided to try another function of the availability:

$$\Delta = \frac{B_n}{B_n} (T - T_0) \quad (6)$$

If this driving force is applied to a case in which sensible heat transfer alone is involved, it will be noted that $\Delta = T - T_0$. Thus the driving-force difference is

$$(\Delta - \Delta_i) = (T - T_0) \quad (7)$$

$$- (T_i - T_0) = T - T_i$$

The rate of heat transfer for a non-condensing gas is then

$$dq/dA = C(\Delta - \Delta_i) = C(T - T_i) \quad (8)$$

Comparing this equation with the usual equation for transfer of sensible heat one will see that $C = h_g$ for the case of a noncondensing gas. For the case of transfer of both latent and sensible heat the coefficient C based on the equivalent temperature driving force will be denoted by h_g' .

For the case of saturated gas-vapor mixtures it has been shown (17) that

$$\Delta = (T - T_0) + RT_0 \left[n_s \ln \frac{P}{P_0} - \ln \frac{\pi - P_0}{\pi - P} \right] \quad (9)$$

$$+ nC_p \left[1 - \frac{T_0}{T - T_0} \ln \frac{T}{T_0} \right]$$

For a superheated gas-vapor mixture it was assumed that

$$\Delta_{sup} = \Delta_{sat} + (T_{sup} - T_{sat}) \quad (10)$$

Values of Δ for mixtures of a particular gas and a particular vapor can be calculated from Equation (9), if data on vapor pressures and molal heat capacities are available. The results of such calculations (17) for several systems are given in Table 4.

To make use of this driving force it is

necessary to know the interface temperature, which can be determined by noting first that

$$dq_T = h_g'(\Delta - \Delta_i)dA \quad (11)$$

$$= h_{oi}(t_i - t_L)dA$$

$$\frac{h_{oi}}{h_g'} = \frac{\Delta - \Delta_i}{t_i - t_L} \quad (12)$$

Solution of this equation for t_i and Δ_i is by trial, the required second equation being given by the relation between Δ_i and t_i defined by Equation (9). This can also be done directly by plotting Equation (12) on the Δ vs. t diagram.

Values of the rate coefficient h_g' for the experimental runs were determined from the equation

$$dq_T = h_g'(\Delta - \Delta_i)dA \quad (13)$$

Several simplifications were possible in this work. The data indicated quite clearly that the major resistance to heat transfer was in the gas phase, and so Δ_i did not differ greatly from Δ_L in most cases. The variation in mass flow rate through the condenser was small enough that an average value of G could be used. Since it was assumed that in any one run h_g' was variable only to the degree that G and c vary, an average value of the heat transfer coefficient h_g' for each run was used. After Equation (13) had been integrated graphically a number of times, the results were compared with those obtained by using a logarithmic mean driving force and found to be nearly identical.

The calculated values* of $h_g' D_i^{0.2} / c$ are presented in Figure 4. The experimental data of Cairns (5, 6) and one run of Smith and Robson (16) were correlated by using the equivalent temperature driving force, and the results are shown on this plot. Also shown is the line representing the equation

$$h_g' D_i^{0.2} / c = 16.6(G')^{0.8} \quad (14)$$

This equation is recommended (14) for estimating values of the gas-film heat

*Sample calculation is given in reference (17).

trans
flow
It
use
work
cient
emp
on s
gase
ment
Equa
devi
water
n-pro
experi
syste
corre
Two
valu
bers
to in
when
the
exp
assu
is no
water
SOLU
EXAM
TEMP
TH
and
proce
temp
prob
water
and
mixt
water
cond
quan
were
quan
dense
coeffi
other
const
coeffi
It
mixt
cond
Int
force
using
lated
Ta
by th
Colb
Th
total
meth
partic
shoul
Houg
more
vapor
equiv

transfer coefficient for gases in turbulent flow in pipes.

It is apparent from Figure 4 that the use of the driving force proposed in this work leads to values of a transfer coefficient which agree with an accepted empirical equation for correlating data on sensible heat transfer coefficients of gases. The agreement between experimental values and those calculated by Equation (14) is quite good (average deviation less than 10%) for the systems water-air, water-carbon dioxide, and *n*-propyl alcohol-carbon dioxide. The experimental points for the helium-water system lie appreciably below the empirical correlation (average deviation -22.5%). Two reasons can be given for the lower values in this case: The Reynolds numbers for the helium runs were low enough to indicate viscous flow in many cases, whereas Equation (14) is applicable in the turbulent flow region; and the experimental data indicate that the assumption of the equality of Δ_i and Δ_L is not as good in the case of the helium-water runs as it is in the other systems.

SOLUTION OF COLBURN AND HOUGEN'S EXAMPLE BY EQUIVALENT TEMPERATURE METHOD

The problem presented by Colburn and Hougen (10) in their classical design procedure was solved by the equivalent temperature method outlined here. This problem involves the condensation of water at 1 atm. from a mixture of nitrogen and water saturated at 95°C. The gaseous mixture is cooled to 40°C. with cooling water available at 25°C. and leaving the condenser at 60°C. Several calculated quantities used by Colburn and Hougen were also used in this solution: the quantity of heat transferred in the condenser at various points, the heat transfer coefficient for the combined resistances other than the gas film $h_{oi} = 310$ (assumed constant), and the value of the gas film coefficient at various points.

It was assumed that the gas-vapor mixture was saturated at all points in the condenser.

Interface temperatures and driving forces at the interface were calculated by using Equation (12). The area was calculated by using

$$A = \int^a \frac{dq_T}{h_g'(\Delta - \Delta_i)} \quad (15)$$

Table 5 compares the results obtained by this method with those obtained by Colburn and Hougen.

The very close agreement between the total areas calculated by these two methods is a coincidence because of the particular temperature range covered. It should be noted that the Colburn and Hougen method predicts a somewhat more rapid rate of heat transfer at high vapor concentrations than does the equivalent temperature method, while the reverse is true at low concentrations;

however agreement between the two methods is reasonably good for either condition over the range covered. The proposed equivalent-temperature procedure is easier to use and requires less time than the Colburn and Hougen method [even with the modifications proposed by Bras (5)], if the Δ vs. temperature data are available.

CONCLUSION

The results of this investigation indicate the possibility that the rate of gas-phase heat and mass transfer may be proportional to the heat transfer coefficient and a single driving force. The driving force suggested here is a function of the difference in availability of energy. While the proposed procedure has successfully correlated experimental data covering a wide range of conditions, it is believed that considerable additional testing of the method against other experimental data is needed. Reliable mass transfer data for gas mixtures containing a high concentration of vapor would be especially useful.

NOTATION

A = area of heat transfer surface, sq. ft.
 B = availability of energy, $\Delta H - T_0 \Delta S$ (see 11)
 B_n = availability of energy of noncondensing gas having same physical properties as gas mixture from which heat is being transferred
 B_{ns} = availability of energy of saturated gas-vapor mixture
 C = general transfer coefficient
 C_p = molal heat capacity at constant pressure $(C_{pn} + n_v C_{pv})/(1 + n_v)$
 c = specific heat
 D = diameter, ft.
 D_i = diameter, in.
 D_g = diffusion coefficient, sq. ft./hr.
 $f(B)$ = function of availability of energy
 G = mass velocity, lb./hr.(sq. ft.)
 G' = mass velocity, lb./sec.(sq. ft.)
 H = enthalpy, B.t.u./lb. mole
 ΔH = enthalpy relative to T_0
 h_g = gas-film heat transfer coefficient, B.t.u./hr.(sq. ft.)(°F.)
 h_g' = instantaneous gas film heat transfer coefficient based on total heat transferred (sensible plus latent) and equivalent temperature driving force, B.t.u./hr.(sq. ft.)(°F.)
 \bar{h}_g' = average gas-film heat transfer coefficient based on total heat transferred (sensible plus latent) and equivalent temperature driving force, B.t.u./hr.(sq. ft.)(°F.)
 h_{oi} = heat transfer coefficient for combined resistances other than gas film, based on inside surface, B.t.u./hr.(sq. ft.)(°F.)
 k = thermal conductivity, B.t.u./hr.(sq. ft.)(°F./ft.)
 k_g = gas film mass transfer coefficient lb. mole/hr.(sq. ft.)(atm.)
 \ln = natural logarithm

M = molecular weight
 n = number of moles = $1 + n_v$
 n_v = number of moles of vapor per mole of noncondensable gas
 P = vapor pressure, atm.
 p = partial pressure, atm.
 P_{nm} = mean partial pressure of noncondensing gas, atm.
 q_T = rate of flow of sensible heat plus latent heat, B.t.u./hr.
 R = gas constant
 S = entropy, B.t.u. / (lb. mole)(°F.)
 ΔS = entropy relative to T_0
 T = absolute temperature, °R.
 t = temperature, °F.
 W = weight flow rate, lb./hr.

Greek Letters

Δ = finite difference when followed by a function
 Δ_i = equivalent temperature driving force
 μ = viscosity, lb./hr.(ft.)
 π = total pressure, atm.
 ρ = density, lb./cu. ft.
 λ = latent heat, B.t.u./lb.-mole

Subscripts

i = interface
 n = noncondensing gas
 0 = datum state
 L = liquid or cooling water
 $sat.$ = saturated
 $sup.$ = superheated
 v = vapor

LITERATURE CITED

1. Bras, G. H., *Chem. Engr.*, **60**, 223 (April, 1953) and 238 (May, 1953).
2. *Ibid.*, **61**, 190 (May, 1954).
3. *Ibid.*, 191 (December, 1954), and **62**, 195 (January, 1955).
4. ———, *Chem. Eng. Sci.*, **6**, 277 (1957).
5. Cairns, R. C., *ibid.*, **2**, 127 (1953).
6. *Ibid.*, **3**, 215 (1954).
7. Chilton, T. H. and A. P. Colburn, *Ind. Eng. Chem.*, **26**, 1183 (1934).
8. Colburn, A. P., "General Discussion on Heat Transfer," p. 1, *Inst. of Mech. Engrs. and Am. Soc. Mech. Engrs.* (1951).
9. ———, and O. A. Hougen, *Ind. Eng. Chem.*, **22**, 522 (1930).
10. *Ibid.*, **26**, 1178 (1934).
11. Dodge, B. F., "Chemical Engineering Thermodynamics," McGraw-Hill Book Company, Inc., New York (1944).
12. Gilmour, C. H., *Chem. Engr.*, **61**, 209 (March, 1954).
13. McAdams, W. H., "Heat Transmission," 3 ed., McGraw-Hill Book Company, Inc., New York (1954).
14. Perry, J. H., "Chemical Engineer's Handbook," 3 ed., McGraw-Hill Book Company, Inc., New York (1950).
15. Silver, L., *Trans. Inst. Chem. Engrs. (London)*, **25**, 30 (1947).
16. Smith, J. C., and Robson, H. T., "General Discussion on Heat Transfer," p. 38, *Inst. Mech. Engrs. and Am. Soc. Mech. Engrs.* (1951).
17. Votta, Ferdinand, Jr., D. Eng. dissertation, Yale University, New Haven (1958).

Manuscript received March 3, 1958; revision received July 17, 1958; paper accepted July 17, 1958.

Dissolution Rates of Solids in Mercury and Aqueous Liquids: The Development of a New Type of Rotating Dissolution Cell

J. A. R. BENNETT and J. B. LEWIS, Atomic Energy Research Establishment, Harwell, near Didcot, Berkshire, England

A new type of corrosion problem arises when liquid metals, for example, sodium or mercury, are used as heat transfer fluids, since the solubilities of some structural metals in the liquid metals, although extremely small, are often markedly temperature dependent. This may cause a progressive dissolution of metal from the pipe wall in the hot region of the circuit with subsequent crystallization in the colder regions. Although this type of corrosion problem is being studied in many parts of the world, most of the results hitherto published are of an empirical nature; in particular there is little information about whether the rate controlling step during dissolution is a transport or chemical process.

In the present investigation the rate-controlling factors during the dissolution of lead, tin, and zinc in mercury were examined. The dissolution of specimens of these metals in mercury was compared with the dissolution of benzoic acid in water and, in order to extend the range of values of Schmidt groups, in aqueous sucrose solution. It was found that, apart from the dissolution of zinc in mercury, all the processes were transport controlled, the rate factors being correlated by a single hydrodynamic equation involving the Reynolds numbers and Schmidt groups. A chemical rate factor entered into the dissolution of zinc in mercury; the significance of this is discussed elsewhere (1).

To ensure reproducible and uniform hydrodynamic conditions during dissolution a large number of possible stirring conditions were first examined. In the system selected a stationary cylindrical specimen was mounted along the axis of a rotating vertical cylindrical vessel which contained the solvent. This technique, which as far as the authors know has not been used before, avoided the formation of Taylorian vortices at the surface of the specimen which otherwise caused a marked unevenness during the dissolution of the appreciably soluble metals. Since the reverse procedure, rotation of a cylindrical specimen in a stationary vessel, has been used by a number of previous investigators, some experiments were also carried out with the dissolution of benzoic acid in water and sucrose solution in the same apparatus with the vessel stationary and the speci-

men rotating. A different correlation between the dissolution rate and the Reynolds numbers and Schmidt groups was then obtained, which has been compared with the correlations reported by other workers for this type of stirring mechanism.

MECHANISM OF TRANSPORT PROCESSES

As is well known, the turbulence present in the bulk of an agitated liquid is suppressed in the vicinity of any solid surface. There is at present, however, some difference of opinion as to the exact nature of the flow pattern in the zone immediately adjacent to the surface. The earlier and more conventional theories assume that a laminar sublayer is always present in which the flow is parallel to the surface (22). Transport of solute molecules across this region will thus take place by molecular diffusion, which is a much slower process than the eddy or turbulent diffusion operative in the bulk phase. Between the sublayer and the bulk phase there exists a transition region (buffer layer) where turbulence is diminished and both molecular and eddy diffusion are important. The major resistance to transport between the

surface of the solid and the bulk phase, therefore, lies in molecular diffusion across the sublayer. It is convenient in practice to assume that the whole resistance to transfer is due to molecular diffusion alone, the small contribution owing to eddy diffusion being allowed for by taking the diffusional path length to be a fictitious film of a finite thickness, somewhat thicker than the sublayer. The thickness of the film is thus proportional to that of the sublayer, both being dependent on the degree of turbulence in the bulk phase.

Gas absorption and liquid-liquid extraction rates are also usually explained by the concept of the existence of a laminar sublayer at the interface. Alternative theories concerning gas absorption have, however, been proposed by Higbie (10), Kishinevskii (14), and Danckwerts (4) who suggest that the actual surface is constantly being renewed, with turbulent eddies reaching the gas-liquid interface. Kishinevskii further considers that no part at all is played by molecular diffusion. Lewis (15) has reached a similar conclusion, on experimental grounds, for flow at liquid-liquid interfaces. Recently concentration-profile measurements at solid

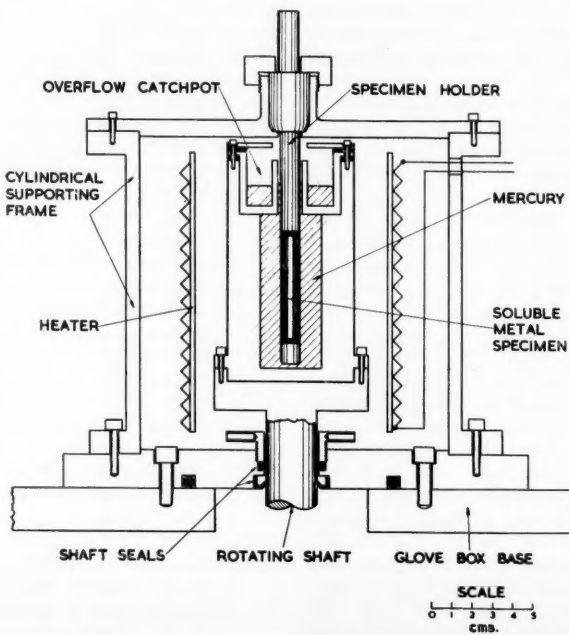


Fig. 1. Rotating cell.

J. A. R. Bennett is at present with Esso Petroleum Company, Fawley, Hampshire, England.

TABLE I. PHYSICAL DATA

Solute	Solvent	Temp., °C.	Density, g./cc.	Viscosity, centipoises	Solubility, g./cc.	Diffusivity, sq. cm./sec. $\times 10^5$	$\left(\frac{v}{D}\right)$
Tin	Mercury	30	13.52	1.49	0.85*	1.60	69
Tin	Mercury	40	13.50	1.44	1.05*	1.50	71
Lead	Mercury	30	13.52	1.49	1.82*	1.25	88
Lead	Mercury	40	13.50	1.44	2.25*	1.07	100
Zinc	Mercury	30	13.52	1.49	2.39*	2.35	47
Zinc	Mercury	40	13.50	1.44	2.86*	2.30	47
Benzoic acid	Water	30	0.996	0.80	4.2†	1.14	708
Benzoic acid	Water	40	0.992	0.66	6.0†	1.43	462
Benzoic acid	Sucrose solution	30	1.18	5.79	3.58†	0.16	31,200
Benzoic acid	Sucrose solution	40	1.19	3.84	4.60†	0.24	13,200

*Solubility expressed as wt. %.

†Solubility expressed as g./liter.

electrodes (16) have been interpreted to indicate that turbulent eddies may reach solid surfaces also (9), and attempts have been made to apply the surface-renewal hypotheses to the description of the flow of mass and heat from solids to liquids (12).

Danckwerts and Kennedy (5) have shown that the laminar sublayer concept yields equations similar to the surface renewal theories. Thus the conventional transport equation can be used irrespectively of the validity of the sublayer hypothesis, and the driving force for the transport process will be $(c^* - c)$ whether or not the flow is by molecular or eddy diffusion.

For the rate of transport

$$N = k_d A (c_i^* - c_i) \quad (1)$$

The proportionality constant k_d will be directly proportional to the molecular diffusivity, if the simple sublayer concept is correct but proportional to some lower fractional power in other cases. Under steady state conditions the transport rate will equal the net rate of transfer of solute from the solid specimen to the liquid immediately adjacent to it. This rate can be expressed in a similar manner (18):

$$N = k_e A (\gamma_{sat.} c_{sat.} - \gamma_t^* c_t^*) \quad (2)$$

(where γ_t is a function of c_t and not t)

Since the surface concentration c_t^* is generally not known, it is necessary for practical purposes to define an *overall* mass transfer coefficient, which can be experimentally measured; thus

$$N = K A (c_{sat.} - c_i) \quad (3)$$

If k_e is much greater than k_d , one can see that c_t^* becomes equal to $c_{sat.}$ and K equal to k_d . The observed transfer coefficient will then have a maximum dependence on the degree of turbulence, that is the Reynolds number. An example of such a transport-controlled system is the dissolution of benzoic acid in water. If, therefore, the dissolution of metals in mercury follows the same general correlation as the dissolution of benzoic acid in water, it may be concluded that these dissolution processes are also diffusion controlled.

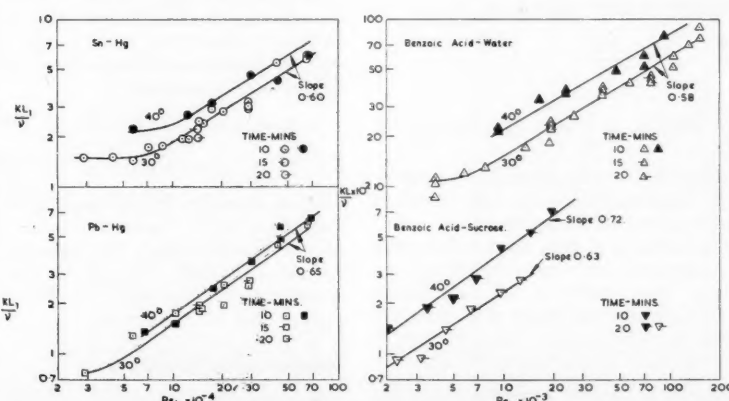
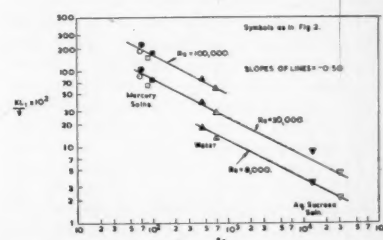
EXPERIMENTAL

Preliminary experiments were carried out with rods of benzoic acid and rods of lead, tin, and zinc, rotating in vessels containing water and mercury respectively. In all cases, even when extensive baffling was used, the surface of the specimens became "corrugated" during dissolution, apparently owing to the presence of Taylorian vortices at the surface (20). The least effect was obtained with the benzoic acid specimens, since the solubility of benzoic acid in water is very small.

When, however, the specimens were kept stationary down the axis of a rotating cylindrical vessel, smooth uniform dissolution was obtained except with zinc specimens, which were invariably etched. Although calculations have been made on the flow pattern between an infinitely long stationary cylinder and an outer rotating cylinder (19, 20), it was clear from the preliminary experiments that the disturbances set up at the top and bottom of the vessel so affected the ideal flow pattern that the hydrodynamics of flow would have to be examined semiempirically.

The metal specimens finally used consisted of tubes 5 cm. long and 1 cm. O.D., which were made from 99.99% pure metal of a very fine grain size. Each tube was threaded onto a stepped stainless-steel holder and held in place by an end cap 1 cm. long, the whole assembly forming a smooth cylinder of uniform external diameter. The specimen holder was accurately positioned along the vertical axis of a cylindrical mild-steel dissolution vessel, 7.3 cm. high and 3 cm. I.D., so that the actual specimen was located in the middle of the vessel. This arrangement minimized the effect on the specimen of the irregular flow patterns at the top and bottom of the vessel. To avoid vortex formation the free surface of mercury was reduced to a minimum by closing the top of the cell with a ring shaped plug which left a clearance of only 1 mm. around the specimen holder. It was found that the volume of mercury remained constant $\approx 49.0 \pm 0.1$ cc., irrespective of the rotational speed. The vessel was mounted on a vertical shaft which could be rotated at speeds up to 4,000 r.p.m. by means of an electronically controlled motor, the exact speed being measured accurately by a stroboscope. A fixed electrical heater mounted around the vessel enabled the temperature of the mercury to be controlled to $\pm 0.2^\circ\text{C}$. Experiments were carried out at 30° and 40°C . Since the mercury solutions oxidized exceedingly rapidly in air and produced a scum which tended to contaminate the surfaces of the specimens and reduce the bulk concentration, the dissolution vessel was mounted inside a glove box filled with very pure argon. The rotating shaft passed through gas tight seals in the base of the box. A diagrammatic sketch of the transfer cell is shown in Figure 1.

A similar apparatus constructed entirely of stainless steel and mounted in an air thermostat was used for the benzoic acid dissolution experiments. The benzoic acid specimens were prepared by casting molten benzoic acid onto a 1-cm.-diameter metal rod which was recessed from 1 to 6 cm.

Fig. 2. Plot of KL_1/v vs. Reynolds number—Rotating Cell.Fig. 3. Plot of KL_1/v vs. Schmidt group—Rotating Cell.

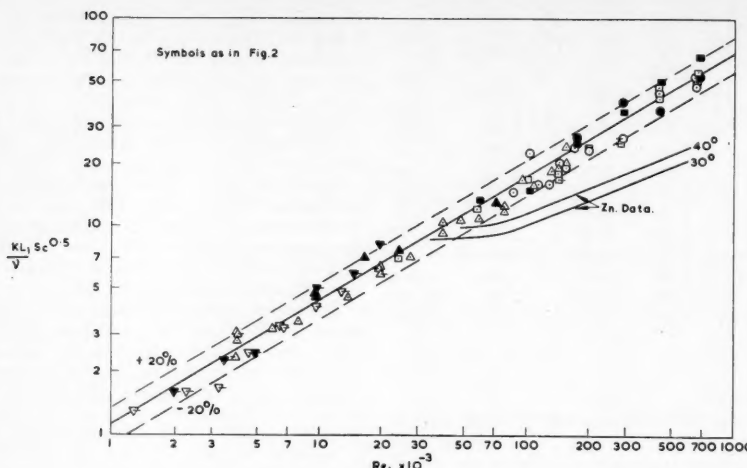


Fig. 4. Plot of $KL_1/\nu \cdot Sc^{1/2}$ vs. Reynolds number—Rotating Cell.

from the end. Surplus acid was machined away leaving a smooth specimen 5 cm. long and integral with the rod. The whole assembly was geometrically identical to the mercury apparatus, but the volume of water was slightly less, being 47.0 cc. Aqueous sucrose solution of concentration 500 g./liter was used.

Owing to the nature of the apparatus it was only possible to take samples of the liquid at the end of each experiment. Normally these were of 10 min. durations, but with the metal experiments some experiments were carried out for 15 and 20 min. to see if the transfer coefficients varied with time and therefore concentration. The lead and tin solutions in mercury were analyzed by evaporating off the mercury from a sample of known weight by heating to 300°C. in a current of nitrogen. This method proved to be quantitatively accurate. A similar technique was adopted with zinc solutions, but as the solid residue invariably contained about 9% by weight of mercury this was dissolved in aqua regia and analyzed polarographically. The benzoic acid solutions were titrated against $N/100$ sodium hydroxide solutions.

The solubilities of tin and zinc in mercury and benzoic acid in sucrose solution were experimentally determined at 30° and 40°C. All other solubility data were taken from the literature.

The viscosities and densities of all solutions were taken to be the same as those of the solvents, since the concentrations obtained during the experiments were low. No data were available for the diffusion coefficients of the various metals in mercury at 30° and 40°, but some data were available at 25° and lower temperatures. These were plotted as the logarithm of the diffusion coefficient against the reciprocal temperature, which is normally linear, and the best extrapolated values of the diffusivities obtained by inspection. Diffusion coefficients at 30° and 40°C. for benzoic acid in water and sucrose solution were calculated by using the Stokes-Einstein equation and Wilke's (7) data at 25°C. for the diffusion coefficient of benzoic acid in water. All relevant physical data are summarized in Table 1.

RESULTS

The multicrystalline zinc specimens gave an etched surface on dissolution, apparently owing to the individual crystal grains dissolving at different rates. This suggested that a chemical rate factor entered into the dissolution process and varied with the nature of the crystal face exposed. Confirmatory evidence was obtained from the dissolution of cylindrical specimens consisting of single crystals when it was found that the various crystallographic faces did indeed dissolve at markedly different rates. Similar effects are known to occur during the dissolution of zinc in various aqueous acid solutions; therefore the phenomenon is not peculiar to the dissolution of zinc in mercury. The chemical rate factors have been evaluated for the dissolution of zinc, and the results are given in detail elsewhere (1). Since zinc dissolution is thus not an entirely transport controlled process, the zinc data cannot be correlated along with those for other systems, as is shown later.

The rates of mass transfer were obtained from the final concentration of the mercury solution; thus since

$$N = \frac{Vdc}{dt} t \quad (4)$$

$$\therefore Kdt = -\frac{V}{A} \cdot d \ln (c_{sat.} - c_t) \quad (5)$$

and hence K can be obtained by integration. Since samples could only be taken at the end of each experiment, the calculated values of K were mean values over the concentration range $c = 0$ to $c = c_t$. There was, however, no significant difference between values of K obtained after 10 to 20 min.*

*Tabular material has been deposited as document 5768 with the American Documentation Institute, Photoduplication Service, Library of Congress, Washington 25, D. C., and may be obtained for \$1.25 for photoprints or \$1.25 for 35-mm. microfilm.

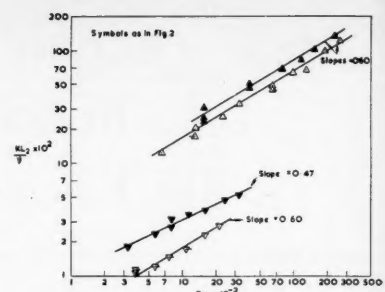


Fig. 5. Plot of KL_2/ν vs. Reynolds number—Rotating Specimen.

A fundamental theoretical approach is rarely possible when considering flow patterns in agitated systems owing to the complexity of the mathematics involved. The data are therefore usually correlated by the use of dimensional analyses, when one assumes that the mass transfer coefficient in a transport-controlled system is a function of the relevant parameters affecting the hydrodynamics of the system. With the rotating vessel experiments these were taken to be the viscosity, density, and solute diffusivity. The same parameters were used with the rotating specimens experiments except that the characteristic velocity and density were different. The diameter was not chosen in accordance with Eisenberg, Tobias, and Wilke (7). Hence one can write

$$k_d = f(\mu, \rho, D, u, L) \quad (6)$$

Three dimensionless groups can be formed from these six variables, and these can be conveniently arranged as follows:

$$k_d L/\nu = f[(Lu/\nu), (\nu/D)] \quad (7)$$

where the kinematic viscosity replaces μ/ρ , and the two groups on the right hand side are the Reynolds number and Schmidt group, respectively. In most instances Equation (7) can be approximated by a product of power functions, that is

$$k_d L/\nu = \text{const. } N_{Re}^a \cdot N_{Sc}^b \quad (8)$$

This expression may also be written in the following alternative forms, the groups on the left hand side being comparable with the Stanton and Nusselt heat transfer numbers, respectively

$$k_d/u = \text{const. } N_{Re}^{a-1} \cdot N_{Sc}^b \quad (8a)$$

$$k_d L/D = \text{const. } N_{Re}^a \cdot N_{Sc}^{b+1} \quad (8b)$$

When Equation (8) was applied to the correlation of the present data, it was necessary to investigate the variations of the experimentally determined over-all transfer coefficients with the Reynolds number and Schmidt group.

INTERPRETATION OF RESULTS

Rotating-Vessel Data

The over-all coefficients in the form

KL_1 , number for ν . If k slope Schi system slope lead and $30^\circ C$ for b. Whe man were to the step. value owing tributary expone

The simil again co-on used data of slo order group there N_{Sc}^0 , corre about The

(KL) i.e.

The plott curve elude below unlike depen fit the appr the

8

Vol.

KL_1/ν were plotted against Reynolds number N_{Re_1} on logarithmic coordinates for each system studied (see Figure 2). If k_d and K are equal, linear plots of slope 'a' should be obtained, since the Schmidt group is a constant in any one system. Linear plots were obtained with slopes in the range 0.60 ± 0.05 for tin and lead in mercury, benzoic acid in water, and benzoic acid in sucrose solution at 30°C ; a higher exponent 0.72 was found for benzoic acid in sucrose solution at 40°C . When the zinc data were plotted in this manner, linear plots with slopes of 0.45 were obtained, the lower slope being due to the existence of a significant chemical step. The graphs flattened out at low values of the Reynolds number, probably owing to the proportionally greater contribution from convection currents at low stirring speeds. Because of the experimental scatter of the results a mean exponent of 0.60 on the Reynolds exponent has been adopted.

The Schmidt group exponents 'b' were similarly obtained by plotting KL_1/ν against the Schmidt group on logarithmic co-ordinates with the Reynolds number used as a parameter (see Figure 3). The data were well correlated by straight lines of slope -0.50 which extended over three orders of magnitude of the Schmidt groups. All the experimental data were therefore plotted in the form $(KL_1/\nu)N_{Sc^{0.5}}$ against N_{Re_1} . A reasonably good correlation with an over-all scatter of about $\pm 20\%$ was obtained (Figure 4). The equation to the solid line is

$$(KL_1/\nu) \cdot N_{Sc^{0.5}} = 0.018N_{Re_1}^{-0.6} \quad (9)$$

i.e.

$$(KL_1/\nu) = 0.018N_{Re_1}^{-0.6} \cdot N_{Sc^{0.5}}$$

The zinc-mercury data were also plotted in this manner, and smoothed curves representing the results are included in Figure 4. These curves lie below the general correlation and also, unlike the other data, are temperature dependent. The benzoic acid-sucrose data fit the correlation to a fair degree of approximation, although, since at 40°C . the Reynolds exponent is greater than

0.60 with this system, the 40° points lie across the correlation at a shallow angle.

Rotating-Specimen Data

The data for the dissolution of rotating specimens of benzoic acid in water and aqueous sucrose solution were treated in the same manner as the rotating-cell data. A linear logarithmic plot was obtained between KL_2/ν and the Reynolds number N_{Re_2} in all cases (see Figure 5). The slopes of the lines were again 0.60 for water at 30° and 40° and for sucrose solution at 30°C ; with aqueous sucrose at 40°C . the slope was 0.45. In Figure 6 a logarithmic plot is given of (KL_2/ν) against the Schmidt group, and the data are best correlated by lines of slope -0.6.

The data are replotted in Figure 7, and, with the exception of the sucrose solution at 40°C . which again crosses the main correlation at a shallow angle, are correlated to within $\pm 20\%$:

$$(KL_2/\nu)N_{Sc^{0.6}} = 0.135N_{Re_2}^{-0.6}$$

i.e. (10)

$$(KL_2/\nu) = 0.135N_{Re_2}^{-0.6} \cdot N_{Sc^{0.6}}$$

DISCUSSION

The correlation of the tin-mercury and lead-mercury data along with the benzoic acid-water data is conclusive evidence that the rates of dissolution of these metals are also transport controlled over the range of turbulence investigated. The 40° benzoic acid-sucrose data tends to diverge from the correlation because the exponent on the Reynolds number is different, probably since the use of a simple power function is a good approximation only over the range of Schmidt groups obtained with mercury and water, that is 47 to 708. The extension of this expression to the much higher Schmidt groups obtained with sucrose solution, 13,200 and 31,200 at the two different temperatures, is much less valid. It is not clear however why the sucrose data at 30° fit the correlation better than those

obtained at 40°C . The divergence of the zinc data arises from the presence of a slow chemical step at the surface of the crystal lattice during dissolution. These results have been discussed in detail elsewhere, and values have been derived for the chemical rate constant.

It is interesting to note that the same exponent of the Reynolds number was obtained for both the rotating vessel and the rotating specimen experiments. The 0.6 power falls in the 0.5 to 1.0 range of Reynolds exponents previously reported by various authors for a variety of flow condition [Vielstich (21) and Bircumshaw and Riddiford (22)]. Eisenberg, Tobias, and Wilke have recently carried out a comparable rotating specimen experiment (7) and obtained a correlation which, when expressed in the form of Equation (8a), gives a Reynolds exponent of 0.7; however the use of a simple power function relation to cover the whole range of experimental results is of limited validity. Over the range of Reynolds numbers equivalent to those used in this paper the Reynolds exponent is somewhat lower.

The Schmidt group exponent is of considerable theoretical interest as it indicates the relative importance of molecular and turbulent diffusion. The well-known Chilton-Colburn equation (3) derived from the relationship between heat transfer and fluid friction gives an exponent of $\frac{2}{3}$ on the Schmidt group. This can be written

$$(K/u) = f(N_{Re}) \cdot N_{Sc}^{-2/3} \quad (11)$$

Linton and Sherwood (17) have shown that this expression can be used to correlate their experimental results for mass transfer in pipe flow. Eisenberg, Tobias, and Wilke (7) reported a slightly lower exponent 0.644 on the Schmidt group for rotating specimen experiments; other authors however have found values of the Schmidt exponent significantly greater or smaller than two thirds. King and Howard (13) measured the mass transfer coefficients for the dissolution of thin metal wires in various liquid reagents by using stationary specimens mounted

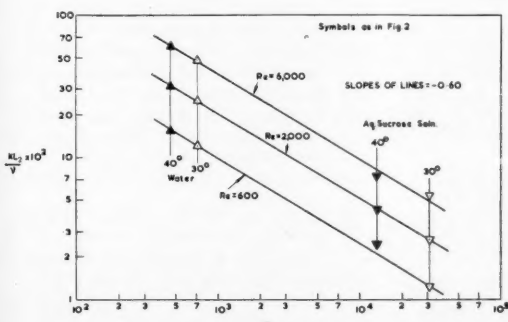


Fig. 6. Plot of KL_2/v vs. Schmidt group—Rotating Specimen.

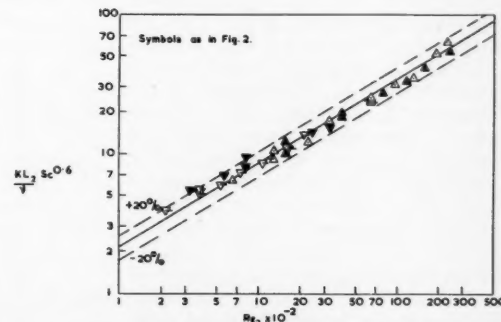


Fig. 7. Plot of $KL_2/v \cdot Sc^{0.6}$ vs. Reynolds number—Rotating Specimen.

inside a rotating cylindrical stirrer and the rate of heat transfer from electrically heated platinum wires to aqueous sucrose solutions. Exponents of about 0.70 were found on both the Schmidt groups and Prandtl numbers. These results cannot be compared directly with stirred vessel experiments discussed in this paper since the cylindrical stirrer was grooved, open at both ends, and immersed in a large vessel of liquid. Longitudinal flow past the specimen would thus take place, the flow pattern being further complicated by vortex formation at the free surface of the liquid. A different type of turbulent flow existed in the stirred vessel, which approximated that investigated by Taylor (20). Higher Schmidt exponents, up to 0.83, have been obtained by King (13) in earlier experiments with rotating cylindrical metal specimens.

On the other other hand Davion (6) found an exponent of 0.63 for the dissolution of single crystals of salts in water, while Gaffney and Drew (8) reported that the best exponent on the Schmidt group for the dissolution of organic acid pellets in a packed extraction column was 0.58. Hixson and Baum (11) and Johnson and Huang (12) reported values of 0.50 for mass transfer in paddle-stirred systems. The latter authors suggest that this low value indicates that the Danckwerts surface-renewal theory can be applied to solid-liquid dissolution as well as to gas-liquid absorption. Two different exponents on the Schmidt group were obtained in the experiments conducted by the authors of this paper, 0.50 with the cell rotating and 0.60 with the specimen rotating.

Since values of the Schmidt exponent ranging from 0.50 to 0.82 have been reported by various authors, it is clear that the Danckwerts theory cannot generally be applied in its original and simplest form which would give a 0.50 exponent only. If it is assumed that solutes can penetrate through the laminar sublayer before the sublayer is destroyed by an eddy, then exponents greater than 0.50 can be postulated. The exponents should be greater the greater the local turbulence in the apparatus used. This is indeed the case in the authors' experiments, 0.60 with the actual specimen rotating as compared with 0.50 when the cell rotated. Since values of the Schmidt exponents in the range reported can also be postulated by modifications of the conventional boundary layer theory (2, 21), these results do not themselves confirm or disprove the surface renewal hypothesis. It is clear that the geometry and stirring conditions used by the various workers have a direct bearing on the value of the Schmidt exponent obtained by them. More data, especially on the exact nature of the turbulence present at the surfaces of the various dissolving specimens, are needed before the theory can be rigorously proved.

CONCLUSIONS

1. A comparison between the dissolution of lead and tin in mercury with the dissolution of benzoic acid in water, which is known to be transport controlled, indicated that the metal dissolution rates are also transport controlled.

2. The dissolution rate of zinc in mercury is lower than would be anticipated from the data for the other metals, and this has been shown to be owing to a slow chemical step at the surface of the crystal lattice.

3. Taylorian vortices are inevitably obtained at the surfaces of rotating specimens. They can be prevented only by circulating the solvent around the specimen, as for example by rotating the containing vessel. Data for the dissolution of stationary rods under these conditions of stirring are correlated to $\pm 20\%$, over a range of Reynolds numbers from 1,000 to 440,000 and a range of Schmidt groups from 47 to 700, by the relation

$$(KL_1/v) = 0.018(L_1u_1/v)^{0.60}(\nu/D)^{-0.50}$$

This correlation can be extended to Schmidt groups of 31,000, that is dissolution of benzoic acid in aqueous sucrose solution, with a slight loss of accuracy.

4. Data for the dissolution of rotating specimens of benzoic acid in water are correlated by the following expression which differs somewhat from that of Wilke:

$$(KL_2/v) = 0.135(L_2u_2/v)^{0.60}(\nu/D)^{-0.60}$$

5. There is insufficient evidence to confirm or disprove the validity of the surface renewal theory for the dissolution of solids in liquids.

NOTATION

A	total surface area of specimen, sq. cm.
c	concentration, wt. % for mercury solutions; g./litre for aqueous solutions
D	diffusivity, sq. cm./sec.
f	function of
k	individual mass transfer coefficient, cm./sec.
K	observed 'over-all' mass transfer coefficient, cm./sec.
L_1	characteristic dimension of rotating cell hydraulic diameter of the annulus, cm.
L_2	characteristic dimension of rotating specimen specimen diameter, cm.
N	rate of mass transfer, g./sec.
t	time of dissolution, sec.
u_1	characteristic velocity of rotating cell peripheral velocity of the inner surface cm./sec.
u_2	characteristic velocity of rotating specimen peripheral velocity of the specimen, cm./sec.
V	volume of solvent, cc.

γ	= activity coefficient
μ	= viscosity of solvent, g.//(sec.)(cm.)
ν	= kinematic viscosity of solvent, sq. cm./sec.
ρ	= density of solvent—g./cc.
N_{Re}	= Reynolds number, Lu/ν
N_{Sc}	= Schmidt number, ν/D

Subscripts

c	= chemical rate
d	= diffusional rate
sat.	= at saturation
t	= value at time t

Superscript

$*$	= value at solid-liquid interface
-----	-----------------------------------

LITERATURE CITED

1. Bennett, J. A. R., and J. B. Lewis, *J. Chim. phys.*, p. 83 (1958).
2. Bircumshaw, L. L., and A. C. Riddiford, *Quart. Rev.*, **6**, 157 (1952).
3. Chilton, T. H., and A. P. Colburn, *Ind. Eng. Chem.*, **26**, 1183 (1934).
4. Danckwerts, P. V., *ibid.*, **43**, 1460 (1951).
5. Danckwerts, P. V., and A. M. Kennedy, *Trans. Inst. Chem. Engrs.*, **32**, S49 (1954).
6. Davion, Maurice, *Ann. Chim. (Paris)*, **8**, 259 (1953).
7. Eisenberg, M., C. W. Tobias and C. R. Wilke, *Chem. Eng. Progr. Symposium Series*, No. 16, **51**, 1 (1955).
8. Gaffney, B. J., and T. B. Drew, *Ind. Eng. Chem.*, **42**, 1120 (1950).
9. Hanratty, T. J., *A.I.Ch.E. Journal*, **2**, 359 (1956).
10. Higbie, Ralph, *Trans. Am. Inst. Chem. Engrs.*, **31**, 365 (1935).
11. Hixson, A. W., and S. J. Baum, *Ind. Eng. Chem.*, **33**, 478, 1433 (1941).
12. Johnson, A. I., and Cheng-Jung Huang, *A.I.Ch.E. Journal*, **2**, 412 (1956).
13. King, C. V., and P. L. Howard, *Ind. Eng. Chem.*, **29**, 75 (1937).
14. Kishinevskii, M. Kh., and A. V. Pamfilov, *Zhur. Priklad. Khim.*, **22**, 1173 (1949).
15. Lewis, J. B., *Chem. Eng. Sci.*, **3**, 248 (1954).
16. Lin, C. S., R. W. Moulton, and G. L. Putnam, *Ind. Eng. Chem.*, **45**, 636, 640 (1953).
17. Linton, W. H., and T. K. Sherwood, *Chem. Eng. Progr.*, **46**, 258 (1950).
18. Moelwyn-Hughes, E. A., "Kinetics of Reactions in Solution," p. 375, Oxford University Press (1947).
19. Schlichting, Hermann, "The Boundary Layer Theory," Pergamon Press, London (1955).
20. Taylor, G. I., *Trans. Roy. Soc. (London)*, **223**, 289 (1923); *Proc. Roy. Soc. (London)*, **A.151**, 494 (1935).
21. Vielstich, Wolf, *Z. Elektrochem.*, **57**, 646 (1953).
22. Whitman, W. G., *Chem. Met. Eng.*, **29** (4), 146 (1923); Lewis, W. K., and W. G. Whitman, *Ind. Eng. Chem.*, **16**, 1215 (1924).

Manuscript received January 7, 1958; revision received April 21, 1958; manuscript accepted April 28, 1958.

Surface Dynamics of Fluidized Beds and Quality of Fluidization

W. J. RICE and R. H. WILHELM

Princeton University, Princeton, New Jersey

Solutions of linearized Navier-Stokes equations have been developed for the motion of arbitrary two-dimensional waves occurring at any interface between the emulsion phase of a fluidized bed and the particle-free, fluid phase. In all cases for which the bed particles are denser than the fluidizing fluid the solutions showed that the lower interface of a bed always is unstable and the upper, stable. The quality of fluidization is suggested to be related at least in part to the rate of growth of surface waves, this rate depending upon physical properties of the system and length of the disturbing wave.

The question of the stability of interfaces between two fluids of different physical properties (density, viscosity, etc.) has attracted considerable interest in recent years (1, 3, 8). In this paper the approach is extended by means of the Taylor instability theory (8) to the stability of interfaces between the dense bed phase of a fluidized bed and the particle-free fluid phase. In particular, instabilities at the bed entrance are studied as contributors to bed quality through initiation of bubbles at this site, and instabilities at the upper surfaces of bubbles are investigated as a mechanism tending to limit bubble growth. By solving linearized Navier-Stokes equations describing the motions of an interface in terms of arbitrary, two-dimensional waves for models of fluidized beds, one finds that the lower interface of a bed composed of particles denser than the fluidizing fluid (hereafter called the support fluid) is always unstable and the upper, stable. Unstable interfaces are those on which an imposed disturbance grows in amplitude with time; stable interfaces are those on which a disturbance is damped out.

Taylor's theory, first discussed in 1950, concerns a stability analysis of interfaces between two fluids of different densities when the fluids are accelerated either mechanically or gravitationally in a direction perpendicular to the interface. It was shown by solution of the linearized fluid dynamical equations for systems subject only to gravitational acceleration, with viscosity and surface tension neglected, that, if a horizontal interface at rest under gravity is displaced into the form of small waves, this surface is stable or unstable according to whether the acceleration of gravity is directed from the lighter to the heavier fluid or vice versa. Lewis (3) verified these conclusions experimentally for air-water, air-glycerine, and benzene-water interfaces. The experimental phenomena for fluid interfaces photographed by Lewis are suggestive of fluidized-bed behavior. Bellman and Pennington (1) made theo-

retical extensions to include effects of viscosity and surface tension.

When one applies a Taylor type of analysis to fluidized beds, the assumption is made that the system is, as an approximation, composed of two distinct fluid phases: the support fluid (liquid or gas) and the dense-phase fluidized bed itself. In a bed there are a number of positions where an interface between two fluids of different physical properties occurs: at the top of the bed, at the bottom support, and at slugs, bubbles, or other discontinuities that rise through the bed. Figure 1 shows an idealized general view of a cross section of a bed containing bubbles.

BED MODELS

A number of idealized and simplified models of the bed will be introduced at this point and will incorporate two types of physical characteristics: the dense-phase intensive properties of density and viscosity and the relative motion of solid particles and the support fluid. These models were selected as mathematically amenable approximations to true behavior of fluidized beds and thus at best only approach actuality. While the emphasis here is directed to the properties of the dense phase, the support-fluid properties of density and viscosity, which are important also, are those associated with a normal fluid. In all models turbulence has been included only in the sense of serving as a possible source of interfacial disturbances. Turbulent motion is not represented directly in equations.

Two basic models have been devised which consider fraction voids in the dense-bed phase to be constant for any given system and flow rate. Local variations in support-fluid velocity, which constitute the direct source of interfacial disturbances, are assumed to occur, producing displacements of the bed particles. It is these displacements appearing at an interface of the bed which constitute the visible interfacial disturbances.

Model 1 uses a fixed-bed approach because it postulates particles remaining more or less in fixed geometrical array. There is movement of particles only as is

necessary to accommodate the displacement of interfaces. In coursing through the array the support fluid encounters frictional resistance, and its velocity also is modified. As a convenient but not necessary assumption, density and viscosity of the dense-bed phase and of the support fluid are taken to be the same. The interface is assumed to move so as to maintain a constant slip velocity.

In model 2 the dense bed phase is assumed to be an emulsion in which particles tend to follow fluid motions more closely than in model 1, but a constant slip velocity still is maintained. Bed density is taken as a weighted average of solid and support-fluid densities. Bed-phase viscosity is taken at a value considerably greater than that of the support fluid. Bed viscosity may be estimated from experiments on fluidized beds or on hindered settling of particles. Here bed viscosities have been estimated from the work of Matheson, Herbst, and Holt (5) and Long (4) with rotating spindles in fluidized beds.

A variant of model 2 (model 2a) considers the slip velocity to be constant only in the steady flow condition. The interface is considered to move under the influence of changes in the drag force produced by velocity fluctuations; the rate of movement of the interface is determined by acceleration caused by this unbalanced force. Here the drag force is estimated by utilizing Stokes's Law, and so the analysis must be limited to cases of particles sufficiently small for this to be a satisfactory approximation.

THEORY

Transference of the interfacial stability analysis into quantitative terms requires formulation in precise mathematical terms. Theory is clarified by a treatment of the physical picture at the point of introduction into the mathematical development; therefore the essential points involved will be illustrated for one interface of one model. Final expressions for the various other cases are then presented. Details of all derivations are available elsewhere (7).

Equations for motion of an interface are basically the same for models 1 and 2 except for the presence of a friction term for the bed phase in model 1. Only the outline of derivation for the lower

W. J. Rice is at Villanova University, Villanova, Pennsylvania.

interface in model 1 will be traced in this section.

A two-dimensional, sinusoidal velocity wave in u and v is imposed at the lower interface of the bed. Associated with this velocity wave is a two-dimensional, sinusoidal, vertical displacement (η) of the interface of identical wave length. Linearized equations of motion and continuity for bed-phase and support-fluid phase are solved in terms of potential functions.

An equation of continuity is

$$\frac{\partial u}{\partial x} + \frac{\partial v}{\partial y} = 0 \quad (1)$$

Equations of motion are

$$\frac{\partial u}{\partial t} + \frac{1}{\rho} \frac{\partial p}{\partial x} = \frac{\mu}{\rho} \left(\frac{\partial^2 u}{\partial x^2} + \frac{\partial^2 u}{\partial y^2} \right) - F_x \quad (2)$$

$$\frac{\partial v}{\partial t} + \frac{1}{\rho} \frac{\partial p}{\partial y} + g = \frac{\mu}{\rho} \left(\frac{\partial^2 v}{\partial x^2} + \frac{\partial^2 v}{\partial y^2} \right) - F_y \quad (3)$$

In accordance with the well-known convenience of fluid mechanics, transformations are made into potential functions ϕ and ψ . These are defined by

$$u = -\frac{\partial \phi}{\partial x} - \frac{\partial \psi}{\partial y} \quad (4)$$

$$v = -\frac{\partial \phi}{\partial y} + \frac{\partial \psi}{\partial x} \quad (5)$$

$$p = p_0 - g\rho y + \rho \frac{\partial \phi}{\partial t} - F_y \rho \quad (6)$$

with the further restriction

$$\frac{\partial^2 \phi}{\partial x^2} + \frac{\partial^2 \phi}{\partial y^2} = 0 \quad (7)$$

$$\frac{\mu}{\rho} \left(\frac{\partial^2 \psi}{\partial x^2} + \frac{\partial^2 \psi}{\partial y^2} \right) = \frac{\partial \psi}{\partial t} \quad (8)$$

To satisfy these equations for the bed phase, a solution is written in the following equations:

$$\phi_1 = Ae^{-K_y+nt} \cos Kx + My \quad (9)$$

$$\psi_1 = Be^{-m_y+nt} \sin Kx \quad (10)$$

$$p_1 = p_0 - g\rho_1 y + \rho_1 \frac{\partial \phi}{\partial t} - F_y \rho_1 \quad (11)$$

where

$$m_1 = +\sqrt{K^2 + \frac{\rho_1 n}{\mu_1}}$$

Similarly for support-fluid phase these equations provide a solution:

$$\phi_2 = Ce^{K_y+nt} \cos Kx + Ny \quad (12)$$

$$\psi_2 = De^{m_y+nt} \sin Kx \quad (13)$$

$$p_2 = p_0 - g\rho_2 y + \rho_2 \frac{\partial \phi}{\partial t} \quad (14)$$

where

$$m_2 = +\sqrt{K^2 + \frac{\rho_2 n}{\mu_2}}$$

With the interfacial position denoted by $\eta(x, t)$, the rate of movement of the interface when one applies the condition of constant slip velocity is given by

$$\frac{\partial \eta}{\partial t} = v_2 - C' \quad (15)$$

Alternately after one employs Equations (5), (12), and (13)

$$\frac{\partial \eta}{\partial t} = Ke^{nt} \cos Kx(-C + D) - N - C' \quad (16)$$

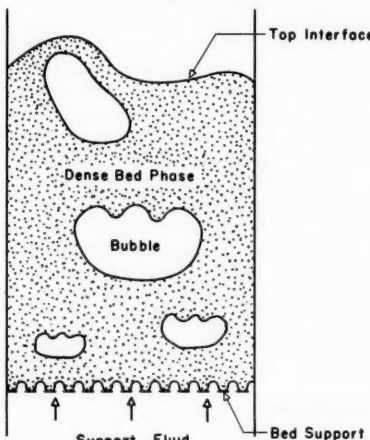


Fig. 1. Cross section of a fluidized bed.

On integration Equation (16) yields

$$\eta = \frac{K(-C + D) \cos Kx}{n} e^{nt} + (-N - C')t + C_1 \quad (17)$$

If interfacial position at time zero is now taken as

$$\eta_0 = \frac{K(-C + D) \cos Kx}{n} \quad (18)$$

then $C_1 = 0$ and $C' = -N$. Therefore

$$\frac{\eta}{\eta_0} = e^{nt} \quad \text{at any } x \quad (19)$$

This important relation shows that the rate of change of amplitude of an interfacial disturbance is proportional to the exponential (nt).

To relate the constant n to the wave length of the surface disturbance as well as to the physical properties of the fluid phases the following interfacial boundary conditions are imposed:

$$u_1 = u_2 \quad (20)$$

$$v_1 = v_2 + \frac{C'(1 - \epsilon)}{\epsilon} \quad (21)$$

$$-p_1 + 2\mu_1 \frac{\partial v_1}{\partial y} = -p_2 + 2\mu_2 \frac{\partial v_2}{\partial y} \quad (22)$$

$$\mu_1 \left(\frac{\partial v_1}{\partial x} + \frac{\partial u_1}{\partial y} \right) = \mu_2 \left(\frac{\partial v_2}{\partial x} + \frac{\partial u_2}{\partial y} \right) \quad (23)$$

Equations (20) and (21) result from material balances across the interface and (22) and (23) from equating components of the stress tensor at the interface. On substitution of Equations (9), (10), (12), and (13) into (4), (5), (11), and (14) and then into (20), (21), (22), and (23) these four conditions on the constants A , B , C , and D are secured as follows:

$$KA + m_1 B - KC + m_2 D = 0 \quad (24)$$

$$A + B + C - D = 0 \quad (25)$$

$$\left(-\rho_1 n - 2\mu_1 K^2 + \frac{F_y \rho_1 K}{n} \right) A + \left(-2\mu_1 m_1 K + \frac{F_y \rho_1 K}{n} \right) B + (\rho_2 n + 2\mu_2 K^2) C - 2\mu_2 m_2 D = 0 \quad (26)$$

$$2\mu_1 K^2 A + \mu_1 (K^2 + m_1^2) B + 2\mu_2 K^2 C - \mu_2 (K^2 + m_2^2) D = 0 \quad (27)$$

Such equations have nontrivial solutions when the determinant of the coefficients vanishes. The solution in the form of n as a function of K for this case (that is, model 1, lower interface) is

$$[-F_y K \rho_1 + (\rho_1 + \rho_2)^2] [(\mu_1 K + \mu_2 m_2) + (\mu_2 K + \mu_1 m_1)] + 4nK[(\mu_1 K + \mu_2 m_2)(\mu_2 K + \mu_1 m_1)] = 0 \quad (28)$$

When $\mu_1 = \mu_2 = \mu_f$ and $\rho_1 = \rho_2 = \rho_f$, Equation (28) degenerates to

$$[-F_y K \rho_f + 2\rho_f n^2] + 2nK\mu_f(K + m) = 0 \quad (29)$$

where

$$F_y = \frac{(1 - \epsilon)(\rho_s - \rho_f)g}{\rho_f} \quad [\text{Ref. (9)}] \quad (30)$$

By somewhat similar procedures (7), the following equations are obtained for other cases

Model 1, Upper Interface

$$[F_y K \rho_1 + (\rho_1 + \rho_2)^2] [(\mu_1 K + \mu_2 m_2) + (\mu_2 K + \mu_1 m_1)] + 4nK[(\mu_1 K + \mu_2 m_2)(\mu_2 K + \mu_1 m_1)] = 0 \quad (31)$$

Model 2, Lower Interface

$$[-Kg(\rho_1 - \rho_2) + (\rho_1 + \rho_2)n^2] \cdot [(\mu_1 K + \mu_2 m_2) + (\mu_2 K + \mu_1 m_1)]$$

+4

Model

[-Kg

+4n

Wh

can be

[\rho_1(n^2

Model

[H

+G

+μ

+K

+K²

+4μ₁

+K

+2μ₁

+μ₂

+μ₂

where

+μ₂

and

Model

[-H

+G

+μ

+K

+K

+4

Vol.

$$+4nK[(\mu_1K + \mu_2m_2)(\mu_2K + \mu_1m_1)] = 0 \quad (32)$$

Model 2, Upper Interface

$$[-Kg(\rho_2 - \rho_1) + (\rho_1 + \rho_2)n^2]$$

$$\cdot [(\mu_1K + \mu_2m_2) + (\mu_2K + \mu_1m_1)]$$

$$+4nK[(\mu_1K + \mu_2m_2)(\mu_2K + \mu_1m_1)] = 0 \quad (33)$$

When $\mu_2 \ll \mu_1$ and $\rho_2 \ll \rho_1$, Equation (33) can be simplified to

$$[\rho_1(n^2 + Kg)]$$

$$+ \frac{4\mu_1^2 m_1 K^2}{\rho_1} (m_1 - K) = 0 \quad (34)$$

Model 2a, Lower Interface

$$\left[\frac{H}{G} + (\rho_1 + \rho_2)n \right] [K(\mu_1 + \mu_2)]$$

$$+ \mu_1 m_1 + \mu_2 m_2]$$

$$+ K^3 \left[\mu_2^2 \left(1 - \frac{1}{G} \right) + \mu_1 \mu_2 \left(3 + \frac{1}{G} \right) \right]$$

$$+ K^2 \left[\mu_2^2 m_2 \left(1 + \frac{3}{G} \right) + \mu_1 \mu_2 m_1 \left(1 - \frac{1}{G} \right) \right]$$

$$+ 4\mu_1^2 m_1 \left[\frac{1}{G} \right]$$

$$+ K \left[(\mu_2^2 m_2^2 + \mu_1 \mu_2 m_2^2) \left(-1 + \frac{1}{G} \right) \right]$$

$$+ 2\mu_1 \mu_2 m_1 m_2 \left(1 + \frac{1}{G} \right) \left[\frac{1}{G} \right]$$

$$+ (\mu_2^2 m_2^3 + \mu_1 \mu_2 m_1 m_2^2) \left(-1 + \frac{1}{G} \right) = 0 \quad (35)$$

where

$$G = \frac{1}{\epsilon} \left[\frac{\epsilon + \frac{\rho_s d^2 n}{18\mu_1}}{1 + \frac{\rho_s d^2 n}{18\mu_1}} \right] \quad (36)$$

and

$$H = \frac{-gK(\rho_1 - \rho_2)}{n \left(1 + \frac{\rho_s d^2 n}{18\mu_1} \right)} \quad (37)$$

Model 2a, Upper Interface

$$\left[-\frac{H}{G} + (\rho_1 + \rho_2)n \right] [K(\mu_1 + \mu_2)]$$

$$+ \mu_1 m_1 + \mu_2 m_2]$$

$$+ K^3 \left[\mu_1^2 \left(1 - \frac{1}{G} \right) + \mu_1 \mu_2 \left(3 + \frac{1}{G} \right) \right]$$

$$+ K^2 \left[\mu_1^2 m_1 \left(1 + \frac{3}{G} \right) + \mu_1 \mu_2 m_2 \left(1 - \frac{1}{G} \right) \right]$$

$$+ 4\mu_2^2 m_2 \left[\frac{1}{G} \right]$$

$$+ K \left[\mu_1^2 m_1^2 \left(-1 + \frac{1}{G} \right) \right]$$

$$+ \mu_1 \mu_2 m_1^2 \left(-1 + \frac{1}{G} \right)$$

$$+ 2\mu_1 \mu_2 m_1 m_2 \left(1 + \frac{1}{G} \right) \left[\frac{1}{G} \right]$$

$$+ \left[\mu_1^2 m_1^3 \left(-1 + \frac{1}{G} \right) \right]$$

$$+ \mu_1 \mu_2 m_1^2 m_2 \left(-1 + \frac{1}{G} \right) \left[\frac{1}{G} \right]$$

$$= 0 \quad (38)$$

where G and H are defined by Equations (36) and (37).

Table 1 summarizes the distinctions in the physical properties of the phases used in the equations for the various models.

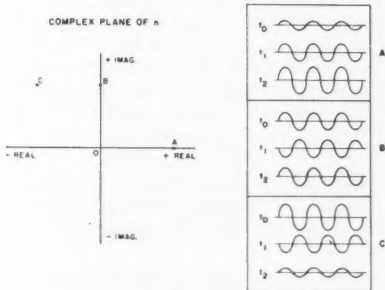


Fig. 2. Significance of n .

TABLE 1

Physical property	Model 1	Model 2 and 2a
ρ_1	ρ_f	$\epsilon \rho_f + (1 - \epsilon) \rho_s$
ρ_2	ρ_f	ρ_f
μ_1	μ_f	μ_b
μ_2	μ_f	μ_f
F_y	$\frac{(1 - \epsilon)(\rho_s - \rho_f)g}{\rho_f}$	0

Equations (28), (31), (32), (33), (35), and (38) are tenth-order polynomials in n , and Equations (29) [a simplified version of (28)] and (34) [a simplified version of (33)] are of the fourth order. Application of the principle of the argument from complex variables allows determination to be made of the location in the complex n plane of roots which satisfy the physical conditions that were introduced through initial and boundary conditions.

The preceding mathematical development was limited to sinusoidal disturbances of some wave length ($\lambda = 2\pi/K$). However, since the differential equations used were linear, arbitrary disturbances may be expected to be handled by Fourier analysis. Questions of convergence in somewhat similar cases are considered in (1).

DISCUSSION

Three aspects of fluidized-bed interfaces deserve special consideration. First, likely sources of interfacial disturbances are commented upon. Second, consideration is given to the physical interpretation of the characteristic n vs. wave-length relations which have been developed, particularly in terms of effect on bubble initiation and bubble stability. Third consideration is given to the relationship between behavior within beds after the bubble initiation has already occurred and the interface is stable.

The analysis to this point has dealt with the problem of how the fluidized-bed system, in particular its interfaces, reacts to disturbances of different wave lengths. The formulation of the problem does not include any statement of how these disturbances may be generated. A number of disturbance sources suggest themselves from the physical arrangements of fluidized beds. Prominently there is the influence of screen or similar bed support which serves to distribute the support fluid at the bed entrance and at the same time imposes a spatially periodic velocity profile at the lower interface. The bed support may introduce some measure of turbulence as a component of disturbance. The support also restricts or prevents net downward motion of particles. The bed support as a contributor to local quality of fluidization has been studied experimentally by Morse and Ballou (6) and by Grohse (2) using bed capacity and X-ray absorption respectively to measure local particle concentration.

Within the bed one may visualize disturbances that range in wave length from the order of individual particle diameter to that of a full bed, the latter being due to gross circulation patterns. Between these likely limits there may be an almost continuous range of disturbance wave lengths owing to grids, baffles, heat exchanger tubes, thermocouple wells, passage of bubbles or slugs, etc. Observation of fluidized beds suggests that behavior in close vicinity to entrance grids is indeed subject to local disturbance contributions by the grids, whereas interfaces in bubbles, slugs, or at the top of the bed, that is, far removed from the grid, are subject to disturbances characteristic of the bulk of the bed; such interfaces are commonly no longer directly influenced by the grid support.

Turning now to the interpretation of stability analyses as applied to fluidized beds, one can see [Equation (19)] that the amplitude of an interfacial disturbance changes exponentially (as e^{nt}). Furthermore the only allowable root for n at the lower interface of the bed (or upper interface of a bubble) is a positive real number [Equations (28), (29), (32), and (35)]. At the upper interface of the bed (or lower interface of a bubble) the allowable roots of n are a complex con-

jugate pair with negative real parts [Equations (31), (33), (34), and (38)]. These particular locations of roots in the complex n plane signify that the lower bed interface is inherently unstable, the size of n being a direct index of magnitude of instability, whereas the upper bed interface is inherently stable. At the latter position the imaginary part of n indicates oscillatory motion (reminiscent of ocean waves) with frequency $I(n)/2\pi$; the real part represents damping of the oscillation. These matters are summarized in Figure 2 which reviews the significance of the location of n in the complex plane for allowable roots in terms of the time variation of a wave from t_0 to t_1 to t_2 . Condition *A* represents an unstable interface with a nonoscillating wave, *B* a neutral oscillating interface, and *C* a stable oscillating interface (that is, with damping).

Unstable Interface

Figures 3 and 4 illustrate typical relations for models 1 and 2 between n and a wave number. The curves were computed to represent diverse gas- and liquid-solid systems known to include different quality characteristics. A maximum value of n appears at some wave length for each system. In their studies of the interface between two normal fluids Bellman and Pennington (1) first reported such a characteristic curve, and they called the wave length corresponding to maximum n the *most dangerous* because the amplitude of the wave corresponding to this disturbance grows more rapidly than all others. As shown in Figures 3 and 4 the maximum is quite broad in some cases.

One immediate conclusion that may be drawn from Figures 3 and 4 is independent of the model of fluidization; the ordering of systems by relative values of n , taken at the maxima, is identical with the ordering of visual quality of fluidization as observed in the laboratory of the authors as well as in those of other investigators. The particular systems considered here are lead shot-air, glass beads-air, Aerocat catalyst-air, lead shot-water, glass beads-water, and Socony-Mobil catalyst-beads-water. Similar ordering occurs if comparisons are made at any given wave length rather than at the wave length corresponding to maximum n . Thus as a first approximation experimental quality of fluidization (or bubbling tendency) is linked with mathematical analysis.

The effect of bed viscosity as a variable is isolated in Figure 5. The sole effect of increasing bed viscosity is to reduce the value of n at higher values of K (that is, the smaller wave lengths) without affecting values of n at longer wave lengths. Thus in the viscosity-insensitive, long-wave-length region of the parametric curves, typical numbers might be 10- or 100-cm. wave lengths, corresponding to K values of about 0.6 and 0.06 cm.⁻¹, respectively. By contrast it is clear that at short wave lengths viscosity does play an important role in stabilizing the interface.

The various properties of unstable interfaces previously discussed also suggest possible behavior within a fluidized bed as well as at the surface. An instability initiated at an interface may grow and develop into a bubble that rises through the bed. Such a bubble

may continue to grow by itself or by chance coalescence with others. If the instability of the system is not large, as in cases known to give particulate fluidization, no recognizable bubbles may develop in the bed. Furthermore the effect of the supporting grid spacing may be explained in terms of the wave length of the primary disturbance produced by the grid. Spacings introducing disturbance wave lengths corresponding to large values of n should tend to lower the quality of fluidization in the vicinity of the grid by more rapidly initiating bubbles, as confirmed by observations (2, 6). With systems of high bed viscosity having extremely poor quality fluidization observations indicate little or no effect of grid spacing. This is consistent with the fact that for such systems the maximum value of n occurs at considerably longer wave lengths than are produced by the usual grid spacings.

On the other hand present analysis may be interpreted as containing elements that act in the direction of reducing bubble size, should it fortuitously become excessive. Large bubbles in gas-solid systems, for example, are observed experimentally to have a raining phenomenon from the roof of the bubble, with pour points at definite position intervals. [See Lewis (3) for analogous behavior with a water-air system.] Such tendencies toward bubble destruction through instability at the upper bubble surface may be discussed in terms of viscosity (Figure 5).

Let there be, for convenience, a bubble that is large compared to the wave length of maximum n for its system. It will also be assumed, as before,

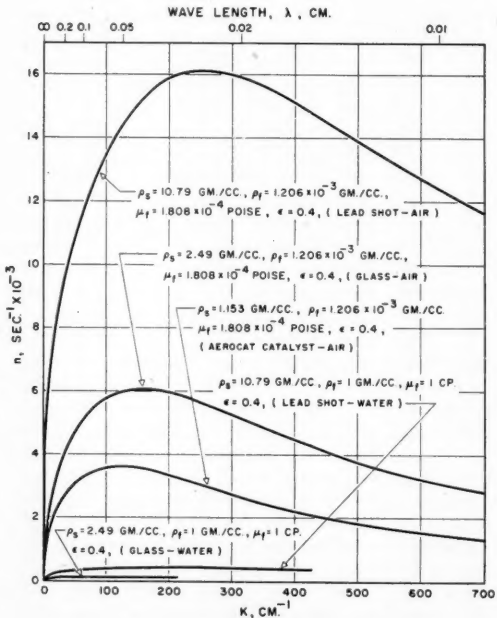


Fig. 3. Typical values of n for model 1, unstable interface.

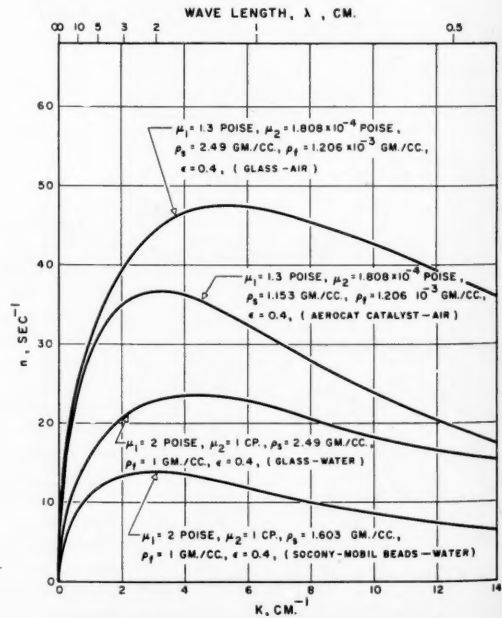


Fig. 4. Typical values of n for model 2, unstable interface.

160
140
120
100
80
60
40
20
0
Fig. 5
that
spon
other
of
Figur
destro
insta
to sm
high
visco
n occ
1 to
7 cen
a wa
than
tion
those
liabili
other
tend
than
tend
tion.
with
Herb
Stabl
Fi
betw
bed)
beca
vari
cons
negat
dam
part
Freq
has
Tay

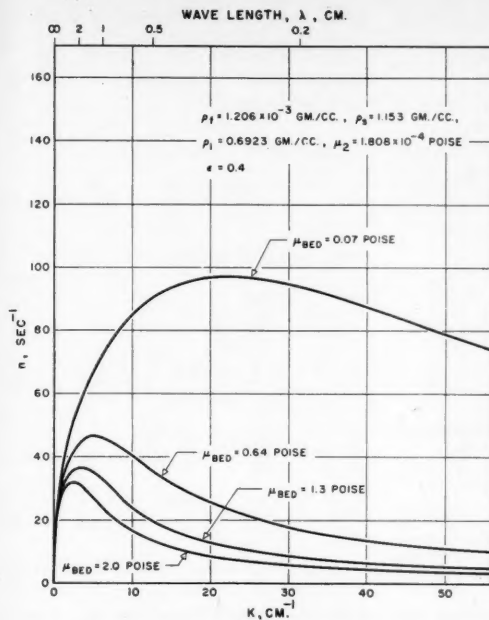


Fig. 5. Effect of bed phase viscosity for model 2 system: Aerocat catalyst-air, unstable interface.

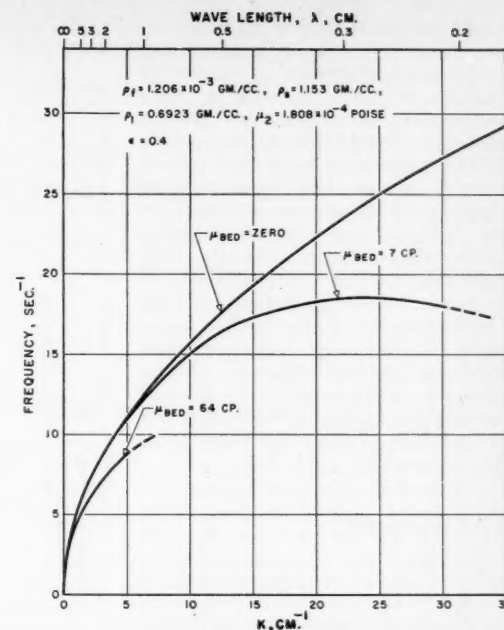


Fig. 6. Effect of bed phase viscosity for model 2 system: Aerocat catalyst-air, stable interface.

that disturbances of wave lengths corresponding to maximum n will outgrow others and predominate, given a spectrum of disturbances. Thus, as noted in Figure 5, low-viscosity beds would favor destruction of the oversize bubble with instabilities on its upper surface leading to smaller entities than would beds of high viscosity. For the three high-viscosity beds in the figure the maximum n occurs for wave lengths in the order of 1 to 2 cm. For the low bed viscosity of 7 centipoises this maximum occurs near a wave length of 0.3 cm. Bubbles larger than 0.3 cm. would be liable to destruction for the latter case; whereas only those larger than 1 or 2 cm. would be liable to destruction for the former. In other words beds of high viscosity would tend to form and maintain larger bubbles than would beds of low viscosity, thus tending toward poorer quality of fluidization. These conclusions are consistent with the reported findings of Matheson, Herbst, and Holt (5).

Stable Interface

Figure 6 illustrates typical relations between n and K for the stable (upper bed) interface by using model 2, selected because it includes bed viscosity as a variable. Roots of n at stable interfaces consist of a complex conjugate pair, the negative real part corresponding to damping of amplitude and the imaginary part to oscillation frequency of the wave. Frequency of the damped wave ($I(n)/2\pi$) has been plotted vs. K . For comparison Taylor's equation (8) for nonviscous fluids

$$\left\{ n = +\sqrt{\frac{[-gK(\rho_1 - \rho_2)]}{[\rho_1 + \rho_2]}} \right\}$$

also is represented. In Table 2 there are assembled all roots for the system properties represented in Figure 6.

TABLE 2. ROOTS OF n FOR THE STABLE INTERFACE (MODEL 2)

System: Aerocat catalyst-air; $\epsilon = 0.4$, $\rho_1 = 1.153$ g./cc., $\rho_2 = 1.206 \times 10^{-3}$ g./cc., $\mu_2 = 1.808 \times 10^{-4}$ poise

K , centi- cm. ⁻¹	μ_1 , poises	n , sec. ⁻¹	
	Taylor equation	Equation (34)	
5	7	$\pm 70i$	$-4.44 \pm 69.1i$
10	7	$\pm 99i$	$-15.4 \pm 94.6i$
20	7	$\pm 140i$	$-46.1 \pm 115.0i$
30	7	$\pm 171i$	$-74.6 \pm 113.2i$
2	64	$\pm 44.2i$	$-5.84 \pm 42.9i$
5	64	$\pm 70i$	$-24.73 \pm 54.9i$

As wave length becomes larger, that is as the wave number approaches zero, damping and frequency both approach zero; thus long waves have a low frequency of oscillation and very little damping, while very short waves are damped rapidly. However, because of the maximum in the frequency-vs.-wave-number relation given in Figure 6, frequency of oscillation tends toward small values at both large and small wave lengths. As bed viscosity is taken to approach zero, the frequency component approaches parabolic form (Taylor equation); that is, the maximum goes to very

high wave numbers. In this limit there is, of course, no damping of an imposed wave.

Figure 6 shows also that bed viscosity is a significant variable in its effect on the wave characteristics of inherently stable upper interfaces of fluidized beds. However possibility of discrimination between frequency values in beds of different viscosities tends to disappear at small wave numbers (large wave lengths). The frequency-wave-number relationships suggest experiments for measuring bed viscosity based upon these relationships and avoiding the necessity of inserting substantial obstructions in the bed, as is customary in some methods. When one assumes that support fluid and particle properties as well as fraction voids are obtainable, viscosity measurements would entail determination of wave lengths for oscillations at a series of definite frequencies produced in the upper surface by means of paddles or similar devices. Actually only one frequency would be needed if the bed phase were a Newtonian fluid, but the use of several different frequencies allows the evaluation of the viscosity for the actual non-Newtonian bed phase.

Solutions of the linearized Navier-Stokes equations presented here relate to the behavior of fluidized-bed interfaces and not to the interior of such beds. However the techniques developed by Morse (6), Grohse (2), and others for determining the quality of fluidization by the capacitance of some region in the bed or the absorption of X-rays along some path through the bed relate directly

to the quality of fluidization within the bed. Nevertheless the indirect approach to the quality of fluidization by stability analysis of the bed interface yields results which show the same dependence on bed properties as the direct approach. The correspondence is not quite perfect, perhaps because full development of bubbles or similar discontinuities involves the nonlinear terms which relate velocity to the rate of change of velocity. Nonlinearities may also be essential in describing bubble interactions, as have been suggested to occur in vortex interaction in the classic fluid mechanical transition problem. However, despite nonlinear effects, empirical relations between the quality of fluidization and the methods of analysis in this paper may be possible.

ACKNOWLEDGMENT

The authors wish to express their appreciation to the Shell Development Company, Emeryville, California, for support of this investigation through an education-research grant. The assistance of Robert Goerss in programming and machine computation in connection with the extraction of roots is acknowledged with thanks.

NOTATION

d = particle diameter, cm.
 g = acceleration of gravity, cm./sec.²
 i = $\sqrt{-1}$
 m = parameter = $+\sqrt{K^2 + \frac{\rho n}{\mu}}$
 n = reciprocal time constant, sec.⁻¹
 p = pressure, g. (mass)/(sec.²)(cm.)
 t = time, sec.
 u = local velocity in x direction
 v = local velocity in y direction
 x = direction along axis of wave, horizontal
 y = direction perpendicular to axis of wave, vertical
 A, B, C, C_1, D = constants
 C' = slip velocity of interface referred to support-fluid phase, a function of the system and ϵ ; positive direction is upward
 F = body force on fluid per unit mass of fluid due to particle friction
 G = function defined in Equation (36)
 H = function defined in Equation (37)
 $I(n)$ = coefficient of imaginary part of n
 K = wave number = $2\pi/\lambda$
 M, N = slip velocity of particles with reference to support fluid in dense bed phase and support fluid phase respectively

Greek Letters

ϵ = fraction voids in bed
 η = interface position
 λ = wave length
 μ = viscosity

ρ = density
 ϕ, ψ = potential functions

Subscripts

0 = at time zero
 0_1 = at interface on bed side
 0_2 = at interface on support fluid side
 1 = dense bed phase or time one
 2 = support fluid phase or time two
 b = actual bed value
 f = support fluid
 v = virtual ($\rho_v = \rho_s + \frac{1}{2}\rho_f$)
 s = solid particle
 x = in x direction
 y = in y direction

LITERATURE CITED

1. Bellman, Richard, and R. H. Pennington, *Quart. Appl. Math.*, **12**, 151 (1954).
2. Grohse, E. W., *A.I.Ch.E. Journal*, **1**, 358 (1955).
3. Lewis, D. J., *Proc. Roy. Soc. (London)*, **A202**, 81 (1950).
4. Long, F. J., M.S. thesis, Princeton University, Princeton, New Jersey, (May, 1952).
5. Matheson, G. L., W. A. Herbst, and P. H. Holt, 2nd, *Ind. Eng. Chem.*, **41**, 1099 (1949).
6. Morse, R. D. and C. O. Ballou, *Chem. Eng. Progr.*, **47**, 199 (1951).
7. Rice, W. J., Ph.D. dissertation, Princeton University, Princeton, New Jersey (1959).
8. Taylor, G. I., *Proc. Roy. Soc. (London)*, **A201**, 192 (1950).
9. Wilhelm, R. H. and Mooson Kwauk, *Chem. Eng. Progr.*, **44**, 201 (1948).

APPENDIX

The linearized equations of motions (2) and (3) for the Taylor type of analysis used earlier in this paper do not permit the explicit introduction of the effect of slip velocity between particles and support fluid upon the behavior of the bed interface. A modified procedure suggested by analyses of flame fronts of Landau (A1) and Markstein (A2) overcomes this difficulty at the expense of satisfying one less condition at the interface between the bed and support fluid. This appendix compares conclusions from the Taylor and Landau types of stability analyses.

The models of beds utilized are the same as were used previously. Linearized equations of continuity and motion are written and applied to an interface initially sinusoidally disturbed as before. An outline of the derivation for the lower bed interface of a model 2 bed follows. (Complete details of derivation are available in reference 7.)

The local horizontal velocity at any point is given by

$$u = U + u' \quad (39)$$

the local vertical velocity by

$$v = V + v' \quad (40)$$

and the pressure by

$$p = P + p' \quad (41)$$

(By comparison the Taylor type of analysis dealt only with the composite u, v , and p .)

Equation of Continuity

$$\frac{\partial u'}{\partial x} + \frac{\partial v'}{\partial y} = 0 \quad (42)$$

Equations of Motion

$$\begin{aligned} \frac{\partial u'}{\partial t} + V \frac{\partial u'}{\partial y} &= -\frac{1}{\rho} \frac{\partial p'}{\partial y} \\ &+ \frac{\mu}{\rho} \left(\frac{\partial^2 u'}{\partial x^2} + \frac{\partial^2 u'}{\partial y^2} \right) \end{aligned} \quad (43)$$

$$\begin{aligned} \frac{\partial v'}{\partial t} + V \frac{\partial v'}{\partial y} &= -\frac{1}{\rho} \frac{\partial p'}{\partial x} \\ &+ \frac{\mu}{\rho} \left(\frac{\partial^2 v'}{\partial x^2} + \frac{\partial^2 v'}{\partial y^2} \right) \end{aligned} \quad (44)$$

It may be noted in passing that the Landau type of formulation leads to the retention, after linearization, of the second, that is, the convective, term in each of the equations of motion, whereas this term disappears in the Taylor type of formulation [Equations (2) and (3)].

Potential functions ϕ and ψ are now defined as

$$u' = -\frac{\partial \phi}{\partial x} - \frac{\partial \psi}{\partial y} \quad (45)$$

$$v' = -\frac{\partial \phi}{\partial y} + \frac{\partial \psi}{\partial x} \quad (46)$$

$$p' = \rho \frac{\partial \phi}{\partial t} \quad (47)$$

with the restrictions

$$\frac{\partial^2 \phi}{\partial x^2} + \frac{\partial^2 \phi}{\partial y^2} = 0 \quad (48)$$

$$\begin{aligned} \frac{\partial \psi}{\partial t} + V \left(\frac{\partial \phi}{\partial x} + \frac{\partial \psi}{\partial y} \right) &= \frac{\mu}{\rho} \left(\frac{\partial^2 \psi}{\partial x^2} + \frac{\partial^2 \psi}{\partial y^2} \right) \end{aligned} \quad (49)$$

To satisfy these equations for the bed phase a solution is written in the following equations:

$$\phi_1 = Ae^{-Kx+nt} \cos Kx \quad (50)$$

$$\begin{aligned} \psi_1 &= Be^{-m_1 x+nt} \sin Kx \\ &- \frac{KV_1 A}{(KV_1 - n)} e^{-Kx+nt} \sin Kx \end{aligned} \quad (51)$$

$$p_1' = \rho_1 \frac{\partial \phi_1}{\partial t} \quad (52)$$

where m_1 , which must be positive, is given by

$$n = V_1 m_1 + \frac{\mu_1}{\rho_1} (m_1^2 - K^2) \quad (53)$$

(41)

e
of
posite

For the support-fluid phase (the lower phase) these equations provide a solution:

$$\phi_2 = Ce^{Kx+n} \cos Kx \quad (54)$$

$$\psi_2 = \frac{V_2 K C}{V_2 K + n} e^{Kx+n} \sin Kx \quad (55)$$

$$p_2' = \rho_2 \frac{\partial \phi_2}{\partial t} \quad (56)$$

The interfacial position may be given by $\eta(x, t)$. Then

$$\begin{aligned} \frac{\partial \eta}{\partial t} &= v_2' = -\frac{\partial \phi_2}{\partial y} + \frac{\partial \psi_2}{\partial x} \\ &= \frac{-KnC}{V_2 K + n} e^{Kx+n} \cos Kx \quad (57) \end{aligned}$$

Hence on integration

$$\eta = \frac{-KC}{V_2 K + n} e^{Kx+n} \cos Kx \quad (58)$$

When one takes

$$\eta_0 = \frac{-KC}{V_2 K + n} e^{Kx} \cos Kx \quad (59)$$

then

$$\frac{\eta}{\eta_0} = e^{n} \quad \text{at any } x \quad (60)$$

To relate the constant n to the wavelength of the surface disturbance, the physical properties of the fluid phases, and the slip velocity between particles and support fluid, the following interfacial boundary conditions are imposed:

$$u_1' + V_1 \frac{\partial \eta}{\partial x} = u_2' + V_2 \frac{\partial \eta}{\partial x} \quad (61)$$

$$v_1' = v_2' \quad (62)$$

$$\begin{aligned} -gy(\rho_1 - \rho_2) + p_1' - 2\mu_1 \frac{\partial v_1'}{\partial y} \\ = p_2' - 2\mu_2 \frac{\partial v_2'}{\partial y} \quad (63) \end{aligned}$$

Since only three conditions can be satisfied at the interface, the choice of the preceding three is dictated by the need to find solutions which degenerate to other previously known limiting solutions. The condition which has been discarded is the equality of the shear stresses on either side of the interface.

By substitution from Equation (45) to (47), (50) to (52), (54) to (56), and (58) into (61) to (63), the following final solution relating n to K and the other physical properties is obtained for model 2

$$\begin{aligned} g(\rho_1 - \rho_2)K + \rho_1 K^2 V_1 (V_1 - V_2) \\ + \mu_1 K^2 (V_1 - V_2) (m_1 - K) \\ + nK(-2\mu_2 K - \rho_2 V_2 - \rho_1 V_1) \\ - 2\mu_1 m_1 - n^2(\rho_1 + \rho_2) = 0 \quad (64) \end{aligned}$$

Similarly for model 1 the final solution is

$$\begin{aligned} gK(1 - \epsilon)(\rho_s - \rho_f) + \rho_f K^2 V_1^2 (1 - \epsilon) \\ + \mu_f K^2 V_1 (1 - \epsilon) (m_1 - K) \\ + nK[-2\mu_f (K + m_1) - \rho_f V_1 (1 + \epsilon)] \\ - 2\rho_f n^2 = 0 \quad (65) \end{aligned}$$

Equation (65) is identical with Equation (29) when $V_1 = 0$.

These solutions apply to the lower bed

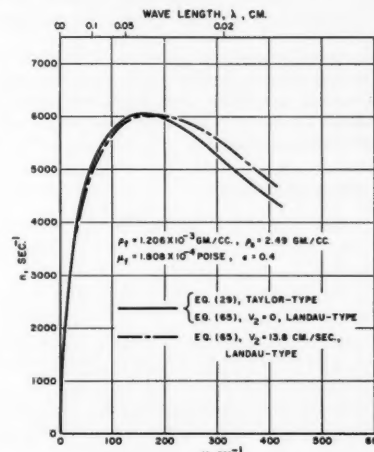


Fig. 7. Comparison of formulations for model-1 system: glass-air, unstable interface for different slip velocities (V_2).

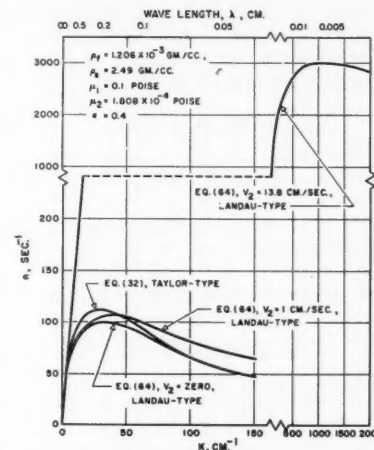


Fig. 8. Comparison of formulations for model-2 system: glass-air, unstable interface for different slip velocities (V_2).

interface, which is unstable; similar equations for the stable, upper bed interface may be obtained in a similar fashion.

Figures 7 and 8 show results of some calculations based on Equations (64) and (65) for fluidization of glass beads in air. Figure 7 compares n vs. K curves for the Taylor type of analysis stemming from Equation (29) with the Landau type, Equation (65), both for model 1. The slip velocity chosen for computation was 13.8 cm./sec. based on the empty column

and corresponding to a velocity somewhat greater than the minimum fluidizing velocity for No. 7 glass beads (diameter = 0.0201 in. or 0.051 cm.), which is 9.15 cm./sec. (9). Even at this rather high slip velocity the difference between the results of the two approaches is very small, the major difference being a slight decrease in n at low K and a slight increase at higher values of K . As previously mentioned, Equation (65) becomes identical with Equation (29) when the slip velocity is zero.

Thus for model 1 in the range of slip velocities encompassing likely fluid-bed behavior the effect of this variable is noted to be small, as indicated by the small difference in the value of n calculated by the two approaches.

Comparisons for model 2 for the results of computations according to the two formulations in question are provided in Figure 8. As a result the following statements may be made:

1. At zero slip velocity ($V_2 = 0$) the Taylor and Landau types of formulations lead to closely similar curve shapes with small vertical displacement between them.

2. In the Landau type of formulation the presence of increasing slip velocities leads to substantial increases in instability, with curve maxima being shifted to increasing values of K . However at the largest value of slip velocity depicted ($V_2 = 13.8$ cm./sec.), the assumptions inherent in model 2 (that is, an emulsion with small slip velocity) became strained and might be considered inconsistent with the model. Thus, as in the case of model 1, model 2 may be concluded (for slip velocities consistent with the model) to be equally well described by the two modes of formulation.

In conclusion the two ways of writing the equations of motion yield results which are very nearly the same for commonly occurring physical situations.

NOTATION

- p' = transient pressure component
- u' = horizontal transient velocity component
- v' = vertical transient velocity component
- P = steady state pressure component
- U = horizontal steady state velocity component
- V = vertical steady state velocity component

LITERATURE CITED

1. Landau, L., *Acta Physicochim. U.R.S.S.*, 19, 77 (1944).
2. Markstein, G. H., *J. Aeronaut. Sci.*, 18, 199 (1951).

Presented at A.I.Ch.E. Chicago meeting. Manuscript received November 29, 1957; revision received April 3, 1958; manuscript accepted April 7, 1958.

Volumetric Properties of Nonpolar Gaseous Mixtures

J. M. PRAUSNITZ and R. D. GUNN

University of California, Berkeley, California

Volumetric data of nonpolar gaseous mixtures are analyzed in terms of the theory of corresponding states. Special attention is given to an analysis of the second virial coefficient and to the calculation of pseudocritical constants.

Second virial coefficients are calculated from experimental data for ten binary systems. These coefficients, with those previously published, are correlated by means of a generalized equation involving three parameters for each component: the critical volume, the reduced temperature, and the acentric factor.

Equations are derived for the pseudocritical temperature and pressure of mixtures. These equations are considerably more accurate than those given by Kay's rule. Because of the complexity of the proposed equations for the pseudocritical parameters, a simplified pseudocritical method is presented which is sufficiently accurate for most chemical engineering purposes, especially at reduced temperatures exceeding 1.3.

Methods are available for predicting with good accuracy the volumetric properties of nonpolar gases in the pure state, but no method of comparable validity has been reported for mixtures of these gases. The volumetric properties of gaseous mixtures not only are of interest for applications similar to those pertaining to pure gases, but they also are required for accurate determination of phase equilibria and for correct specification of the driving force in separation operations and chemical kinetics. In vapor-liquid equilibria, for example, departure from ideal behavior in the gaseous phase at high pressures may be at least as large as that in the liquid phase. The P - V - T - y behavior of a gaseous mixture uniquely determines the fugacity for each component at any particular temperature, pressure, and composition, and the fugacities in turn, determine the equilibrium curve.

Various methods for predicting the properties of gaseous mixtures have been proposed, but for the most part these have been strictly empirical. While such methods have been successful in limited cases, large errors often appear in unexpected instances, demonstrating the basic weakness of a purely empirical approach.

In view of the inadequacy of the present methods this investigation has attempted to develop equations based as much as possible on available theory while remaining within the realm of engineering utility.

The nonideality of gaseous mixtures can be conveniently regarded as consisting of two parts: one part is due to the nonideality of the pure gases and the other to the nonideality of mixing. This paper considers only the second part. The nonideality of pure gases has received much attention previously, and, with the help of corresponding-states correlations, volumetric properties of nonpolar or slightly polar gases can now be predicted accurately. The problem of computing the volumetric properties of a gaseous mixture, therefore, consists of relating the properties of the mixture to the corresponding properties of the pure components.

VIRIAL EQUATION

The volumetric properties of gases are conveniently expressed by an equation of state. The only equation of state with a sound theoretical basis is the virial equation, and, because of its theoretical origin, it is possible to extend this equation to mixtures by establishing an exact relationship between the equation for a mixture and the equations for the pure components. The virial equation is a series in the reciprocal volume

$$z = \frac{PV}{RT} = 1 + \frac{B}{V} + \frac{C}{V^2} + \dots \quad (1)$$

When Equation (1) is applied to a mixture, the virial coefficients are functions of composition as well as temperature. The composition dependence of the virial coefficients is given by (2, 10)

$$B_m = \sum_{ii} y_i y_i B_{ii} \quad (2)$$

$$C_m = \sum_{iik} y_i y_i y_k C_{iik} \quad (3)$$

For a binary mixture Equations (2) and (3) reduce to

$$B_m = y_1^2 B_{11} + 2y_1 y_2 B_{12} + y_2^2 B_{22} \quad (2a)$$

$$C_m = y_1^3 C_{111} + 3y_1^2 y_2 C_{112} + 3y_2^2 y_1 C_{122} + y_2^3 C_{222} \text{ etc.} \quad (3a)$$

B_{11} , C_{11} , B_{22} and C_{222} depend only on the forces acting between like molecules; the remaining coefficients, called *cross coefficients*, depend on the forces acting between unlike molecules.

The nonideality of mixing vanishes only if the following hold for the cross coefficients:

$$B_{12} = \frac{1}{2}(B_{11} + B_{22}) \quad (4)$$

$$C_{112} = \frac{1}{3}(2C_{111} + C_{222}) - (B_{11} - B_{22})^2 \quad (5a)$$

and

$$C_{122} = \frac{1}{3}(C_{111} + 2C_{222}) - (B_{11} - B_{22})^2 \quad (5b)$$

Equations (4) and (5a, b) lead to the following for the virial coefficients for the mixture:

$$B_m = y_1 B_{11} + y_2 B_{22} \quad (6)$$

$$C_m = y_1 C_{111} + y_2 C_{222} - 3y_1 y_2 (B_{11} - B_{22})^2 \quad (7)$$

Equations (6) and (7) and similar equations for the higher virial coefficients are equivalent to Amagat's law of additive volumes or to the identical statement that the compressibility factor of a mixture at constant temperature and pressure is a straight-line function of the composition. This simplification is very rarely valid even for simple gases; to illustrate, Figure 1 shows the observed compressibility factors (11) for mixtures of methane and ethane at 50°C. and 60 atm. Instead of a straight line the plot is a parabola, which is to be expected from Equation (2a), since at this temperature and pressure virial coefficients higher than the second can be neglected.

At moderate densities, where the volumetric properties of gases are adequately described by a virial equation terminating after the second term, the key to the nonideality of mixing lies in the cross coefficient B_{ii} . Compressibility data for mixtures were therefore analyzed to determine these cross coefficients and to relate them to the properties of the pure components. This analysis is described in the next two sections. In a later section the results on second virial coefficients are used to derive formulas for the calculation of pseudocritical constants for gas mixtures.

ANALYSIS OF SECOND-VIRIAL-COEFFICIENT DATA

Volumetric data of ten binary gaseous systems have been analyzed to determine the experimental values of B_{12} at three different compositions, whenever possible, and at several different temperatures. The references and the temperature range for those systems studied are listed in Table 1.

The experimental values used were those at densities less than the pseudo critical density (d_{cm}), which is defined here as

$$d_{cm} = \frac{1}{V_{cm}} = (\sum_i y_i V_{ci})^{-1} \quad (8)$$

1. M.
2. M.
3. M.
4. M.
5. Et.
6. Et.
7. Bu.
8. Ca.
9. Ca.
10. Ca.
11. M.
12. Et.
13. N.
4. Pr.
5. n-
6. i-
7. Pr.
8. C.
1. M.
2. Et.
3. N.
4. M.
5. M.
6. Et.
7. Pr.
8. N.
9. C.
10. H.
11. H.
12. H.
13. H.
The
the
For
was
virial
with
racy
The
the
of a
each
any
by
devia
coeff

TABLE 1. REFERENCES FOR EXPERIMENTAL DATA EMPLOYED

System	Temperature Range, °F.	Reference
<i>A. Volumetric Data for Mixtures</i>		
1. Methane-ethane	32-122	11
2. Methane-propane	100-460	19
3. Methane- <i>n</i> -butane	160-460	21
4. Methane- <i>i</i> -butane	160-460	21
5. Ethane-propylene	220-400	20
6. Ethane-nitrogen	40-460	20
7. Butane-nitrogen	310-400	1
8. Carbon dioxide-nitrogen	77-257	21
9. Carbon dioxide-propane	100-460	20
10. Carbon dioxide- <i>n</i> -butane	220-400	20
<i>B. Volumetric Data or Virial-Coefficient Data for Pure Gases</i>		
1. Methane	100-460	12,22
2. Ethane	100-460	11,22
3. Nitrogen	40-460	8
4. Propane	100-460	19
5. <i>n</i> -Butane	160-460	19
6. <i>i</i> -Butane	160-460	19
7. Propylene	220-460	20
8. Carbon dioxide	100-460	20
<i>C. Published Virial-Coefficient Data</i>		
1. Methane-neopentane	86-266	6
2. Methane-tetramethyl silane	122-266	6
3. Methane-sulfur hexafluoride	104-208	6
4. Methane- <i>n</i> -pentane	100-460	23
5. Methane-carbon dioxide	100-460	23
6. Ethane-carbon dioxide	100-160	23
7. Propylene-carbon dioxide	5-176	7
8. Nitrogen-carbon dioxide	77	12
9. Carbon monoxide-carbon dioxide	77	12
10. Hydrogen-carbon dioxide	77	12
11. Hydrogen-ethylene	77	12
12. Hydrogen-nitrogen	77	12
13. Hydrogen-carbon monoxide	77	12

The volumetric data were represented by the equation

$$V(z-1) = B_m + \frac{C_m}{V} \quad (9)$$

For the range of densities mentioned it was found that the second and third virial coefficients represented the data with an accuracy comparable to the accuracy of the experimental measurements. The virial coefficients were evaluated by the method of least squares with the aid of a high-speed digital computer. After each analysis the residuals were analyzed; any experimental measurements deviating by more than three times the standard deviation were discarded, and the virial coefficients were reevaluated from the

remaining data. To calculate the B_{12} 's from the second virial coefficients for the mixtures the virial coefficients for the pure components must be known. Table 1 also gives the references for the volumetric data used to evaluate the second virial coefficients of the pure components.

In addition to the systems listed in Table 1, an analysis was made of the compressibility data for the binaries methane-*n*-heptane (17), methane-decane (18), hydrogen sulfide-*n*-heptane (19), hydrogen sulfide-decane (19), propane-isopentane (21), propane-benzene (19), and *n*-butane-decane (19). These mixtures were of special interest, since each one consists of two species of considerably different size, the critical volume ratio ranging up to slightly over six. Unfortunately however the data for these systems were not reported at densities sufficiently moderate to use the truncated virial equation, and an indirect method of analysis was used. The compressibility data for these systems were fitted by a set of pseudocritical constants in a manner described previously (16). With these pseudocritical constants it was possible to predict the compressibilities at lower densities and hence to compute the second virial coefficients.

The details of the calculations as well as the complete numerical results are given elsewhere (5). The results obtained were analyzed in terms of the theory of corresponding states as described in the next section.

CORRESPONDING-STATES THEORY FOR MIXTURES

The molecular basis for the theory of corresponding states for pure, simple fluids was discussed by Pitzer about twenty years ago (13), and Guggenheim (4) and others have shown that when the reduced second virial coefficient B/V_c (where V_c is the critical volume) is plotted against the reduced temperature, a universal function is obtained which, to a good approximation, repre-

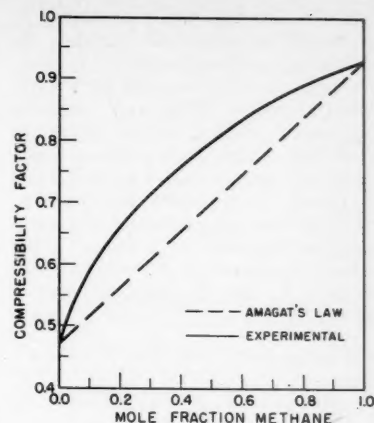


Fig. 1. Compressibility factors for the methane-ethane system at 50°C. and 60 atm.

sents the data for a variety of substances of low molecular weight. It was then shown by Guggenheim and McGlashan (3) that this universal plot could be applied to mixtures by writing

$$\frac{B_{ij}}{V_{cij}} = \theta_B \left(\frac{T}{T_{cij}} \right) \quad (10)$$

For the special case where $i = j$ the characteristic temperature and the characteristic volume become respectively the critical temperature and the critical volume of the pure component. For the case where $i \neq j$ Guggenheim and McGlashan suggested the mixing rules

$$T_{cij} = (T_{cii} T_{cjj})^{1/2} \quad (11)$$

$$V_{cij}^{1/3} = \frac{1}{2} (V_{cii}^{1/3} + V_{cjj}^{1/3}) \quad (12)$$

This extension of the corresponding-states theory to mixtures gives good results for mixtures of light components but progressively worse results as the size of the gas molecules increases. This is not surprising in view of the limitations clearly indicated by Pitzer (13) as in-

TABLE 2. CONSTANTS r AND s^* FOR CALCULATING THE PSEUDOCRITICAL TEMPERATURE

T_r/ω	0		0.25		0.10		0.15		0.20	
	r	s	r	s	r	s	r	s	r	s
1.0	3.197	1.524	4.936	1.718	7.626	1.969	11.79	2.283	18.80	2.725
1.25	2.389	1.420	3.642	1.577	5.483	1.773	8.394	2.033	13.15	2.381
1.50	1.899	1.351	2.871	1.484	4.242	1.645	6.460	1.866	9.897	2.151
2.00	1.326	1.263	1.988	1.364	2.871	1.484	4.317	1.653	6.422	1.862
3.00	0.823	1.175	1.222	1.245	1.708	1.323	2.526	1.439	3.621	1.575
T_r/ω	0.25		0.30		0.35		0.40		0.48	
	r	s	r	s	r	s	r	s	r	s
1.0	31.11	3.333	57.07	4.310	119.47	5.988	352.51	9.901	T_{cm} is given by $\left(\frac{\gamma}{V_{cm}} \right)^{1/2}$	
1.25	21.69	2.882	38.68	3.650	80.91	5.025	227.89	8.065		
1.50	16.26	2.577	28.27	3.205	58.81	4.367	162.66	6.897		
2.00	10.46	2.193	17.66	2.660	36.73	3.571	95.25	5.405		
3.00	5.779	1.802	9.307	2.105	20.47	2.817	46.25	3.937		

*The lower limit of the Pitzer compressibility tables is for a reduced temperature of 0.8. Values of r and s at $T_r = 1.0$ may be used with sufficient accuracy for the range of reduced temperatures of 0.8 to 1.0.

herent in any two-parameter theory of corresponding states. To extend the corresponding-states treatment to pure, nonsimple fluids of nonpolar (or slightly polar) character, Pitzer and coworkers (14) recently showed that the volumetric properties of such fluids could be correlated by introducing one additional parameter. It was found that the compressibilities of a large class of substances could be expressed as functions of the reduced temperature T_r , the reduced pressure P_r , and the acentric factor ω defined by

$$\omega \equiv -\log_{10} P_r$$

$$(\text{saturated at } T_r = 0.7) - 1.00 \quad (13)$$

The acentric factor is a measure of the deviation from simple-fluid behavior; for simple fluids (argon, krypton, xenon, and methane) the acentric factor is zero. These ideas can also be applied to a correlation of second virial coefficient data. Pitzer and Curl (15) showed that for a large number of pure substances the reduced second virial coefficient B_{P_c}/RT_c (where P_c and T_c are the critical pressure and temperature) could be expressed in the form

$$B = B^0 + \omega B' \quad (14)$$

with

$$\frac{B'P_c}{RT_c} = \theta_B^0(T_r)$$

and

$$\frac{B'P_c}{RT_c} = \theta_B'(T_r) \quad (15)$$

The interpretation of second virial coefficient data for mixtures as presented here is based on an extension of the method of Guggenheim and McGlashan within the framework of the three-parameter theory of corresponding states.

In the generalized equation for second virial coefficients reported by Pitzer and Curl [Equation (15)] the virial coefficients

are reduced by the quantity P_c/RT_c rather than by the critical volume. For pure gases the former is preferred because critical pressures are usually more accurately known than critical volumes; however for gaseous mixtures the latter is more convenient because a characteristic critical volume is more readily calculated than a characteristic critical pressure. The characteristic critical volumes and temperatures are each proportional to one of the parameters in the intermolecular potential function for the interaction of dissimilar molecules, whereas the characteristic critical pressure is not directly related to either of these parameters. It was preferable therefore to make the following modification of the Pitzer and Curl equation. By definition the compressibility factor at the critical point is

$$z_c = \frac{P_c V_c}{RT_c} \quad (16)$$

When $B^0/V_c = B_{rv}^0$; $B'/V_c = B_{rv}'$, from Equations (14), (15), and (16)

$$z_c (B_{rv}^0 + \omega B_{rv}') = \theta_B^0 + \omega \theta_B' \quad (17)$$

The compressibility tables reported by Pitzer and coworkers (14) show that the critical compressibility factor is given by

$$z_c = z_c^0 + \omega z_c' = 0.291 - 0.08\omega \quad (18)$$

For simple fluids, which have zero acentric factors, Equation (17) reduces to

$$B_{rv}^0 = \frac{\theta_B^0}{0.291} \quad (17a)$$

When one subtracts Equation (17a) from Equation (17) and rearranges,

$$B_{rv}' = \frac{0.274\theta_B^0 + \theta_B'}{0.291 - 0.08\omega} \quad (19)$$

The extension of the three-parameter theory of corresponding states therefore is of the form

$$\frac{B_{ij}}{V_{c_{ij}}} = B_{rv}^0 \left(\frac{T}{T_{c_{ij}}} \right) + \omega_{ij} B_{rv}' \left(\frac{T}{T_{c_{ij}}} \right) \quad (20)$$

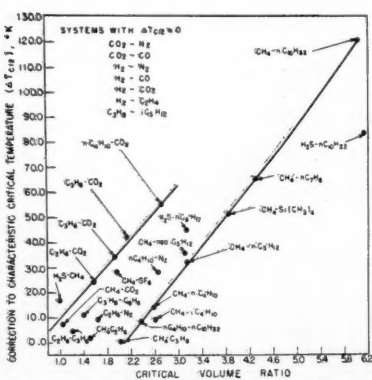


Fig. 2. Corrections to the characteristic critical temperature for several nonpolar gaseous systems.

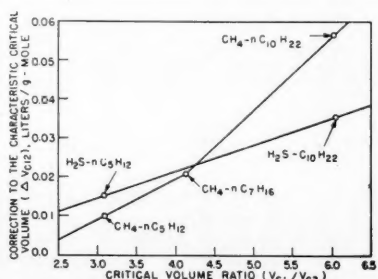


Fig. 3. Correction to the characteristic critical volume ($V_{c_{12}}$) for several systems.

where B_{rv}^0 and B_{rv}' are given by Equations (17a) and (19) respectively.

The accuracy of the experimental B_{12} 's is insufficient to establish unequivocal values for the three parameters ω_{12} , $T_{c_{12}}$, and $V_{c_{12}}$; therefore simple algebraic rules were adopted for two characteristic parameters:

$$\omega_{12} = \frac{1}{2}(\omega_1 + \omega_2) \quad (21)$$

$$V_{c_{12}} = \frac{1}{2}(V_{c_1} + V_{c_2}) \quad (22)$$

The value of $T_{c_{12}}$ was then adjusted to fit the experimental data. Because the acentric-factor correction at reduced temperatures greater than unity is generally, relatively small and often not much greater than the experimental error, it is difficult empirically to obtain an unambiguous expression for the characteristic acentric factor. Of the various simple algebraic combinations Equation (21) appeared to give the best results.

Equation (22) is less conventional than the frequently employed Lorentz combination

$$V_{c_{12}}^{1/3} = \frac{1}{2}(V_{c_1}^{1/3} + V_{c_2}^{1/3}) \quad (23)$$

However, when the ratio of the critical volumes of the pure components (V_{c_1}/V_{c_2}) is close to unity, the numerical difference between the linear combination [Equation (22)] and the Lorentz combination [Equation (23)] is smaller than the experimental error, and when the ratio of the critical volumes is much larger than unity, neither equation can be expected to be very accurate. Of the five gaseous systems studied by Guggenheim and McGlashan the B_{12} values for four systems did not depend significantly on the method chosen for predicting the characteristic critical volume; the linear average and the Lorentz average give almost identical results. The remaining system, the methane-*n*-butane study, will be disregarded, since the virial coefficients used by Guggenheim and McGlashan are believed to be inaccurate.

On the basis of the mixing rules given by Equations (21) and (22) a value of the characteristic critical temperature was chosen for each system such that the experimental values of B_{12} for each temperature agreed with the values calculated by Equation (20).* Within the experimental error these characteristic critical temperatures were constant with respect to temperature. In several cases, for structurally or chemically similar gases, the experimental values of the characteristic critical temperature agreed with those predicted by the Guggenheim method [Equation (11)]. However with increasing difference in size and nature of the molecules the predicted and experimental values diverge.

When

*For hydrogen fictitious critical values were used. These are $T_c = 43.4^\circ\text{K}$, $V_c = 50 \text{ cc./g.-mole}$, and $\omega = 0$.

it was $\Delta T_{c_{12}}$ limit similar shows again pure of the These with criticalical to (V_{c_1}/V_{c_2}) arithmetic of the asymmetric agreement proposed including characteristic shows defined

The volume n -pen decan hydroperatuations are co. Although obtain characture 2 system binary droplets menta critical ethane propene by the correct of crit exceede late this $\Delta T_{c_{12}}$ critical aliphatic. For ing ve characteristic less the heim nature is ether functi

$$\Delta T_{c_{12}} = (T_{c_1} T_{c_2})^{1/2}$$

$$- T_{c_{12}} \text{ (experimental)} \quad (24)$$

it was found for all cases studied that $\Delta T_{c_{12}}$ was positive, becoming zero in the limit when the two components were of similar size and chemical nature. Figure 2 shows a plot of the correction $\Delta T_{c_{12}}$ against the critical volume ratio of the pure components with the critical volume of the larger component in the numerator. These data indicate that for mixtures with components of widely different critical volumes the characteristic critical temperature is always less than that given by the geometric mean of the pure-component critical temperatures.

When the ratio of critical volumes (V_{c_1}/V_{c_2}) exceeds three, the characteristic critical volume is no longer quite the arithmetic average of the critical volumes of the pure components. For these highly asymmetric systems it was found that agreement within the general framework proposed here could be improved by including a small correction term for the characteristic critical volume. Figure 3 shows a plot of this correction ($\Delta V_{c_{12}}$) defined by

$$\Delta V_{c_{12}} = \frac{1}{2}(V_{c_1} + V_{c_2}) - V_{c_{12}} \text{ (experimental)} \quad (25)$$

The corrections were calculated from volumetric data for the systems methane-*n*-pentane, methane-*n*-heptane, methane-decane, hydrogen sulfide-*n*-pentane, and hydrogen sulfide-decane. Like the temperature corrections the volume corrections are always positive; however they are considerably less important.

Although it appeared impossible to obtain a unique correlation for the characteristic critical temperatures, Figure 2 shows that families of related systems obey definite trends. For example, binary mixtures containing aliphatic hydrocarbons will be considered. Experimental values for the characteristic critical temperature for the methane-ethane system and for the methane-propane system agree with those predicted by the Guggenheim method, and the correction $\Delta T_{c_{12}}$ is zero. When the ratio of critical volumes of the components exceeds two, the experimental and calculated critical temperatures diverge. For this family of systems the correction $\Delta T_{c_{12}}$ is nearly a linear function of the critical volume ratio (Figure 2). Similar behavior is observed for mixtures of aliphatic hydrocarbons with carbon dioxide.

For nonpolar gaseous systems containing very dissimilar molecules the characteristic critical temperature is consistently less than that predicted by the Guggenheim method. Since the critical temperature is proportional to the energy parameter in the intermolecular potential function, the low values for $T_{c_{12}}$ indicate

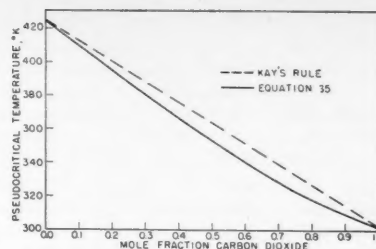


Fig. 4. Pseudocritical temperature for the carbon dioxide-*n*-butane system at a reduced temperature of 1.0.

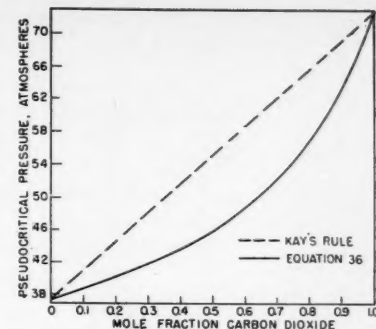


Fig. 5. Pseudocritical pressure for the carbon dioxide-*n*-butane system at a reduced temperature of 1.0.

that the energy parameter corresponding to the interaction between two dissimilar molecules is smaller than that predicted by the geometric mean. This behavior is to be expected for systems whenever the dominant intermolecular forces are dispersion forces. In his original paper on dispersion forces London (9) showed that the energy of interaction between unlike molecules of different sizes is always less than the product of the square roots of the pure-component energies, the geometric mean being an upper limit which is approached only as the sizes of the unlike molecules become identical. The experimental results shown in Figure 2 are therefore in complete qualitative agreement with London's theory.

Although the use of corresponding-states theory does not correlate the available data as completely as might be desired, it is nevertheless possible to make a very good estimate of the second virial coefficient of any binary or multi-component gas mixture containing nonpolar (or slightly polar) components. With the help of Figure 2 corrections to the characteristic critical temperature can be estimated for most binary interactions, and in highly asymmetric systems a small, relatively unimportant correction can be estimated from Figure 3. These corrections, in conjunction with the critical temperatures, critical volumes, and acentric factors of the pure components, define the characteristic parameters by which corresponding states theory for pure gases and vapors can be extended to their mixtures.

CALCULATION OF PSEUDOCRITICAL CONSTANTS

The pseudocritical constants for a mixture are defined in such a way that, when applied to the generalized-compressibility-factor tables, they predict the correct compressibility factor for the mixture; that is, the reduced temperature and pressure for a mixture are given by

$$T_r = \frac{T}{T_{c_m}} \quad (26)$$

$$P_r = \frac{P}{P_{c_m}} \quad (27)$$

The reduced temperature and pressure in conjunction with the Pitzer compressibility tables correctly predict the volumetric behavior of the gaseous mixture at the temperature and pressure under consideration; to utilize the Pitzer tables an acentric factor is also required. For a mixture an acentric factor ω_m can be calculated by

$$\omega_m = \sum_i y_i \omega_i \quad (28)$$

This rule has no basis in theory; however since the correction to the compressibility factor owing to the acentric factor is generally quite small, the method of averaging the acentric factors of the pure components in a mixture is relatively unimportant.

The pseudocritical temperature and pressure can be determined conveniently from volumetric data in a manner described previously (16). This was done for a variety of binary systems, and it was found (16) that these pseudocritical parameters are predicted with only low accuracy by the simple linear equations known as *Kay's Rule*.

PREDICTION OF THE PSEUDOCRITICAL CONSTANTS

Because the pseudocritical temperature is such a complicated function of the composition, it appears necessary to include some information on the nature of the interaction between unlike molecules in any successful method of prediction. The equations for the second virial coefficient of a mixture provide a convenient theoretical base from which the equation for the pseudocritical temperature can be derived. As discussed earlier the second virial coefficient for a mixture is a quadratic function of the mole fractions of the components [Equation (2)], where the virial coefficients with like subscripts are those of the pure components and the virial coefficients with unlike subscripts are those arising from the interaction of pairs of unlike molecules.

Equation (2) forms the theoretical basis on which the prediction of pseudo-

TABLE 3. SUMMARY OF CALCULATED COMPRESSIBILITY FACTORS FOR VARIOUS SYSTEMS

System	Number of mixtures	Temperature range, °K.	Pressure range, atm.	Number of points	% Deviation from experimental values		
					Maximum deviation	Kay's P.p.m.* Rule	Average deviation
H ₂ S-CH ₄	3	278-444	119-544	16	2.8	—	1.0
H ₂ S-nC ₄ H ₁₂	3	444	41-544	10	5.5	18.8	2.0
H ₂ S-C ₁₀ H ₂₂	3	380-444	27-476	13	1.4	—	0.7
CO ₂ -H ₂	2	273-473	200-500	8	2.2	7.9	1.3
CO ₂ -nC ₄ H ₁₀	16	344-411	34-476	19	2.2	26.1	1.0
C ₆ H ₆ -C ₆ H ₆	2	511	34-408	7	2.6	—	0.9
CH ₄ -C ₁₀ H ₂₂	3	377-511	102-306	9	2.6	—	1.3
CH ₄ -nC ₅ H ₁₂	3	311-511	54-340	16	2.6	7.9	0.4
(CH ₄ -nC ₄ H ₁₀ -C ₁₀ H ₂₂)	2	344-511	85-306	11	0.9	7.4	0.4
H ₂ -N ₂ -CO ₂							
CO-CH ₄	1	278-344	136-272	4	0.4	4.3	0.2
							2.8

*P.p.m. = proposed pseudocritical method.

critical constants is based. When one uses Equation (2) together with a modification of the equation of Pitzer and Curl (15), expressions have been derived for the pseudocritical temperature, volume, and pressure of a mixture having an arbitrary number of components. The details of the derivation are presented elsewhere,* only the results are given below.

PROCEDURE FOR COMPUTING PSEUDOCRITICAL CONSTANTS

1. After the critical temperature, critical volume, and the acentric factor for each component have been obtained, the characteristic critical temperatures and volumes for all possible different pairs of components are calculated from the following equations:

$$T_{c_{ij}} = (T_{ci} T_{cj})^{1/2} - \Delta T_{c_{ij}} \quad (29)$$

$$V_{c_{ij}} = \frac{1}{2}(V_{ci} + V_{cj}) - \Delta V_{c_{ij}} \quad (30)$$

The appropriate $\Delta T_{c_{ij}}$ and $\Delta V_{c_{ij}}$ corrections, if required, may be estimated from Figures 2 and 3. The correction $\Delta V_{c_{ij}}$ is needed only in highly asymmetric cases, and even then it is small (7).

2. The pseudocritical volume and the acentric factor for the mixture are computed from

$$V_{cm} = \sum_{ij} y_i y_j V_{c_{ij}} \quad (31)$$

$$\omega_m = \sum_i y_i \omega_i \quad (32)$$

3. Quantities β and γ are computed:

$$\beta = \sum_{ij} y_i y_j (V_c T_c)_{ij} \quad (33)$$

$$\gamma = \sum_{ij} y_i y_j (V_c T_c^2)_{ij} \quad (34)$$

4. The pseudocritical temperature is calculated:

$$T_{cm} = \frac{\beta + \sqrt{\beta^2 + r V_{cm} \gamma}}{2s V_{cm}} \quad (35)$$

*Tabular material has been deposited as document 5767 with the American Documentation Institute, Photoduplication Service, Library of Congress, Washington 25, D. C., and may be obtained for \$2.50 for photoprints or \$1.75 for 35-mm. microfilm.

Constants r and s are obtained from Table 2. To use this table a preliminary value of the reduced temperature is required. It may be approximated with sufficient accuracy by $T_c / (\beta / V_{cm})$.

5. The pseudocritical pressure is

$$P_{cm} = \frac{RT_{cm}}{V_{cm}} \sum_i y_i z_{ci} \quad (36)$$

The proposed method requires a knowledge of the critical volumes of all components in the mixture. Critical volumes are difficult to determine experimentally; whenever reliable values of the critical volume are not available, it is best to compute them from the more accurately known critical temperature, critical pressure, and acentric factor [Equations (16) and (18)]. Critical volumes computed in this way are accurate to better than 2% for almost all cases.

COMPARISON OF PREDICTED AND EXPERIMENTAL COMPRESSIBILITY FACTORS

Compressibility factors have been calculated by using Kay's Rule and the preceding equations; the calculated values are compared with the experimental ones for ten different nonpolar systems, including one ternary and one five-component system. The comparisons are made mainly at high pressures because at these pressures the discrepancies between calculated and experimental compressibility factors are greatest and the severest test is placed upon any correlation. A summary of the results for these ten systems* is presented in Table 3. With one exception the compressibility factors predicted by the proposed pseudocritical method agree within 3.0% or less of the experimental values. Kay's Rule is decidedly less accurate, although in many examples it is sufficiently accurate for engineering calculations. The results show that the proposed pseudocritical method is successful in both liquid and gaseous phases throughout the entire

*Detailed results for these ten systems are given elsewhere (5).

range of the Pitzer compressibility tables from reduced temperatures of 0.8 to 4.0 and from reduced pressures of 0.2 to 9.0.

The *n*-butane-carbon dioxide system was subjected to special calculations. Kay's Rule and the pseudocritical method proposed here were tested for accuracy in predicting the volumetric behavior in both liquid and gaseous phases at the two-phase boundary at pressures of 500 to 1,100 lb./sq. in. abs. Maximum deviation for the proposed pseudocritical method for both phases is 2.2%; for the liquid phase Kay's Rule gives very poor agreement with 26% error in one case. In the gas phase at moderate pressures there is a fortunate cancellation of the errors owing to the wrong pseudocritical pressure, and agreement is better than in the liquid phase; at high pressures in the gaseous phase this cancellation is not effective, and errors are again very large. The over-all average error of Kay's Rule is slightly more than 10%. Figures 4 and 5 show the composition dependence of the pseudocritical temperature and of the pseudocritical pressure according to Kay's Rule and the equations derived in this work. The large disagreement in the pseudocritical pressure as predicted by the two methods illustrates the main reason why Kay's Rule is so inaccurate for this system.

The proposed method for calculating the pseudocritical constants is considerably more accurate than Kay's Rule. Of course in all cases the $\Delta T_{c_{ij}}$ correction for the characteristic critical temperature was obtained from virial coefficients or other volumetric data as explained earlier. When such data are not available, the characteristic temperature correction (and for highly asymmetric systems the volume correction) must be estimated, and the method proposed here is necessarily somewhat dependent on the accuracy of such estimates.

MIXTURES WITH HYDROGEN

Mixtures containing hydrogen must be treated with caution. At 100°C. the reduced temperature of hydrogen exceeds 8.0, twice the range of validity of the virial equations used to derive the pseudocritical method. Compressibility factors for two hydrogen-containing systems reported in Table 3 were predicted with excellent accuracy; however the mixtures were at high reduced temperatures, where the compressibility factors are relatively insensitive to errors in the pseudocritical constants. Because the reduced temperature of hydrogen at room temperatures is beyond the range of validity of the virial equations used, the predicted pseudocritical parameters for hydrogen-containing systems may be less accurate than those for other systems.

Owing to quantum effects, pseudocritical parameters instead of the experimental critical constants are used for

hydrogenation. pseudocritical pseudocritical and an

SIMPLIFI

The p a fairly for calcu

accuracy for rap

critical pseudoc

Kay's R that, for the line

perature combin

pseudo

deviations

experi

contain

differen

ten sys

is 7%

pressur

50% in

sulfide

several

all ten

that the

Rule w

rac

T

P

For mo

rules s

The m

of criti

ratio o

of 3.2

system

widely

Kay's

perat

As s

5%

in

produ

pressure

show t

reduc

in 5 to

lated o

temper

reduc

theref

Kay's

The s

respect

ture a

compon

predic

hydrogen in a corresponding-states correlation. The recommended values are a pseudocritical temperature of 43.4°K., a pseudocritical volume of 50 cc./g.-mole, and an acentric factor of zero.

SIMPLIFIED PSEUDOCRITICAL METHOD

The proposed pseudocritical method is a fairly complicated procedure; therefore for calculations in which only moderate accuracy is required a method is desired for rapidly approximating the pseudocritical constants. Comparison of the pseudocritical constants predicted by Kay's Rule and those proposed here shows that, for the ten systems listed in Table 3, the linear combination of critical temperatures is more accurate than the linear combination of critical pressures. For the pseudocritical temperature the maximum deviation of Kay's linear rule from the experimental value occurs for systems containing components with extremely different critical temperatures. For the ten systems studied the greatest deviation is 7%. The linear combination of critical pressures is much worse, being more than 50% in error for the system hydrogen sulfide-decane and as much as 20% for several other systems. The linear combination of critical volumes however is accurate to within better than 4% for all ten systems. Therefore it is proposed that the following modifications of Kay's Rule will considerably increase its accuracy:

$$\omega_m = \sum_i y_i \omega_i \quad (37)$$

$$T_{cm} = \sum_i y_i T_{ci} \quad (38)$$

$$P_{cm} = \frac{RT_{cm}}{\sum_i y_i V_{ci}} \quad (39)$$

For most nonpolar mixtures the last two rules should be accurate to within 5%. The methane-decane system with a ratio of critical volumes, V_{c1}/V_{c2} , of 6.1 and a ratio of critical temperatures, T_{c1}/T_{c2} , of 3.2 represents an extreme example of a system containing components with widely different critical constants; yet Kay's Rule for the pseudocritical temperature is in error by only 7%.

As shown in Equation (39) an error of 5% in the pseudocritical temperature produces an error of 5% in the critical pressure. The Pitzer compressibility tables show that an error of about 5% in the reduced temperature and pressure result in 5 to 6% maximum error in the calculated compressibility factors for reduced temperatures of 1.3 and above. In the reduced-temperature range above 1.3 therefore the proposed modification of Kay's Rule should be quite satisfactory. The smaller the difference between the respective values of the critical temperatures and the critical volumes of the pure components, the more accurate are the predicted pseudocritical constants as

predicted by any of the methods discussed here, particularly if the T_{ci} corrections are small. The propane-benzene system is an example of this, since the ratio of critical volumes is only 1.3 and the ratio of critical temperatures is 1.5. In spite of the great dissimilarities in the molecular structure of the two compounds the errors in the pseudocritical constants predicted by Kay's Rule are actually negligible.

The simplified pseudocritical method is satisfactory for a majority of practical cases; however near the critical region it cannot be expected to be accurate generally, and more complicated procedures are required.

PREDICTION OF PHASE BEHAVIOR

The pseudocritical method developed in this work appears to represent the volumetric properties of a variety of mixtures with good accuracy in both gas and liquid phases. It should therefore be possible to compute the fugacities of all components in the mixture. The form of Equations (29) to (36) is not very convenient for such computations, but in principle the method developed here should be useful in the prediction of phase equilibria.

ACKNOWLEDGMENT

The authors are grateful to Dean K. S. Pitzer for his interest in this work and to the American Petroleum Institute for their financial aid in the form of a summer grant.

NOTATION

B, C, D = second, third, and fourth virial coefficients which are functions of temperature and composition

d	= molar density
P	= pressure
P_{c1}	= characteristic critical pressure
P_{cm}	= pseudocritical pressure
P_r	= reduced pressure
R	= universal gas constant
r, s	= parameters in pseudocritical temperature equation
T	= temperature
T_{ci}	= characteristic critical temperature
ΔT_{ci}	= correction to characteristic critical temperature
T_{cii}	= temperature characteristic of interaction between molecule of species i and molecule of species j
T_{cm}	= pseudocritical temperature
T_r	= reduced temperature
V	= volume
V_{ci}	= characteristic critical volume
ΔV_{ci}	= correction to characteristic volume
V_{cii}	= volume characteristic of interaction between molecule of species i and molecule of species j

y_i	= mole fraction of component i
z	= compressibility factor

Greek Letters

α	= $\sum_{ij} y_i y_j V_{cii}$
β	= $\sum_{ij} y_i y_j (V_c T_c)_{ij}$
γ	= $\sum_{ij} y_i y_j (V_c T_c^2)_{ij}$
θ_B	= generalized universal function for second virial coefficient
ω	= acentric factor

Subscripts

c	= critical
i, j, k	= components i, j , and k
$1, 2$	= components 1 and 2
m	= property for a mixture and signifies that quantity is for mixture as whole
r	= reduced, dimensionless property

LITERATURE CITED

1. Evans, R. B., and G. M. Watson, *Ind. Eng. Chem. Data Series*, **1**, 67 (1956).
2. Fuchs, Klaus, *Proc. Roy. Soc. (London)*, **A179**, 408 (1941).
3. Guggenheim, E. A., and M. L. Mc-
Glashan, *Proc. Roy. Soc. (London)*, **A206**, 448 (1951).
4. Guggenheim, E. A., *Rev. Pure and
Appl. Chem.*, **3**, 13 (1953).
5. Gunn, R. D., M.S. thesis, Univ. Calif.,
Berkeley (1958).
6. Hamann, S. D., J. A. Lambert, and
P. B. Thomas, *Australian J. Chem.*, **8**,
149 (1955).
7. Haselden, G. G., et al., *Proc. Roy. Soc.
(London)*, **A240**, 1 (1957).
8. Hilsenrath, Joseph, *Tables of Thermal
Prop. of Gases*, National Bureau of
Standards Circular 564 (1955).
9. London, Fritz, *Z. phys. Chem.*, **B11**, 235
(1930).
10. Mayer, J. E., *J. Phys. Chem.*, **43**, 71
(1939).
11. Michels, Antonius, and G. W. Neder-
bragt, *Physica*, **6**, 656 (1939).
12. Michels, Antonius and A. J. H. Boer-
boom, *Bull. soc. chim. Belges*, **62**, 119
(1953).
13. Pitzer, K. S., *J. Chem. Phys.*, **7**, 583
(1939).
14. —, et al., *J. Am. Soc.*, **77**, 3427
(1955).
15. —, and R. F. Curl, Jr., *ibid.*, **79**,
1269 (1957).
16. Prausnitz, J. M., and R. D. Gunn,
to be published.
17. Reamer, H. H., B. H. Sage, and W. N.
Lacey, *Ind. Eng. Chem. Data Series*, **1**,
29 (1957).
18. Sage, B. H., and W. N. Lacey, "Ther-
modynamic Properties of the Lighter
Paraffin Hydrocarbons," Am. Petrol.
Inst., New York (1950).
19. —, "Some Properties of the
Lighter Hydrocarbons," Am. Petrol.
Inst., New York (1955).
20. Tang, W. K., *Tech. Rept. WIS-OOR-13*,
Univ. Wisconsin (1956).
21. Zaalishvili, S. D., *Uspekhi Khim.*,
24, 759 (1955).
22. —, *Zhur. Fiz. Khim.*, **30**, 1891
(1956).

Manuscript received February 27, 1958; revision received June 16, 1958; manuscript accepted June 20, 1958.

Kinetics of Steady State Phase Transitions

A fundamental investigation of the departure from equilibrium in steady-state phase transitions has been made in terms of irreversible thermodynamics and absolute rate theory. The present status of the concept of accommodation coefficients was reviewed and hypotheses were advanced for the reconciliation of opposing viewpoints. Formulas for the magnitude of the departure from equilibrium were derived for single- and multi-component systems. The deviation from equilibrium appeared to be small for ordinary rates of phase change, but interpretation of the available data was hampered by lack of a detailed molecular picture of the phase-change process.

The purpose of the present treatment is to investigate the thermodynamics and kinetics of steady-state phase transitions from a fundamental point of view, to ascertain the nature and magnitude of the departure from equilibrium. On examination of the nature of phase transitions, it appears obvious that an interface across which a net flow of matter is occurring cannot be in equilibrium. An example is a closed container of a pure liquid in equilibrium with its vapor and governed by the usual equilibrium relations, that is, equal chemical potentials in both phases. A necessary corollary of equilibrium is that the system be in a time-invariant condition; that is, the rates of evaporation and condensation at the liquid surface must be equal. However if one imagines the ends of the container removed and liquid supplied at one end and vapor removed at the other, one or both of the rates must change. Thus the conventional equilibrium conditions, such as the Clausius-Clapeyron equation, should not apply. A relatively simple treatment should still be possible if a steady state can be assumed. A steady (or stationary) state is the time-invariant condition of an open system, in contrast to equilibrium, the time-invariant condition of a closed system. *A priori*, it would be expected that the departure from equilibrium would be small in view of the very large (unidirectional) rates of most phase changes relative to net rates of mass transfer between phases; however, the departure would also be expected to be greater for high rates of material flow in particular cases of interest, for example, propellant burning. An example of the model considered above is given in the work on burning ethyl nitrate by Hildenbrand and others (1), who measured the surface temperature at sufficiently low rates (~ 0.1 cm./cm./sec.) to ensure meaningful thermocouple measurements and found it to be about 30°C . less than the corresponding boiling point at the bomb pressure. (The ethyl nitrate apparently volatilizes intact below about 10 atm.) The difference is not especially quantitative in view of the uncertainty of the surface location, but it does indicate a measurable departure from equilibrium conditions. The difference would be expected to be greater for higher burning rates.

A fundamental treatment of steady-state phase transitions will have wide

application not only in propellant burning but also in conventional mass transfer processes such as extraction, humidification, and distillation. A usual assumption in these latter processes is thermodynamic equilibrium at the transfer interface. There have been numerous attempts to investigate this assumption, but none have employed the recent developments in steady-state irreversible thermodynamics.

A result which may be interpreted as the maximum rate of evaporation from a surface at equilibrium is given by the Knudsen equation (2):

$$G = \alpha \left(\frac{W}{2\pi RT} \right)^{1/2} P \quad (1)$$

This relation comes from kinetic theory and gives the number of molecules striking (and remaining on) the surface. Hence it may be equated to the evaporation rate *only* at equilibrium. The accommodation coefficient is the ratio of the actual rate to the number of molecules striking the surface. Unfortunately, there is no way to predict it *a priori*.

Apparently the only previous attempt at a fundamental study of nonequilibrium at phase interfaces was that of Schrage (3), who recognized the necessity of such a situation and developed many interesting ideas. The significance of his results, however, is lessened by several questionable assumptions, notably that the departure from equilibrium in the gas phase may still be found from an equilibrium velocity-distribution function, with a consequent modification of the rate of condensation. Also, he employs classical kinetic theory throughout, effectively limiting the treatment to monoatomic molecules and excluding the more powerful and searching techniques of absolute-rate theory. Penner, from absolute-rate theory (4), derived an expression for the (unilateral) rate of evaporation which agreed with the Knudsen equation within a factor of e . The activated complex was assumed to be a molecule moving gaslike in two degrees of freedom in an area $(V^*)^{2/3}$. The other translational degree of freedom is along the reaction coordinate. The internal degrees of freedom are, at first, assumed to be equal in the initial state and activated complex. The simple free-volume theory is used for the initial liquid state.

KENNETH A. WILDE

Rohm and Haas Company, Huntsville, Alabama

The result is an equation for the rate of evaporation larger than the Knudsen equation by a factor of e . Penner attributes this to lack of equilibrium between the initial state and the activated complex (a fundamental postulate of rate theory) and employs Hirschfelder's simple, non-equilibrium rate theory (5), which reduces the rate by a factor of approximately $1/e$. However, as Penner notes, there are no compelling reasons for using Hirschfelder's particular nonequilibrium formulation (between initial state and activated complex, *not* the general steady-state departure from equilibrium). It would seem that there are better places to look to improve the simple-rate-theory picture: the nature of the activated complex, the detailed molecular picture of the evaporation process, and improvements in the description of the liquid state. If a good expression for the evaporation process is obtained, it should be possible to relate the transmission coefficient of rate theory to the accommodation coefficient of the Knudsen equation.

The question as to whether the accommodation coefficient is close to unity or appreciably less has been the subject of much discussion and experimentation since the advent of the Knudsen equation (ca. 1880). Schrage has reviewed the older literature and concludes that the evidence for an accommodation coefficient less than unity is unreliable. Some careful and thorough work by Hickman and coworkers (6) on the absolute rate of vaporization of glycerol, water, and high-boiling phthalate esters in high-vacuum falling-film stills indicates that the accommodation coefficient is essentially unity, even for polar molecules such as glycerol and water, at least for a moving, fresh surface. They found that the vacuum-evaporation rate decreased markedly if the surface was contaminated or not continually renewed. This observation explains the low results obtained with many "stagnant" surfaces in the past. Penner, on the other hand, has drawn attention to the quantitative correlation between the accommodation coefficient as measured by several different workers, techniques for stagnant systems, and the free-angle ratio of Eyring and Kincaid (7). In a rough model the free-angle ratio may be interpreted as the ratio of the rotational partition function in the gas and liquid phase and thus is a measure of the hindered rotation of polar molecules in the liquid. It may be found by several methods, the most reliable being the comparison of free volumes from vapor

pressure
former
rotati
latter
rate th
ratio b
equati
panyin
obtai

Liquid
CCl₄
C₆H₆
CHCl₃
C₂H₅OH
CH₃OH
H₂O
glycer

The
ently
oratio
hypot
(or su
cases
the ev
heat
by ra
Little
sized
that a
found
alcoh
degree
subsidi
suppor
in ev
chang
which
suppl
order
exists
molec
hindri
surfa
renew
disapp
norma
Kaud
hydro
mass
Emm
gas a
the a
less p
of th
appar
of th
porta

BASIC
ONE-C

In
steadi
but n
be va
relati
found
reacti
confu

pressure and velocity-of-sound data. The former should include the hindered rotation (or vibration) effect, but the latter should not. In Penner's absolute-rate theory of evaporation, the free-angle ratio becomes a multiplier of the Knudsen equation [Equation (1)]. The accompanying table illustrates the agreement obtained (8).

Liquid	Experimental Accommodation coefficient	Theoretical Free-angle ratio
CCl_4	1.0	1.0
C_6H_6	0.90	0.85
CHCl_3	0.16	0.54
$\text{C}_2\text{H}_5\text{OH}$	0.020	0.018
CH_3OH	0.045	0.048
H_2O	0.036-0.040	0.04
glycerol	0.052-0.105	0.077

These two well-substantiated but apparently conflicting situations for the evaporation can be explained by either of two hypotheses. (1) The lowered evaporation (or sublimation) rate is due in many cases to a lowering of the temperature of the evaporating surface because of the heat of vaporization, which is supplied by radiation from the surroundings. Littlewood and Rideal (9) have emphasized this point of view and have shown that the *accommodation coefficients* they found for several long-chain acids and alcohols could be explained by a few degrees of temperature difference. Other subsidiary experiments are cited to support this contention, such as the rise in evaporation rate when the phase change took place on a mercury droplet, which presumably improved the heat supply to the surface. (2) Alternately, an ordered layer (of unknown thickness) exists on stagnant surfaces of polar molecules which exhibits the expected hindrance to evaporation, but as the surface becomes turbulent or is constantly renewed some of the liquid forces disappear and the evaporation becomes normal, that is, approaches the maximum Knudsen rate. Thus there should be a hydrodynamic effect on the interphase mass transfer, at least for polar liquids. Emmert and Pigford (10), in studying gas absorption in flowing liquids, found the accommodation coefficient more or less proportional to the Reynolds number of the flowing liquid (water). It is not apparent why the molecular constitution of the condensed phase should be important for liquids and not for solids.

BASIC RELATIONS FOR A ONE-COMPONENT SYSTEM

Initially a pure liquid evaporating in a steady-state system will be considered, but many of the relations developed will be valid for any phase transition. Two relatively uncommon variables will be found convenient: ξ , the progress of reaction, and A , the affinity (not to be confused with the Helmholtz free energy);

both parameters were introduced by DeDonder (11, 12) in his formulation of thermodynamics to include the irreversibility of chemical reactions. ξ usually describes the fractional extent of completion of a chemical reaction but may be used with physical transformations such as phase changes and order-disorder transitions in alloys. The affinity A is a thermodynamic state function which is closely related to the irreversibility in the system, owing to the chemical reaction of certain physical changes as above. It is defined by

$$dQ' = Ad\xi \geq 0 \quad (2)$$

where dQ' is the quantity needed to make the Second Law an equality. For a reversible process

$$dS = dQ/T$$

dQ' is then defined by

$$dS - \frac{dQ}{T} = \frac{dQ'}{T} > 0 \quad (3)$$

for an irreversible process. dQ is the energy the system exchanges with its environment, and dQ' arises from irreversible changes in the interior of the system. Thus dQ' and A are always positive (or zero). The usual array of thermodynamic relations may be derived involving the affinity (see references 11 and 12 for details). In particular, the affinity may be expressed in terms of the chemical potentials (μ_i) of the chemical components or phases undergoing the changes being considered

$$A = - \sum \nu_i \mu_i \quad (4)$$

Also, the temperature and pressure dependence are given by

$$\frac{\delta}{\delta T} \left(\frac{A}{T} \right)_{P,\xi} = \frac{1}{T^2} \left(\frac{\delta H}{\delta \xi} \right)_{T,P} \quad (5)$$

and

$$\left(\frac{\delta A}{\delta T} \right)_{T,\xi} = - \left(\frac{\delta V}{\delta \xi} \right)_{T,P} \quad (6)$$

It is now possible to derive an expression for the affinity of a phase change in a steady-state system. The affinity will then be related to the net and unilateral rates of the transformation. The starting point is the total differential of A/T in the variables T , P , and ξ . The variable ξ here measures the transition liquid \rightarrow gas.

$$d\left(\frac{A}{T}\right) = \left[\frac{\delta\left(\frac{A}{T}\right)}{\delta T} \right]_{P,\xi} dT + \left[\frac{\delta\left(\frac{A}{T}\right)}{\delta P} \right]_{T,\xi} dP + \left[\frac{\delta\left(\frac{A}{T}\right)}{\delta \xi} \right]_{P,T} d\xi \quad (7)$$

In terms of dA Equation (7) becomes, with the aid of Equations (5) and (6),

$$dA = \frac{A + \left(\frac{\delta H}{\delta \xi} \right)_{T,P} dT}{T} - \left(\frac{\delta V}{\delta \xi} \right)_{T,P} dP - \left(\frac{\delta A}{\delta \xi} \right)_{P,T} d\xi \quad (8)$$

Two important properties of open steady-state systems are now utilized: time independence of all properties, that is, $dA = 0$; and the fact that an open system which undergoes a change with all composition variables constant behaves like a closed system with ξ constant; that is, $d\xi = 0$. In other words, the problem is to find the variation of dP with dT in the system at constant affinity and composition. Equation (8) thus becomes

$$\frac{A + (\delta H / \delta \xi) dT}{T} = \left(\frac{\delta V}{\delta \xi} \right) dP \quad (9)$$

For evaporation of a pure liquid

$$\frac{\delta H}{\delta \xi} = Q_{\text{vap}}, \quad \frac{\delta V}{\delta \xi} = \Delta V_{\text{vap}} \quad (10)$$

An equation analogous to the Clausius-Clapeyron equation results, but for an open system:

$$\frac{dP}{dT} = \frac{A + Q_{\text{vap}}}{T \Delta V_{\text{vap}}} \quad (11)$$

With the usual approximations of the ideal gas law and neglect of the liquid volume compared to the gas volume, Equation (11) becomes

$$\frac{dP}{P} = (A + Q) \frac{dT}{T^2} \quad (12)$$

For a closed system (no net mass transfer) $A = 0$, and Equation (12) reduces to the conventional Clausius-Clapeyron equation. Both A and Q in Equation (12) are always positive quantities, and so the effect of a nonzero value of A is to increase the effective heat of vaporization. On an $\ln P$ vs. $1/T$ plot, therefore, the line for an open system will lie above the static vapor pressure. This is precisely the situation in burning ethyl nitrate (below about 10 atm.).

An expression for the affinity in terms of the rates of the phase change may be derived from Equation 4. In this case

$$A = \mu_L - \mu_G \quad (13)$$

If the phases are in equilibrium, $A = 0$ and $\mu_L = \mu_G$. Otherwise the chemical potentials in the two phases are not equal. For a chemical reaction it may readily be shown that Equations (4) and (13) take the form

$$A = RT \ln \frac{K}{Q} \quad (14)$$

It may now be supposed that the rates of phase changes may be written in terms of rate constants and concentration factors.

$$M_f = k_f F_f(C) \quad (15)$$

$$M_b = k_b F_b(C)$$

for the forward and back *reaction* rates. In terms of these rates, Equation (14) becomes

$$A = RT \ln \frac{k_f/k_b}{[F_b(C)/F_f(C)]} \quad (16)$$

since $K = k_f/k_b$ and $Q = F_b(C)/F_f(C)$. M is given by

$$M = M_f - M_b = M_f \left(1 - \frac{M_b}{M_f}\right)$$

$$= M_f \left(1 - \frac{k_b F_b(C)}{k_f F_f(C)}\right) \quad (17)$$

If the affinity is introduced with the aid of Equation (16), Equation (17) becomes

$$M = M_f \left[1 - \exp \left(-\frac{A}{RT}\right)\right] \quad (18)$$

Equation (18) is a general relation between reaction rate and affinity. It is usually nonlinear, in contrast to other irreversible processes such as diffusion and heat conduction. Only when $A/RT \ll 1$ does Equation (18) yield a linear relation between rate (flux) and affinity (force):

$$M = M_f \cdot \frac{A}{RT}, \quad \frac{A}{RT} \ll 1 \quad (19)$$

For a measurable nonequilibrium effect in phase changes, the exponential relation, Equation (18), must be used. Solving Equation (18) for A and substituting in Equation (12), one obtains

$$\frac{d \ln P}{d(1/T)} = \frac{-Q}{R} + T \ln \left(1 - \frac{M}{M_f}\right) \quad (20)$$

The second term on the right of Equation (20) is a correction to the Clausius-Clapeyron equation. M_f is usually quite large compared with M , and the correction is quite small, but each particular case must be investigated. Especially in propellant burning, there are likely to be appreciable departures from equilibrium at the high phase-change (burning) rates.

The vapor pressure and bomb pressure are functions of temperature and surface temperature in Figure 1 for burning ethyl nitrate, the departure from equilibrium of the surface temperature being outside the limits of experimental error. The expected effect on the basis of the value of M_f from the Knudsen equation is not so great. For $M = 0.028 \text{ cm./sec.}$, $t_{\text{surface}} = 105^\circ\text{C.}$, there results from Equation (1) for EtONO₂

$$M_f^* = 23.7\phi \text{ cm./sec.} \quad (21)$$

where M_f^* is the forward (evaporation) rate at equilibrium, and ϕ is the free-angle

ratio or accommodation coefficient. The best estimate of ϕ is 0.07; therefore the correction term in Equation (20) is negligible. Equation (21) applies only at equilibrium and hence is an upper limit to the true value of the evaporation rate.

In principle one should be able to calculate both M and M_f in Equation (20) from absolute-rate theory, but this is not possible with the present knowledge of the structure of the liquid and the detailed molecular picture of the evaporation process.

MULTICOMPONENT SYSTEMS

An expression for the departure from equilibrium at a phase interface in a multicomponent system may be derived from Equations (14) and (18):

$$\frac{Q_i}{K_i} = 1 - \frac{M}{M_{f,i}}, \quad (22)$$

$$M = M_{f,i} \left(1 - \frac{Q_i}{K_i}\right)$$

where K and Q are now interpreted as the equilibrium and nonequilibrium distribution coefficients for component i . The departure from equilibrium is given by the ratio of $M/M_{f,i}$, as with a one-component system. The problem of comparing this equation with experiment is the same as before: lack of a means of calculating M_f . Also, in any practical system one must necessarily have *intraphase* transfer effects, which complicate the observation of *interphase* processes. There have been several such studies in the chemical engineering field (10, 13, and 14).

One of the objects of all these studies was to determine the validity of the usual assumption in mass-transfer work of physical equilibrium at the transfer interface. The lack of agreement of the data with equations based on the equilibrium assumption was interpreted as evidence of departure from equilibrium.

Sinfelt and Drickamer employed a semiempirical equation at the transfer interface which is very similar to Equation (22):

$$M = \frac{\text{net flux}}{\text{flux}} = \alpha \left[C(0^-, t) - \frac{C_{0^-}^+}{C_{0^+}^+} C(0^+, t) \right] \quad (23)$$

where α is the *interface transfer coefficient*, $C(0^-, t)$ and $C(0^+, t)$ are the actual concentrations on either side of the interface, and the superscript crosses denote equilibrium quantities. Thus for no resistance $\alpha \rightarrow \infty$, and for high resistance $\alpha \rightarrow 0$. It is readily seen on comparing (22) and (23) that

$$M_f = \alpha C(0^-, t) \quad (24)$$

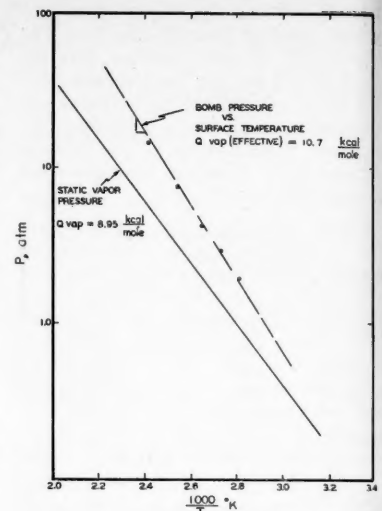


Fig. 1.

that is, the unilateral forward rate is taken to be proportional to the interface concentration, and α has the nature of a rate constant. Sinfelt and Drickamer give an equation for α from absolute-rate theory and experimental barrier heights ΔF^* for several systems. It would be desirable to calculate these ΔF^* 's from an *a priori* molecular model of the interface transfer process.

In connection with a study of the evaporation of small drops of high-boiling esters, Monchick and Reiss (15) have also derived an expression similar to (22). They assumed the rate of emission from the liquid surface to be given by the Knudsen equation while the condensation rate was found from the gas distribution function, modified to account for the flux to the surface. The result, in the present notation, is

$$M = \frac{M_{f,i} \left(1 - \frac{n_i}{n_i^0}\right)}{1 - \alpha'/2}$$

where n_i is the actual number density at the surface, and n_i^0 is the equilibrium density corresponding to the surface temperature. It is not apparent how the factor $(1 - \alpha'/2)$ is to be reconciled with Equation (22).

NOTATION

A = thermodynamic state function, g./
(sq. cm.)(sec.)
 a = interface transfer coefficient
 a = accommodation coefficient
 dQ = energy the system exchanges with
its environment
 dQ' = uncompensated heat
 G = rate of evaporation

K = usual equilibrium constant
 M = net rate of phase change
 n_i = number density at surface
 n_i^0 = equilibrium density
 P = pressure
 Q = nonequilibrium concentration function
 R = usual gas constant
 T = absolute temperature
 V^* = volume/molecule in the liquid
 W = molecular weight

Greek Letters

μ_i = chemical potentials of the chemical components or phases undergoing the changes being considered
 ν_i = stoichiometric coefficients

LITERATURE CITED

- Hildenbrand, D. L., and A. G. Whitaker, *J. Phys. Chem.*, **59**, 1024 (1955).
- Kennard, E. H., "Kinetic Theory of Gases," p. 69, McGraw-Hill Book Company, Inc., New York (1938).
- Schrage, R. W., thesis, Columbia Univ., New York (1951), Columbia Univ. Press (1952).
- Penner, S. S., *J. Phys. Chem.*, **56**, 475 (1952).
- Hirschfelder, J. O., *ibid.*, **16**, 22 (1948).
- See, for example, D. J. Trevoy, *Ind. Eng. Chem.*, **45**, 2366 (1953); and K. C. D. Hickman, and D. J. Trevoy, *ibid.*, **44**, 1882 (1952), **46**, 1442 (1954).
- Eyring, Henry, and J. F. Kincaid, *J. Chem. Phys.*, **6**, 620 (1938).
- Wyllie, G., *Proc. Roy. Soc. (London)*, **197A**, 383 (1949).
- Littlewood, Roy, and E. K. Rideal, *Trans. Faraday Soc.*, **52**, 1598 (1956).
- Emmert, R. E., and R. L. Pigford, *Chem. Eng. Progr.*, **50**, 97 (1954).
- De Donder, Théophile, and Pierre Van Rysselberghe, "Thermodynamic Theory of Affinity," Stanford Univ. Press, Stanford, Calif. (1936).
- Prigogine, I., and R. Defay, "Chemical Thermodynamics," 2 ed., Longmans, Green and Company, New York and London, (1952), tr. by D. H. Everett.
- Higbie, Ralph, *Trans. Am. Inst. Chem. Engrs.*, **31**, 365 (1935).
- Sinfelt, J. H. and H. G. Drickamer, *J. Chem. Phys.*, **23**, 1095 (1955).
- Monchick, Louis, and Howard Reiss, *ibid.*, **22**, 831 (1954).

Manuscript received Sept. 18, 1957; revised Nov. 29, 1957; accepted Nov. 29, 1957.

On Phase Equilibrium at the Gas-Liquid Interface During Absorption

L. E. SCRIVEN and R. L. PIGFORD

University of Delaware, Newark, Delaware

That phase equilibrium exists at the gas-liquid interface during gas absorption is usually assumed in the analysis and design of absorption equipment, but the validity of this assumption has been in doubt since Higbie's pioneering gas-absorption studies. Accurate measurements are reported herein of the absorption rates at 25°C. of carbon dioxide into short water jets in which the liquid was in laminar flow. The jets issued from circular nozzles of about 1.5-mm. diam., flowed intact downward through an atmosphere of carbon dioxide at average velocities of from 75 to 550 cm./sec. over distances of 1 to 15 cm., and were collected in a receiver slightly larger in diameter than the nozzles. The measured absorption rates are in excellent agreement with predictions based on unsteady state diffusion theory, when one assumes interfacial equilibrium. It is concluded from these results and those of other investigators that equilibrium prevails at a freshly formed, relatively clean, carbon dioxide-water interface and that the same statement probably applies to the absorption of other slightly soluble gases in water.

Evidence is discussed which indicates that an accumulation of minute quantities of surface-active materials may seriously reduce the rate of gas absorption, either by affecting the hydrodynamic characteristics of the system or perhaps by offering resistance to the transfer of solute molecules across the interface.

That phase equilibrium exists at the gas-liquid interface has commonly been assumed in applications of the film theory (21, 32) and the more realistic penetration theory (6, 15, 16, 32) to gas absorption. In attempting to test the validity of this assumption, various previous investigators have obtained conflicting results (4, 7, 8, 11, 16, 23, 25, 35). It seems likely that this lack of agreement is due principally to inadequate knowledge of the fluid dynamics of the different flow systems employed, although in certain cases it may arise from unknown chemical reaction effects, inaccurate diffusivity values, and so forth. Several careful studies have been published recently. From data obtained with their novel rotating-drum apparatus Danckwerts and Kennedy (7) concluded that there may be a small interfacial resistance to mass transfer in the carbon

dioxide-water system. Lynn, Straatemeier, and Kramers (23) decided on the basis of their wetted-wall column experiments that interfacial equilibrium exists in the sulfur dioxide-water system.

Cullen and Davidson (4) concluded from jet-absorber experiments that interfacial equilibrium exists in the carbon dioxide-water system, and in a companion study employing a wetted-sphere absorber (8) they confirmed this conclusion and found that it is probably also true in the absorption of a number of other slightly soluble gases.

The present investigation was undertaken to resolve the controversy on the basis of careful physical-absorption measurements carried out at short liquid-exposure times and with a relatively simple flow system amenable to mathematical analysis. At the time of its inception laminar liquid jets similar to those described herein had been utilized in surface-tension studies (27) and in a few absorption studies (9, 24, 25); subsequent applications in absorption

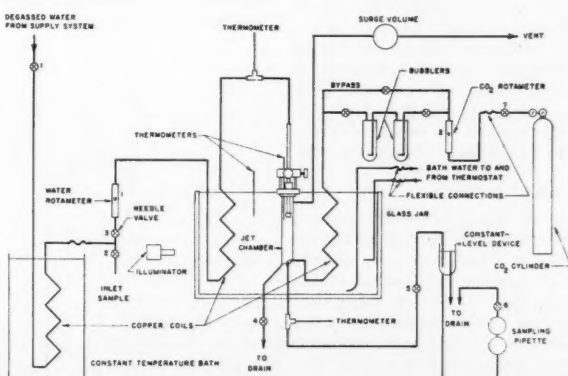


Fig. 1. Flow diagram of jet apparatus.

L. E. Scriven is with the Shell Development Company, Emeryville, California.

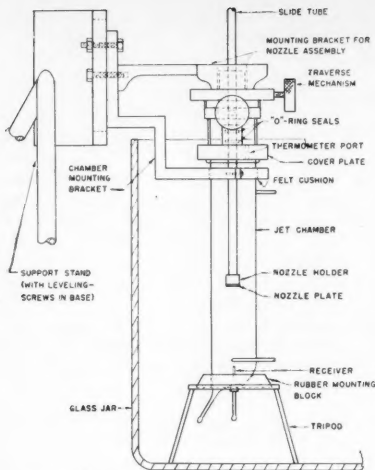


Fig. 2. Jet chamber assembly for gas absorption studies.

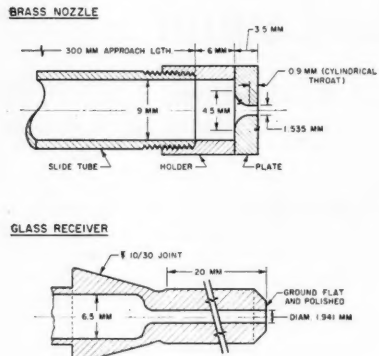


Fig. 3. Jet nozzle and receiver.

studies include those of Edwards et al. (10) and Cullen and Davidson (4).

APPARATUS AND PROCEDURE

Figure 1 shows a schematic diagram of the apparatus. Gas-free distilled water from a constant-head system and 99.9% pure carbon dioxide, dry or presaturated with water vapor, were fed through various temperature control baths to a jet chamber, within which a jet of water issued from a circular nozzle about 1.5 mm. I.D., flowed intact downward through an atmosphere of carbon dioxide at an average velocity of from 75 to 550 cm./sec. over a distance of 1 to 15 cm., and was collected in a glass capillary receiver of about 2 mm. I.D. The nominal contact time of liquid with gas $t_s = \pi h d_0^2 / 4q$ varied from 0.003 to 0.05 sec.

Jet Chamber Assembly

The nozzle was mounted on the end of a slide tube which passed through a double O-ring seal in the brass cover plate used to seal the top of the glass jet chamber (Figure 2). The open top of the chamber was ground flat, and the surface of the cover plate was polished to a fine finish so that a gas-tight seal allowing sliding motion was possible with the aid of stopcock grease. Jet length was adjusted by raising or

lowering the slide tube. A traversing mechanism permitted easy horizontal alignment of the nozzle with the jet receiver. The whole assembly was immersed in a large, glass water bath (Figure 2). The jet chamber, a glass vessel 5 cm. in diam. by 25 cm. in length was provided with a tangential gas entry near the bottom, an overflow port in the bottom, a gas outlet near the top, and a carefully aligned female tapered joint blown into the bottom to hold the receiver. To avoid vibration insofar as possible the main water bath was placed on a massive table, which in turn rested on a vibration-damping mounting. The entire apparatus was located in a basement room relatively free of building vibration. All lines leading to the equipment in the bath were provided with flexible sections of rubber tubing.

Nozzles

Several nozzle designs were considered, two of which were employed for absorption measurements. The first of these was a glass nozzle, prepared by joining a short length of 1.4-mm. I.D. capillary to a piece of 6-mm. tubing, reworking the joint to obtain a smooth transition, and then grinding away most of the capillary section to leave only 1 mm. or so of throat. The jets produced by this nozzle were not entirely satisfactory (30); finally a small flow nozzle of brass was carefully turned to the shape shown in Figure 3. The profile of the converging section was made to approach a quadrant of an ellipse as closely as possible, and the throat and face surfaces were polished to a smooth finish. The nozzle face was coated with a very thin film of paraffin wax to prevent wetting.

Receiver

The receiver, shown in Figure 3, was made from a 2-cm. length of select capillary tubing of 1.94 mm. I.D. joined to a standard-taper male joint member. The face of the receiver was ground flat and polished. The downstream end was connected to a constant-level overflow, which was mounted on a vertical slide rod and provided with a fine-adjustment leveling screw.

Operation

The jet was horizontally aligned with the receiver by setting a relatively high feed rate from the constant-head supply system to the nozzle and manipulating the traverse mechanism until the jet striking the receiver formed a symmetrical, mushroom-shaped film about the receiver, as in Figure 4(a).

During this procedure the outflow line leading from the receiver was closed off. If the film were symmetrical about the receiver, upon opening the outflow line the jet would pass entirely into the receiver.

The operation of the receiver was controlled by varying the elevation of the constant-level overflow in the outlet line. When the overflow level was slightly too high, not all the jet was collected in the receiver; some of the liquid spilled over, as shown in Figure 4(b). When the overflow level was too low, the free jet continued several millimeters down into the receiver before reaching a point (labeled *i*) at which liquid completely filled the tube, as in Figure 4(c). With this condition small gas bubbles were entrained in the rapidly moving liquid at *i*. For absorption measurements the overflow was adjusted to give the condition shown in Figure 4(d), in which there was neither spillover of liquid nor entrainment of gas (30). Figure 5 is a photograph of a laminar water jet in flight.

In the absence of sudden jars and strong vibration, steady operation of the jet with condition (d) at the receiver was possible for extended periods; operating troubles, when they occurred, seemed to arise from occasional small fluctuations in the liquid feed rate. The maximum operable jet length depended upon the liquid feed rate and was limited by the instability of the moving liquid column with respect to breakup.

Jet length was measured by a cathetometer with an accuracy of 0.005 cm. Flow rate was determined by weighing the liquid discharged in a timed interval during each experiment. Temperatures of the liquid entering and leaving and of the gas entering the jet chamber were measured to an accuracy of 0.02°C. Sampling was commenced only after these temperatures ceased varying. In all cases the three temperatures fell within a 0.1°C. range.

Sampling

Outflow from the receiver entered the constant-level overflow well beneath the liquid surface. The point of discharge was immediately above the entrance to another line, through which part of the effluent flowed continuously to a special sampling pipette, from which samples were periodically withdrawn with precaution to ensure adequate purging of the sampling system. With this arrangement it was possible to draw several samples without disturbing the operation of the jet. The sampling pipette consisted, in essence, of two glass bulbs

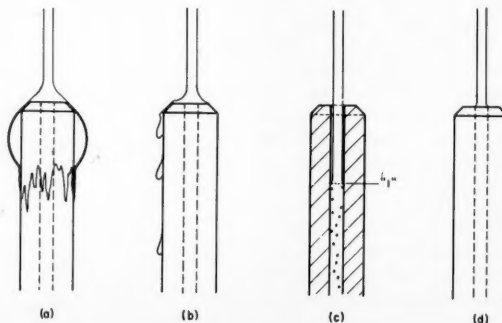


Fig. 4. Operation of jet receiver.

Fig. 5.
the
between
but t
chiefly
full of
of de
sample
taken
each j
Chem
Liq
sampl
reage
atmos
sisted
barium
stands
barium
the ca
slow b
ing of
end
chlori
certain
be tak
carbon

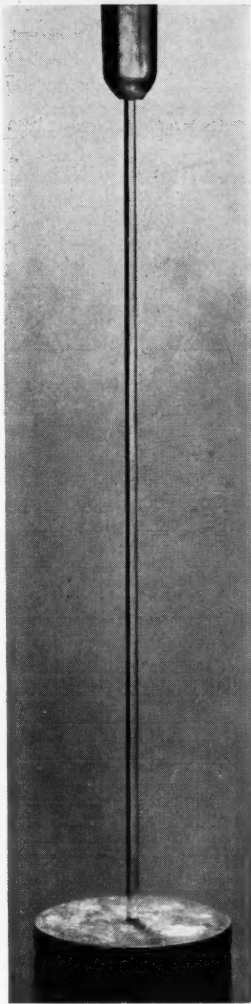


Fig. 5. Laminar liquid jet, nozzle above and receiver below.

connected in series. In discharging a sample, the volume withdrawn was measured between reference marks on the upper bulb, but the liquid actually withdrawn came chiefly from the lower bulb, which remained full of liquid, thus minimizing the possibility of desorption of carbon dioxide during sampling. Samples of the feed water were taken before and after every set of runs at each jet length.

Chemical Analysis

Liquid samples were discharged from the sampling pipette into flasks containing reagent solution beneath an inert nitrogen atmosphere. The analytical scheme consisted of precipitation of carbon dioxide as barium carbonate from a solution of dilute, standard sodium hydroxide and excess barium chloride (to suppress ionization of the carbonate at the endpoint), followed by slow back-titration under nitrogen blanketing of the residual hydroxide to a pH 8.8 end point with dilute, standard hydrochloric acid. This method is well known, but certain precautions, often overlooked, must be taken to obtain accurate results at low carbon dioxide concentrations (19, 20, 30).

In the present case the range of concentrations analyzed in the effluent water was 10 to 44 p.p.m.; both the precision and accuracy of analysis were found to be about 0.4 p.p.m.

TREATMENT OF DATA

The experimental absorption rate was calculated from the measured change in average concentration experienced by the liquid in passing through the jet. Very small adjustments were made in the experimental absorption rates in order to reduce them all to the same bases of 25°C., 760 mm. Hg total pressure, and standard flow rates. This was done by means of the equation for absorption (when one assumes interfacial equilibrium) into an *ideal* jet, that is, a jet throughout which the velocity is constant and equal to the average velocity at the point of emergence; for an ideal jet it follows from the penetration theory (4, 30, 32), that

$$\phi_* = \frac{2}{\sqrt{\pi}} (C_* - C_0) (\pi d_0 h) \sqrt{\frac{D}{t_*}} = 4(C_* - C_0) \sqrt{Dgh} \quad (1)$$

Thus the adjusted absorption rate is given by

$$\phi = q(C_{av} - C_0)(1 + \delta) \quad (2)$$

$$1 + \delta = \frac{\phi}{\phi'} \cong \frac{\phi_*}{\phi_*} = \frac{C_e - C_0}{C_e' - C_0'} \sqrt{\frac{Dq}{D'q'}} \quad (3)$$

where primes denote values at experimental conditions and unprimed symbols represent values at the standard condi-

tions selected. In no case did the quantity δ exceed 0.01.

The solubility of carbon dioxide in water at 25°C. and 760 mm. Hg partial pressure was taken as 3.39×10^{-5} g.-moles/cc., a value based on the results of numerous investigators, all in substantial agreement (30). The diffusivity of carbon dioxide in water at 25°C. has not been so well established, although from the data shown in Figure 6 it is apparent that the best estimate lies between 1.9 and 2.0×10^{-5} sq. cm./sec. The value 1.97×10^{-5} sq. cm./sec. was adopted in this work.

RESULTS

Experimentally determined absorption rates at 25°C. and 760 mm. Hg total pressure are shown in Figures 7 and 8. The agreement of replicate measurements is, with few exceptions, excellent over the twelvefold range of jet length and the twofold variation of liquid velocity reported.

While the jets produced with the glass nozzle are not subject to the theoretical analysis discussed below because of serious wetting of the nozzle face and periodic variation of cross sectional shape with length, the data obtained with them (Figure 8) are nevertheless of interest. They indicate that there is no significant effect of presaturating with water vapor the carbon dioxide fed to the jet chamber. Thus the gas immediately adjacent to the jet surface is very nearly saturated with water vapor, even if the feed gas is dry, and therefore the proper partial pressure of carbon dioxide to use in

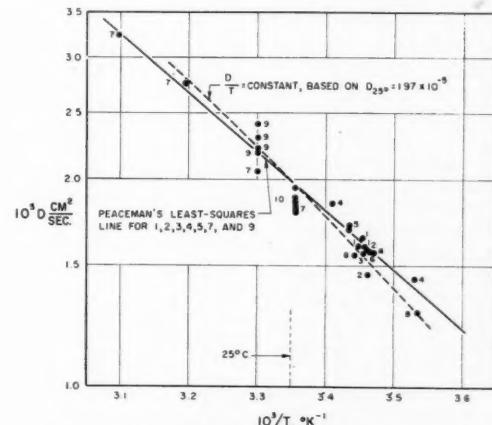


Fig. 6. Diffusivity of carbon dioxide in water.

1. Steady state capillary (33).
2. Unsteady state capillary (33).
3. Hydrophane plate (17).
4. Agar-agar solution (18).
5. Counterdiffusion of potassium chloride (1).
6. Counterdiffusion of potassium chloride (3).
7. Unsteady state capillary (20).
8. Agar-agar solution (34).
9. Diaphragm cell (26).
10. Diaphragm cell (30).

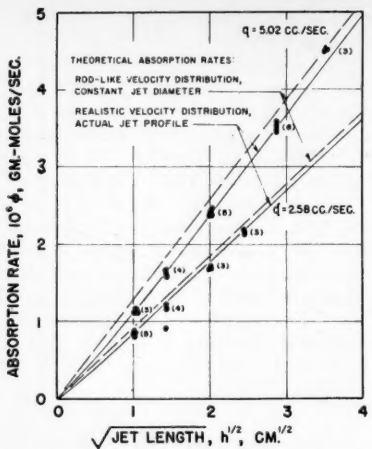


Fig. 7. Absorption of carbon dioxide in water jets issuing from 1.535-mm. I.D. paraffin-coated brass nozzle. The number of measurements in each group is shown in parenthesis.

calculating predictions of the absorption rate is nearly equal to the total pressure less the vapor pressure of water at the temperature of the experiment.

The dashed lines in Figures 7 and 8 were calculated from Equation (1). As far as absorption rates are concerned, the jets employed in this work were evidently similar to ideal jets. However, viscous effects close to the wall in the throat of the nozzle produce a nonuniform velocity distribution in a real jet. Owing to momentum interchange between the surface layers and the more rapidly moving core, a flat velocity profile is approached downstream. Gravitational acceleration further complicates the velocity distribution in a vertical jet. Both agencies result in contraction of the jet as it flows downward.

A quantitative understanding of the fluid dynamics is necessary for the accurate prediction of absorption rates into the jets of interest here. A method of deducing equations describing the liquid flow near the jet surface from measurements of jet diameter *vs.* length and by analogy with closely related flow situations, *viz.* the laminar wake behind a thin flat plate oriented parallel to the flow and the fall of a nonviscid liquid jet in a gravitational field, has been presented elsewhere (30, 31).

Because the penetration depth of the diffusing carbon dioxide molecules is small compared with the jet diameter under the conditions of the experiments reported here, the absorption can be described in terms of a two-dimensional model by using Cartesian coordinates. The differential equation governing the diffusion of carbon dioxide within the jet is

$$U \frac{\partial C}{\partial X} + V \frac{\partial C}{\partial Y} = D \frac{\partial^2 C}{\partial Y^2} \quad (4)$$

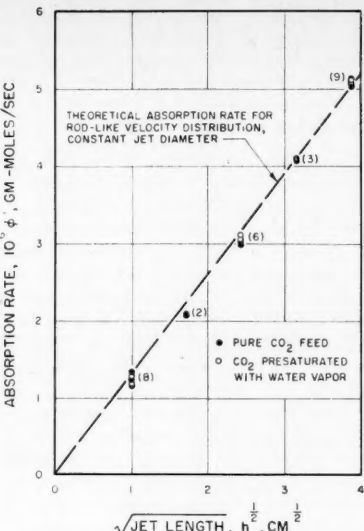


Fig. 8. Effect of presaturating carbon dioxide feed with water vapor. Absorption of carbon dioxide in water jet issuing from 1.414-mm. I.D. glass nozzle at 5 cc./sec.

Two of the boundary conditions are

$$C = C_0 \text{ for } X < 0, \quad Y \geq 0 \quad (5)$$

$$C = C_0 \text{ for } X > 0, \quad Y = \infty \quad (6)$$

If interfacial equilibrium is assumed, the third boundary condition is

$$C = C_e \text{ for } X \geq 0, \quad Y = 0 \quad (7)$$

An approximate but nevertheless quite accurate solution of this boundary-value problem for rates of absorption into the jets employed in this work has been given elsewhere (30, 31). The solution was obtained through a kind of perturbation technique in which the ideal jet (previously mentioned) was taken as the undisturbed system, and deviations in absorption rate caused by nonuniform velocity profiles at the nozzle and gravitational acceleration were derived. The computed deviation never exceeded 10% of the ideal-jet absorption rate. Predicted absorption rates, which are plotted as solid lines in Figure 7, are subject to no more than a few percent uncertainty arising from the approximation.

Agreement of the data with the theoretical predictions at the higher flow rate, 5 cc./sec., is outstanding; agreement at the lower flow rate, 2.6 cc./sec., though not as striking is quite good. It is felt that the agreement establishes the validity of the assumption of phase equilibrium at the freshly formed carbon dioxide-water interfaces obtained in the jet apparatus.

DISCUSSION

End Effects in Absorption Experiments

Matsuyama (25) reported that the carbon dioxide absorption rate which he

measured with a laminar water jet 0.3 cm. long was only about 40% of the predicted value for an ideal jet according to Equation (1). Noting that the longer the jet the better the agreement with ideal-jet predictions, he presumed that because of the high surface tension of water there existed a very short surface film which covered the liquid column attached to the end of his glass nozzle. Absorption rates lower than ideal-jet predictions are to be expected in the case of very short jets, for the surface layers immediately after emerging from the nozzle are moving much more slowly than the average velocity of the liquid, absorption proceeds farther in a given distance traveled, and absorption rate falls off. Unfortunately, as Matsuyama described neither the design of his nozzle nor the downstream contraction of his jet, it is impossible to determine the extent to which the velocity profiles of his jet deviated from the flat profile he tacitly assumed.

If the face of his nozzle was wetted with water, which is likely, a more or less stagnant ring of liquid undoubtedly surrounded the jet for a short distance below the nozzle. The notion of a surface film, however, was based on experiments in which carbon dioxide was absorbed into concentrated barium hydroxide solutions with the formation of easily visible barium carbonate precipitate which accumulated at the face of the nozzle and at the horizontal surface of the receiver. Under certain conditions a film of precipitate surrounding the jet column grew up from the receiver all the way to the nozzle, and absorption of carbon dioxide ceased even though the flow of liquid continued. The same sort of film was produced by Cullen and Davidson (4) by sprinkling talc onto the surface of their jet. It seems reasonable that, as they have perceptively suggested, the stability of such films derives from the force with which the particles adhere to the water surface and the strength in compression of their structures, which are supported by solid surfaces at the nozzle and receiver. The stability of such a film does not necessarily indicate that any part of the surface of the jet is stagnant in the absence of the film.

Similar stable films, composed of fine solid particles and extending upstream as much as 2 cm. from a solid obstacle touching the liquid surface, can be produced on the surface of the falling liquid film in a short wetted-wall column (23, 36) and on the surface of the moving liquid in a rotating-drum apparatus (20). It is highly unlikely that a free liquid surface can assume a rigid structure over such distances in the absence of solid particles or other surface-active impurities capable of forming a rigid surface film.

During the normal operation of a wetted-wall, rotating-drum, or jet absorber a family of standing, capillary

waves moving downstream, outlet Tests injected is near waves. From rates dioxides column effect is very that t and ex The r disturbance surge down exit is that slowly reached (36) f short nated causing outlet inter Capi surface At a l of wa about (See i was in waves (the h in Fig. barely the fa that ported affected that v and ro Effects The surface sent w stream liquid wetted appear or se drastic the su explain capillary of the suffici inacti associ highly matr resiste cules. Han a sim compa

waves exists on the free surface of the moving liquid at a greater or lesser distance upstream from the exit slot, outlet knife edge, or receiver, respectively. Tests with powder blown onto, and dye injected into, the surface indicate that it is nearly stagnant between the standing waves and the exit aperture (20, 23, 36). From careful measurements of absorption rates of carbon dioxide and sulfur dioxide in water in short wetted-wall columns the presence of an exit end effect has been established; this end effect is very well accounted for by supposing that the surface between standing waves and exit is inactive in absorption (23, 36). The most striking feature of the wave disturbance is that following a sudden surge in liquid flow which carries it downstream over the solid obstacle at the exit it is immediately reestablished at that obstacle, and thereupon it very slowly climbs upstream until it has reached its original position. Wendel (36) found that the exit end effect in a short wetted-wall absorber can be eliminated almost completely by deliberately causing momentary spill over at the outlet slot at regular, widely spaced intervals.

Capillary waves were observed on the surfaces of the jets employed in this work. At a low flow rate (1.25 cc./sec.) a family of waves was clearly visible, extending about 1 mm. upstream of the receiver. (See *w* in Figure 4(d).) As the flow rate was increased, the height to which the waves extended decreased; at 5 cc./sec. (the higher of the two flow rates reported in Figure 7) a single standing wave was barely discernible about 0.1 mm. above the face of the receiver. It is concluded that the absorption measurements reported in this paper were *not* significantly affected by an exit end effect similar to that which exists in wetted-wall-column and rotating-drum apparatus.

Effects of Surface-Active Contaminants

The conclusion seems inescapable that surface-active contaminants, initially present within the apparatus or in the feed streams, accumulate on the surface of the liquid film at the downstream end of both wetted-wall-column and rotating-drum apparatus, and there they form a rigid or semirigid surface structure which drastically impedes liquid flow close to the surface. The presence of this structure explains the observed behavior of the capillary-wave disturbance. Stagnation of the liquid adjacent to the surface is sufficient to account for the relative inactivity in absorption of the region associated with the exit end effect, but a highly compressed film of surface-active material may itself offer appreciable resistance to the passage of solute molecules.

Hammerton and Garner (12) reached a similar conclusion with regard to a comparable situation. Their studies of gas

TABLE 1. SUMMARY OF RECENT INVESTIGATIONS
Physical Absorption of Slightly Soluble Gases in Water

Investigator(s)	Type of absorber	Nominal liquid exposure time, sec.	Solute <i>D</i> used, 10^5 gas sq. cm./sec.	Value of equilibrium theory	Departure of absorption rates from interfacial theory
Kennedy (20)	Rotating drum	0.008-0.22	CO ₂ 2.02(25°C.)	5 to 20% below theory	
Lynn <i>et al.</i> (23)	Wetted-wall columns Single wetted spheres	0.01-0.98 0.05-1.78	SO ₂ 1.46(20°C.) SO ₂ 1.46(20°C.)	None (see text) None (theory according to reference 8)	
Wendel (36)	Short wetted-wall column	0.02-0.20	CO ₂ 1.97(25°C.)	None	
Cullen and Davidson (4)	Orifice jet	0.01-0.34	CO ₂ 1.92(25°C.)	None	
Davidson and Cullen (8)	Wetted sphere	0.12-0.57	CO ₂ 1.92(25°C.) O ₂ 2.44(25°C.) H ₂ 6.85(25°C.) N ₂ O 2.12(25°C.)	None	
Authors	Jet	0.003-0.05	CO ₂ 1.97(25°C.)	None	

absorption from single bubbles demonstrated clearly that contamination of the surface of a rising bubble by surface-active material initially present in trace amount can convert a mobile, free liquid surface into a rigid structure and that such a conversion is accompanied by a marked reduction in absorption rate.

There is ample evidence of the presence of minute amounts of surface-active materials in all but the most extraordinarily carefully purified water (13, 14). The effect upon absorption of adding to water measurable quantities of surfactants, such as Teepol and Petrowet, has been investigated by a number of workers (3, 11, 20, 23). In long wetted-wall columns the addition of a wetting agent markedly affects both the liquid-flow regime, causing the disappearance of rippling in the falling film under certain conditions, and the rate of absorption, which is much reduced in the absence of rippling. In shorter columns the wetting agent does not noticeably affect the rate of absorption, although it does influence the amplitude and position of the capillary waves described. The wetting agent likewise affects the position of the capillary waves above the receiver of a jet absorber. Cullen and Davidson (4) showed convincingly that this effect is a free-energy phenomenon. The same investigators found that the influence of commercial wetting agents on absorption is apparently related to the small amounts of impurities which they contain (3). Apart from a reduction of mixing in a liquid film when rippling is suppressed the action of surface-active agents on absorption is not yet understood. The action probably depends upon the rate at which they diffuse from the bulk liquid to freshly formed surface, the properties of the adsorbed film they form on the surface, and possibly interaction between them and the solute molecules.

Phase Equilibrium at the Interface

The principal conclusion drawn from the present work, that phase equilibrium

prevails at freshly formed, relatively clean interfaces between water and slightly soluble gases, answers the question of interfacial resistance in gas absorption, first posed on the basis of Higbie's data (5, 15, 16). It is corroborated by recent, careful studies of several investigators, whose results are summarized in Table 1. Only Kennedy's data give any significant indication of an interfacial resistance. However his theoretical predictions are based on the assumption that his liquid films accelerated *instantaneously* to the drum velocity. The data fall farthest below the predictions at the shortest liquid exposure times, that is, at conditions under which the undetermined acceleration entrance effect was greatest (20). At the longest contact times he achieved, the departure of his data is scarcely significant because of the uncertainty regarding the value of diffusivity which he used. Wendel (36) evidently was successful in allowing for the acceleration entrance effect in his short wetted-wall column by means of an equation derived by Scriven (30) and in eliminating the stagnation end effect (already discussed) by deliberately causing momentary spill over at the outlet slot at regular widely spaced intervals.

Predicted absorption rates are proportional to the square root of diffusivity [Equation (1)], the values of which are subject to greater uncertainty in the cases of sulfur dioxide and oxygen and much greater uncertainty in the cases of nitrous oxide and hydrogen than in the case of carbon dioxide. Nevertheless the agreement of the data for gases other than carbon dioxide with predicted absorption rates based on reasonable diffusivity values is impressive. There remains the task of confirming the diffusivity values of these gases, and it would perhaps be desirable to extend downward the liquid exposure times in absorption measurements made with them.

The absorption measurements of earlier workers (11, 15, 16, 24, 25, 26, 35) are

subject to rather more experimental error than those included in Table 1. Generally they do not differ by more than 20 or 30% from predictions (which are in every case open to question because of undetermined hydrodynamic and surface effects) based on unsteady state diffusion theory and the assumption of interfacial equilibrium, and this is not, in the writers' opinion, sufficient to invalidate the conclusion already drawn. Higbie (15, 16) took no account of the intricate flow regime surrounding his bubbles, and his reported absorption rates represent relatively small differences between two sets of values, those obtained from *absorption runs* and a *parallel series of blank runs*. Thus his results are of doubtful significance. Vivian and Peaceman (26, 35) were unable to give an adequate accounting, and Emmert and Pigford (11) did not recognize the importance of end effects in their short wetted-wall columns. The latter also reported absorption and desorption rates, measured in long wetted-wall columns with a wetting agent present, which fell below their theoretical predictions. Their results may reflect interference of an accumulation of surface-active material with the passage of solute molecules through the interface.

Phase equilibrium is probably established as rapidly as sufficient solute molecules arrive at the liquid surface to saturate the first few molecular layers of liquid. According to estimates based on the Knudsen equation of gas kinetic theory,

$$\Gamma = \frac{p}{\sqrt{2\pi M RT}} \quad (8)$$

the time required for this to occur, with the exception of very low partial pressures of solute gas, is many orders-of-magnitude less than the shortest time of contact of liquid with gas yet studied, 0.003 sec. Schrage (29) has treated the case in which the rate of incidence of gas molecules on the liquid surface becomes a controlling factor in absorption. The apparent interfacial resistance to mass transfer in earlier absorption studies was explained in terms of an *accommodation coefficient* (5, 7, 11). It now seems certain that the accommodation coefficient of a clean water surface absorbing a slightly soluble gas, in particular carbon dioxide, is no smaller than 0.001, and it is quite possible that it approaches unity. It is worthy of mention that the evaporation coefficients (equivalent to the accommodation coefficient in gas absorption) of pure substances have been found to be unity when proper allowance was made for thermal effects in the experimental determinations (22).

There is mounting evidence that small, possibly infinitesimal, amounts of surface-active materials may bring about a much reduced rate of absorption into a flowing

liquid or from a rising bubble. It is important to determine whether this reduction is the result of hydrodynamic effects or of an interfacial resistance to mass transfer. The need for additional data is great, for the implications of the available evidence are obvious in commercial mass transfer operations, where high-purity process streams and apparatus free of possible surface contaminants are rare indeed. Hickman several years ago expressed surprise that chemical engineers and physical chemists continue to treat water as though its surface were H_2O (14). Drawing upon his experience in high-vacuum distillation he stated that liquids are inherently self-soiling: "It is axiomatic that an ordinary liquid is contaminated (13)."

ACKNOWLEDGMENT

Thanks are due to M. M. Wendel for helpful discussions of portions of this work and W. J. Bauer for assistance in the taking of data. The investigation was made possible in part by National Science Foundation and Shell Fellowship Committee fellowships received by L. E. Scriven.

NOTATION

C = liquid concentration, moles/cc.
 C_e = equilibrium liquid concentration, moles/cc.
 C_0 = initial liquid concentration, moles/cc.
 C_{av} = average (outlet) liquid concentration, moles/cc.
 d_0 = nozzle diameter, cm.
 D = diffusivity, sq. cm./sec.
 h = jet length, cm.
 M = molecular weight, g./mole
 p = partial pressure, dyne/sq. cm.
 q = volumetric flow rate, cc./sec.
 R = gas constant, 8.316×10^7 (dyne/cm.)/(mole) $^{\circ}K$.
 t_* = nominal exposure time, sec.
 T = absolute temperature, $^{\circ}K$.
 U = velocity parallel to jet surface, cm./sec.
 V = velocity normal to jet surface, cm./sec.
 X = distance parallel to jet surface, cm.
 Y = distance normal to jet surface, cm.

Greek Letters

Γ = molecular flux in gas phase, moles/(sq. cm.)(sec.)
 δ = dimensionless quantity defined in Equation (3)
 μ = liquid viscosity, g./(cm.)(sec.)
 ϕ = absorption rate, moles/sec.
 ϕ_* = absorption rate into ideal jet, moles/sec.

LITERATURE CITED

- Carlson, T., *J. Am. Chem. Soc.*, **33**, 1027 (1911).
- , *Medd. vetenskapsakad. Nobelinst.*, **2**, 2 (1913).
- Cullen, E. J., and J. F. Davidson, *Chem. Eng. Sci.*, **6**, 49 (1956).
- , *Trans. Faraday Soc.*, **53**, 113 (1957).
- Danckwerts, P. V., *Research (London)*, **2**, 494 (1949).
- , *Ind. Eng. Chem.*, **43**, 1460 (1951).
- , and A. M. Kennedy, *Trans. Inst. Chem. Engrs. (London)*, **32**, S53 (1954).
- Davidson, J. F., and E. J. Cullen, *Trans. Inst. Chem. Engrs. (London)*, **35**, 51 (1957).
- Dirken, M. N. J., and H. W. Mook, *Biochem. Z.*, **219**, 452 (1930).
- Edwards, G., R. Robertson, F. Rumford, and J. Thomson, *Trans. Inst. Chem. Engrs. (London)*, **32**, S6 (1954).
- Emmert, R. E., and R. L. Pigford, *Chem. Eng. Progr.*, **50**, 87 (1954).
- Hammerton, D., and F. H. Garner, *Trans. Inst. Chem. Engrs. (London)*, **32**, S18 (1954).
- Hickman, K. C. D., *Ind. Eng. Chem.*, **44**, 1892 (1952).
- , and W. A. Torpey, *ibid.*, **46**, 1446 (1954).
- Higbie, R. W., Ph.D. dissertation, Univ. of Michigan, Ann Arbor (1934).
- , *Trans. Am. Inst. Chem. Engrs.*, **31**, 365 (1935).
- Hüfner, G., *Ann. Physik. Chem.*, **60**, 134 (1897).
- , *Z. phys. Chem.*, **27**, 227 (1898).
- Hughes, R. R., and E. R. Gilliland, *Chem. Eng. Progr. Symposium Ser. No. 16*, **51**, 101 (1955).
- Kennedy, A. M., Ph.D. dissertation, Cambridge Univ. (1954).
- Lewis, W. K., and W. G. Whitman, *Ind. Eng. Chem.*, **16**, 1215 (1924).
- Littlewood, R., and Sir Eric Rideal, *Trans. Faraday Soc.*, **52**, 1598 (1956).
- Lynn, S., J. R. Stratemeyer, and H. Kramers, *Chem. Eng. Sci.*, **4**, 49, 58, 63 (1955).
- Manogue, W. H., Ph.D. dissertation, Univ. of Delaware, Newark (1957).
- Matsuyama, T., *Mem. Fac. Eng. Kyoto Univ. (Japan)*, **15**, No. 11, 142 (1953) (in English).
- Peaceman, D. W., Sc.D. thesis, Mass. Inst. Tech., Cambridge (1951).
- Rideal, E. K., and K. L. Sutherland, *Trans. Faraday Soc.*, **48**, 1109 (1952).
- Ringbom, A., *Z. anorg. u allgem. Chem.*, **238**, 94 (1938).
- Schrage, R. W., "A Theoretical Study of Interphase Mass Transfer," Columbia Univ. Press, New York (1953).
- Scriven, L. E., Ph.D. dissertation, Univ. of Delaware, Newark (1956).
- , and R. L. Pigford, *A.I.Ch.E. Journal*, to be published.
- Sherwood, T. K., and R. L. Pigford, "Absorption and Extraction," 2nd ed., McGraw-Hill, New York (1952).
- Stefan, J., *Sitzber. Akad. Wiss. Wien., Math. Naturw. Kl.* **77** II, 371 (1878).
- Tammann, G., and V. Jessen, *Z. anorg. u allgem. Chem.*, **179**, 125 (1929).
- Vivian, J. E., and D. W. Peaceman, *A.I.Ch.E. Journal*, **2**, 437 (1956).
- Wendel, M. M., Ph.D. dissertation, Univ. of Delaware, Newark (1956).

Manuscript received January 9, 1958; revision received May 22, 1958; paper accepted May 22, 1958.

CH
Flu

Some
measur
and rat
Room-
a crush
in parti
Verti
bed sup
of bubb
conditi
the res
predicti

Liter
nology
mass t
building
of the r
from a
appara
"pocke
upward
more c
izatio
results
upon s
gas po

In t
pocket
change
bubble,
gas-flui
in the
viewpo
erable
phase b
other g

The
beds f
strated
(1). In
a react
variatio
bed wo

The
initial
size an
frequen
and th
them.
transm
probes
bed an
to elec
and rea

Other
Geo
Palo Alto

Characteristics of Gas Pockets in Fluidized Beds

GEORGE YASUI and L. N. JOHANSON

University of Washington, Seattle, Washington

Some characteristics of gas pockets rising through beds of fluidized solids have been measured directly with a light probe technique. The vertical thickness, numerical frequency, and rate of rise of the bubbles were obtained from oscillographs of dual probe signals. Room-temperature air at 1-atm. pressure was used in 4- and 6-in. columns. Glass beads, a crushed rock, commercial cracking catalysts, coal, and hollow resin spheres were studied in particle sizes from $12\text{-}\mu$ fluid cracking catalyst to $450\text{-}\mu$ coal.

Vertical bubble thickness was found to increase with particle size, distance above the bed support, and gas velocity. Size growth upon rising was mainly the result of coalescence of bubbles. The rise velocity ranged from 1 to 2 ft./sec., relatively unaffected by operating conditions. Bubble frequency decreased with height above the bed support owing to coalescence. Total bed-depth variation from 1.0 to 2.5 ft. did not significantly influence the results, which should be of interest in studying gas-by-passing in fluidized beds and predicting the slugging behavior and fluidization uniformity.

Literature about fluidized-solids technology in the fields of heat transfer, mass transfer, and reaction kinetics is building up rapidly. As insight is gained of the mechanism of fluidization resulting from such studies, it becomes more apparent that the nature of the "pockets," or "bubbles," of gas passing upward through a fluidized bed must be more completely determined. A generalization of the heat and mass transfer results now available may well depend upon such increased knowledge of these gas pockets.

In this work the terms *bubble* and *pocket* are used with complete interchangeability, mainly because the term *bubble*, representing the dilute phase of gas-fluidized beds is fairly well entrenched in the literature. From a semantic viewpoint the term *pocket* may be preferable to some, since there is no real phase boundary separating this gas from other gas within the fluidized bed.

The consideration of the use of fluidized beds for nuclear reactors has demonstrated another need for such information (1). In calculations for the design of such a reactor for neutron balance, voids or variation of solids density within the bed would be of paramount importance.

The present work was undertaken as an initial study to determine directly the size and size distribution, the numerical frequency, the rate of rise of such bubbles, and the process variables influencing them. The method is based upon the transmission of light between small probes submerged within the fluidized bed and conversion of the light signal to electrical impulses which are amplified and recorded.

Other techniques have been used in

attempts to record the nature of the dense and disperse phases in a gas-fluidized bed or the extent to which the system deviates from the *smooth* or *particulate* fluidization observed in solids fluidized by liquids. The degree to which a system approaches such an idealized, smooth fluidization model has been termed *uniformity of fluidization* (2). Electrical capacitance probes (2, 3), pressure-sensitive strain gauges (4), X-rays (5, 6), viscometers (7, 8, 9), and surface-tension measurements (10) have all been used to measure this quality of fluidization. The results obtained have been very helpful in making qualitative comparisons of fluidized beds. Because of the indirect nature of the observation, however, it has not been possible, with the exception of X-ray techniques (5), to utilize them to obtain properties of individual bubbles.

Photographs of these disperse regions in fluidized beds have been made by Mathis and Watson (11) and Ohmae and Furukawa (12). Mathis and Watson utilized their data by scanning still photographs to obtain integrated densitometer values as a measure of fluidization quality, analogous to the work previously noted.

Direct evidence of the quantitative relation between the amount of gas in the form of bubbles and the inlet gas velocity was reported by Ohmae and Furukawa (12). High-speed photographs of air bubbles in beds of fluidized polyvinyl-acetate resin and of air bubbles in a glycerin solution having the same viscosity as the fluid bed of solids were examined. The behavior of bubbles in fluidized solids was said to be analogous to that in the liquid glycerin system. Small bubbles were initially formed just above the screen support and then grew

in size by coalescing during their ascent. The frequency of bubbles therefore decreased with height above the bed support. A plot of volumetric flow rate of air bubbles vs. superficial air velocity under nonslugging conditions shows a family of slightly curved, nearly parallel lines representing the data for various diameters of the resin particles. For slugging conditions nonparallel straight lines with much steeper slopes were obtained. The size of the rectangular glass column used by Ohmae and Furukawa was not specified. Air-bubble volumetric flow rate was found to increase with increase in the ratio of L/D .

The results of Ohmae and Furukawa and also of Mathis and Watson were obtained by using flat-plate-walled columns, with the gas pockets rising adjacent to the glass wall. It is doubtful whether such data could be safely assumed to represent conditions within a larger fluidized bed, in which the gas pocket is not contacting the wall.

The current work was undertaken to determine properties, particularly of the gas pockets, which are not in contact with the column wall and which would therefore ordinarily not be visible externally. Such pockets however should be more representative of conditions within a larger fluidized bed than those at the wall. It was recognized at the outset that gas bubbles or pockets would vary considerably in size, shape, frequency of occurrence, position, and rise speed. Results for a given set of operating conditions thus would have to be based upon sufficient measurements of individual bubbles to allow significant differences between operating conditions to be revealed. The variables which could be expected to have a possible influence on bubble characteristics were

George Yasui is with Lockheed Aircraft Company, Palo Alto, California.

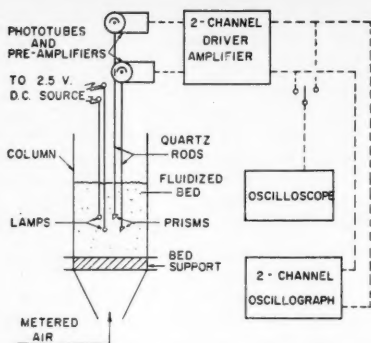


Fig. 1. Diagram of experimental apparatus.

many; it was not known initially which of these would be significant or whether they would act independently, that is, without interaction. This suggested a factorial design (13) for at least the early experiments, with randomized order of tests to minimize the influence of unknown variables. Complete details of the approach used are available elsewhere (14).

These considerations necessitated restricting the scope of the current investigation. In most of the work the vertical depth or thickness of a gas pocket, the speed of rise of the pocket, and the frequency with which the bubbles passed between the probes in a given position comprised the three items of data. Probe positions were restricted radially to the vertical column axis. Thorough investigation was made of three particle sizes of each of two materials. The effect of gas velocity, total (fixed) bed height, and the ratio of probe height above bed support to total height were investigated. The results of the last-named investigation were later converted to probe height above bed support when the height, rather than height ratio, proved to be the primary variable.

Additional tests supplemented studies of the major variables. The effect of column diameter; radial position of the probes; type of bed support; mixtures of sized particles; and solids of varying density, shape, and particle size were briefly investigated.

EXPERIMENTAL

Figure 1 is a schematic illustration of the apparatus. The sensing elements of a probe pair consisted of a light source and a light-reflecting prism. A $\frac{1}{8}$ -in.-diameter Grain of Wheat tungsten-filament lamp, coupled to one end of a 3/32 in. O.D. metal tube through which ran an insulated wire lead, served as the light source. Facing the lamp was a small mirrored-glass prism cemented to one end of a 4-mm.-diameter clear-quartz rod which was wrapped with aluminum foil. With two pairs of probes, one above the other but offset in vertical planes approximately at right angles to each other, a rising gas bubble passing between the elements of the probes was detected by the lower and then the upper probe pair.

As the gas pocket occupied the space between the lamp and the prism, light was transmitted to the prism and reflected out through the quartz rod into a type-929 vacuum phototube; there it was converted into electrical signals, which subsequently were amplified through two stages of a D.C. balanced-bridge type of vacuum-tube circuit. A cathode follower circuit enabled the signals to operate the pen motor of a BL-202, Brush dual-channel oscilloscope. An oscilloscope was used in the preliminary work.

The probe system was 40 in. long to allow placement at any level of a 3-ft.-deep fluidized bed. Distance between the lower and upper probe pairs, between light and prism of each probe, and radial position within the bed were all adjustable.

Four- and six-inch-inside-diameter Pyrex pipes were used as columns. In most of the experiments a 1 1/2-in.-thick porous ceramic disk supported the bed of solids. Separate experiments were conducted to test the effects of various porous plates and a 200-mesh screen. Laboratory air was filtered through cotton, and the air flow rate was controlled by a pair of pressure-reducing valves. Metering of the air flow rate was accomplished with rotameters or with orifice meters, depending on the range; these meters were calibrated by direct displacement of water at constant air-exhaust pressure. Air leaving the column was vented directly to the atmosphere.

Owing mainly to the inertia of the inking-pen system of the oscillosograph, corrections were necessary for the measured oscilloscope trace widths. About 1/100-sec. response time was noted for the pen to rise to or fall from the full amplitude upon the application or removal of an instantaneous input voltage to the oscilloscope. In addition to the expected pen overshoot and undershoot the oscilloscope showed that about 1/25 sec. elapsed while the pen oscillated back to the base line. On this basis the minimum interval between individual apparent bubble traces was chosen as 1/25 sec. Signal-trace amplitude was linear with input voltage except near the maximum height.

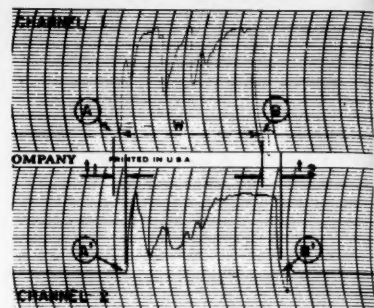


Fig. 2. Measurements obtained from signal traces with chart speed of 125 mm./sec.

By interposing the paper belt between the probes and recording the results in the same manner as was used for the fluidization work, one could calibrate the system for the corrected hole or bubble size and rise speed. Only the bubble-size correction, which was a function of both rise speed and hole size, was significant.

Materials

Most of the data were obtained on the glass-bead-air and the olivine-air systems, but other materials investigated were coal, hollow phenolic resin, magnetite catalyst, new UOP microspheroidal catalyst, and regenerated fluid-cracking (FCC) catalyst. The physical properties of the solids are given in Table 1. Unless otherwise specified, the surface-based diameter, obtained from experimental permeability data and use of Ergun's (15) equation, is used throughout this report. For purposes of comparison the 5 and 95% passing size and the mean surface diameters (16) based on the Tyler screen analysis of the various materials are also shown in Table 1.

Two mixtures of different-sized glass beads were also tested for their effects on bubble characteristics. Mix C was composed of an equal weight mixture of 75- and 175- μ glass beads; Mix D was an equal-weight mixture of 41-, 75-, and 175- μ beads.

A wide range in particle density was

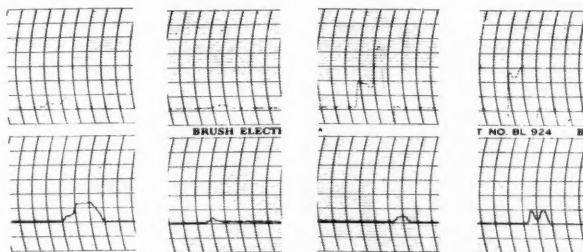


Fig. 3. Oscilloscope traces for 75- μ glass beads at chart speed of 125 mm./sec.

The complete bubble-detecting and -recording system was calibrated under simulated conditions, wherein holes on an endless moving belt were measured. This moving belt consisted of a strip of paper in which were cut rectangular holes 0.25, 0.75, and 1.5 in. wide, spaced at known distances apart. The belt was driven by pulleys and a variable-speed motor.

afforded by the choice of solids used. The lightest material was the hollow phenolic resin with a particle density of 21 lb./cu. ft. and the heaviest was magnetite with a particle density of 304 lb./cu. ft. An attempt was made to remove the extreme fines by elutriation with air or water; however only partial success was obtained in the case of materials of wide size range.



Fig. 4. In a procedure.

Procedure

In all cases at room pressure into porous and unporous materials were taken the chart speed of 5 and 125 mm./sec.

In most cases from results ratio of the size of the solid to the size of the gas bubbles few high in the column and FCC at minimum 2.5 ft. from 5 in. depend excepting probe probe of experiments where particles Groups designed.

The pockets were examined signal particular illustrations 1 trace probe probe from the distance wave-front B-B' at time lag average this results the bubbles the low chart speed lag the air formula.

The

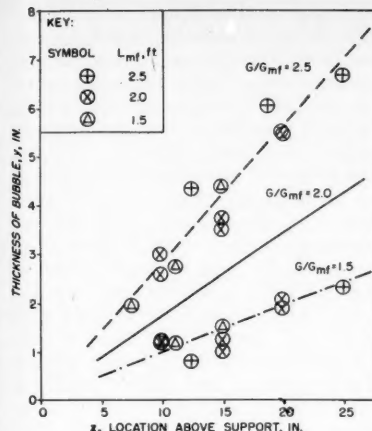


Fig. 4. Average vertical thickness of bubbles in 4 in. column, 242- μ glass beads.

Procedure

In all experiments solids were fluidized at room temperature and atmospheric pressure. The light probes were lowered into position when the bed was fluidized, and under steady state conditions oscilloscopes of the light signals from the probes were taken over $\frac{1}{2}$ - to 1-min. periods with the chart speed at 125 mm./sec. Speeds of 5 and 25 mm./sec. were also employed to check bubble frequency.

In most cases the air flow rates ranged from reduced mass velocities (defined as the ratio of mass velocity to minimum fluidization velocity) of 1.5 to 2.5, although a few higher air velocities were employed in the cases of olivine, hollow resin, UOP, and FCC catalysts. Bed heights measured at minimum fluidization ranged from 1 to 2.5 ft. The location of the probes varied from 5 to 25 in. above the bed support, depending upon the bed height. With one exception all runs were made with the probes at the axis of the column. The order of experimental treatments was randomized where practical to minimize statistical bias. Groups of runs for a given material were designed as factorial experiments.

The average characteristics of the air pockets or bubbles in the fluidized beds were calculated from measurements of the signal traces on the oscilloscopes. A particular tracing shown in Figure 2 will illustrate the method of calculation; channel 1 traces indicate light signals from the lower probe pair, and channel 2 traces the signals from the upper pair. The measured difference $A-A'$, or t_1 , represents the signal wave-front time lag, and the distance $B-B'$, or t_2 , corresponds to the wave-rear time lag. The time lag was obtained by averaging all the t_1 's and t_2 's for a given run; this represents the average time taken by the bubbles to rise the 1-in. distance from the lower to the upper probes. With the chart speed at 125 mm./sec. and the time lag in millimeters the average rise speed of the air bubbles was computed by the formula

$$v = \frac{1/12}{t/125} = 10.42/t \text{ ft./sec.} \quad (1)$$

The average thickness or vertical dimen-

TABLE 1. PHYSICAL PROPERTIES OF SOLID MATERIALS

Property	Material									
	Glass beads		Olivine rock		Hollow resin		UOP cat.		Coal cat.	
Shape	Sphere	Irreg.		Sphere	Gran.	Gran.	Irreg.	Irreg.		
Particle density, lb./cu. ft.	154	154	154	176	208	208	21	61	86	304
Avg. diam., μ (Permeability)*	41	75	175	242	42	100	150	81	60	450
(Mean surface)†	(57)	92	208	267	84	161	233	111	78	692
5% Retained size, μ	105	240	320	110	210	270	240	160	920	300
95% Retained size, μ	70	165	220	66	140	190	54	35	580	20
										<30

*Calculated from permeability measurements, by Ergun's equation (15).

†Mean surface diameter (16) from Tyler screen analysis.

TABLE 2. COMPOSITE DATA: REPRESENTATIVE RESULTS

System code	Operating conditions				Average bubble data						
	Particle diameter, G/G_{mf} , μ	Air flow, G , lb./hr.	Bed Ht. L , in.	Probe ht. Z , in.	Rise speed, v_r , ft./sec.	Frequency, n , 1/sec.	Frequency, y , $v_r n$	Thickness, y , in.	Vol. Q_b , cu. ft./min.	G_b/G	
G-11	41	2.0	8.8	30.8	12.5	1.10	0.38	0.33	0.05	0.28	0.026
G-11	41	2.5	11.0	18.5	7.5	1.41	0.42	0.41	0.08	0.36	0.055
G-13	75	2.5	25	24.0	10	1.37	2.54	0.83	0.92	1.96	0.083
GS-1	175	1.5	68	25	10	1.28	2.06	1.12	1.00	0.79	0.11
G-9	175	2.0	90	26	10	1.23	2.14	1.47	1.38	0.82	0.15
G-13	175	2.5	113	27.3	10	1.16	1.86	2.31	1.88	0.90	0.23
G-7	242	2.0	145	28	10	1.25	2.39	1.61	1.68	0.63	0.16
G-12	242	2.0	145	28	10	1.14	1.77	1.87	1.45	0.54	0.19
G-1*	175	2.0	90	25.4	19.5	1.57	1.63	2.31	3.70	0.95	0.12
"D"†	2.5	25	24	10	1.72	1.81	1.04	0.82	1.74	0.10	
O-3	150	2.0	200	28.8	10	1.20	1.68	1.38	1.01	0.24	0.14
O-3	150	2.0	200	28.8	20	1.64	0.94	4.49	1.84	0.46	0.23
C-5	450	1.75	333	22.5	10	1.22	1.15	2.73	1.37	0.21	0.27
HR-4	81	6.75	27	24.5	10	2.04	0.82	0.37	0.13	0.25	0.037
M-1	70	2.0	100	19	10	1.75	1.06	0.65	0.30	0.16	0.065
U-1	60	2.0	8	25.8	15	11.9	0.42	0.43	0.08	0.53	0.029
U-1	60	20.3	81	25.3	15	1.83	2.32	2.24	2.27	1.44	0.149

*6 in. I.D. column. All other results, 4 in. column.

†Equal weight mixture of 41, 75, and 175 μ glass beads.

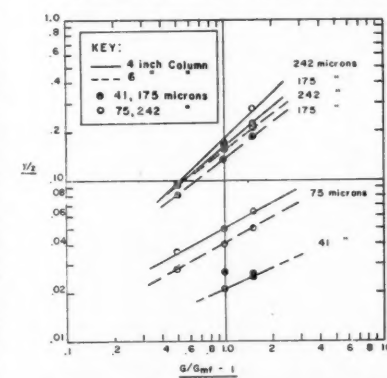


Fig. 5. Average y/z ratio for glass beads.

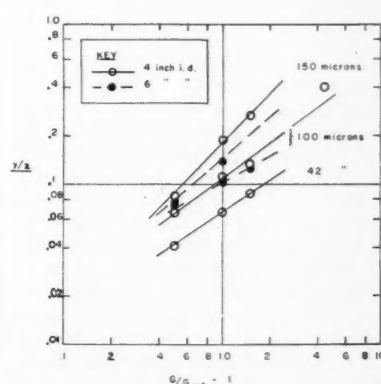


Fig. 6. Average y/z ratio for olivine.

sion of the bubbles was found from the average width

$$y = w/t \quad (2)$$

which gives y in inches for the distance between lower and upper probes of 1 in.

and w and t in consistent units. For vertical probe separation differing from 1 in. these equations would be multiplied by the probe separation in inches. For air bubbles of a thickness less than about 2 in. significant corrections obtained from calibration data

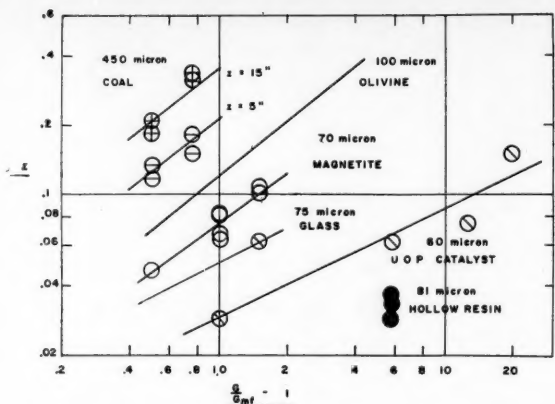


Fig. 7. Average y/z ratio for various materials in 4-in. column.

were employed. The average bubble frequency per second was determined by counting the number of signals and dividing by the elapsed time in seconds.

Since the average widths or horizontal dimensions of the air bubbles were not determined in these experiments, the present data do not afford a direct measurement of the volume or quantity of bubbles. Comparison with the work of Baumgarten and Pigford, however, suggests that vertical and horizontal bubble dimensions do not differ greatly.

An estimate can also be made on the basis of the data taken at the column axis. In this estimate of the volumetric flow rate of air bubbles, the bubbles were assumed to be uniformly distributed over the cross-sectional area of the column. If A_c is the column cross section in square feet and A_p is the horizontal projected area between the probe elements in square feet, then

$$Q_b = \frac{60nyA_pA_c}{12A_p} = 5nyA_c \text{ cu. ft./min.} \quad (3)$$

RESULTS

Figures 2 and 3 show two examples of the types of light-signal traces obtained at a chart speed of 125 mm./sec. for the 242- and the 75- μ glass beads, respectively. The irregular traces which have been obtained may indicate a rain of solid particles falling through the air pockets. Occasionally the oscilloscopes do not show a corresponding signal trace on the two channels, but this is not surprising in view of the dynamic system in which the air bubbles occur. Pulsations in the flow of air, particularly under slugging conditions, may give widely different time lags. The circulation pattern may cause bubbles to travel askew, or even downward. Many other considerations enter into the interpretation of the oscilloscopes.

Table 2 is an indication of the type of data obtained. Each line of bubble data represents the average results of measurements of a number of bubble traces. For example, the average number of bubble

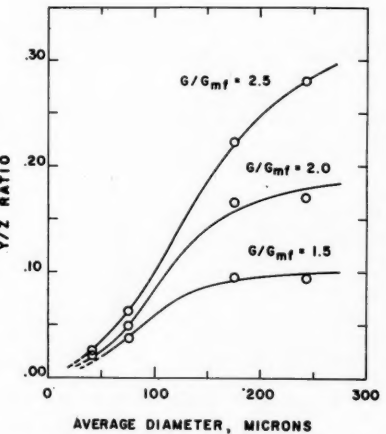


Fig. 8. Effect of particle diameter on bubble size ratio, glass beads in 4-in. column.

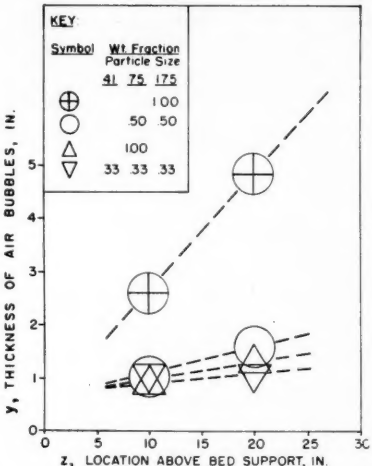


Fig. 9. Bubble thickness for mixed sizes of glass beads, $G/G_{mf} = 2.5$.

measurements for thickness is forty-six. Of a total of 375 such sets ten were based on fewer than ten bubbles, nineteen on fewer than twenty bubbles, and five on more than one hundred bubbles. Although this procedure decreased the standard

deviation considerably, it is still fairly high when compared with physical measurements of typical nonstatistical nature. In the figures the large size of the symbols indicates the approximate standard deviation of the ordinate values. Complete composite data, of which Table 2 comprises less than 10%, are available as Tables 2 to 15 of reference 14.* The system code number represents the type of solid material and the run series, with symbols defined in the notation. The first six columns represent operating conditions, the next three under *average bubble data* represent the primary result of this work, namely the gas-pocket rise speed, numerical frequency, and vertical pocket thickness. These will be analyzed separately. The last three columns of Table 2 are discussed later.

The factorial design approach used in the planning and execution of the experiments afforded a convenient means of estimating the level of significance of the effect of each controlled variable upon the measured results and the degree of interaction. Standard deviation estimates were based upon duplicate results and higher order interactions (13). By this means it was found that over-all bed height was not a significant variable; the type of bed support is discussed later. The column diameter and radial position of the probe were found to be significant factors, but investigation of these factors was of limited extent. The major variables influencing the characteristics of the rising gas pockets were type of particle (roughness, density, etc.), particle size, vertical position of the probes, and mass velocity of gas. It may be noted that bubble expansion owing to decrease in pressure as the bubble rises is negligible compared with the magnitude of the effect of probe height found in this work. Since air at 1 atm. is the only gas investigated thus far, no information on the influence of gas properties is available.

Average Bubble Thickness

Generally the average thickness of the air bubbles was found to increase with increases in air flow rate, position above the bed support, particle diameter, and particle density. As shown in Figure 4 for the 242- μ glass-beads system, y appeared to be a linear function of the height above the bed support. For clarity, points are omitted for $G/G_{mf} = 2.0$. Extrapolation of the curves to the point of origin indicated that y approached very small values. As an approximation in view of the large error variance straight lines were drawn from the origin of y vs. z graphs to follow the experimental points; the average y/z ratios were obtained from the slopes of these lines at various gas velocities. The effect of the bed height was not significant.

*Available as microfilm or photostats from University Microfilms, Ann Arbor, Michigan.

When these average y/z ratios were plotted against $G - G_{mf}$ or $(G - G_{mf})/G_{mf}$ on logarithmic coordinates, straight lines with different slopes and intercepts resulted for the various particle sizes investigated (Figures 5, 6, and 7). From the data for glass beads and olivine systems the following empirical equation was derived:

$$y/z = Bd^m(G/G_{mf} - 1)^{C \cdot 0 \cdot 003} \quad (4)$$

Values for B , m , and C for glass beads are 0.00012, 1.4, and 0.35, respectively; for olivine the values are 0.003, 0.8, and 0.5; for the 6-in. column, B values are about 15% lower.

In Figure 8 the effect of particle diameter on the y/z ratio is shown more clearly to be rather complex. The apparent approach to asymptotic values indicated by Figure 8 for glass spheres was not brought out by the olivine data; however an extension of the data beyond the present scope may reveal a similar trend for such crushed material.

The lines for various materials in Figure 7 appear to be arranged mainly as a function of particle diameter. The low position of spherical hollow resin relative to spherical glass beads suggests y/z also increases with particle density. Comparison of the glass sphere, olivine rock, and magnetite data indicate the importance of other factors such as particle shape and size distribution; this study did not attempt to investigate such variables exhaustively. The following equation, of simpler form than Equation (4), incorporates the influence of particle density. It represents the data for all solids studied, although the coefficient of variation (percentage of standard deviation) is 56%.

$$\frac{y/z}{pd} = 1.6 \left(\frac{G - G_{mf}}{G_{mf}} \right)^{0.63} \quad (5)$$

Two size mixtures of glass beads were investigated to determine the effect of size distribution on air-bubble characteristics. Mix C consisted of an equal-weight mixture of 75- and 175- μ glass beads, mix D of an equal weight mixture of 41-, 75-, and 175- μ glass beads. The effects of these mixtures on the average bubble thickness may be seen in Figure 9, which shows that at $G/G_{mf} = 2.5$ the bubble size for the mixtures is less than that expected on the basis of average particle size alone. This particular effect is similar to that depicted in Figure 12 in the paper by Morse and Ballou (2).

RISE SPEED OF BUBBLES

For practically all the materials within the scope of the experiments the average rise speeds of air bubbles in the fluidized beds ranged between 1 and 2 ft./sec. The effects of many of the variables were minor, being masked by the relatively large error variance. For example the

difference in rise speed between the approximately 40- μ -diameter glass beads and olivine illustrated in Figure 10 was

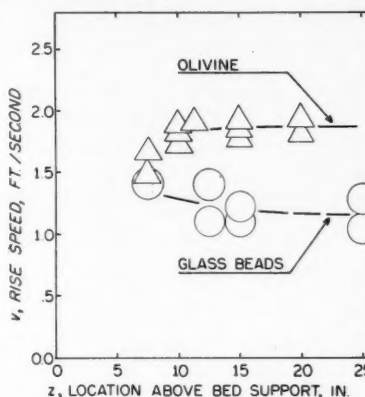


Fig. 10. Comparison of rise speed, 42- μ olivine and 41- μ glass beads in 4-in. column, G/G_{mf} of 2.0 and 2.5.

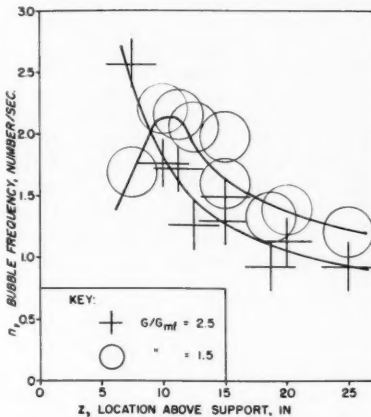


Fig. 11. Bubble frequency for 175- μ glass beads, 4-in. column, $L_{mf} = 1.5$ to 2.5 ft.

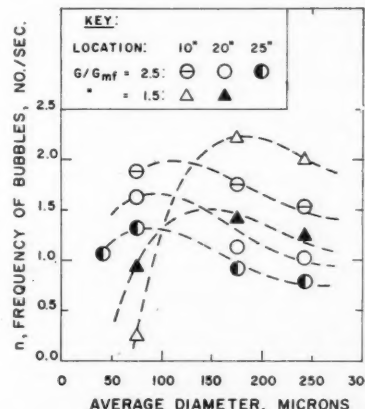


Fig. 12. Combined bubble-frequency data, glass beads in 4-in. column.

not noticeable for the larger sizes of the two materials. This graph of average bubble rise speed vs. location of the probes above the bed support indicates

that the effect of the probe height is small except perhaps just above the bed support. Data for other systems show a slight increase of bubble velocity with position above the support in some cases and no change in others.

There was a small increase in the rise speed as the air velocity was increased for a given material. However the values of the rise speeds did not depend upon the absolute magnitude of the gas velocities. For the UOP catalyst system the rise speed of air bubbles was found to be greater than the average total gas velocity, which is defined as the superficial velocity divided by the void fraction. The coal-air system data yielded bubble velocities approximately equal to the average gas velocity.

On the basis of buoyancy the rise speed of bubbles would be expected to increase with increasing bed density, but such a trend was not clearly discernible. Other factors, such as bed viscosity and solids circulation, may affect the bubble velocity. The *wall effect* probably acts as a drag force to slow down large air bubbles, for the solids are pushed out of the way and flow down countercurrent to the rising mass of air when the bubble is large with respect to the column diameter. The relatively constant bubble velocity found for the fluidized beds is similar to the behavior of gas bubbles in a given liquid in which the drag coefficients and wall effects are such as to give only a small increase in bubble velocity with increase in bubble size, within the ordinary range of bubble diameters. In gas-liquid systems however liquid density and viscosity have a pronounced effect on the rate of rise of bubbles.

In view of the large range of particle density, particle size, and air velocity used in this work these considerations can be only a partial explanation of the limited range of rise speed. The data strongly suggest that the major factor influencing the rate of rise is the rate of fall of the particles through and around the low density region. The irregularities of oscillograph traces show that considerable quantities of solids may rain down through the void regions. Since gas velocity in most fluidized beds is a small fraction of the free fall velocity of the particles, those particles no longer supported from below by the dense phase could accelerate downward at a rate dependent mainly upon the earth's gravitation. If it is assumed that particles are essentially at rest at the roof of the void and fall freely through the $\frac{3}{4}$ to 4 in. of bubble height, the average velocity of bubble rise (or particle fall) would range from 1.0 to 2.3 ft./sec., which is the same magnitude as the velocity observed. If this is the mechanism of bubble rise, it would suggest there is much less bypassing of the solid by the gas than the actual volumes of the bubbles.

TABLE 3. EFFECT OF BED SUPPORT ON BUBBLE CHARACTERISTICS

Run 4-GAS-1	175 μ glass beads	$G_0: G/G_{mf} = 1.5$							
	Column diameter = 4 in.	$G_1: G/G_{mf} = 2.5$							
	$L_{mf} = 2$ ft.	$z_0 = 10$ in.							
	Probe spacing, $s = \frac{1}{4}$ in.	$z_1 = 20$ in.							
	Type of bed support								
Code	Porosity	Thickness	G_0	G_1					
	μ	in.	Z_0	Z_1	Z_0	Z_1			
			Average characteristics						
			Rise speed, ft./sec.						
A	20	$\frac{1}{8}$	Porous stainless steel	1.19	1.50	1.21	1.69		
	55	$1\frac{1}{2}$	Porous ceramic	1.38	1.55	1.25	1.77		
	55	$\frac{1}{2}$	Porous ceramic	1.25	1.42	1.33	2.11		
	110	$1\frac{1}{2}$	Porous ceramic	1.42	1.45	1.30	1.94		
	110	$\frac{1}{2}$	Porous ceramic	1.27	1.44	1.33	1.90		
	74	.002	Screen, stainless steel	1.16	1.57	1.18	1.74		
(Average)						1.28	1.49	1.27	1.86
Thickness, in.									
A	20	$\frac{1}{8}$	Porous stainless steel	1.09	2.45	3.18	4.90		
	55	$1\frac{1}{2}$	Porous ceramic	1.04	2.31	2.31	4.52		
	55	$\frac{1}{2}$	Porous ceramic	0.96	2.07	2.94	5.71		
	110	$1\frac{1}{2}$	Porous ceramic	1.11	2.09	3.20	5.13		
	110	$\frac{1}{2}$	Porous ceramic	1.21	2.33	2.50	5.37		
	74	.002	Screen, stainless steel	1.31	2.89	2.88	4.77		
(Average)						1.12	2.36	2.84	5.07
Frequency, No./sec.									
A	20	$\frac{1}{8}$	Porous stainless steel	1.94	1.35	1.36	1.13		
	55	$1\frac{1}{2}$	Porous ceramic	2.44	1.40	1.98	1.21		
	55	$\frac{1}{2}$	Porous ceramic	2.27	1.41	1.74	1.12		
	110	$1\frac{1}{2}$	Porous ceramic	2.00	1.38	1.59	1.10		
	110	$\frac{1}{2}$	Porous ceramic	2.16	1.32	1.88	1.04		
	74	.002	Screen, stainless steel	1.54	1.15	1.63	1.25		
(Average)						2.06	1.34	1.70	1.14

TABLE 4. BUBBLE-SIZE DISTRIBUTION-RUN 4-GA-6

Trace width or trace height, mm.		Number of observations								1.25	1.5	1.75	2.0	1.25	1.5	1.75	2.0
		of trace width at G/G_{mf} equals			of trace height at G/G_{mf} equals												
		1.25	1.5	1.75	2.0	1.25	1.5	1.75	2.0	1.25	1.5	1.75	2.0	1.25	1.5	1.75	2.0
0-5	30	7	7	0	72	30	23	5									
5-10	96	44	17	6	38	33	21	12									
10-15	13	71	30	10	16	36	21	21									
15-20	0	38	47	22	11	20	19	31									
20-25	0	3	32	31	6	26	28	16									
25-30	0	1	2	21	3	13	21	11									
30-35	0	0	0	11	3	6	2	5									
Total No.	139	164	135	101	139	164	135	101									

Data from Run 4-GA-6, 242 μ glass beads in 4 in. column, probes at 20 in.

TABLE 5. EFFECT OF HORIZONTAL PROBE SPACING ON MEASUREMENT OF AVERAGE BUBBLE CHARACTERISTICS

Probe spacing, in.	Average bubble characteristics											
	Rise speed, ft./sec.				Thickness, y , in.				Frequency, No./sec.			
	G/G_{mf}	1.5	2.5	1.5	2.5	1.5	2.5	1.5	2.5	1.5	2.5	1.5
$\frac{1}{4}$	10	20	10	20	10	20	10	20	10	20	10	20
$\frac{5}{8}$	1.23	1.31	1.07	1.59	0.81	2.04	2.58	5.52	2.08	1.30	1.64	1.06
1	1.63	1.34	1.06	1.49	0.85	1.61	1.67	4.46	1.34	1.19	1.94	1.04
	1.98	1.31	0.98	1.62	0.81	1.22	1.34	4.06	0.66	0.91	1.37	1.09

Data from Run 4-GA-7, 242- μ glass beads in 4-in. column.

Bubble Frequency

The observed air-bubble frequencies in the present experiments ranged from 0 to almost 3 bubbles/sec. Detection of air bubbles by the probes depends to some extent on the spacing between the lamp

and the reflecting prism, upon the location of the probes with respect to the bulk of the bubbles in the bed, and upon the size of the bubbles. Probe spacing between the lamp and reflecting prism was $\frac{1}{4}$ in. except for a special investigation of this

variable discussed later. It was found that bubbles smaller than about $\frac{1}{2}$ in. could not be detected easily, and consequently bubble-frequency data are low and probably not reliable for bubble thicknesses of less than $\frac{1}{2}$ in. Quite apart from the difficulty of detecting very small bubbles the data indicated a decrease in the number of bubbles as their dimensions increased, suggesting that bubbles grew in size by coalescing. Analysis of variance indicated much interaction of the effects of operating variables upon frequency. A correlation of factors contributing to detected frequency was not found. For the glass beads the type of curves shown in Figure 11 appear to relate bubble frequency with the location of the probes above the bed support. The 175 μ glass beads system shows for $G/G_{mf} = 1.5$ a typical increase in frequency starting from a low bed height (small bubble size) and then after a maximum value decreasing in an exponential manner. The zone of decreasing frequency is attributed to the rate of bubble coalescence. At the higher ratio of G/G_{mf} the bubbles were already large and therefore readily detectable in the range shown, so that the zone of increasing frequency is not present; this is born out by the data for other sizes of glass beads.

Figure 12, showing the average bubble frequency as a function of average particle diameter for glass beads in the 4-in. column, illustrates the complex relationship existing. The shapes of these curves are explained by previous considerations and by recalling that bubble size increased with particle size, location above the bed support, and increasing gas velocity.

If consideration is restricted to conditions giving bubble thicknesses of 1 in. and greater, gas velocity does not appear to greatly affect the average bubble frequency. More detailed results may be found in reference (14).

Other Considerations

Separate investigations show the influence of bed support on gas pocket characteristics, the effect of horizontal light source-to-prism spacing of the probes, and the effect of radial position of the probes. The trace width and trace height distribution (which correspond to gas pocket height and diameter, respectively) were also investigated for 242- μ glass beads.

Table 3 compares five porous plate bed supports of varying thickness and pore diameter and one 200-mesh screen for their influence on average bubble rise speed, thickness, and frequency. The differences between the types of support are statistically significant for this and similar data at other conditions only for the effect of the screen upon bubble frequency. Since drilled plate supports were not investigated, comparison with the porous plates and screen used in this

work and grids bubbles Other fluidi porous suppor suppor insur suppor Cerai 55- μ the 1 conditio through to 10 bed D co 20% value Ta the size. 5-mm spon betw verti meas peak a pos the a sma small part wou width appa Rep ence data indic aver in T A the prisi chanc vari spaci ness the som pro sign pro poe

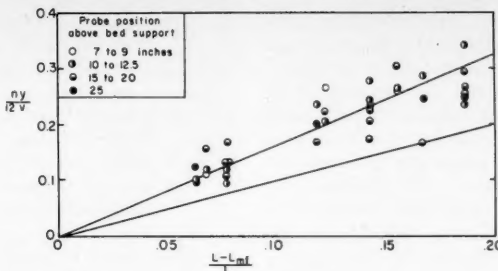


Fig. 13. Comparison of fractional voids within bed as entrained bubbles vs. bed expansion, 242- μ glass beads.

work is not possible. The larger hole size and spacing of most drilled plates or grids would probably influence not only bubble frequency but bubble size as well. Others have observed differences in fluidization uniformity between grids and porous plates, at least near the bed support. The major purpose of the bed support investigation in this work was to insure that unknown variations in bed support would not influence the results. Ceramic disk supports 1½ in. thick with 55- μ mean pore diameter were used for the major experimental work. For the conditions of Table 3 pressure drop through this plate (B) ranged from 50 to 100% of the pressure drop through the bed proper. For porous plates A, C, and D comparable values ranged from 4 to 20%, while for plate E and screen F values were approximately 1%.

Table 4 summarizes measurements of the statistical variation of gas pocket size. Counts were made of trace size in 5-mm. increments. Trace width corresponds to the time a gas pocket is between the lower probe pair or its vertical thickness. Trace height is a measure of the light transmitted at the peak of the trace. A high trace indicates a pocket at least as large in diameter as the distance between probes (5/8 in.); a smaller trace indicates a pocket of smaller diameter or one containing solid particles. The edge of a large bubble would result in smaller trace length and width. The results therefore are only an approximate indication of pocket size. Replicate runs served to show the existence of a common variance for the various data by Bartlett's test (17). Table 4 indicates the range of data which were averaged to obtain results such as found in Table 2.

A related investigation was that for the effect of probe spacing from light to prism upon measurements of bubble characteristics. The data and analysis of variance indicate an effect of probe spacing on bubble frequency and thickness strongly dependent on the level of the factors z and G . Table 5 indicates some of the results. The influence of probe spacing upon bubble frequency is significant at low mass velocity and low probe height. Under these conditions gas pockets are small, and the larger probes

do not detect the smaller pockets. For this reason 1/4-in. probe spacing was used in the major experimental work; even this probe spacing may fail to detect the smallest bubbles present at low probe height and low mass velocity. This is also a limitation of other detecting devices which have been reported such as electrical capacitance probes and X-ray technique. With the latter technique there is a possibility of classifying a number of such small bubbles in the ray path as a single larger bubble. Fortunately such small bubbles would be of secondary importance in bypassing or bed uniformity. The decrease in observed bubble thickness for wide probe spacing may reflect the short time that a bubble completely fills the zone between widely spaced probes. Again the use of small probe spacing should minimize this difficulty.

Discussion

A speculative description of the nature of flow in a gas-fluidized bed can be based upon the results obtained. Almost immediately upon increasing gas flow beyond minimum fluidization velocity, regions of low solid density begin to form. These regions are small near the bed support, and their diameter increases as they rise by coalescence of smaller bubbles. The diameter of such regions is increased by increasing particle size, particle density, and gas flow rate and by decreasing particle-size range. With the column sizes used in this work total bed height was not a significant variable. The bubbles are extremely irregular in outline and relatively nonuniform in size.

For bubbles larger than about 3/4 in. detected frequency decreases with increasing probe height, thus suggesting growth by coalescence. For materials such as cracking catalyst and hollow resin, which are characterized by smooth fluidization, bubble frequency increased with increasing air velocity. For larger, heavier particles frequency is relatively unaffected by increasing air flow rate. Bubbles in such media tend to coalesce easily and grow large.

The rate of rise of bubbles is only moderately affected by operating conditions. For laboratory scale systems such as those studied in this work this

may be in part the result of wall effect and solids circulation patterns. The major explanation proposed is that voids are moved upward mainly by collapse of the solids through and around the voids. At ordinary fluidization velocities the rate of collapse approaches that resulting from gravitational attraction of the solid.

The product of bubble frequency and size should be a measure of the volume of gas passing through the bed in the form of bubbles. This product divided by the average bubble velocity and by the column cross-sectional area should represent the volume fraction of gas as bubbles retained within the fluidized bed at any time. The latter is plotted vs. the fractional bed expansion $(L-Lmf)/L$ in Figure 13 for 242- μ glass beads. If the bed expansion is due entirely to the presence of bubbles in the bed, the ordinate and abscissa values should agree; if the dense phase of the bed is expanded, the abscissa should exceed the ordinate value. It is apparent that the volume of bubbles retained within the bed, as calculated from the data, correlates with the fractional bed expansion but equals or exceeds this value in every case. On the basis of Figure 13 it may therefore be concluded conservatively that the dense-phase portion of the bed remains at essentially the density found at minimum fluidization velocity. The figure indicates that the group $ny/12v$ may be too large, since it is difficult to visualize the dense phase being fluidized with less air than required at minimum fluidization velocity. The most probable reason for large values of this group is that gas bubbles preferentially seek the center of the bed, and the center-line probe therefore yields size data greater than the average value over the cross-sectional area. The points plotted show no consistent trend with the height of the probe above the bed support, a further indication that the volume of gas as bubbles remains constant vs. bed height, bubbles being more frequent at low levels but larger at high levels.

The ratio of gas flowing as bubbles to that required to fluidize is plotted vs. $(G-Gmf)/Gmf$ in Figure 14 for the same solid used in Figure 13. The abscissa represents gas flow in excess of

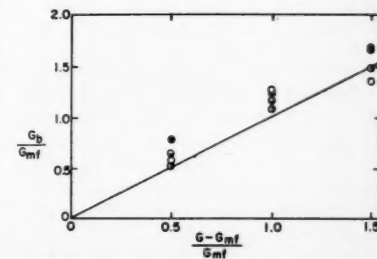


Fig. 14. Comparison of bubble flow rate vs. excess fluidizing gas, 242- μ glass beads.

minimum fluidization. If the two-phase theory of fluidization (18) were followed in its strictest sense, this quantity should be equal to the ordinate value. Since Figure 13 indicated that measured bubble volumes were probably higher than average values for the entire bed, the ordinate values shown in Figure 14 are also probably somewhat high. It is evident from these results that the measured bubble volume is about that expected, if all gas in excess of minimum fluidization velocity were in the form of bubbles. Data of Figure 14 for 242- μ glass beads correlated better than most data plotted similarly, but the same qualitative results were evident for most of the systems studied. Typical values of G_0/G are shown in Table 2.

The recent work of Baumgarten and Pigford (5) closely parallels the present work; these authors measured the instantaneous bed density in a rectangular column by the extent of gamma-ray absorption, with a technique similar to that of Grohse (6). Baumgarten and Pigford were able to deduce values representing bubble diameter (horizontal width), bubble frequency, and bubble rate of rise. The rise rate was obtained indirectly, from a knowledge of bubble frequency; bubble width was obtained from the instantaneous density at a trace peak and time average bed density. Solids used were glass beads of about the same size ranges as used in this work and a fluid cracking catalyst.

In agreement with this work they found bubble-size increases with gas velocity, height above bed support, and particle size. Although results were not conclusive, bubble frequency appeared to decrease somewhat with probe height in agreement with this work. They observed a marked, though somewhat erratic, influence of distance from the wall upon bed density and bubble frequency. This variable was not explored appreciably in the present work.

They conclude from their work that the rate of rise of bubbles increases rather markedly with increasing probe height. This conclusion necessitates postulating a transfer of gas from the dense phase to bubble phase as the gas rises through the bed, since bubble size and frequency do not decrease correspondingly. The present work is not in agreement with this conclusion; rather it postulates a minor change in rise speed with probe height and relatively constant total gas volume vs. probe height. Additional work may clarify this point. Although both investigations indicate increase in bubble size with height above support, Figure 7 of the work of Baumgarten and Pigford does not readily extrapolate to zero at the bed support as does the present work.

Ohmae and Furukawa (12) photographed bubbles in a rectangular column. The technique suffers somewhat in

restricting observation to bubbles adjacent to the wall. These authors found the volume of gas as bubbles increased, though not linearly, with total gas flow. They also found bubbles to grow sufficiently to cause slugging at a lower total bed height for increasing gas velocity. This is consistent with bubble size increasing with both gas velocity and height above bed support. Zenz (19) has interpreted slugging to represent growth of bubbles to column diameter size. Bubble diameters determined in this manner from the work of several authors increase with bed height and particle diameter in agreement with work previously discussed. Quantitative comparison of bubble sizes is uncertain because results in general do not specify the gas velocity as well as the bed height for slugging conditions.

In conclusion, data on gas-bubble characteristics for a variety of materials are presented. In agreement with the limited available results of other authors, these data show gas bubbles to increase in size with particle size, probe height, and gas velocity and to decrease in frequency with probe height. It is postulated without verification by other work that though bubble size increases with probe height by coalescence, the quantity of gas as bubbles remains substantially constant. The rise velocity was also found to remain relatively constant with probe height in disagreement with the conclusions of Baumgarten and Pigford.

ACKNOWLEDGMENT

The authors are indebted to The Texas Company, represented by Roland Beck, for financial support of this work.

NOTATION

Q_0	= volumetric flow rate of air bubbles, cu. ft./min.
t	= average time lag of channel 1 and 2 traces, mm.
v	= average rise velocity of air bubbles, ft./sec.
w	= width of oscilloscope trace, mm.
y	= average thickness, or linear dimension measured vertically, of the air bubbles, in.
z	= height of probes above bed support, in.
ρ	= particle density, lb./cu. ft.
Run Code Letters	
A	= air
C	= coal
D	= mixture
G	= glass beads
MR	= hollow resin
M	= magnitite
O	= olivine
S	= support variation run
U	= UOP catalyst
LITERATURE CITED	
1.	Morris, J. B., J. B. Nicholls, and F. W. Fenning, <i>Trans. Inst. Chem. Engrs. (London)</i> , 34 , 168 (1956).
2.	Morse, R. D., and C. O. Ballou, <i>Chem. Eng. Progr.</i> , 47 , 199 (1951).
3.	Dotson, J. M., Paper presented at the Chicago AIChE Meeting, December, 1957.
4.	Schuster, W. W., and Peter Kisliak, <i>Chem. Eng. Progr.</i> , 48 , 455 (1952).
5.	Baumgarten, P. K. and R. L. Pigford, Paper submitted to the <i>A.I.Ch.E. Journal</i> , 1957.
6.	Grohse, E. W., <i>A.I.Ch.E. Journal</i> 1 , 358 (1955).
7.	Dickman, Robert, and W. L. Forsythe, <i>Ind. Eng. Chem.</i> , 45 , 1174 (1953).
8.	Furukawa, Junji, and Tsutomu Ohmae, <i>J. Chem. Soc. Japan, Ind. Chem. Sect.</i> , 54 , 798 (1951).
9.	Matheson, G. L., W. A. Herbst, and P. H. Holt, <i>Ind. Eng. Chem.</i> , 41 , 1099 (1949).
10.	Fritz, J. C., Jr., Ph.D. thesis, Univ. Wisconsin, Madison (1955).
11.	Mathis, J. F. and C. C. Watson, <i>A.I.Ch.E. Journal</i> , 2 , 578 (1956).
12.	Ohmae, Tsutomu, and Junji Furukawa, <i>J. Chem. Soc. Japan, Ind. Chem. Sect.</i> , 56 , 909 (1953).
13.	Davies, Owen L., ed., "The Design and Analysis of Experiments," Hafner Pub. Co., New York (1956).
14.	Yasui, George, Ph.D. thesis, Univ. Washington, Seattle (1956).
15.	Ergun, Sabri, <i>Chem. Eng. Progr.</i> , 48 , 89 (1952).
16.	Heywood, Harold, <i>Symp. on Particle Size Analysis, Trans. Inst. Chem. Engrs. (London)</i> , 25 , 14 (1947).
17.	Ostle, Bernard, "Statistics in Research," The Iowa State College Press, Ames (1954).
18.	Toomey, R. D., and H. F. Johnstone, <i>Chem. Eng. Progr.</i> , 48 , 220 (1952).
19.	Zenz, F. A., <i>Petroleum Refiner</i> , 36 , No. 4, 173 (1957).

Manuscript received December 18, 1957; revision received May 13, 1958; paper accepted May 13, 1958.

Extraction of Sugar from Beets

H. H. YANG and J. C. BRIER

University of Michigan, Ann Arbor, Michigan

This paper presents the results of a previous investigation on the continuous countercurrent extraction of sugar beets (3) and its correlations. The relationship between the continuous diffusion and the simple diffusion is discussed from the standpoint of extraction rate.

ANALYSIS OF PROBLEM

The extraction of beet sugar may be resolved into two steps as far as mass transfer is concerned: (1) diffusion of sugar solution through the permeable membrane of beet cells toward the interface between the beets and the extracting solution, and (2) mass transfer of sugar through a liquid film at the interface into the extracting solution. These mechanisms will be discussed separately.

Diffusion Through Cell Membrane

A theory of fundamental interest regarding the diffusion phenomenon is that of simple molecular diffusion. The derivation of this theory is comprised of two familiar differential equations of the Fick's Law of Diffusion

$$P = -D \frac{\partial c}{\partial x} \quad (1)$$

and

$$\frac{\partial c}{\partial t} = D \frac{\partial^2 c}{\partial x^2} \quad (2)$$

Equation (1) gives the rate of permeation per unit area of a medium in terms of the diffusion coefficient and the concentration gradient across the medium ($-\partial c / \partial t$). The second equation, referring to an unsteady diffusion operation, expresses the rate of accumulation of mass at a given point in the medium.

Equation (2) may be solved by the method of boundary value problems under unsteady state of flow. The following assumptions and boundary conditions are specified in the derivation of a formal solution.

1. The extracted material is porous but rigid in its structure and is chemically inert.

2. The extracted material has uniform initial solute concentration.

H. H. Yang is with the Texas-U. S. Chemical Company, Port Neches, Texas.

3. The solute concentration in the liquid surrounding the extracted material is *constant* and uniform.

4. The liquid-film resistance to mass transfer at the interface is negligible.

5. The equilibrium solute concentration in the extracted material is a function of the solute concentration in the extracting liquid.

When one considers a solid slab of finite thickness $L = 2a$, the following boundary values exist

$$c = c(t, x)$$

$$c = c_i$$

for $-a \leq x \leq a$ at $t = 0$.

$$c = c_e$$

for $x = -a$ and $x = a$ at all t .

An integrated solution of Equation (2) is obtained as follows (1)

$$\bar{c} = \frac{1}{2a} \int_{-a}^a c \, dx \quad (3)$$

and

$$\bar{c} = c_e + (c_i - c_e) \frac{8}{\pi^2} \sum_{m=0}^{\infty} \frac{1}{(2m+1)^2} \cdot \exp \left[\frac{-D(2m+1)^2 \pi^2 t}{L^2} \right] \quad (4)$$

Sherwood (9) and Newman (7), by a simple transformation of Equation (4), obtained the following equation:

$$E = \frac{\bar{c} - c_e}{c_i - c_e} \quad (5)$$

$$E = \frac{8}{\pi^2} \sum_{m=0}^{\infty} \frac{1}{(2m+1)^2} \cdot \exp \left[\frac{-D(2m+1)^2 \pi^2 t}{L^2} \right] \quad (5a)$$

It may be seen that E is dimensionless and expresses in a sense the fraction of extractable solute in an extracted ma-

terial. The magnitude of E ranges from unity to zero; thus $E = 1.0$ for any unextracted material. The value of E reduces to a fraction during the course of extraction. It can also be seen that the right hand side of Equation (5a) is a rapidly converging series. If D and L are constant, E will nearly be a linear function of the extraction time on a semilogarithmic coordinate. This was confirmed for systems involving solids of uniform, porous structure and negligible liquid-film resistance (2, 6, 8).

Mass Transfer through Liquid Film

The mass transfer rate through liquid film at the solid-liquid interface may be expressed by the following equation

$$-\frac{dc}{dt} = k_i A (c_e - s) \quad (6)$$

where $(c_e - s)$ is the concentration gradient across the liquid film. Actually for a material such as sugar beets, the term c_e in Equation (6) should represent the true sugar concentration in the natural beet juice rather than the sugar concentration in the beets. A term $c_{e,i}$ may therefore be used to denote the true equilibrium sugar concentration in the beet juice under diffusion. Equation (6) reduces to

$$-\frac{dc}{dt} = k_i A (c_{e,i} - s) \quad (7)$$

If the liquid-film resistance is negligible, the mass transfer coefficient should be substantially independent of the relative velocity of extracting liquid, temperature, solid particle size, etc. This may be regarded as the criterion of a diffusion-controlled solid-liquid extraction process.

The extraction of sugar from beets is generally considered a diffusion-controlled phenomenon. If this can be experimentally confirmed, it is then logical to

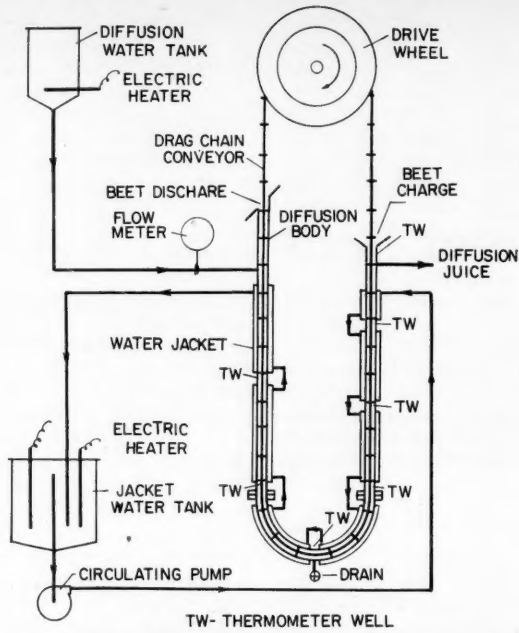


Fig. 1. Flow diagram of continuous diffusion equipment.

correlate the extraction data of beet sugar in terms of E , as defined by Equation (5), and the extraction time. Such correlation may be made in the following manners.

Continuous Countercurrent Diffusion

If the distribution of solute concentration in the extracted solid and in the extracting liquid in the entire diffuser are known, the local values of E along the diffusion path can be calculated accordingly. Also define the extraction time as the time of traverse for the extracted solid since entering the diffuser. Knowing the speed of the conveyor which transports the extracted solid, therefore, one can determine the distribution of E in the diffuser as a function of the extraction time. Such an E - t relationship represents a generalized correlation of mass transfer in a continuous diffuser, since E is an explicit function of c_1 , c_e , and \bar{c} .

The rate of change in E in a continuous diffuser can be obtained by differentiating E against the extraction time:

$$\frac{\partial E}{\partial t} = \frac{(c_1 - c_e) \frac{\partial \bar{c}}{\partial t} - (c_1 - \bar{c}) \frac{\partial c_e}{\partial t}}{(c_1 - c_e)^2} \quad (8)$$

where $\frac{\partial \bar{c}}{\partial t}$ represents the rate of change in solute concentration in the extracted solid or the instantaneous extraction rate, and $\frac{\partial c_e}{\partial t}$ represents the rate of change in equilibrium solute concentration. $\frac{\partial E}{\partial t}$ may be regarded as the generalized instantaneous extraction rate of a continuous diffusion process.

the same conditions of temperature, solute concentrations, particle size, etc. Therefore the authors postulate that the rate data of simple diffusion may be manipulated to simulate a continuous countercurrent diffusion system. For example the change in E in a continuous diffuser may be estimated by using the rate data of simple diffusion in the following manner:

$$\Delta E = \int_{t_1}^{t_2} \left(\frac{\partial E}{\partial t} \right) dt \quad (10)$$

Also the required extraction time of a continuous diffusion process may be calculated by

$$\Delta t = \int_{E_1}^{E_2} \frac{1}{\left(\frac{\partial E}{\partial t} \right)} dE \quad (11)$$

In the present investigation Equations (10) and (11) were suggested to interrelate the extraction rates of continuous diffusion and simple diffusion and examine the feasibility of applying the E - t data to diffusion calculations.

EXPERIMENTAL—CONTINUOUS COUNTERCURRENT DIFFUSION

Simple Diffusion

Simple diffusion means that the diffusion process can be carried out under the conditions defined in the derivation of Equations (4) and (5a), particularly item 3. It is actually possible to obtain experimental diffusion data under these conditions. That is a batch of solid may be extracted by a solution with constant solute content. The results thus obtained represent the change in solute concentration in the extracted solid with respect to the diffusion time. Since the solute concentration in the extracting liquid is known, the simple diffusion data can be readily converted into E as a function of diffusion time.

Differentiation of the E - t function of simple diffusion also gives the rate of change in E . Under the conditions of simple diffusion however the equilibrium solute content of the extracted solid is a constant value. We have therefore

$$\frac{\partial E}{\partial t} = \frac{1}{c_1 - c_e} \frac{\partial \bar{c}}{\partial t} \quad (9)$$

The E - t correlations for the continuous countercurrent diffusion are apparently different from those for the simple diffusion. A continuous diffusion system however may be comprised of infinite number of simple diffusion systems. At each point in a continuous diffuser there may be a simple diffusion system, where the local solute concentration in the extracting liquid is momentarily constant; if so Equation (8) reduces to Equation (9). Thus the local diffusion rate at any point in a continuous diffuser is equal to that of a simple diffusion system under

The equipment employed in the present investigation was originally constructed to develop a continuous countercurrent process for the extraction of beet sugar. Figure 1 shows the flow diagram of the diffusion equipment. The diffuser was in the shape of a U tube and was fabricated from a $\frac{1}{2}$ in. brass sheet. The major part of the diffuser was provided with several sections of hot water jacket. These sections were designed to allow the installation of sampling taps and thermometer wells along the diffusion path. The diffuser body was made square in its cross-section to permit a drag chain conveyor which transported the sugar beets to be extracted. The entire conveyor consisted of a large number of chain units; each was 4 in. in its effective length. Each chain unit was composed of a 9/12 in. diam. shaft and a screen plate in its middle. The screen plate was 1-13/32 in. sq. in cross section, providing a total clearance of not more than $\frac{1}{2}$ in. to the diffuser wall. There were thirty-two evenly spaced perforations of $\frac{1}{16}$ in. diam. to permit the flow of extracting solution. The extracting solution flowed countercurrent to the sugar beets.

The conveyor was driven at a constant speed of 1.494 in./min. This speed allowed the manual charging of beets into the diffuser. The diffusion water was fed to the diffuser by means of gravity flow. An inverted manometer was available to control the flow rate of diffusion water. The average effective diffusion path was 88.5 in. corresponding to a total diffusion time of 59.25 min.

The experiments of continuous countercurrent diffusion were carried out with the Michigan sugar beets almost exclusively. To imitate commercial operation sugar beets were cut into 0.0383 in. thick, $\frac{1}{4}$ in. wide, and $\frac{1}{2}$ -1 in. long V-shaped chips, commercially called the *cossettes*. During

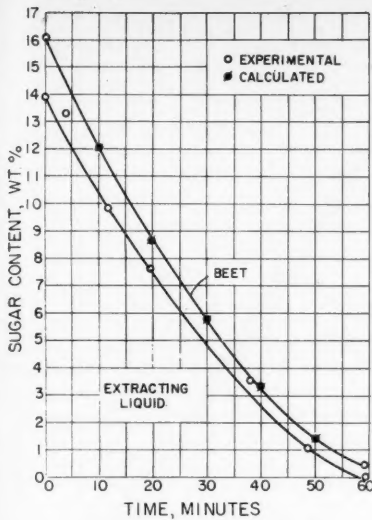


Fig. 2. Typical continuous diffusion curves of Michigan sugar beets.

the experiment cossettes were charged into the diffuser at a rate of 61 g./conveyer unit. This resulted in a diffusion bed about 50% packed, which generally prevails in commercial diffusers. While the cossettes were charged at a constant rate, the diffusion water was fed countercurrently at a relative rate of 1, 1.1, or 1.2 lbs./lb. of fresh cossettes. The diffusion temperature, which was regulated by circulating the jacket water, was kept constant at 65, 70, 75, or 80°C.

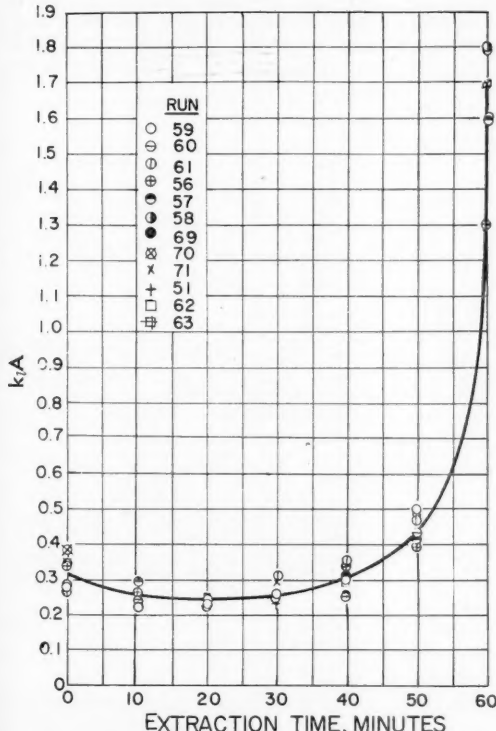


Fig. 4. Correlation of $k_l A$ in continuous countercurrent diffuser.

At the steady-state of a diffusion test, samples of diffusion juice were withdrawn from the sampling taps along the diffuser. These samples were analyzed for their sugar content by the refractometric method (4). The sugar content of the fresh and exhausted cossettes was determined by the official polarimetric method (4). The sugar content of the fresh and exhausted cossettes was determined by the official polarimetric method (4). The sugar content of the beets is expressed in the weight percentage of the beets rather than in the weight percentage of the natural beet juice. It is known that the weight fraction of inert materials in the beets is generally constant.

A series of twelve experiments was devoted to the study of the continuous diffusion phenomenon. Each experiment was conducted at constant temperature and solvent/feed ratio with cossettes of a uniform size. Table 1 presents the results of these experiments and the data of Runs 5, 7, and 8, made with the California beets.*

CORRELATION OF CONTINUOUS DIFFUSION DATA

In correlating the continuous diffusion data the relative positions of all sampling taps along the diffuser are converted into the extraction time of cossettes by a consideration of the conveyer speed. This establishes the distribution of sugar concentration in the extracting liquid as

*Tabular material has been deposited as document 5764 with the American Documentation Institute, Photoduplication Service, Library of Congress, Washington 25, D. C., and may be obtained for \$1.25 for photoprints or \$1.25 for 35-mm. microfilm.

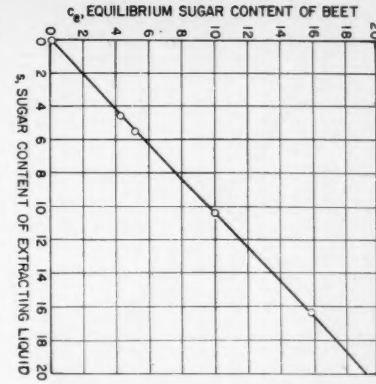


Fig. 3. Equilibrium concentration curve of Michigan sugar beets.

a function of extraction time along the entire diffuser. The sugar content of the cossettes was known at the inlet and outlet of the continuous diffuser only. Its distribution in the diffuser had to be calculated by material balance between the cossettes and the extracting liquid. Figure 2 illustrates a typical concentration-time plot of the continuous countercurrent diffusion experiment, the lower curve representing the distribution of sugar concentration in the diffusion juice throughout the entire diffuser and the upper curve the distribution of sugar concentration in the beets throughout the diffuser. It is plotted with the experimental values of sugar concentration at the inlet and outlet and the calculated sugar concentrations at inter-

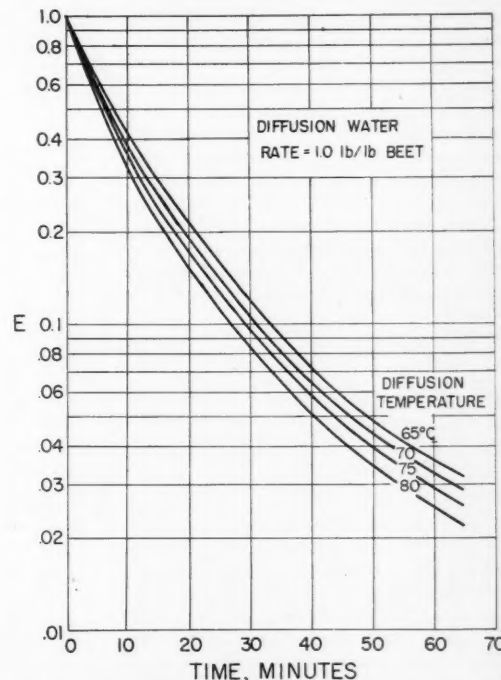


Fig. 5. Generalized plot of continuous diffusion data of Michigan sugar beets.

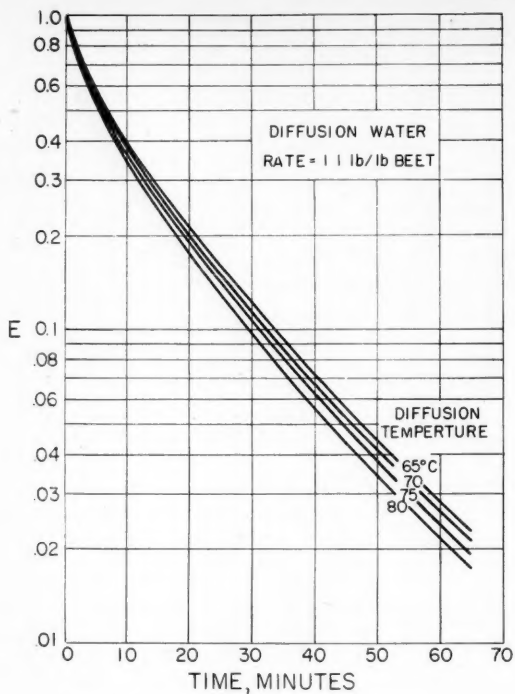


Fig. 6. Generalized plot of continuous diffusion data of Michigan sugar beets.

mediate points of the diffuser. These calculated values of sugar concentration are summarized in the middle part of Table 1 accordingly.

For the purpose of correlation the equilibrium sugar content of Michigan beets was determined experimentally by the simple diffusion method. In Figure 3 the equilibrium sugar content of beets is plotted as a function of the sugar content of the extracting liquid. Applying the sugar concentrations in Table 1, one may readily obtain the corresponding equilibrium sugar concentrations from Figure 3; these values of c_e are entered in Table 1.

This paper now proceeds to determine whether the extraction of beet sugar is a diffusion-controlled phenomenon by using experimental data. From Equation (7)

$$k_l A = -\frac{d\bar{c}}{dt} \frac{1}{c_{ei} - s} \quad (12)$$

The true equilibrium sugar concentration in the preceding equation can be computed from the experimental values of c_e in Table 1 according to

$$c_{ei} = \frac{100c_e}{74 + c_e} \quad (13)$$

since the average water content of Michigan sugar beets weighed about 74% (5). The interfacial area (A) may be assumed to be constant because the size of cossettes was kept uniform and constant in this investigation. The term $k_l A$ is therefore indicative of the liquid-film transfer coefficient.

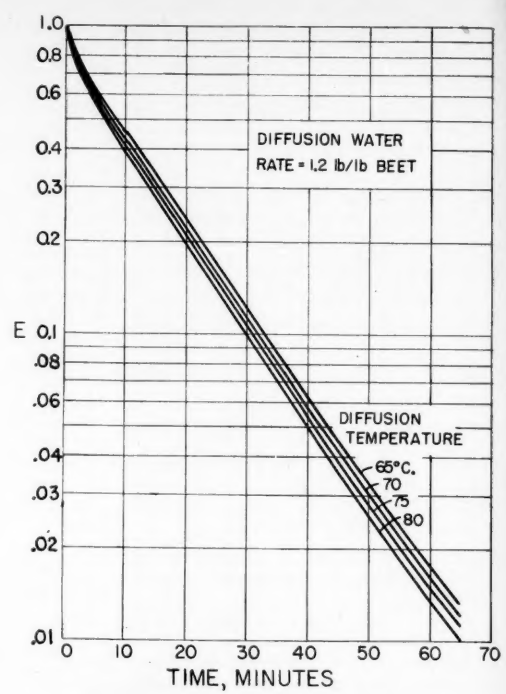


Fig. 7. Generalized plot of continuous diffusion data of Michigan sugar beets.

The values of $k_l A$ calculated according to Equation (12) are plotted against the extraction time in the continuous countercurrent diffuser in Figure 4. Almost all experiments tabulated in Table 1 are included in this plot. It is seen that the distribution of $k_l A$ in the continuous diffuser is not affected by the extraction temperatures and diffusion water rates employed in various runs. Therefore the liquid-film resistance is negligible, and

the extraction of beet sugar is predominantly a diffusion-controlled process.

On the basis of this conclusion the continuous countercurrent diffusion data may be advantageously correlated in terms of the function E and the extraction time. Thus Equation (5) is applied to evaluate the distribution of E in the continuous diffuser.

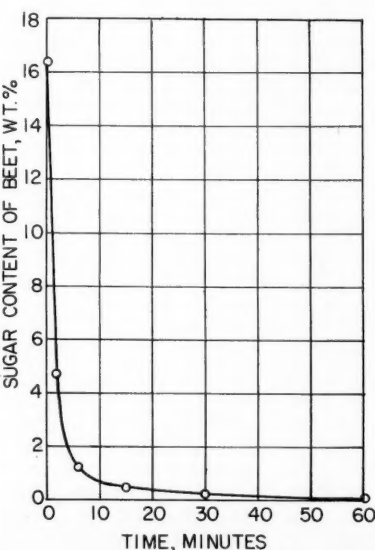


Fig. 8. Typical simple diffusion curve of Michigan sugar beets (Run 67).

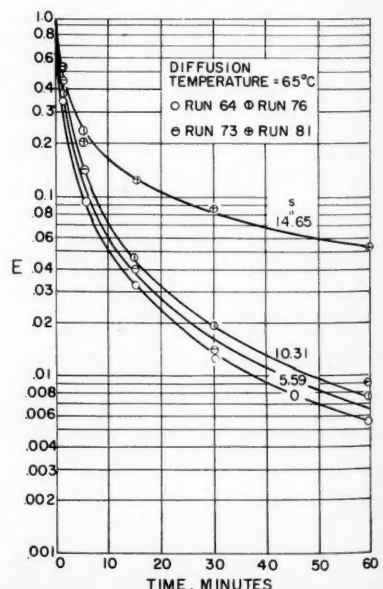


Fig. 9. Correlation of simple diffusion data of Michigan sugar beets.

For example in Table 1, under Run 51,

$$c_1 = 16.65$$

$\bar{c} = 13.32$ at 10 min. of extraction

$s = 11.39$ at 10 min. of extraction

From Figure 3 one obtains

$$c_e = 10.90$$

Hence,

$$E = \frac{13.32 - 10.90}{16.65 - 10.90} = 0.421$$

This value is entered in Table 1 along with the other calculated E values.

The calculated values of E from Table 1 are plotted in Figures 5, 6, and 7 against the extraction time, with the water/beet ratio and diffusion temperature used as the parameters; these experiments were carried out with cosettes of a uniform size. These correlations were examined with the experimental data of twenty-three continuous diffusion tests (10). The deviation between the calculated and experimental data was found to be about $\pm 5\%$. One may conclude that the correlations presented in Figures 5 to 7 have a generalized nature.

EXPERIMENTAL—SIMPLE DIFFUSION

The apparatus employed in the study of simple diffusion consisted of a 1 liter beaker with a fitted detachable screen batch. The cosettes to be extracted were placed in the screen batch and packed to roughly the same degree as in the continuous diffuser. Also cosettes of the same size as those employed in the continuous diffusion tests were employed. A sugar solution having a constant sugar concentration was then introduced into the batch through several nozzles and continually overflowed. In a series of simple diffusion experiments cosettes from the same stock were extracted in several batches separately for 2, 6, 15, 30, and 60 min. with a sugar solution of the

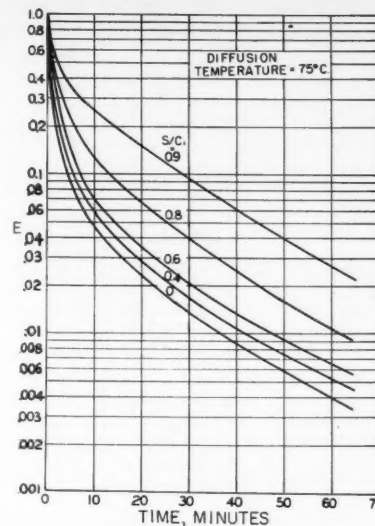


Fig. 11. Generalized plot of simple diffusion data of Michigan sugar beets.

same strength. The extracted batches were then analyzed for their sugar content.

Table 2* presents the operating conditions and the concentration-time data of the simple diffusion experiments. The sugar content of the fresh cosettes of each run is referred to zero time of extraction, while the equilibrium sugar content relative to the diffusion liquid is referred to infinite time of extraction. A typical plot of the concentration and time data is shown in Figure 8.

A special series of simple diffusion experiments was conducted to determine the equilibrium sugar content of Michigan sugar beets. Each diffusion batch was extracted by a solution of constant sugar content for a period of more than 24 hr. The residual sugar content of the beets was then regarded as the equilibrium sugar

*See footnote on page 455.

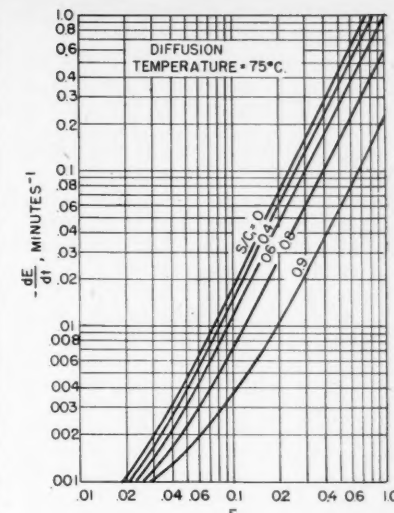


Fig. 13. Generalized plot of instantaneous diffusion rate of Michigan sugar beets.

content. Results of these tests were employed to construct the equilibrium curve in Figure 3.

CORRELATION OF SIMPLE DIFFUSION DATA

The correlation of simple diffusion data includes the E - t relationship and the generalization of simple diffusion rate. Since the sugar concentration in the extracting solution was constant, the equilibrium sugar concentration in the beets in each run was constant. This makes the calculation of E a rather simple matter.

For example in Table 2, under Run 65,

$$c_1 = 18.25$$

$$s = 0$$

$$c_e = 0.04$$

At 6 min. of extraction,

$$\bar{c} = 2.34$$

Therefore

$$E = \frac{2.34 - 0.04}{18.25 - 0.04} = 0.127$$

The calculated values of E are presented in the lower part of Table 2. These data, when plotted against diffusion time as in Figure 9, scatter around widely. A family of curves are drawn according to the constant sugar concentration in the extracting liquid. This is different from King's correlation (6), where a single E - t curve is plotted. The plot in Figure 9 indicates that the rate of change in E decreases with increasing sugar concentration in the extracting solution. One would question why the dimensionless number E , being a function of the equilibrium sugar concentration and others, is still affected by the sugar

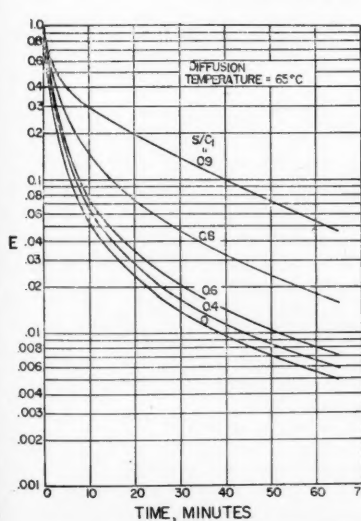


Fig. 10. Generalized plot of simple diffusion data of Michigan sugar beets.

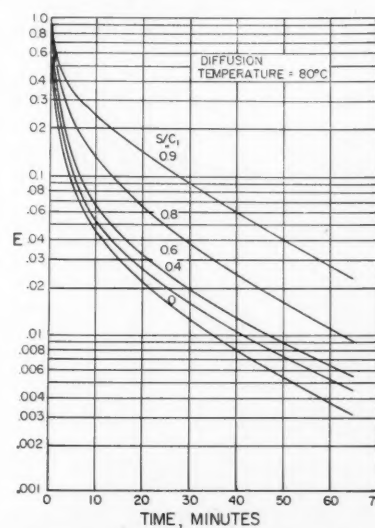


Fig. 12. Generalized plot of simple diffusion data of Michigan sugar beets.

concentration. The following discussion may perhaps be offered.

According to the simple diffusion theory the diffusion coefficient is constant at constant temperature. The value of E as given in Equation (5a) is a unique function of diffusion time at constant diffusion temperature and constant thickness of the extracted solid slab. In the nonidealized diffusion, such as the extraction of beet sugar, the diffusion coefficient is no longer a constant owing to the nonuniform structure of beet cells. Therefore such a system deviates from Equation (5a) not only in that the $E-t$ plot is curvilinear but in that E is dependent on the sugar concentration (s) in the extracting liquid.

The value of E can be affected by the solute concentration in the extracting liquid under certain circumstances. Thus E will remain at unity in a diffusion system, if the sugar concentration is such that the corresponding equilibrium sugar concentration equals the initial sugar concentration in the natural beet juice. Under such condition of course the net mass transfer by diffusion should be zero. It may be shown mathematically that

$$E = \lim_{\substack{\bar{c} \rightarrow c_1 \\ \bar{c} = c_1}} \frac{\bar{c} - c_e}{c_1 - c_e} = \frac{\frac{\partial}{\partial c_e} (\bar{c} - c_e)}{\frac{\partial}{\partial c_e} (c_1 - c_e)} = 1$$

For a nonideal system therefore the effect of solute concentration on E is pronounced appreciably at a high concentration level (Figure 9).

The diffusion of beet sugar is complicated by the fact that up to 18% of the beet cells are ruptured mechanically in the preparation of cosettes. There is always considerable washing effect in such a diffusion process. This is indicated by the abrupt concentration change of the simple diffusion curve in Figure 9. The diffusion mechanism is further complicated by the phenomenon of fluid flow through a packed bed in the diffuser.

To generalize the correlation as suggested in Figure 9 it is necessary to employ a dimensionless parameter instead of the sugar concentration. The concentration ratio of s/c_1 is therefore introduced for this purpose. The significance of using s , here can be derived from the argument that $E = 1$ at all time when c_e approaches c_1 . With reference to Figure 3 this prevails when $s/c_1 = s/c_e = 1.04$ to 1.06 in the high concentration range. If the experimental data are plotted as E vs. s/c_1 with the extraction time used as the parameter, all curves should converge at $E = 1$ and $s/c_1 = 1.04$ to 1.06. It is then possible to extrapolate the experimental data and obtain the $E-t$ functions at even values of s/c_1 . Such correlations are shown in Figures 10, 11, and 12 for diffusion tests at 65, 75, and 80°C., respectively.

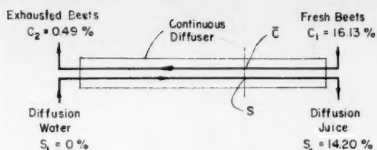


Fig. 14. Terminal conditions of example.

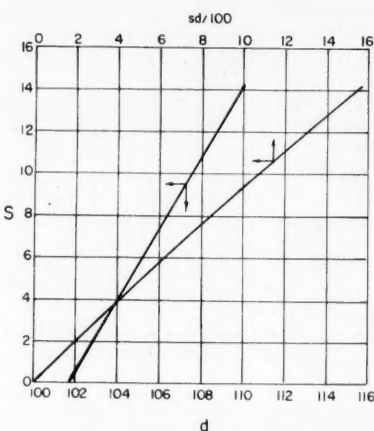


Fig. 15. Example, estimation of distribution of diffusion liquid in a continuous counter-current diffuser.

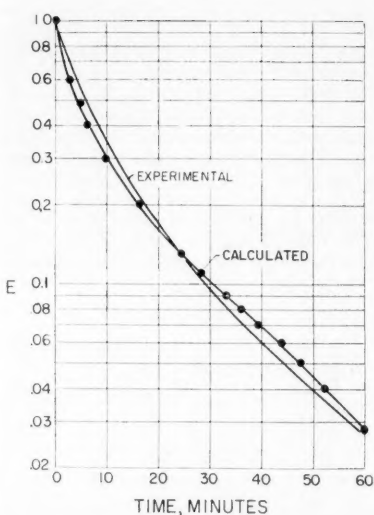


Fig. 16. Example, comparison of experimental and calculated continuous diffusion data.

These simple diffusion curves may be differentiated readily to yield the generalized diffusion rate ($\partial E / \partial t$). Figure 13 shows a plot of $-\partial E / \partial t$ vs. E for simple diffusion at 75°C.

SIMPLE DIFFUSION AND CONTINUOUS DIFFUSION

As has been suggested the rate data of simple diffusion may be integrated

according to Equation (10) or (11) to simulate a continuous diffusion process. The experimental data of both simple diffusion and continuous countercurrent diffusion can now be employed to verify such a postulation. The following example illustrates the principles of mathematical manipulation and provides an evidence of verification:

EXAMPLE

Michigan sugar beets are to be processed in a continuous countercurrent diffuser as shown in Figure 14. The cosettes are 0.0383 in. thick and $1/2$ to 1 in. long, so that the correlation in Figure 13 can be applied. The required time of extraction is estimated under the following operating conditions.

Diffusion temperature = 75°C.
Diffusion water rate = 1.017 lb. water/lb. fresh beets
 $c_1 = 16.13$ lb. sugar/100 lb. wet beets
 $c_2 = 0.49$ lb. sugar/100 lb. wet beets
 $s_1 = 0$
 $s_2 = 14.20$ lb. sugar/100 lb. extracting solution

Diffusion juice produced = 1.102 lb./lb. fresh beets

The value of diffusion juice produced often deviates from what it should be according to the material balance of diffusion water rate and amount of sugar extracted. This is assumed to result from the counterdiffusion of water into the beet cells. No correlation regarding the weight loss of the exhausted beets is available.

SOLUTION

To simulate the continuous countercurrent diffusion operation it is necessary to establish first the distribution of E along the entire diffuser. The relative amount of extracting liquid is assumed to increase linearly with its sugar content. From the given conditions the following terminal figures are known.

$$s_1 = 0, \quad d_1 = 101.7; \\ s_2 = 14.20, \quad d_2 = 110.2.$$

A straight line may then be drawn through these values on a $s-d$ plot in Figure 15.

It can be seen that the value of $sd/100$ represents the amount of sugar in pounds per 100 lb. of fresh beets. The $s-d$ plot in Figure 15 enables one to calculate $sd/100$ as a function of s , which is plotted in the same figure. If the sugar concentrations at two points in the diffuser are known, the corresponding values of $sd/100$ can be obtained readily from this graph. The difference between two local values of $sd/100$ will then represent the amount of sugar extracted between the same points.

At a certain point near the inlet of fresh cosettes for instance, let the average sugar content of the beets be 14.0%. The amount of sugar already extracted from the fresh beets since entering the diffuser is approximately equal to

$$16.13 - 14.0 = 2.13 \text{ lb./100 lb. fresh beets.}$$

This m
convert
free bas
change
extracti
 $s_2 d_2 / 10$

Hence s
 $s_2 d_2 / 10$

From t
this po

The di
then b
Since

From 1

This
ment
remain
button
may t
marize
At t

The
estima

Gr
was ca
colum
time v
expiri
for Ru
of E a
in Fi
expiri
Figure
curve
concen
the ag
experi

CONC

1. T
diffus

*See

Vol.

This material balance is made without converting the concentrations into solute-free basis. It is true only if the beets did not change in weight at a small amount of extraction, and if the counterdiffusion of water equals that of sugar juice. Since

$$s_2 d_2 / 100 = (110.2)(14.20) / 100 = 15.54$$

Hence at the point under consideration

$$\begin{aligned} sd / 100 &= s_2 d_2 / 100 - \Delta (sd / 100) \\ &= 15.54 - 2.13 \\ &= 13.41 \end{aligned}$$

From the s - d plot in Figure 15 therefore

$$s = 12.30 \text{ at this point.}$$

From Figure 3 $c_e = 11.55$. Consequently at this point

$$E = \frac{14.0 - 11.55}{16.13 - 11.55} = 0.535$$

The diffusion rate $\partial E / \partial t$ at this point may then be obtained in the following manner. Since

$$s/\bar{c} = \frac{12.30}{14.0} = 0.878$$

From Figure 13 at $E = 0.535$

$$-\frac{\partial E}{\partial t} = 0.075 \text{ min.}^{-1}$$

This procedure is followed by small decrements in the sugar concentration in the remaining part of the diffuser. The distribution of E and $\partial E / \partial t$ in the entire diffuser may thus be established. Table 3* summarizes the results of such evaluation.

At the end of the diffusion process

$$E_2 = \frac{0.49 - 0.04}{16.13 - 0.04} = 0.028$$

The total extraction time may therefore be estimated by applying Equation (11) as

$$\Delta t = \int_{0.028}^1 \frac{1}{\left[-\frac{\partial E}{\partial t} \right]} dE$$

Graphical integration of this expression was carried out and tabulated in the last column of Table 3. The calculated extraction time was found to be 59.90 min. against an experimental value of 59.25 min. as required for Run 69 (Table 1). The calculated values of E are plotted against the extraction time in Figure 16 and compared with the experimental E - t curve transposed from Figure 5. The peculiar shape of the calculated curve is probably owing to the use of sugar concentrations on the wet basis. However the agreement between the calculated and experimental curves is satisfactory.

CONCLUSION

1. The extraction of sugar beets is a diffusion-controlled process. As is ex-

pected the liquid-film mass transfer coefficient of the beet-water system is independent of the diffusion temperature, the extracting liquid rate, etc.

2. The continuous diffusion data may be correlated in the form of E vs. the extraction time by using the diffusion temperature, the extracting liquid rate, etc. as the parameters. Such a correlation, as illustrated in Figures 5 to 7, offers some merits on account of its generalized nature. It is questionable however if this type of correlation would be suitable for the solid-liquid leaching process, where the liquid-film resistance has considerable influence on the extraction rate.

3. The simple diffusion experiments proved to be a valuable technique in the study of solid-liquid diffusion phenomena. This method can be equally applied to determine the effects of alternate variables such as the particle size of the extracted solid and the packing effect of the extracted bed.

4. The E - t correlation of simple diffusion data of the beet-water system reveals the influence of sugar concentration on the extracting liquid. The rate of change in E decreases with increasing sugar concentration in the extracting liquid. This effect is considerably pronounced at high sugar concentration close to the sugar concentration in the fresh beets. A dimensionless concentration ratio of s/c_1 is introduced as a parameter in the E - t correlation.

5. The relationship between the simple diffusion and the continuous diffusion was studied. On the basis of the verification of Equation (11) by numerical calculation in the preceding example, it is feasible to assume that a continuous diffusion system consists of an infinite number of simple diffusion systems operated under the same local conditions. The generalized simple diffusion data may therefore be manipulated to simulate a continuous diffusion system in process or scale up calculations.

ACKNOWLEDGMENT

The authors wish to express their sincere appreciation to the U. S. Department of Agriculture, Western Regional Research Laboratory, Albany, California, and to the Farmers and Manufacturers Beet Sugar Association, Saginaw, Michigan, for supporting this research project at the University of Michigan, Ann Arbor, Michigan.

NOTATION

- A = solid-liquid interfacial area for mass transfer, sq. ft.
- a = one half thickness of the extracted solid slab, ft.
- c = solute concentration in the extracted solid or sugar concentration in the beets, lb./100 lb. of wet beets

c_1 = initial solute concentration in the extracted solid

c_2 = final solute concentration in the extracted solid

c_e = equilibrium solute concentration in the extracted solid

c_{ei} = true equilibrium sugar concentration in the natural beet juice, lb. of sugar/100 lb. of beet juice

\bar{c} = average solute concentration in the extracted solid slab as defined by Equation (3)

d = relative rate of the extracting liquid, lb./100 lb. of the extracted solid or the fresh beets

d_1 = relative rate of the extracting liquid when entering a diffuser

d_2 = relative rate of the extracting liquid when leaving a diffuser

D = diffusion coefficient, sq. ft./min.

E = fraction of extractable solute of an extracted solid as defined by Equation (5)

k_l = liquid-film mass transfer coefficient, lb. of sugar extracted/100 lb. of wet beets/sq. ft./min.

L = full thickness of the extracted solid slab, ft.

m = positive integer

s = solute concentration in the extracting liquid or sugar concentration in the extracting sugar solution, lb./100 lb. of extracting liquid

s_1 = initial solute concentration in the extracting liquid

s_2 = final solute concentration in the extracting liquid

P = rate of permeation in a diffusion process, lb./sq. ft./min.

t = time of extraction, min.

x = distance of diffusion within the solid slab being extracted, ft.

LITERATURE CITED

1. Barrer, R. M., "Diffusion In and Through Solids," Macmillan, Cambridge (1941).
2. Boucher, D. F., J. C. Brier, and J. O. Osburn, *Trans. Am. Inst. Chem. Engrs.*, **38**, 967 (1942).
3. Brier, J. C., and H. H. Yang, "A Study on the Continuous Countercurrent Diffusion of Beet Sugar," Univ. Mich., *Dept. Eng. Research, Eng. Research Bull.* No. 2322 (July 1955).
4. Browne, C. A., and F. W. Zerban, "Physical and Chemical Methods of Sugar Analysis," 3rd ed., John Wiley and Sons, New York (1941).
5. Howell, J. L., Michigan Sugar Company, Saginaw, Michigan, private communication.
6. King, C. O., D. L. Katz, and J. C. Brier, *Trans. Am. Inst. Chem. Engrs.*, **40**, 5, 533 (1944).
7. Newman, A. B., *Trans. Am. Inst. Chem. Engrs.*, **27**, 310 (1931).
8. Osburn, J. O., and D. L. Katz, *Trans. Am. Inst. Chem. Engrs.*, **40**, 5, 511 (1944).
9. Sherwood, T. K., *Ind. Eng. Chem.* **21**, 12 (1929).

Manuscript received November 7, 1958; revision received April 7, 1959; paper accepted May 11, 1959.

*See footnote on page 455.

Radial Porosity Variations in Packed Beds

L. H. S. ROBLEE, R. M. BAIRD and J. W. TIERNEY

Purdue University, Lafayette, Indiana

The radial variation of void fraction in randomly packed beds of spheres, cylinders, Raschig rings, and Berl saddles was investigated. After packing, the beds were filled with paraffin, which was then allowed to solidify. Slabs were cut from the bed, and annular rings were removed by two different experimental techniques. An analysis of experimental error revealed that reproducibility, for the sample size used, between different parts of the same bed and different beds was quite good.

For highly irregular shapes such as Berl saddles results indicate that the void fraction decreases regularly from one at the wall to the average porosity at about 1 particle radius from the wall. This is in agreement with work of other investigators using irregularly shaped packings; most commercial packings would probably fit in this category.

For regularly shaped particles results are quite different. For spheres and cylinders cycling was observed for more than 2 particle diam. into the bed, the amplitude decreasing as distance from the wall was increased. The maxima and minima were observed at integral multiples of the particle radius. For Raschig rings a hump was observed at about 1/2 particle radius from the wall. The void fraction then decreased to its average value at 1 particle radius and then remained constant.

A common technique in the chemical industry for obtaining extended solid-fluid interfacial areas or good fluid mixing is to pass the fluid through a bed of solid particles. Such systems as catalytic reactors, packed absorption and distillation towers, packed filters, and pebble type of heat exchangers depend on this technique. The design of these units is based upon mechanisms of heat and mass transfer, fluid flow, and pressure drop of the fluid through the bed of solid. These mechanisms in turn are all sensitive to the porosity of the bed. Since the particles in a packed bed are normally arranged in a random order, coupled with the fact that the particles are often of highly irregular shapes, the mathematical treatment of porosity is difficult. In addition, it has long been recognized that the confining wall of the packed bed exerts a decided influence on the porosity of the bed, especially in the region close to the wall, and wall effects have received some attention. The packing in this region is not so tight as in the core of the bed; thus the porosity near the wall is relatively high.

The present work was designed therefore to study the influence of the confining wall on the porosity in a packed bed and was limited to uniformly shaped particles in a cylindrical bed. In the following section a few of the basic mathematical concepts necessary for this work are reviewed. In succeeding sections experimental results are presented and discussed.

THEORY

Definitions of Void Fractions

In a volume partially filled with solid particles each point can be identified as either being in a solid particle or not. A point void fraction can thus be defined as

R. M. Baird is with E. I. DuPont de Nemours and Company, Inc., Niagara Falls, New York, and J. W. Tierney is with Remington Rand Univac, St. Paul, Minnesota.

$$\delta_p = \begin{cases} 0 & \text{if the point is located inside} \\ & \text{a solid particle} \\ 1 & \text{if the point is not located} \\ & \text{inside a solid particle} \end{cases}$$

If the point void fractions are summed along some line in the volume, then a line void fraction can be defined as

$$\delta_L = \frac{1}{L} \int_L \delta_p dL \quad (1)$$

where L is the total length of the line. An area and volume void fraction can be similarly defined

$$\delta_A = \frac{1}{A} \int_A \delta_p dA \quad (2)$$

$$\delta_V = \frac{1}{V} \int_V \delta_p dV \quad (3)$$

In some very regular systems one or more of the void fractions may be true constants or regular functions of system dimensions. In the more usual case however the void fraction varies in some statistical fashion, and average values must be used to represent the void fractions. It is of course important to separate random variation from regular variations which are functions of the system parameters. The work described in this paper is concerned with cylindrical packed beds, and since the chief source of nonrandom variations in the void fraction is the outer wall, it would be expected that one could properly represent the void fraction of an area which is concentric with the outer wall by an average value. There is no reason to suspect any orienting forces other than those of the outer wall, and since all points on a concentric shell are equally affected, only random local variations should be present. Throughout all of the work reported here this assumption has been made. The assumption was checked and verified as will be described later. The void fraction values given then

in this paper are primarily the area void fractions δ_A .

Void Fractions in Regular Beds

In conjunction with experimental measurements of void fraction, calculations were also made for some regular arrangements of spheres in cylindrical beds; spheres were used because they showed the most radial variation of void fraction and are the easiest to handle mathematically. In Figure 1 the area void fraction is plotted vs. distance from the wall for two types of regular packing arrangements and for some experimental data. Each arrangement consists of layers of spheres, the particles in each layer being arranged in a hexagonal pattern. The difference between the two packing arrangements is in the relative location of two adjacent layers of spheres; in the hexagonal-cubic arrangement adjacent layers are identical. The centers of the spheres in each layer are directly over the centers of the corresponding spheres in the layer below. The center of a sphere was arbitrarily placed in the center of the bed. A similar curve would result if an interstice were placed at the center of the bed. In the hexagonal-hexagonal packing the centers of the spheres in one layer are directly over the interstices in the row below; this results in a denser packing than the hexagonal-cubic. The values in Figure 1 were calculated by obtaining the expression for the area of intersection of a sphere and a cylinder and evaluating the resultant elliptic integral by a series expansion. The radial values of area void fraction then were integrated over the appropriate ranges to give points which are comparable to the experimental values. A smooth curve was then drawn through the points.

Also of interest theoretically are the curves for void fractions of spherical particles against a plane wall. These are shown in Figure 2 for two orientations: a cubic arrangement (A) in which the spheres next to the wall are arranged in a square pattern and the adjacent layer is identical (distance between layers is 1 particle diam.), and a hexagonal-cubic arrangement (B) in which the layer touching the wall is hexagonal and the adjacent layer is identical with a 1-particle-diam. distance between layers. Results are shown for 1 particle diam. from the wall. As in Figure 1 the points represent integrated averages, and the curves were drawn through the points.

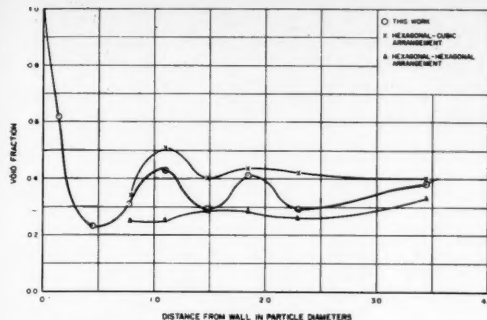


Fig. 1. Calculated area void fraction for regular packing arrangements in the center of a bed and experimental void fractions from Figure 3 plotted vs. distance from the wall.

WORK OF PREVIOUS INVESTIGATORS

In the past, work has been done on over-all voidage (2, 3, 4, 8) incidental to the study of a specific mechanism. Relatively little work has been done to investigate porosity differences within packed beds.

Shaffer (7) measured void space by rotating a packed column 90 deg. to a horizontal position and introducing a known amount of liquid into this section, raising the liquid level in increments. He assumed that void space would be the same everywhere at the same radial position, and by introducing imaginary annular sections of the same width as the height of the liquid level increments he was able to estimate void fraction as an average value for an annular area. He applied the results from the first annular section in calculating the next by assuming that the part of the second liquid-level increment that also includes the first annular section has the same void fraction as that of the first annular section. His results indicated that this assumption was in error; therefore the quantitative value of his results are questionable.

Makoto, et al. (5) measured radial void fraction variations by putting crushed calcium carbonate in a glass tube and filling it with paraffin. After solidification the glass was removed and the rod-shaped section shaved on a lathe, much the same as one of the techniques used in the present work. Their packing material, as a result of the method by which it was prepared, consisted of a variety of shapes and sizes. Their results are not applicable to beds of regularly shaped particles.

EXPERIMENTAL TECHNIQUES

The area void fraction is the desired experimental measurement, and some consideration was given to direct measurement (for example, by photographic techniques). However experimental difficulties were great, and the method selected was to measure the volume void fraction of a series of thin concentric rings. These values are

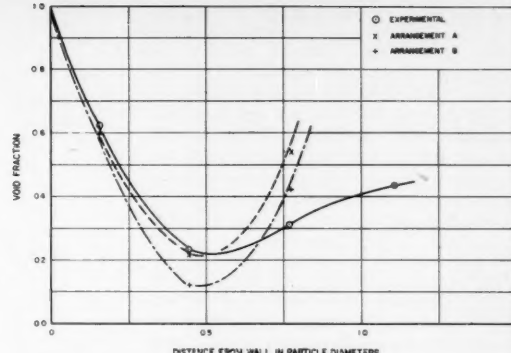


Fig. 2. Calculated area void fraction for regular packing arrangements against a flat wall and experimental void fractions from Figure 3 plotted vs. distance from the wall.

then approximations to the area void fraction. Beds were prepared by pouring the packing into a cardboard cylinder. Several methods of pouring were compared for reproducibility by measuring the over-all void fraction of a test bed. It was found that without tamping results were reproducible within about $\pm 1\%$ and that methods of pouring differed by approximately $\pm 2\%$. Tamping the side of the cylinder thoroughly until no further change occurred produced about a 5% decrease in over-all void fraction. Two somewhat different methods of filling beds were used. For the experiments which will be described in section 1 the beds were filled by inserting a 3.35-in.-diameter tube inside the 6.70-in.-diameter bed, filling the inner tube with spheres, and slowly raising the inner cylinder. This method has been discussed by Leva (4). The bed was not tamped. In the experimental technique of section 2 the bed was filled by simple, rapid pouring and tamped two or three times. In both cases the top row of particles was manually leveled by arranging a few particles, and a screen was placed on the bed to prevent the packing from floating in the hot wax. The bed was preheated to 180°F., and molten wax was added in five or six small batches at about 15-min. intervals to allow air to escape. A soaking period of about 1 hr. at 180°F. was followed by a slow cooling period of more than 8 hr. The cardboard cylinder was then removed and the samples were prepared for analysis.

Two methods were used for preparing and analyzing these samples:

1. The bed was divided into a series of slabs of approximately 1 particle diam. thickness. This thickness was selected rather arbitrarily, but subsequent analysis showed it to be satisfactory. These slabs were cut in half along a diameter, and then each semicircular slab was cut into a number of annular rings by using a set of specially constructed holders. All the slabs were carefully identified during the analysis, since one of the important problems under study was the reproducibility of measurements made in different parts of the bed. The bed used in this part of the work was 6.70 in. in diam., and cork spheres of 0.76 in. diameter were used as packing. Slabs were $\frac{3}{4}$ in. thick and annular rings approximately $\frac{1}{4}$ in. in width.

Analysis for void fraction was made by accurately measuring the volume of the slab before and after removal of the annular ring, melting the material removed, separating the cork from the wax, and calculating the void volume from the weight of wax

and its density. A material balance was made for each measurement by adding the weight of wax and cork and comparing it with the loss in weight of the slab. All balances checked within 0.61%. The void fraction was calculated from the void volume and the total volume.

2. This method worked satisfactorily for cork spheres; however it was found to be unsatisfactory for more brittle material such as those used in the Berl saddles. Consequently another technique for obtaining annular rings was devised. A slab of the bed was mounted in a lathe chuck turning at 3,200 rev./min. Annular rings were shaved off with a sharp tool bit. Some chipping was observed at the edges of the slab, and therefore it was necessary to enclose the slab between two wooden supporting disks which were turned down with the bed disk. A collecting hood was devised to surround the lathe chuck, and the resulting annular ring was obtained as a fine powder consisting of paraffin chips, packing chips, and wood supporting-disk chips. The material from each annular ring was weighed on a triple beam balance, and the sum of these weights was checked against the difference in weight of the disks before and after being turned down. All balances checked within 1%. After weighing, the paraffin was separated from the wood retainer and packing by dissolving the paraffin in boiling benzene. The mixture was filtered, and the filtrate passed through a steam heated condenser. The benzene vapor leaving the collecting flask was condensed and recovered, and the hot wax was air-stripped to remove any remaining benzene. Residual solid material was washed four or five times with benzene to remove residual paraffin.

In addition to the weights of each annular ring, measurements were made of the dimensions of the disks before and after being turned down. The wood-retainer-disk volume was calculated from the dimensions taken for each ring; this was multiplied by the wood density to get the equivalent weight of wood moved. When this weight was subtracted from the weight of solids separated from the paraffin, the weight of packing was obtained. The packing volume was then calculated by using the known packing density, and the volume of wax was obtained from the weight of wax and the density of the wax.

A volume balance was made by checking the sum of the volumes of the component parts against the volume removed as calculated from the dimensions of the section. This deviation for individual cuts was as high as 10%, the average deviation was about 3%, and the deviation for the over-all volume was less than $\frac{1}{2}\%$. These inaccuracies in volume balances may be accounted for by the limited precision in the diameter measurements. Because of small increments in the large diameter of the disks an error in measuring the diameter could cause a deviation of up to 10%. The excellent over-all volume check and the fact that the material balances checked so closely are reasons for believing that the volumes of paraffin and packing are quite accurate. The void fraction was calculated by dividing the volume of paraffin by the volume of packing plus paraffin.

A total of five beds were studied in this manner. Four of the beds had a 6.7-in. diameter, and the packings used were $\frac{1}{2}$ -in. nominal-size Berl saddles made of carbon-wood cylinders $\frac{1}{2}$ in. in diameter and height; carbon Raschig rings with 0.496-in. O.D., I.D. 0.358 in., and height 0.498 in.; and $\frac{1}{2}$ -in. spheres made of composition cork. A fifth bed was prepared by packing a 3.35-in.-diameter bed with $\frac{1}{2}$ -in. nominal-size Berl saddles made of carbon.

EXPERIMENTAL RESULTS

Experimental results are presented in Figures 3 to 6 and Figure 7. The points indicated on the graphs are, as described previously, actually void volumes for a small annular ring about the point. Smooth curves have been drawn through the points, and these curves are approximations to the area void fraction. In Figures 4, 5, and 6 each point represents an experimental value; in Figure 3 however each point represents an average of several experimental values. In Table 1 the values from which the Figure 3 averages were obtained are shown. Detailed experimental results can be obtained in References 1 and 6.

EXPERIMENTAL ERROR

The results in Table 1 are particularly significant, since they reveal the reproducibility of measurements made at the same radial position but at different parts of the bed. Because a sample volume is subject to

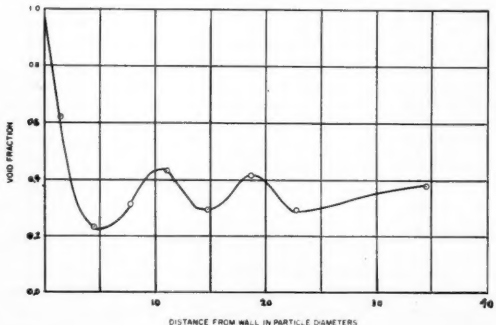


Fig. 3. Area void fraction vs. distance from the wall for 0.76-in.-diam. spheres in a 6.7-in.-diam. cylindrical bed.

TABLE 1. EXPERIMENTAL VOID FRACTIONS FOR BED OF SPHERES

Bed diameter = 6.70 in.
Sphere diameter = 0.76 in.

Disk and section	Radius of annular ring (in.)							
	Distance from center of bed to center of ring							
	3.24	3.01	2.76	2.51	2.23	1.93	1.61	0.72
1A	0.60	0.27	0.29	0.42	0.30	0.33	0.25	0.36
4A	0.62	0.25	0.30	0.38	0.31	0.37	0.30	0.36
4B	0.61	0.24	0.34	0.45	0.27	0.45	*	*
6A	0.64	0.25	0.31	0.40	0.22	0.39	0.29	0.42
6B	0.63	0.22	0.28	0.40	0.31	0.35	0.23	0.34
8A	0.57	0.18	0.36	0.45	0.28	0.48	0.34	0.37
8B	0.63	0.17	0.37	0.48	0.30	0.47	0.26	0.40
9A	0.68	0.30	0.27	0.43	0.27	0.40	0.34	0.38
9B	0.57	0.20	0.32	0.48	0.30	0.41	0.25	0.42
Average	0.62	0.23	0.31	0.43	0.29	0.41	0.29	0.38

*Unable to analyze owing to bed imperfection. Paraffin did not fill voids satisfactorily.

random variations in void fraction, it was important in this work to establish the effect of position in the bed on the experimental void fractions. One bed was divided into nine disks, and each disk was cut on a diameter into two parts. One part was labeled *A* and the other *B*; the *A* parts were all from the same original half of the bed. The results in Table 1 are shown for each half disk and for each of the number of annular rings from this half disk. An analysis of variance was made on the data in Table 1. This analysis showed that there was a highly significant difference in porosity between samples taken at different radial distances, while no significant difference in porosity existed between samples from sections *A* and *B*, that is, opposite sides of the bed or samples at different horizontal levels within the bed. These results indicate that at least for the size samples taken in this work the only significant source of variation in void fraction is the radial distance from the center of the bed. When the results in Table 1 are put together, a standard deviation was determined for the average void fraction. This deviation was 0.0126 expressed in void fraction units. Two confidence limits, 50% and 95%, were determined on the average void fraction by using the *t* test. These were ± 0.009 void fraction units at the 50% level and ± 0.025 void fraction units at the 95% level. These limits were quite low, in fact surprisingly so, and simply mean that void fractions can be

predicted quite accurately with small samples.

It should be emphasized that each of the average void fractions in Table 1 differs significantly from each of the others. For example the last two columns in Table 1 are for distances from the wall of 2.32 and 3.46 particle diam. and would be expected to show the least difference. Yet the probability that these could be samples from the same population can be determined by a *t* test and is less than one in a thousand.

Since the beds were randomly packed, one would normally expect to have essentially no more variation between layers in the same bed than between layers in corresponding beds. This assumption was not checked directly, although other results with spheres as shown in Figure 4 were consistent. In Figures 4, 5, and 6 results are reported for one or two disks as indicated in the figures. Corresponding values were not obtained in each disk, and thus direct comparison is difficult. However the results as plotted in these figures indicate a very good check between corresponding disks. This is further confirmation of the theory that the samples chosen were of such size that they gave good estimates of the void fractions.

DISCUSSION OF RESULTS

Spheres

The experimental results for the radial variation of void fraction of spheres are

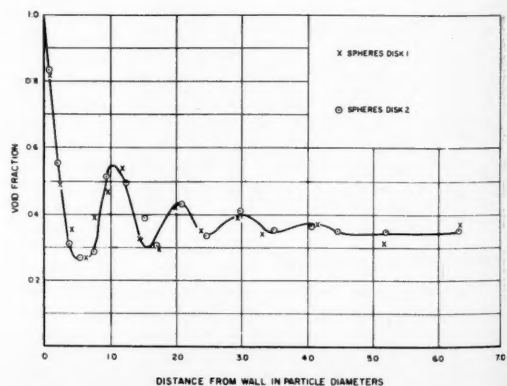


Fig. 4. Area void fraction vs. distance from the wall for 0.49-in.-diam. spheres in a 6.7-in.-diam. cylindrical bed.

Fig. 5.
 showing the v
 of 1 :
 1 par
 maxi
 wall,
 dista
 data
 toget
 were
 not b
 would
 1 pa
 expla
 consi
 the w
 the w
 which
 more
 adjac
 conce
 radiu
 mini
 Simil
 will t
 norm
 maxi
 orient
 some
 Figur
 void
 flat
 ment
 a cu
 and
 wall
 show
 Once
 regul
 made
 data,
 throu
 In
 from
 the
 ing
 hexa
 desc
 resul

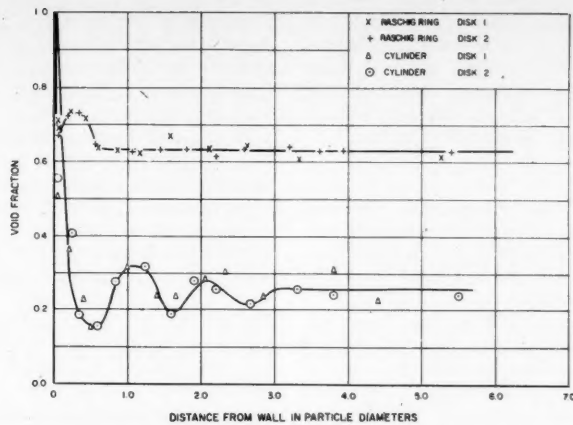


Fig. 5. Area void fraction vs. distance from the wall for 1/2-in. cylinders and 1/2-in. Raschig rings in a 6.7-in.-diam. cylindrical bed.

shown in Figures 3 and 4. In each case the void fraction has the limiting value of 1 at the wall, reaches a minimum at 1 particle radius from the wall and a maximum at 1 particle diam. from the wall, and continues cycling for some distance into the bed. In Figure 7 the data from Figures 3 and 4 are plotted together for comparison. These results were rather unexpected, in that it had not been anticipated that the wall effect would continue to have an effect beyond 1 particle diam. from the wall. The explanation however is quite simple and consists of recognizing that because of the wall a layer of spheres is oriented on the wall. In fact each sphere in the bed which touches the wall is thus uniquely oriented. The net effect will then be that more spheres than usual are located adjacent to the wall, resulting in a concentration of sphere centers at 1 radius from the wall and a consequent minimum in porosity at that point. Similarly at 1 diam. from the wall there will tend to be a greater porosity than normally because this is the point of maximum porosity for a sphere which is oriented at the wall. This can be shown somewhat more graphically by examining Figure 2 which shows the variation in void fraction for a layer of spheres at a flat wall. The values for two arrangements of spheres on the wall are shown: a cubic arrangement on the wall (A) and a hexagonal arrangement on the wall (B). Experimental results are also shown in Figure 1 for the data in Table 1. Once again the calculated values for the regular arrangements were integrated to make them comparable with experimental data, and smooth curves were drawn through the points.

In Figure 1 the experimental results from Figure 3 are plotted together with the calculated results obtained by assuming a hexagonal-cubic or hexagonal-hexagonal arrangement in the bed as described under Theory. The actual results are intermediate between the

two types of regular packing. The effect of the wall, which is not included in the calculations for the regular beds, accounts for the increased cycling.

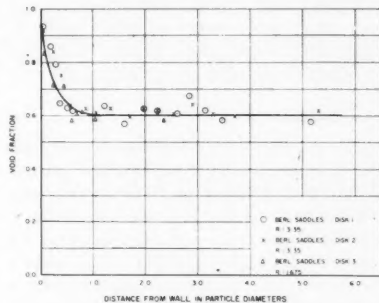


Fig. 6. Area void fraction vs. distance from the wall for 2/1-in. Berl saddles in 6.7- and 3.35-in.-diam. cylindrical beds.

The combination of a layer of particles adjacent to the wall and a regular arrangement in the bed can thus give a qualitative explanation of the cycling observed. However because of the random nature of the actual packing arrangement it is not likely that the curves can be

calculated, and experimental results such as Figure 7 should be used rather than any calculation for regular arrangements.

In Figure 7 separate curves are drawn for each bed-diameter-to-particle-diameter ratio (the term *diameter ratio* will be used in the following). Examination of these curves shows that the maximum and minimum points occur essentially at fixed multiples of particle radius. This clearly indicates that the orienting influence of the wall provides layers of spherical particles the centers of which are separated by 1 diam. from the next layer. There is some indication that for the bed with the smaller diameter ratio the spacing is somewhat less than 1 diam. after $1\frac{1}{2}$ radii from the wall. It is difficult to determine whether this effect is significant. If it is, then it might be explained by the fact that since the diameter ratio is small, there might be a tendency for hexagonal clusters in the center of the bed to be uniquely oriented. This is supported by the observation that the cycling does not damp out as regularly for the smaller diameter ratio bed. In general the results from the two different sets of data agree quite well, with the exception of the maximum point at the first particle diameter from the wall. This discrepancy might be explained by either of two causes:

1. Since the two sets of data were obtained by different experimenters, using different techniques and different diameter ratios, the difference might be attributed to variations in experimental technique and methods of packing the bed. However the reproducibility of results indicated under Experimental Errors and the data of Figure 4 plus the excellent agreement of the data in Figure 7, with the exception of that at 1 particle diam. from the wall, leads the authors to feel that this is not the explanation.

2. It is difficult to estimate what effect the diameter ratio has on the void fraction at 1 particle diam. from the wall; however a qualitative explanation of the observed difference can be made. It has been shown that near the wall the

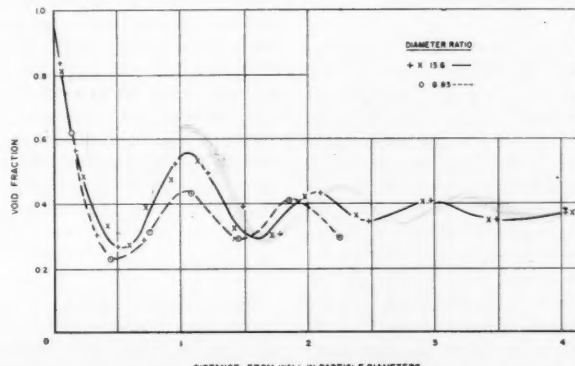


Fig. 7. Area void fraction vs. distance from the wall for 0.76- and 0.49-in.-diam. spheres in a 6.7-in.-diam. cylindrical bed.

particles are oriented in cylindrical layers 1 particle diam. thick. The porosity at 1 diam. is thus a measure of the degree of separation of the first two layers. At certain diameter ratios there could be exactly room for an integral number of spheres in the outer layer and an integral number in the next row. It would then be expected that there would

TABLE 2. A COMPARISON OF VOID FRACTIONS FOR SPHERES AND CYLINDERS

Distance to wall, particle diam.	δ_A (spheres)	δ_A (cylinders)	Ratio
0.5	0.27	0.16	0.59
1.0	0.54	0.32	0.59
1.5	0.31	0.21	0.68
2.0	0.42	0.27	0.64
2.5	0.34	0.22	0.65
3.0	0.40	0.25	0.63

be a minimum of mixing and a high porosity. At other diameter ratios there will be a certain amount of mixing taking place with a subsequent lowering of the porosity. This failure of the outer two layers each to contain an integral number of particles would seem to be more critical for smaller diameter ratios, where the number of spheres involved in any one layer is smaller. It might be expected that this effect would persist beyond the first diameter, but the damping plus experimental variations makes it difficult to detect.

It will be noted in Figure 7 that the experimental points are much closer together for the large-diameter ratio and consequently represent smaller annular rings. As has been discussed previously, the area void fraction is a point property, and if an average value is obtained over a volume, some smoothing must result. However for the data shown in Figure 7 no significant changes occur if the data for the 13.6-diam. ratio bed is smoothed to make it comparable with that for the 8.8-diam. ratio bed. The void fraction in the center of the bed is 0.38 for Figure 3 and 0.35 for Figure 4; the discrepancy may be owing to differences in the manner of packing or to the difference in diameter ratio.

Cylinders

The variation of void fraction with radial position for a bed of cylinders is shown in Figure 5 and is very similar to that obtained with $1/2$ -in.-diameter spherical particles in the same size bed. The cylinders tested were $1/2$ in. in height and diameter. When these results are compared to the results for spheres in Figure 4, an interesting result is observed; the ratio of any point void fraction in the bed of cylinders to the same point in the bed of spheres is approximately 0.67. This is shown in Table 2. This ratio happens to be the ratio in volume of a sphere and a cylinder. Because of the similarity between the shapes of these

cylinders and spheres, it would be expected that their radial porosities would be quite similar, although there does not seem to be any reason why the void fraction ratio should be inversely proportionate to particle diameter.

Raschig Rings

Contrary to expectations the void fractions in Figure 5 obtained with Raschig rings showed no relation to the void fractions of the cylinders. The over-all porosities would naturally be much higher for the Raschig rings than for the cylinders. The first $1/8$ diam. in from the retaining wall did yield a void-fraction value close to that obtained for cylinders; however at $1/8$ diam. the inner void ring of the Raschig ring began, and at $1/4$ diam. the void fraction increased from 0.69 to 0.73. A maximum value was obtained at approximately $1/4$ diam. from the wall and then decreased to 0.63 at $1/2$ diam. The void fraction then remained substantially constant for the remainder of the bed. Some calculations made with a solid row of Raschig rings arranged symmetrically on the outer wall of the container indicated that the hump could be explained by such an arrangement.

Berl Saddles

Two beds of Berl saddles were examined, the results being given in Figure 6. The ratio of bed to particle diameter for the second bed was just one-half the ratio for the first bed. The void fraction for each bed decreased from unity at the retaining wall to a relatively constant value 1 particle radius from the wall. The average value for the larger bed was approximately 0.62 and for the smaller bed 0.59; no significance is attached to this difference. The constant void fraction across the bed could be expected because of the irregularity in the shape of the saddles, which did not allow any appreciable orientation which might result in a definite pattern. It should be noted that only one disk was analyzed in the case of the smaller bed; however it agreed well with the data obtained from the larger bed.

These results agree quite well with those of Makoto, et al. (5). For beds of irregularly shaped particles they found a regular decrease in void fraction from the wall to a point about 0.6 diam. from the wall. The void fraction was constant throughout the rest of the bed. Their packing material undoubtedly included a variety of sizes and shapes of packing.

CONCLUSIONS

The radial variation of porosity in packed beds varies significantly with the type of packing used. For commercial packings, which are normally widely varying in size and highly irregular in shape, the porosity can well be assumed

to vary from 1 at the wall to the average porosity value at about 1 particle radius from the wall. This was verified by using Berl saddles and is in agreement with work of other investigators.

However for regularly shaped particles such as spheres, cylinders, and Raschig rings the situation is much different. This is particularly important because many of the theoretical studies of heat transfer, mass transfer, and fluid flow in packed beds have been made by using spheres and other regularly shaped particles. The results for these particles can be summarized as follows:

1. For spheres a minimum porosity was observed at 1 particle radius from the wall, with alternate maximums and minimums occurring at successive particle radii. The amplitude of the cycling decreased as distance from the wall increased, but significant differences were found beyond 3 particle diam. from the wall. As a preliminary conclusion it can be stated that the data seemed independent of bed to particle diameter with the exception of the maximum value at 1 particle diam. from the wall. The data in Figures 3, 4, and 7 summarize these results.

2. For cylinders the results were quite similar to those for spheres. Results are given in Figure 5. It should be observed, however, that the only cylinders tested in this work had a diameter equal to their height; for other shapes different results might be obtained.

3. For Raschig rings a minimum void fraction at $1/4$ particle radius from the wall was observed with a maximum at $1/2$ radius. After 1 particle radius from the wall the void fraction remained constant through the bed. Results are given in Figure 5.

ACKNOWLEDGMENT

This work is the result of two Master of Science theses at Purdue University. The authors would particularly like to acknowledge the assistance and encouragement given them by Professors J. M. Smith and J. M. Woods.

LITERATURE CITED

1. Baird, R. M., M.S. thesis, Purdue University, Lafayette (1956).
2. Carman, P. C., *Trans. Inst. Chem. Engrs. (London)*, 15, 150 (1937).
3. Denton, W. H., et al., A.E.R.E. E/R 1095 (1953).
4. Leva, Max, and Milton Grummer, *Chem. Engr. Progr.* 43, 713 (1947).
5. Makoto, Kimura, Nono Kazuo, and Kaneo Takaho, *Chem. Eng. (Japan)*, 19, 397 (1955).
6. Roblee, L. H. S., M.S. thesis, Purdue University, Lafayette (1956).
7. Shaffer, M. R., M.S. thesis, Purdue University, Lafayette (1952).
8. Westman, A. E. R. and H. R. Hugill, *J. Am. Ceram. Soc.*, 13, 10, 767 (1930).

Manuscript received September 5, 1957; revision received May 15, 1958; paper accepted May 20, 1958.

P
D

Exp
toluen
1/16,
plate
ten, a
It v
ratio
lower
Effi
lation

Me
plates
rates
rates
lishin
Effici
(2, 12
proper
the e
and 1
(4, 5
liqui
reten
and 1
system
vapor
The p
ft. E
design
single
proper
of ge
plate
effect
on e
some
ties
can
as a
result
sys

The
of m
oper
tane
of th
of 1.0
been
was c

Perforated Plate Efficiency-Effect of Design and Operating Variables

J. D. HELLUMS, C. J. BRAULICK, C. D. LYDA and MATHEW VAN WINKLE

The University of Texas, Austin, Texas

Experimental plate efficiency and pressure drop data were obtained on the *n*-octane-toluene system in a 5 plate, 6 in. diam. column at atmospheric pressure. Hole sizes of 1/16, 1/8, and 3/16 in.; 5.68 and 12.5% free areas; weir heights of 1, 2, and 3 in.; and plate spacings of 6, 12, 18, and 24 in. were studied. Reflux ratios of one, two, four, five, ten, and total were utilized to determine the effect on efficiency.

It was found that hole diameter, free area, plate spacing, and a wide range of reflux ratio had relatively small effect on efficiency and pressure drop; however weir height and lower reflux showed relatively larger effects on both variables.

Efficiencies and pressure drops were lower than those predicted from published correlations particularly at low flow rates.

Mechanical design features of the plates and column and vapor and liquid rates are important variables in establishing distillation column performance. Efficiency correlations in the literature (2, 12) include the effects of some physical properties but in general do not include the effects of design features and vapor and liquid rates. Gerster and co-workers (4, 5, 6, 7) have related gas film and liquid film efficiencies in terms of liquid retention in the froth on both bubble cap and perforated fractionating plates. The systems studied involved water, water vapor, air, and water, oxygen, and air. The plate diameters were 13 in. and 13 ft. Experimental data on the effects of design and operating variables by using single systems of constant physical properties are needed before techniques of general applicability for estimating plate efficiency can be developed. The effect of design and operating variables on efficiency undoubtedly depends to some extent on system physical properties. Extensive data on a single system can serve to establish the relative importance of the variables and can serve as a basis from which to evaluate the results of less extensive work on other systems.

This investigation covers wide ranges of most of the important design and operating variables on the system *n*-octane-toluene. Results of an earlier part of this program where column diameters of 1.02, 1.83, and 3 in. were used have been reported (17, 18). This investigation was carried out in a 6 in. diam. column

and encompassed the variables, reflux ratio, and plate spacing which were not studied previously. Data of the effect of weir height were obtained in the range of usual commercial practice, and additional tests on the effects of hole size and free area were carried out.

As a matter of interest the effect of composition on efficiency data previously reported (17) was recalculated after carefully resmoothing the relative volatility data of Berg and Popovac (1). The trend showing increasing efficiency with increasing toluene concentration as previously reported was substantiated at low toluene concentrations. However the change in efficiency seems to be less than previously reported, and efficiency seems to be essentially independent of composition in the midrange of concentrations. Similar results on the influence of composition on plate efficiency have been reported by Wijk and Thijssen (20), Volland (19), and Langdon and Keyes (11). At low concentrations of either component or near an azeotrope the low diffusional driving force seems to result in reduced efficiency. Column terminal concentrations were maintained at the same level for each test in this work to eliminate any effect of composition on efficiency.

EQUIPMENT

The column was constructed of 6 in. I.D. glass pipe with accessory equipment (Figure 1). Openings in the insulation were provided to permit visual observa-

tion of plate operation. The dimensions of the column and ranges of variables studied are given in Table 1. Free area and downcomer area are in percentage of the column superficial area.

Plate spacing was varied in multiples of 6 in. by using glass pipe sections of appropriate lengths. Downcomers were constructed of 1 5/8 in. O.D. copper tubing. The upper ends of the downcomers extended 1/2 in. above the plates and were machined to allow replaceable circular weirs of various heights to be used. The bottoms of the downcomers extended to within 1/4 in. of the plates below. Plate inlet weirs and splash baffles were not used.

Plate layout is shown in Figures 2 and 3. A larger hole spacing was used for the plates of smaller free area, so that

TABLE 1. DIMENSIONS OF COLUMN AND VARIABLES

Column Diameter, in.	6
Plate Spacing, in.	6, 12, 18, 24, 30
Number of Plates	5, 5, 3, 2, 2
Plate Thickness, in.	1/8
Weir Height, in.	1/2, 1, 2, 3
Hole Diameter, in.	1/16, 1/8, 3/16
Hole Pitch/Diameter Ratio	2, 3
Percentage Free Area of Holes	5.68, 12.5
Percentage Downcomer Area	7.1
Reflux Ratio, L/D	1, 2, 4, 5, 10, total
Vapor Rate	
F_A , Hole F Factor	1 to 15
G , lb./hr.-sq. ft.	100 to 1400

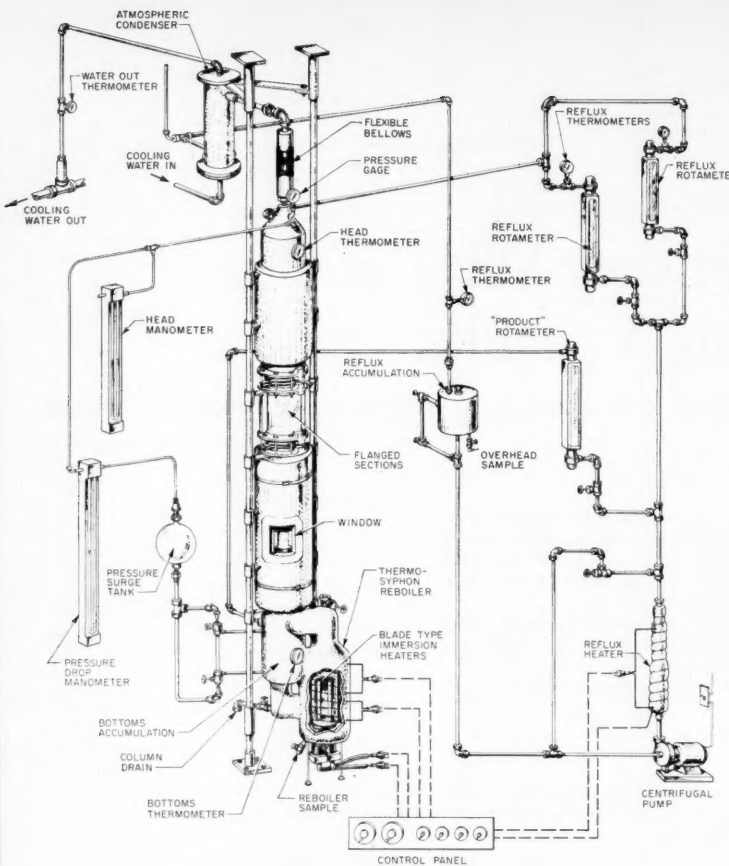


Fig. 1. Distillation column and its accessories.

substantially the same effective plate area was covered by perforations in each case. The holes were drilled on equilateral triangular pitch in all cases.

COLUMN INSIDE DIAMETER

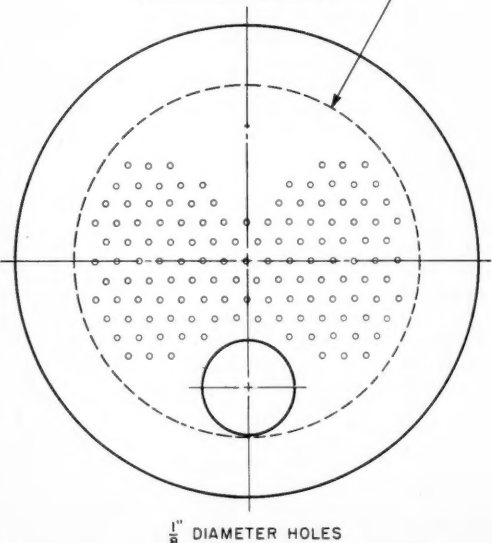


Fig. 3. Perforated plate layout, 5.68% free area.

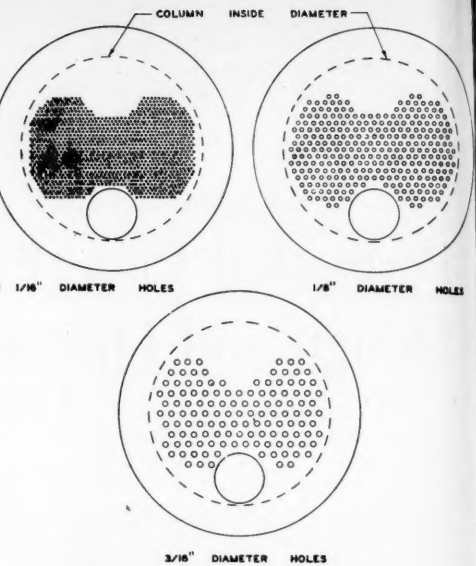


Fig. 2. Hole layout for perforated plates.

PROCEDURE

The *n*-octane-toluene binary system was used throughout this investigation as the test system. The materials and analytical techniques have been described (17, 18).

Results of preliminary column tests showed that steady-state operation could be reached 90 min. after column startup or 30 min. after a subsequent change in operating conditions. To insure steady-state operation $2\frac{1}{2}$ hr. were allowed after column start up, and 1 hr. was

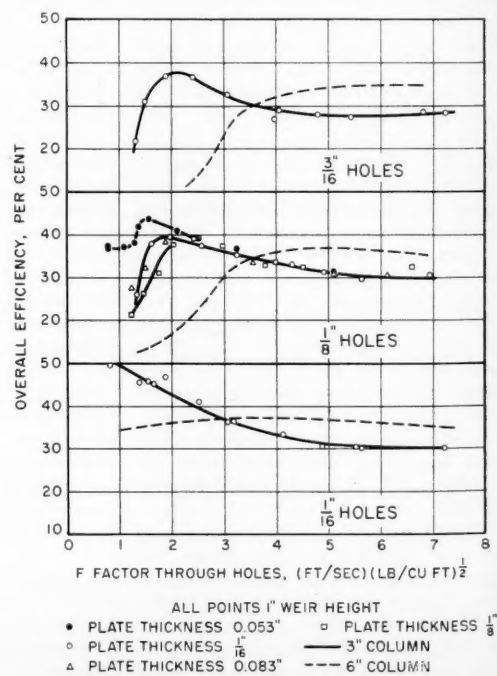


Fig. 4. Comparison of 3 and 6 in. columns.

allowed after a subsequent change in operating conditions before overhead condensate and bottoms samples were taken. A series of runs over the entire range of vapor rates were made after each change in a design variable. The upper limit of column vapor rate was established by the reboiler capacity. In no case was the column flooding point reached. The lower limit of column vapor rate was established by the quantity of reflux or distillate which could be metered effectively.

Weeping was observed to a greater or lesser extent in the case of trays of the larger free area at all vapor rates utilized.

The Smoker equation (16) was used in the efficiency calculations for runs at finite reflux, and the Fenske equation (3) was used for runs at total reflux; these are consistent in that Smoker's equation reduces to Fenske's equations for the case of total reflux. The two equations are based on assumptions of both constant relative volatility and constant molal overflow. The assumption of constant molal overflow is satisfactory because of the small column temperature gradient and the small difference in heats of vaporization of the two components. The relative volatility varied by as much as 25% between column terminal compositions. For this reason a number of runs were calculated plate-to-plate by using Berg's (1) vapor-liquid equilibrium composition data to determine what error might be introduced by assuming constant relative volatility; it was established that no discernible error was introduced. The equations give slightly better reproducibility of results than the plate-to-plate method which requires repeated readings from a chart.

Smoker's equation for the number of theoretical stages required in a rectifying column is

$$n = \frac{\log \frac{(x_d - k)}{(x_b - k)} \left| 1 - \frac{L}{V} \left[1 + (\alpha - 1)k \right] (\alpha - 1)(x_b - k) \right|}{\log \frac{L}{V} \frac{\alpha}{[1 + (\alpha - 1)k]^2}} \quad (1)$$

where

$$k = \pm \frac{1}{2} \left\{ \left[\frac{1}{\alpha - 1} + \frac{x_d}{L} \right. \right. \\ \left. \left. - \frac{V}{L} \frac{\alpha}{(\alpha - 1)} \right]^2 - \frac{4x_d^{1/2}}{L(\alpha - 1)} \right\} \\ - \frac{1}{2} \left[\frac{1}{\alpha - 1} + \frac{x_d}{L} - \frac{V}{L} \frac{\alpha}{(\alpha - 1)} \right] \\ 0 < k < 1$$

In the case of total reflux Smoker's equation reduces to the Fenske equation

$$n = \frac{\log \frac{(x_d)(1 - x_b)}{(x_b)(1 - x_d)}}{\log \alpha} \quad (2)$$

One stage was subtracted from the number computed to account for the reboiler. The remainder was divided by the number of actual plates in the column to obtain over-all efficiency.

Vapor densities for use in computing vapor velocities and *F* factors were calculated by using the ideal gas law at the column average temperature and pressure. Molecular weight was taken as the average of the molecular weight of the distillate and the molecular weight of the vapor in equilibrium with the bottoms product. The compressibility factor of the vapor at column conditions was estimated from charts based on the theory of corresponding states to be about 0.97, which indicates that the error introduced by using the ideal gas law is not significant.

Froth height was observed, but sloshing of the liquid on the plate made accurate determination of froth height impossible. Therefore no complete data were taken with respect to this factor.

RESULTS*

Comparison of 3- and 6-in. Columns

Data obtained from the 3 in. diam. column are shown in Figure 4 and are compared with data derived from the 6 in. diam. column. The efficiency level shown is slightly lower than previously reported (17) because of a small difference in relative volatility data used in the calculations (as already noted). The data are for a 6 in. plate spacing, 12.5% free area, and a 1 in. weir height. The only design feature other than diameter,

on efficiency in the stable operating range, but it does influence the lower limit of effective operation. Thinner plates have a slightly wider range of stable operation. The efficiency obtained from the smaller column rises abruptly to a distinct maximum near the lower limit of operation and then falls to a nearly constant value at higher vapor rates. The maximum efficiency obtained is considerably higher than the nearly constant value obtained at higher vapor rates. The efficiency obtained from the 6 in. column (dotted lines on Figure 4) rises more slowly with increasing vapor rate to a much less distinct maximum.

Except at low vapor rates the larger column is more efficient by about 20% (6 to 7 absolute units of efficiency). Kirschbaum (10) reported a similar higher efficiency for a 400 mm. diam. column in comparison with a 110 mm. diam. column. Kirschbaum (10) and Perry (14) attributed the higher efficiency of larger columns to an increase in countercurrent effect. Increasing column diameter increases vapor flow area by the second power but only increases liquid flow area across the plate by the first power. Kirschbaum states that the higher liquid velocity and longer liquid path both reduce the effect of mixing of liquid on the plate thereby tending to increase efficiency.

The 3 in. column operates more effectively at lower vapor loads than the 6 in. column. The upper limit of operation should be about the same for both columns with the same plate spacing. The upper limit is established by the pressure drop which causes flooding. Kirschbaum (10) also noted a narrower operating range for larger columns with respect to throughput.

Effect of Plate Spacing on Efficiency

Efficiencies were determined at five different plate spacings. The data on Figure 5 are for 12.5% free area plates at a 1 in. weir height with plate spacings of 6, 12, 18, 24, and 30 in. No well defined trend of efficiency with plate spacing over the range of vapor rate and liquid rate tested is apparent. The entrainment rate must be a sufficiently low fraction of the total liquid rate in all cases studied, so that changes in its effect are not detectable within the precision of the work.

Karim and Nandi (9) tested three systems at 6 and 12 in. tray spacings. Increasing the spacing greatly increased the efficiency for the carbon tetrachloride-toluene and acetone-water systems but had little effect on the ethanol-water system.

Kirschbaum (10) tested the ethanol-water system at 1.97, 3.94, and 7.88 in. spacings. The column efficiency and operating range were markedly improved by increasing spacing from 1.97 to 3.94 in. However the improvement was only

*Tabular material has been deposited as document 5762 with the American Documentation Institute, Photoduplication Service, Library of Congress, Washington 25, D. C., and may be obtained for \$3.75 for photoprints of \$2.00 for 35-mm. microfilm.

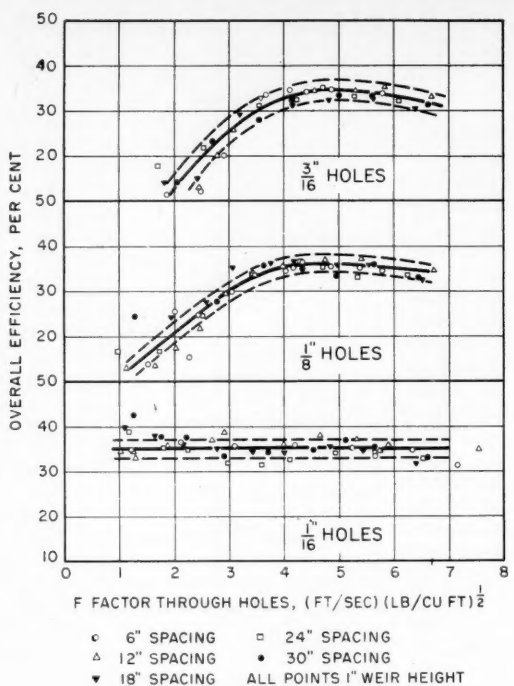


Fig. 5. Effect of plate spacing on efficiency.

on the order of 3% on increasing plate spacing from 3.94 to 7.88 in. Higher spacings were not tested. It seems likely that little or no change would have been found for spacings above 7.88 in.

As a matter of interest Kirschbaum noted that entrainment is much lower

for perforated plates than for bubble cap plates because the higher velocity between bubble caps tends to throw the liquid upward. He attributes the decrease in perforated plate efficiency with increasing vapor rate in the stable operating range to decreased vapor-liquid contact

time. His work shows that bubble plate efficiency is much more influenced by plate spacing than perforated plate efficiency.

It may be concluded that for some systems including *n*-octane-toluene plate spacing above 6 in. is not an important

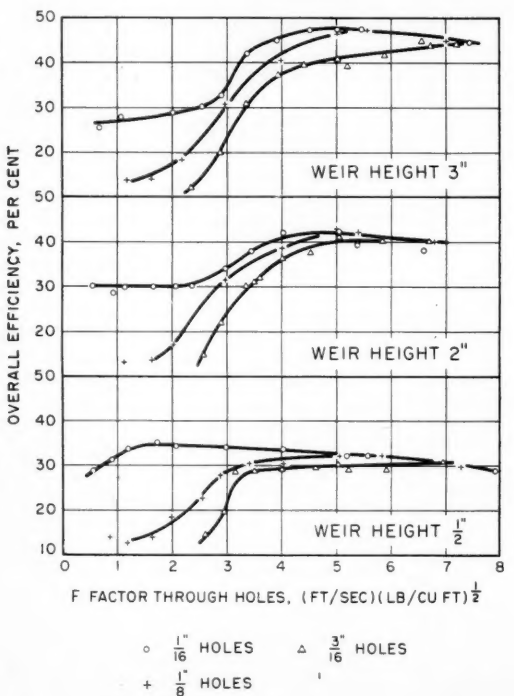


Fig. 7. Effect of hole size on efficiency.

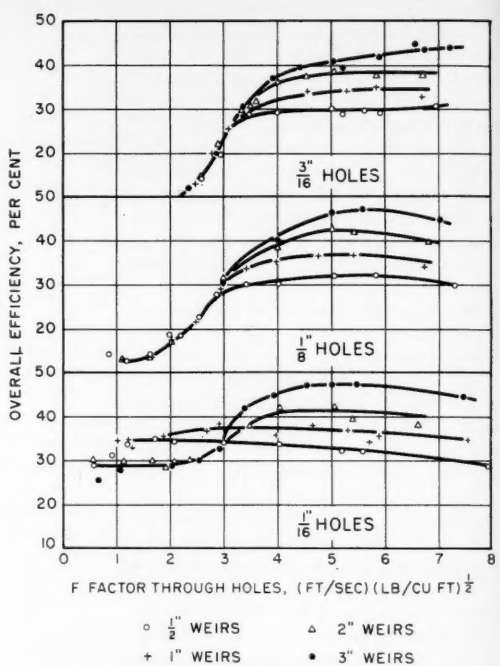


Fig. 6. Effect of weir height on efficiency.

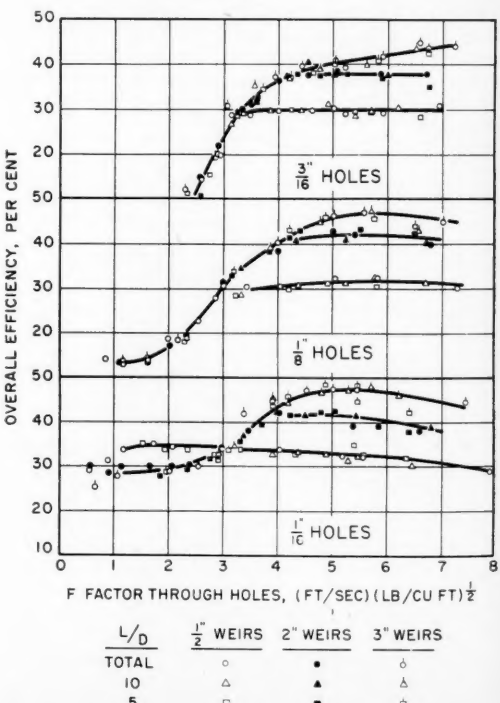


Fig. 8. Effect of reflux on efficiency.

variable
In cert
is indi
importa

Effect of

Data
in t
in Fig
1/2 to 3
by ab
efficien
range.
seems t
of the i
weirs y
has no
through
vapor r
in. hole
on the
vapor c
cient t
weirs
may a
trend
weir h
1/16 in.
Alth

indicat
on eff
may be
level.
levels
proved

Kar
the et
of 1 an
results
height
varies

It is
of K
Baker
system
merge
plates
perform
system
increas
range
report
increas
An e
creati
design
static

Effect

The
in Fig
at th
hole a
at low
of sm
liquid
even
area
interf

Vol.

variable over wide ranges of vapor rate. In certain other systems plate spacing is indicated to be of much greater importance.

Effect of Weir Height on Efficiency

Data at weir heights of $\frac{1}{2}$, 1, 2, and 3 in. in the 6 in. diam. column are shown in Figure 6. Increasing weir height from $\frac{1}{2}$ to 3 in. is shown to increase efficiency by about 50% (15 absolute units of efficiency) in the effective operating range. At low vapor rates weir height seems to have no effect except in the case of the 1/16 in. perforations where higher weirs yield lower efficiency. Weir height has no effect when the liquid weeps through the holes as is the case at low vapor rates for plates with $\frac{1}{8}$ and $\frac{3}{16}$ in. holes. A liquid level was maintained on the plates with 1/16 in. holes at all vapor rates tested. The level was sufficient to cause flow over $\frac{1}{2}$ and 1 in. weirs resulting in less weeping which may account for the inversion of the trend of the curves of efficiency with weir height at low loads on plates with 1/16 in. holes.

Although the experimental results indicate a definite effect of weir height on efficiency, the extent of the effect may be influenced by the lower efficiency level. Further data at various efficiency levels are necessary before this can be proved.

Karim and Nandi (9) found that for the ethanol-water system weir heights of 1 and 2 in. gave substantially the same results. Apparently the effect of weir height as well as that of plate spacing varies with system properties.

It is interesting to compare the results of Kirschbaum (10) and Peavy and Baker (13) who, using the ethanol-water system, studied the effect of static submergence on efficiency of bubble cap plates. Static submergence for bubble plates is analogous to weir height for perforated plates. Peavy and Baker noted systematic increases in efficiency with increasing static submergence over the range 0, $\frac{1}{2}$, 1 and 2 in. Kirschbaum reported no change in efficiency for increasing static submergence over 1 in. An explanation for this apparent discrepancy probably lies in differences in design features other than those involving static submergence.

Effect of Hole Size on Efficiency

The data of Figure 6 are represented in Figure 7 with parameters of hole size at three different weir heights. Smaller hole sizes result in higher plate efficiency at low and moderate vapor rates. Plates of small hole size tend to retain the liquid level required for normal operation even at low vapor rates. For a given free area smaller hole diameter yields greater interfacial area which also tends to increase efficiency. Plates of larger hole

size operate unsatisfactorily at low vapor loads. However the effective operating range should extend to a somewhat higher vapor load because of lower pressure drop.

At the highest vapor rates tested all three holes sizes yield substantially the same efficiency, and it is possible to predict from the shape of the curves that, if still higher rates were tested, the plates of largest hole size would operate with highest efficiency. However there are insufficient data at higher vapor velocities to definitely support such a conclusion. It was observed that the liquid on the plate was agitated into a violent side-to-side sloshing at high vapor rates, and that this sloshing was considerably less violent for plates of larger hole size.

Chu and associates (8) and Karim and Nandi (9) reported effects of hole size similar to those shown in this work.

Effect of Reflux on Efficiency

Results of tests at external or operating reflux ratios of five, ten, and total are shown in Figure 8. Parameters are weir height and reflux ratio at three different hole sizes. Results of the runs at various reflux ratios appear to fall on the same general curves as indicated by the band formed by the dotted lines on Figure 8. Reflux ratio has no discernible effect on efficiency in the range from $L/D = 5$ to $L/D = \infty$.

An additional series of tests was made to determine the effect of reflux ratio over a wider range with respect to relative liquid and vapor flow rates. External reflux ratios used were total, four, two, and one. The additional experimental work was carried out at 1, 2, and 3 in. weir heights on plates of smaller free area, as will be discussed. The curves in Figure 9 indicate that reflux ratios of two or greater yield the same results, but that efficiency is appreciably lower for a reflux ratio of one, particularly at high vapor loads.

The explanation of this effect must lie in consideration of the several factors which influence efficiency. Increasing reflux ratio at a given vapor rate involves only increasing the internal liquid rate, while other factors remain the same. The resulting decreased liquid retention time on the plate tends to reduce efficiency. On the other hand a higher liquid velocity reduces the effect of mixing of the liquid on the plate thereby increasing the countercurrent effect and tending to increase efficiency. Entrainment rate at higher liquid rates becomes a smaller fraction of the total liquid rate causing less concentration change and tending to improve efficiency. Turbulence on the plate induced by higher liquid rates should also tend to improve efficiency. These factors seem to offset each other for reflux ratios above two, while those

tending to promote efficiency predominate at lower ratios.

Volland (19) reported results on the ethanol-water system in which the effect of reflux on efficiency is in surprisingly good agreement with this work on the *n*-octane-toluene system. Similarly Wijk and Thijssen (20) found that for the *n*-heptane-methylcyclohexane system increasing reflux increased efficiency up to an external reflux ratio of about four, above which there was no effect. Kirschbaum (10) and Peters (15) reported efficiency independent of reflux at relatively high reflux ratios.

Effect of Free Area

The results shown in Figure 9 are for plates of 5.68% free area (solid lines) in comparison with results on plates of 12.5% free area (dotted lines). In addition to free area, plate spacing was varied. An 18 in. spacing was used with the 5.68% free-area plates, whereas a 12 in. spacing was used with the 12.5% free-area plates. However spacing has been shown to have practically no influence on efficiency in the ranges of variables tested, and this can be considered a valid comparison. A greater pitch to diameter ratio was selected for the plates of smaller free area to give perforations over substantially the same effective plate area in both cases.

Reducing the plate free-area resulted in the plate operating effectively even at the lowest vapor rates tested. At the lowest vapor rate essentially all liquid flow between plates occurred as the result of weeping. However in spite of this a liquid depth of about $\frac{1}{2}$ in. was maintained on the plate. This liquid depth was sufficient for good plate operation as evidenced by the efficiency attained.

About the same peak efficiency was reached with the plates of different free areas at all three weir heights. The peak efficiency however occurs at considerably different hole vapor velocities.

The data of Figure 9 are presented in Figure 10 with column superficial mass velocity as the abscissa. This plot is of interest as it shows that efficiency is approximately the same for the plates of greatly different free area at a given column vapor rate, providing the rate is high enough for the 12.5% free-area plates to be in effective operation. Comparison of Figures 9 and 10 indicates that column-vapor mass velocity may be preferable to hole-vapor velocity for comparing plates of different free area. On either basis a higher vapor rate is required to attain good operation of the 12.5% free-area plates. The upper limit of operation of the 12.5% free-area plate should be much higher because of lower pressure drop. Reboiler limitations prevented establishment of the upper limit of capacity in this work.

Volland (19) and Foss and Gerster (4)

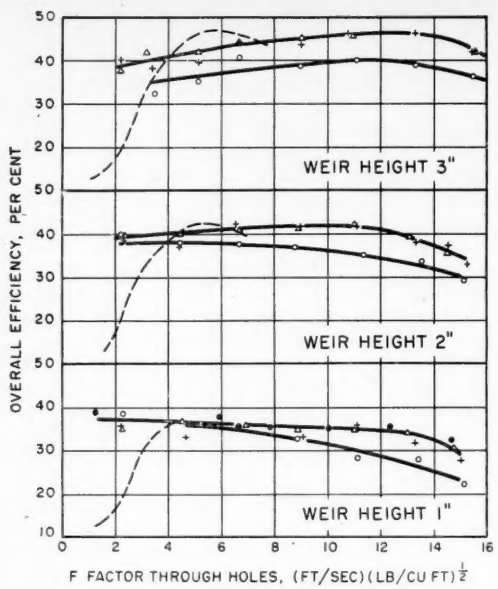


Fig. 9. Effects of free area and reflux on efficiency.

investigated the effect of free area and found it to be slight. Both Volland and Foss and Gerster indicated that plates of about 7 to 8% free area yield slightly higher efficiencies than plates of other free areas. Umholtz (17) and Karim and

Nandi (9) noted no effect of free area on efficiency at vapor rates high enough to insure effective plate operation. Umholtz's tests on efficiency variation with free area were carried out in a 1.83 in. diam. column with a $\frac{1}{4}$ in. weir height.

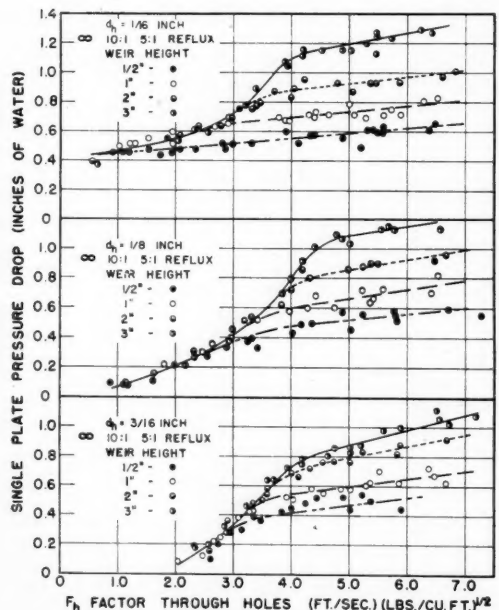


Fig. 11. Effect of hole size and weir height on perforated-plate pressure drop.

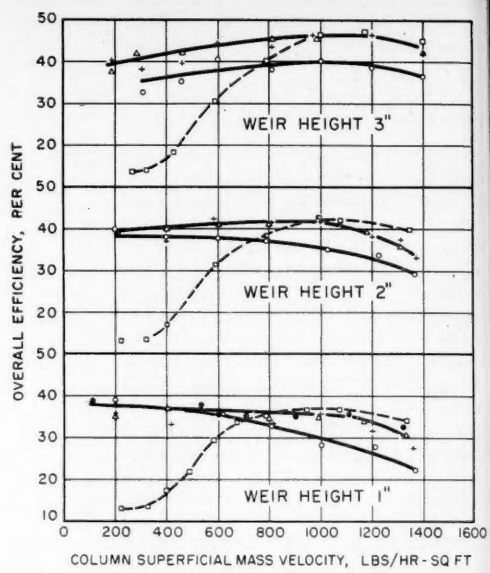


Fig. 10. Effect of free area at various column mass velocities.

Pressure Drop

The effects of plate variables on pressure drop are in some ways similar to their effects on efficiency. Pressure drop results for the 12.5% free-area plates are shown in Figure 11 for various weir

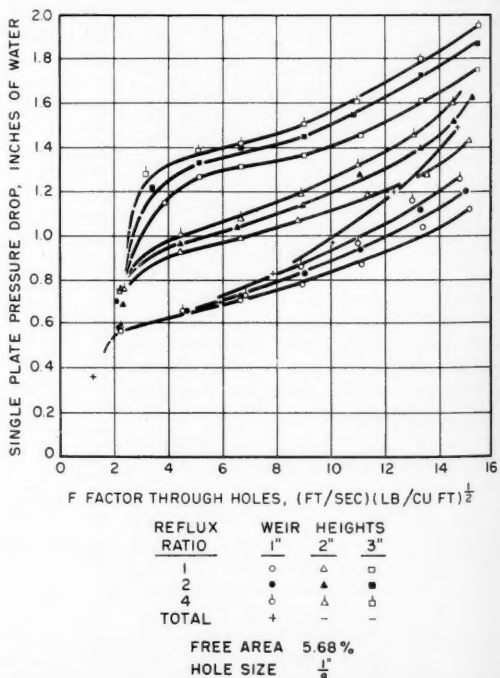


Fig. 12. Effect of reflux and weir height on pressure drop.

TABLE 2.

Variable Studied	Range of Variable	Approximate Effect on Absolute Efficiency		
		Low	Moderate	High
Column Diameter, in.	3, 6	-15 to 30	+5	+7
Plate Spacing, in.	6, 12, 18, 24, 30	0	0	0
Weir Height, in.	1/2, 1, 2, 3	0	+10	+15
Hole Diameter, in.	1/16, 1/8, 3/16	-20	-4	0
Free Area, % of column superficial area	5.68, 12.5	-26	0	+3
Plate Thickness, in.	0.053, 0.063, 0.083, 0.125	-18	0	0
Reflux Ratio, <i>L/D</i>	1, 2, 4, 5, 10, total	0 to +5	+5	+5
Feed (Reboiler Toluene Concentrations)	13, 21	+1	+1	+1
Mole %	21, 46	0	0	0

heights, hole sizes, and reflux ratios. Plate spacing is not shown as a parameter because it did not influence results within the precision of the work. Reflux ratio also seems to have little effect on pressure drop. Larger hole size resulted in lower pressure drop for a given total hole area, and higher weirs resulted in higher pressure drop.

Pressure drop results for the 5.68% free-area plates are shown in Figure 12. Parameters are weir height and reflux ratio. These plates of smaller free area operated with good efficiency over the entire range of vapor rates tested. The pressure drop at a given vapor rate was much higher than that for the plates of larger free area. This higher pressure drop maintained a satisfactory liquid level on the plate, so that effective operation was obtained even at low vapor rates. Increasing liquid rate (at the same vapor rate) caused by increasing reflux ratio increased pressure drop. Such a trend probably also existed in the case of the 12.5% free-area plates, but pressure fluctuation reduced the precision of the measurements so that the trend was not apparent. Extensive weeping was observed in the case of the larger free-area plates at all vapor rates tested.

GENERAL DISCUSSION

The efficiency range of 30 to 45% encountered in this investigation is lower than that predicted from the correlations of Drickamer and Bradford (2), which indicates an efficiency of 63%, and of O'Connell (12), which indicates an efficiency of 65%. These correlations relate in one case the molal average viscosity of the system with efficiency and in the other the product of the molal average viscosity and relative volatility with efficiency and do not include other system, operating, and design variable effects.

Possibly lower efficiencies could be encountered here because of the weeping of liquid through the holes, particularly at low vapor rates and for the larger free-area plates, possibly because no

splash baffles were used. Splash baffles were not used because one set of runs with and without splash baffles indicated the same efficiencies within the limits of experimental error.

The pressure drop data range in this investigation from 0.4 to 1.8 in. of water are slightly lower than those predicted from correlations of Hughmark and O'Connell (9), which range from 1.1 to 2.1 in. of water. Probably the weeping encountered at low vapor rates reduced the liquid head on the plate and therefore the pressure drop. At the higher rates the experimental pressure drops and those predicted are much closer numerically.

An indication of the effect of each variable studied on efficiency as a function of vapor rate is given in Table 2. The change in efficiency shown is that caused by increasing the variable studied over the range indicated. In those cases, where the effect of one variable is influenced by changes in other variables, average values or ranges of values are given. It is interesting to note that plate spacing, hole diameter, free area, plate thickness, reflux ratio, and feed composition all have only a slight influence on efficiency over fairly wide ranges at moderate and high vapor rates. The variable hole spacing is not mentioned; it is considered a dependent function of free area, hole size, and effective plate area covered by perforations.

NOTATION

F_h = hole *F* factor defined as the product of the square root of the vapor density in lb./cu. ft. and the hole vapor velocity in ft./sec.

G = column superficial vapor mass velocity in lb./hr./sq. ft. of column superficial cross sectional area

L/D = external reflux ratio with the reflux rate divided by the distillate rate in moles/mole

n = number of theoretical stages required to accomplish a given separation

ΔP = single plate pressure drop in inches of water

P/D = hole pitch to diameter ratio defined as the smallest center to center distance between holes

x_b = mole fraction toluene in column bottom product

x_d = mole fraction toluene in column distillate product

x = mole fraction toluene in the liquid phase

y = mole fraction toluene in the vapor phase

a = relative volatility defined as $y(1-x)/x(1-y)$, where y and x are equilibrium compositions

ρ = vapor density in lb./cu. ft.

Effective plate operation = general term designating characteristic area of plate operation where efficiency is near its maximum value and is not greatly changed by changes in vapor rate over a wide range

LITERATURE CITED

1. Berg, Lloyd and D. O. Popovac, *Chem. Eng. Progr.*, **45**, 11, 683 (1949).
2. Drickamer, H. G., and J. R. Bradford, Jr., *Trans. Am. Inst. Chem. Engrs.*, **39**, 319 (1943).
3. Fenske, M. R., *Ind. Eng. Chem.*, **24**, 482 (1932).
4. Foss, A. S., J. A. Gerster, *Chem. Eng. Progr.*, **52**, 28 (1956).
5. Gerster, J. A., A. P. Colburn, W. E. Bonnet, and T. W. Carmody, *Chem. Eng. Progr.*, **45**, 716 (1949).
6. Gerster, J. A., W. E. Bonnet, and I. H. Hess, *Chem. Eng. Progr.*, **47**, 523 (1951).
7. Gerster, J. A., W. E. Bonnet, and I. H. Hess, *Chem. Eng. Progr.*, **47**, 621 (1951).
8. Gouveia, W. R., Ju Chin, Chu, and O. P. Kharbanda, Abstracts of Papers, Am. Chem. Soc. Meeting, New York (September, 1954).
9. Hughmark, G. A., and H. E. O'Connell, *Chem. Eng. Progr.*, **53**, 127M (1957).
10. Kirschbaum, Emil, "Distillation and Rectification," 227, Chemical Publishing Co., New York (1948).
11. Langdon, W. M., and O. B. Keyes, *Ind. Eng. Chem.*, **35**, 464 (1943).
12. O'Connell, H. E., *Trans. Am. Inst. Chem. Engrs.*, **42**, 741 (1946).
13. Peavy, C. C., and E. M. Baker, *Ind. Eng. Chem.*, **29**, 1056 (1937).
14. Perry, J. H., "Chemical Engineers' Handbook," 3rd ed., 615, McGraw-Hill Book Co., New York (1950).
15. Peters, W. A., Jr., *Ind. Eng. Chem.*, **14**, 476 (1922).
16. Smoker, E. H., *Trans. Am. Inst. Chem. Engrs.*, **34**, 165 (1938).
17. Umholtz, C. L., P. D. Jones, Mathew Van Winkle, *Ind. Eng. Chem.*, **49**, 226 (1957).
18. Umholtz, C. L., and Mathew Van Winkle, *Petroleum Refiner*, **34**, 7, 114 (1955).
19. Volland, G., *Chem. Fabrik*, **8**, 5 (1935).
20. Wijk, W. R., and H. A. C. Thijssen, *Chem. Eng. Sci.*, **3**, 153 (1954).

Manuscript received December 30, 1957; revision received May 6, 1958; paper accepted May 22, 1958.

A Theoretical-Empirical Approach to the Mechanism of Particle Entrainment from Fluidized Beds

F. A. ZENZ and N. A. WEIL

The M. W. Kellogg Company, New York, New York

A means of calculating the rate of entrainment of solids from commercial-size continuously operating fluidized beds was developed from the combined results of a theoretical and an empirical approach which through different channels arrived at the same fundamental mechanism. The calculation method shows agreement with data obtained from an apparatus simulating flow characteristics in large-scale equipment and compares favorably with smaller scale tests reported in the literature at pressures up to 200 lb./sq. in. gauge.

In vessels containing a fluidized-catalyst bed through which gas is forced upward, the gas leaving the top of the bed will carry with it entrained solid particles. This entrainment varies with a number of factors such as gas velocity, particle-size distribution, height above the bed, specific gravity of the catalyst, and viscosity and density of the gas. The problem is similar to that of entrainment of liquid from distillation trays wherein an optimum relation between tray diameter, number of trays, and tray spacing is used to determine the minimum-cost installation. In the case of particle entrainment in catalytic reactors, a quantitative entrainment correlation would define the relation between disengaging height, number of cyclone stages, and carryover loss, leading again to the over-all minimum-cost arrangement.

Numerous experimental investigations of entrainment in small laboratory-scale equipment have been reported, but no generally applicable empirical relationship has yet been found or proposed. Even within the work of a single investigator apparently inexplicable inconsistencies appear in the data, and some of the most ambitious studies have been able to relate results only qualitatively to the observed nature of the bubbling action in the bed. Entrainment from small-diameter, high L/D , experimental units, in which the gas bubbles within the fluidized mass may reach tube-diameter proportions, giving rise to slugging, can be expected to correlate only by coincidence with the entrainment from large-diameter commercial units, where the emerging bubbles may reach several feet in diameter but never the diameter of the entire vessel. The generalized approach developed in the present study is intended to apply only to such larger diameter nonslugging beds.

THE MECHANISM OF CATALYST ENTRAINMENT

Two approaches to the calculation of entrainment, which upon later comparison were found to converge to a common physical mechanism, are illustrated in Figure 1.

The theoretical approach in Figure 1(a) envisioned particles ejected from the bed surface (at a velocity of the magnitude of the bubble velocity as it bursts through the bed surface) into a concurrent stream of gas rising uniformly at a rate equal to its superficial velocity through the bed. Each particle thus thrust into the gas is then acted upon by inertia and gravitational and drag forces. Some sizes will be carried up continually and some only to certain heights, from which they will fall back onto the bed. Thus a theoretical analysis of this picture results in a curve of concentration versus height above the bed surface for any particular catalyst gas system and operating gas rate.

The empirical approach pictured in Figure 1(b) envisioned the bed as a saturation feed device such that at a sufficient distance above the bed surface (where gas-velocity profiles have stabilized) the containing vessel can be considered as a pneumatic conveying tube and entrainment as a transport phenomenon. It was hypothesized that gas bubbles bursting at the surface of a fluidized bed are analogous to intermittent jets imposing a highly irregular velocity profile across the containing vessel. The jet velocities eventually are dissipated to the superficial gas velocity at some equilibrium height above the bed surface referred to as the *transport Disengaging height*, *T.D.H.* The entrainment above this height is then relatively constant and presumably equal to the maximum or saturation dilute-phase particle-carrying capacity of the gas stream at its superficial velocity as obtained from empirical correlation of pneumatic and hydraulic transport data.

THE THEORETICAL APPROACH THROUGH FORCES ACTING ON THE PARTICLES

In order to approach the conditions

acting on catalyst particles entrained above the bed in process vessels, the behavior of the particles in a moving gas stream must be considered. The motion of any one such particle, with any interparticle forces neglected, is completely described by the equation

$$\text{inertia force} + \text{gravitation force} + \text{drag force} = 0 \quad (1)$$

or, in mathematical terms, upward vectors being considered as positive,

$$m \frac{dv}{dt} + F = -mg \frac{\rho - \rho_0}{\rho} \quad (1)$$

where the right-hand side represents the effective particle weight.

The initial particle velocity as it is thrown upward from the bed surface by the violent action of bursting bubbles is represented as v_0 . However, as soon as it leaves the bed it immediately enters a gas mass flowing at a uniform velocity v_g representing the superficial velocity of the rising process gas above the bed surface. The drag force in Equation (1) can be expressed as $F = C_R R$, where for streamline or laminar motion

$$C_R = k\mu/D\rho_0(v - v_g)$$

and

$$R = \rho_0(v - v_g)^2 A/2$$

so that by substitution

$$F = k\mu A(v - v_g)/2D$$

Equation (1) may now be rewritten as

$$dv/dt + \frac{k\mu A}{2mD} (v - v_g) = -g \frac{\rho - \rho_0}{\rho} \quad (2)$$

If the particles are assumed to be spherical, then

$$A = \pi D^2/4$$

and

$$m = \rho\pi D^3/6$$

so that

$$\frac{2mD}{k\mu A} = \frac{4\rho D^2}{3k\mu} = C \quad (3)$$

Substituting Equation (3) in Equation (2) and applying the boundary conditions that $v = v_0$ at $t = 0$ yields the solution of

F. A. Zenz is with Associated Nucleonics, Inc., Garden City, New York.

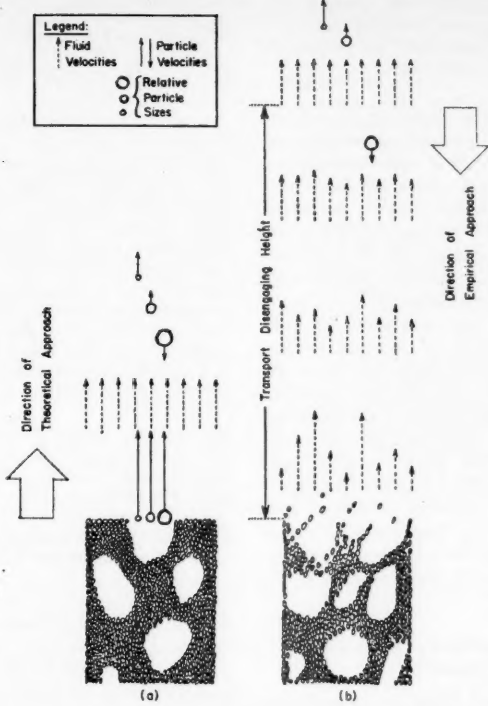


Fig. 1. Illustrations of assumed flow models.

Equation (2) (ρ_0 being assumed negligible with respect to ρ) as

$$v = (C_g - v_0)(e^{-t/C} - 1) + v_0 e^{-t/C} \quad (4)$$

The balancing velocity (v at $t = \infty$) is then

$$v_m = -C_g + v_0 \quad (5)$$

which substituted into Equation (4) gives

$$v = v_m(1 - e^{-t/C}) + v_0 e^{-t/C} \quad (6)$$

At the point of maximum vertical rise $v = 0$, and so from Equation (6) the time for reaching the top elevation is

$$t^* = C \ln \left(1 - \frac{v_0}{v_m} \right) \quad (7)$$

The height of rise can be calculated from the expression

$$h = \int_0^{t^*} v \, dt = \int_0^{t^*} [v_m t + (v_0 - v_m) e^{-t/C}] \, dt$$

which upon integration with the boundary condition that $h = 0$ when $t = 0$ yields

$$h = v_m t - C(v_0 - v_m)(e^{-t/C} - 1) \quad (8)$$

Substituting Equation (7) into (8) for the elapsed time gives the maximum height of rise for the particle:

$$h_{max} = C \left[v_0 + v_m \ln \left(1 - \frac{v_0}{v_m} \right) \right] \quad (9)$$

For irregular particles, k in Equation (3) has a value of approximately 37.5, which

upon substitution in Equations (5), (6), and (9) gives

$$v_m = v_0 - 1.15 \rho D^2 / \mu \quad (10)$$

$$v = (v_0 - v_m) \exp \left(\frac{-28.1 \mu t}{\rho D^2} \right) + v_m \quad (11)$$

$$h_{max} = \frac{\rho D^2}{28.1 \mu} \left[v_0 + v_m \ln \left(1 - \frac{v_0}{v_m} \right) \right] \quad (12)$$

If n represents the number of particles of a given grain size D thrown up by the bubble action over an area of 1 sq. ft. of the bed/sec., then $N = \sum n$ represents the average of the total number of all particles emerging from the bed per square foot per second. If the particle velocity is v at an arbitrary height, a particle having crossed a section will have traveled a distance of v feet upward in 1 sec. Since no particles are destroyed, during this 1 sec. n additional particles will have entered the 1 sq. ft. area. Hence, in a space of 1 cu. ft. there will be

$$E = n/v \quad (13)$$

particles of size D , where E denotes the entrainment of particles continuously carried up by the gas stream. However, those particles thrust upward from the bed surface and falling back thereon must also be considered. Therefore, n may again represent the number of rising particles of a given grain size passing a 1 sq. ft. section/sec. at any arbitrary elevation h . If at this elevation their velocity is v , and it takes t sec. for the particles to complete their rise to the

maximum height and to fall back to the same elevation, then the number of particles above this elevation will be

$$m = n t \quad (14)$$

However, the difference between the total number of particles existing above two successive elevations separated by a vertical distance dh will express the entrainment volumetrically in a cube of 1 sq. ft. base and a height of dh :

$$E = \frac{m(h) - m(h + dh)}{dh} = -\frac{dm}{dh} \quad (15)$$

From Equation (14)

$$\frac{dm}{dh} = n \frac{dt}{dh}$$

which substituted in Equation (15) gives

$$E = -n \frac{dt}{dh} \quad (16)$$

While Equations (14) and (16) appear relatively simple, the real problem is to express E as a function of height above the bed or, in other words, v and dt/dh as functions of h . Equations (6) and (8) give v and h as functions of t ; it is also possible to express h solely in terms of v according to the relation

$$h = C \left[v_0 - v + v_m \ln \frac{v_0 - v_m}{v - v_m} \right] \quad (17)$$

To obtain the $v = v(h)$ function would require inverting Equation (17). This cannot be done in closed form since this equation is of a general transcendental form. Hence, corresponding values of the $v = v(h)$ function must either be obtained by iteration from Equation (17) or by a cross plotting of Equations (6) and (8). A similar situation exists with regard to the quantity dt/dh , which must also be solved by numerical analysis.

In Equations (14) and (16) n designates the number of particles of a given grain size thrust from the bed surface by bursting bubbles, as averaged out over 1 sq. ft. of the bed/sec. In this sense $N = \sum n$ represents the entrainment value immediately at the bed surface. This is arbitrarily taken as 100 times a constant, and so

$$N = 100K = K \sum \bar{n}$$

where it is understood that

$$\sum \bar{n} = 100; \bar{n} = n/K$$

with \bar{n} representing the number (or weight) percentage of a given particle size in the total bed spectrum. These considerations are sufficient to establish an entrainment curve over the height of a vessel on the basis of 100 grains liberated on the average/(sq. ft. of bed surface)(sec.). This entrainment curve can be converted into the actual curve through multiplication by a factor of K . K must be obtained from one or the other of two boundary conditions: the actual entrainment at the bed surface or at a sufficient height above the bed

(> T.D.H.), where entrainment has become relatively constant.

The numerical calculation procedure is carried out as follows:

1. Subdivide the bed-catalyst size distribution into a number of representative grain sizes as illustrated in Figure 2(a).

2. Fix the values of μ , ρ , and ρ_0 and of the v_0 parameter for the initial velocity leaving the bed.

3. Calculate the balancing velocity of each of the representative grain sizes by Equation (10) and separate those particles carried by the gas stream ($v_m < 0$) and those returning to the bed ($v_m > 0$).

4. Calculate particle velocities as a function of time from Equation (6) and plot them as shown in Figure 2(b).

5. Calculate height of rise in terms of time from Equation (8) and plot as shown in Figure 2(c).

6. For particles carried by the gas stream ($v_m < 0$) a cross plot of v vs. h as shown in Figure 2(d) permits calculating the relative entrainments from \bar{n}/v at various heights above the bed.

7. For particles returning to the bed, the residence times, or chord lengths \bar{l} pertaining to given h values, permit drawing a plot of \bar{l} vs. h as shown schematically in Figure 2(e).

8. The tangents drawn at various height to the curves of Figure 2(e) give values of $-dl/dh$ as a function of h as shown schematically in Figure 2(f). Calculate relative entrainment through multiplication by a factor of \bar{n} corresponding to the various grain sizes.

9. The entrainment curves corresponding to each of the various size fractions and to the over-all summation are illustrated schematically in Figure 2(g).

This theoretical approach to entrainment through particle dynamics describes the shape of the entrainment curve with height above the bed, as a function of the initial velocity parameter v_0 as well as the physical properties of the operating system. In the absolute sense it cannot predict entrainment without prior knowledge of n or v_0 . If sufficient data were available for independent prediction of n , this method would serve as a powerful tool for correlating the entire entrainment gradient picture. (The particle Reynolds Numbers encountered in computing the balancing velocities in this study ranged from 0.0053 to 9.7.) The empirical approach to entrainment appears to permit such prediction of n so that the significance of the theoretical analysis becomes clearer by comparison with the empirical study.

THE EMPIRICAL APPROACH THROUGH SATURATION TRANSPORT

It is proposed that at some height above the surface of a fluidized bed, where the velocity profile of the rising fluid stream has become essentially constant, the condition of disperse-phase

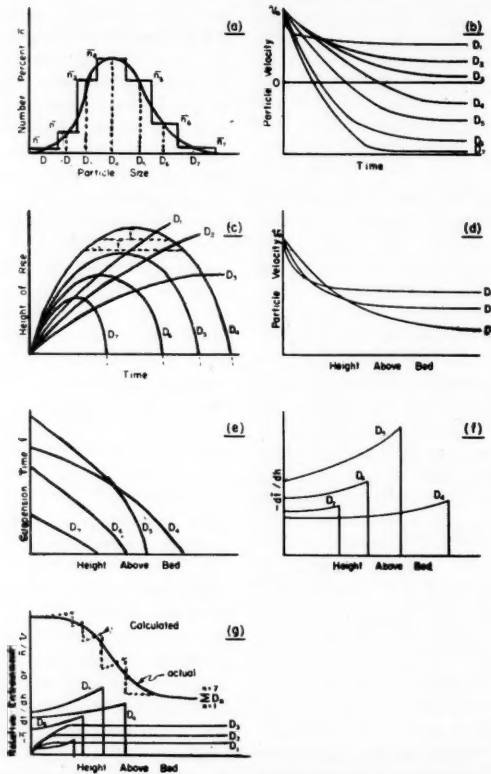


Fig. 2. Outline of stepwise procedure for calculating entrainment by a theoretical approach based on particle dynamics.

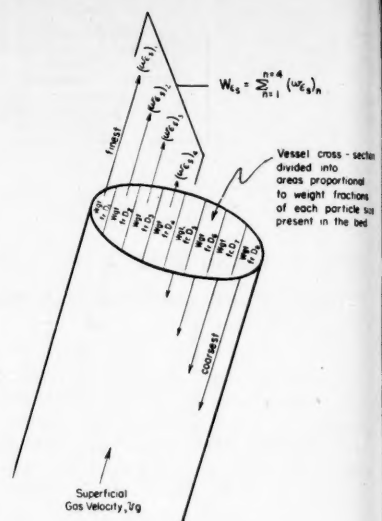


Fig. 3. Illustration of transport entrainment concept at T.D.H.

flow of entrained particles and fluid may be considered as in a carrier line or pneumatic transport line. In the experimental study of such simple vertical transfer lines, in which solids were introduced to the gas stream directly from a hopper, it was found that for a given fluid-solid system there was a maximum particle concentration that could be held in dilute static or flowing suspension. At greater densities, associations between particles caused an increase in effective particle diameter and the suspensions collapsed into slugging beds. These maximum dilute-phase concentrations defined relationships between superficial gas velocity and maximum attainable solids mass flow rate, at that gas velocity, which could be approximated by solids mass flow rate

= solids flowing density \times solids velocity:

$$w_{es} = \rho(1 - \epsilon_s)(V_{ch} - V_{es}) \quad (18)$$

Several sizes in a mixture could then be considered acting in parallel, so that

$$W_{es} = (f \times w_{es}) \quad (19)$$

Since the saturation solids concentration coincides with the condition of incipient bed formation, it is plausible to conceive of a bed replacing the hopper as a solids feed device of relatively infinite capacity and, therefore, of saturation capacity, and so $v_g = V_{ch}$. The model then proposed for the entrainment mechanism would be envisioned as follows:

1. Large bubbles of gas pass up through the bed at velocities of a magnitude several times the balancing velocity of even the largest particle in the mixture. The bubbles erupt at the bed surface and thrust masses of solids into the space above the bed.

2. These masses of solids ejected from the

bed are comprised of the entire spectrum of particle sizes constituting the bed catalyst and contain each component size in the same quantitative distribution as in the bed proper.

3. The intermittent high-velocity bursts of gas impose a fluctuating and highly irregular time-dependent velocity profile over the cross section of the vessel. At successively higher levels above the bed surface, the velocity profile becomes more and more stable, until at and above some finite height the profile remains essentially constant, for example, the rate of change of velocity of all streamlines intersecting any cross-sectional horizontal plane approaches zero. This height has been variously referred to as the transport disengaging height, T.D.H., or equilibrium disengaging height.

4. For any given system the average velocity at T.D.H. may be considered the operating superficial velocity through the vessel. Also at T.D.H. all particles having a balancing velocity greater than the superficial velocity will already have dropped back into the bed. The remaining particles will constitute the entrained material, W_{e_s} .

5. At T.D.H. the vessel cross section may be considered as divided into sections, each of which has an area proportional to the weight fraction of one component particle

size of bed catalyst, in other words, a bundle of transport tubes operating in parallel each at the bed superficial velocity, v_g , as pictured in Figure 3. The bed, acting as a saturation feeder, can supply the component particle sizes to each of these channels at the maximum rate w_s that the gas can transport.

6. At and above T.D.H. the total entrainment, W_{e_s} , is the summation of the component saturation rates w_s .

7. From the bed surface up to the value of T.D.H. the effective velocity dissipates from the surface value of the bubble velocity to the superficial velocity.

The quantitative application of this suggested entrainment mechanism requires means of computing (1) the dilute-phase saturation carrying capacity of a gas stream; (2) the transport or equilibrium disengaging height, T.D.H.; and (3) the rate of effective velocity dissipation.

Equations (18) and (19) give the relation between W_{e_s} and V_{e_h} at saturation; however, it is not possible to solve for W_{e_s} without also knowing e_s and V_{e_h} for each component particle size or for the effective mixture as a whole. A

fairly good estimate can usually be made of V_{e_h} by assuming it equal to the terminal or balancing velocity, but only meager scraps of data are available for estimating e_s . The ranges of the experimental data and the corresponding voidages at saturation density calculated from Equation (18) are given in the literature (16). Since e_s is generally in the range of 0.94 to 1.0, a slight error in this value can make a considerable difference in the value of W_{e_s} . In addition, the few available data hardly provide enough basis for developing a correlation to predict e_s values for various materials. An alternate empirical correlation for V_{e_h} was therefore sought. Experiments had shown that the saturation carrying capacity was identical for horizontal and vertical lines if the particles conveyed were uniform in size. It was, therefore, relevant to include data for liquid-solid systems in this search, though reported investigations with such systems all were conducted in horizontal flow and never specifically performed to measure V_{e_h} ; the accuracy of the data is therefore questionable in nearly all instances. Nevertheless, such data, shown in Figure 4, served as a guide in establishing the final relationship. It will be noted in Figure 4 that the slope of the curves for mixed-size materials differs quite markedly from that for uniform-size particles. Not only is this difference noted with either gas or liquid as the carrying medium, but also the slopes for either medium are almost identical. In marked contrast to the air-transport data the water experiments show little, if any, effect of particle diameter. However, the range of diameters investigated is rather limited. It hardly appears rational to suppose that no particle-diameter effect exists, since in the extreme it is obvious that a higher water velocity would be required to convey 2- to 3-in.-diameter stones than ordinary beach sand. Figure 5 presents the best empirical correlation finally accepted for the data on uniform-size particles. Since Figure 4 showed no diameter effect among the hydraulic experiments, better agreement with the correlants of Figure 5 cannot be expected. Before testing the applicability of Figure 5 in calculating entrainment from fluidized beds, the authors reevaluated a review of the entrainment data from a number of units to determine whether the transport disengaging height could be approximated quantitatively.

The transport disengaging height, T.D.H., above which the rate of decrease in entrainment approaches zero, probably represents in most instances the design optimum for location of cyclones. It appears at the present state of knowledge that this height is some function of the bed diameter and the superficial gas velocity, approximately as shown in Figure 6. The dependence on superficial gas velocity is reasonable since increase

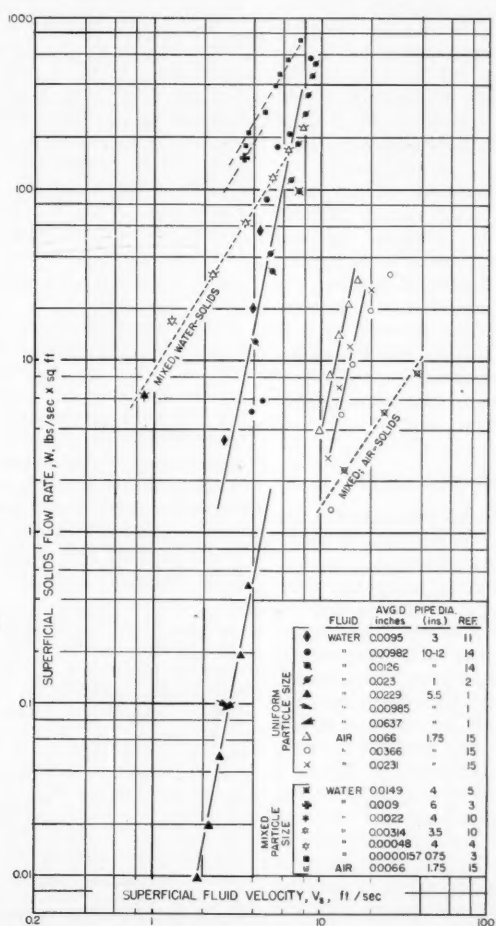


Fig. 4. Experimental saltation data in horizontal flow.

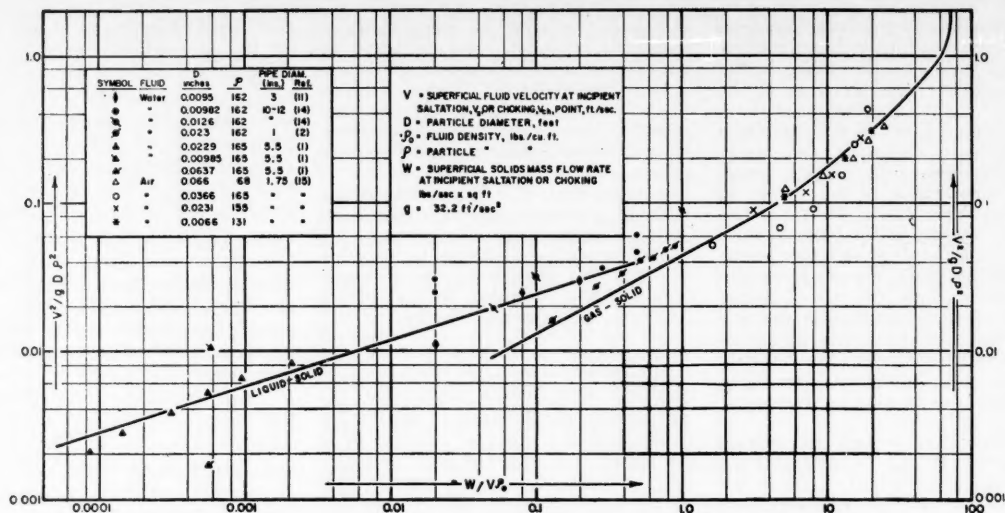


Fig. 5. Empirical correlation of saturation carrying capacity for uniform size particles in horizontal or vertical cocurrent disperse phase flow.

in velocity would increase the rate of rise, and the frequency of eruption, of bubbles at the bed surface, which would in turn require greater distance for dissipation of the fluctuating velocity profiles. The effect of bed diameter may be a result of wall effects at the low diameters and possibly poorer gas distribution at the larger diameter. Figure 6 is based on data from 2-, 3-, 8-, 12-, 24-in. and 16-ft.-diameter vessels. As these data were not obtained solely to establish a relationship for predicting T.D.H., the correlation of Figure 6 must not be considered very accurate; the data were obtained from units operating under a variety of process conditions with different inlet gas distributors and variations in particle-size analyses. The data obtained from small-diameter units may also be suspect because of slugging conditions, which impart distinctly different characteristics to the velocity profiles as well as alternate the bed level, and the effect of size segregation within the bed, which would have less import within large-diameter units, where the solids inventories are greater. Extensive laboratory entrainment experiments car-

ried out at the M. W. Kellogg Company have shown that T.D.H. is not related to the size of the bubbles bursting at the bed surface, as might be suspected. It may, therefore, be supposed that the unstable velocity distribution resulting from small bubbles is augmented by the greater frequency of bubbles to the extent that the disengaging height required to reach a stable profile is equal to that required for large bubbles bursting more violently but less frequently.

To permit calculation of an entire entrainment curve the rate of effective velocity dissipation between the bed surface and the transport disengaging height must be established. In effect, the theoretical treatment of entrainment has partially bridged this gap and so it is appropriate to compare the theoretical and empirical approaches qualitatively before discussing any approximate quantitative correlations.

THE TYPICAL ENTRAINMENT CURVE

Figure 7 illustrates schematically the shape of typical experimentally determined entrainment curves and, in comparison, the extent to which the theoretical and empirical calculation methods generally approach reality. Theory predicts the relative shape of the entrainment curves but requires a quantitative boundary condition, such as, for example, the value of E at T.D.H., in order to translate the entire curve onto an absolute basis. The empirical correlation of Figure 5 could be accepted for this purpose, but theory would still fall short of observed data by too low a prediction of apparent T.D.H. This was to be expected since the maximum height of rise of particles not carried by the gas stream, with the retarding drag forces neglected, would be given by

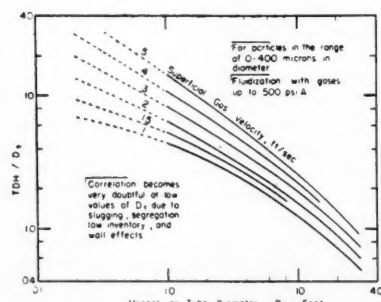


Fig. 6. Empirical correlation for estimating transport disengaging height.

For a 7 ft./sec. bubble velocity and 1 ft./sec. superficial velocity this amounts to only 1.0 ft., compared with observed values of 5 to 15 ft., depending on the vessel size. Point A can be made to coincide with point B in Figure 7 by substituting a bubble-velocity dissipation function in place of the constant superficial velocity assumed as the flow field in the original model illustrated in Figure 1(a). Such an effective velocity dissipation function would also permit carrying on entrainment calculations below T.D.H. by the empirical correlation of Figure 5.

The development of the velocity-dissipation relationship can be carried out directly by measuring velocity profiles downstream of a series of pulsating orifice jets or obtained indirectly by trial and error matching of the theory to experimental entrainment curves and calculating therefrom the required dissipation function. The former method is questionable without the presence of a bed of particles, and exceedingly difficult if not impossible with the presence of a

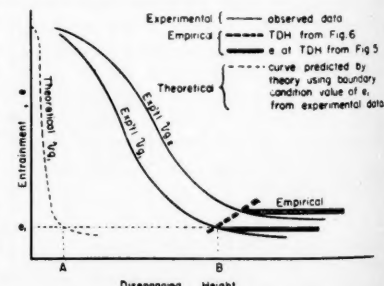


Fig. 7. Schematic comparison of theoretical and empirical entrainment calculations with experimental curve.

bed. most it rec of fu const triati bed a action fully ext trans defin Neith data were these fore, exper signa senta minin bed v

THE T

In desir serva occur particl where are of also studi the s alread was, t "two- ratu sectio vessel in cro clear view reinfo 1 ft. a the a bed le very studyi

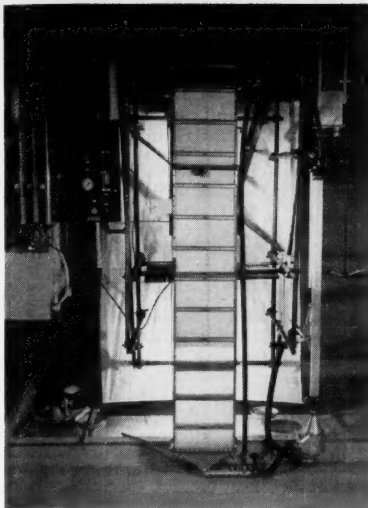


Fig. 8. Over-all view of test apparatus.

bed. The latter method is probably the most readily adapted approach; however, it requires data obtained with a system of fully defined particle-size distribution, constant bed composition (without elutriation or segregation effects), sufficient bed diameter to assure normal bubbling action without slugging tendencies, and fully determined entrainment curves extending above as well as below the transport disengaging height, in order to define exactly this reference point. Neither available commercial operating data nor small-scale experimental results were felt to be sufficiently complete in all these requirements. Attention was, therefore, focused on results obtained in an experimental apparatus particularly designed to give flow characteristics representative of commercial units, with a minimum of bulk and a maximum in bed visibility.

THE TWO-DIMENSIONAL TEST STAND

In the design of any test apparatus it is desirable wherever possible to permit observation of the physical phenomena occurring within the equipment. This is particularly true in a study of fluidization, where bed height and uniformity of flow are otherwise difficult to establish. This is also particularly difficult in fluidization studies since a single layer of particles on the surface of a transparent apparatus already renders it essentially opaque. It was, therefore, proposed to build a so-called "two-dimensional," or rectangular, apparatus simulating a differential vertical section or to slice through a 2-ft.-diameter vessel. The apparatus was made 2 by 24 in. in cross section and built of 11/16-in. thick clear Lucite. Figure 8 shows an over-all view of the test stand. The horizontal reinforcing bars were spaced approximately 1 ft. apart. With strong floodlights behind the apparatus, it was possible to observe bed levels and bed bubbling characteristics very clearly. For flexibility, especially in studying bed-depth effects, and for ease of

construction, the unit was composed of five sections, namely, a bottom grid support and air distribution chamber 18 in. high, one 6-ft. and two 3-ft.-high intermediate sections, and an 8-in. triangular sheet metal cone at the top. Shop air at 60°F. and an average 100 lb./sq. in. gauge was used as the fluidizing medium, admitted through a silica gel and charcoal dryer. A two-stage external cyclone separating unit was used to separate entrained solids from the air stream. The tests were carried out in batches, the bed charge being thoroughly blended with the entrained material following each test in order to minimize bed segregation and to maintain the same composition in each run. Size analyses of the bed at the start of the tests checked with analyses made during and at the end of the program, indicating no net loss of material and a constancy of bed composition.

The size analysis of the cracking catalyst used in the tests is shown in Figure 9. The entrainment data obtained with this material are given in Table 1. Each of the recorded points represents an extrapolation to time zero for a series of measurements of entrainment rate as a function of time during a given run. These data should, therefore, not be subject to either changing particle distribution in the bed, particle-size segregation in the bed, or changing disengaging height due to loss of inventory.

COMPARISON BETWEEN CALCULATED AND EXPERIMENTAL RESULTS

It is proposed to calculate the anticipated entrainment at T.D.H. for the apparatus and solids described in Figures 8 and 9, and to compare the results with the data of Table 1. The procedure is outlined as follows:

1. At a given superficial velocity estimate T.D.H. from Figure 6 for D_T of 2 ft.
2. From the bed particle size analysis (Figure 9) make a component breakdown and tabulate the balancing velocities corresponding to each component.
3. At the superficial velocity of step 1 calculate either
 - the saturation mass flow rates $w_{s,i}$ for each component having a balancing velocity less than the superficial or
 - the saturation rate for a particle diameter equal to the geometric mean (50% point) of all particles with balancing rates less than the superficial.
4. If procedure 3a is followed, multiply each of the component transport rates $w_{s,i}$ by the weight fraction of the component size in the bed catalyst and summate. If procedure 3b is followed, multiply the calculated saturation rate by the total weight fraction of all the component sizes in the bed catalyst making up the mean D used in step 3b. If the catalyst analysis is

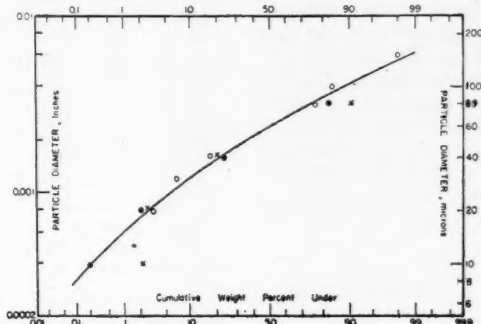


Fig. 9. Size analysis of cracking catalyst.

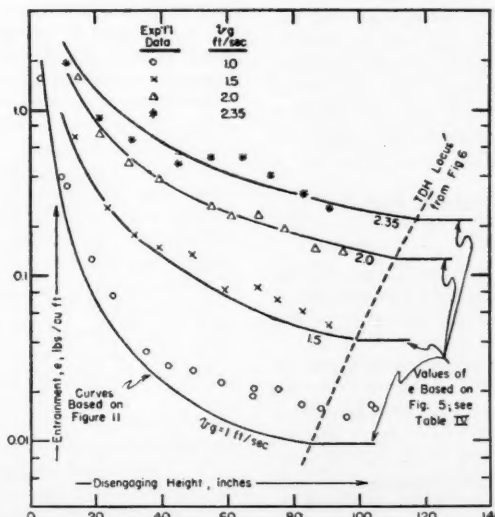


Fig. 10. Comparison between calculated and experimental entrainment data.

broken down into a sufficient number of components, both procedures should give the same result. In general, 3b is simpler, quicker, and less subject to the errors of insufficient component breakdown.

5. Divide the result from step 4 by the superficial gas velocity to obtain the entrainment rate in terms of pounds/cubic feet at T.D.H.

The particle-size breakdown and calculations for the superficial velocities of 1, 1.5, 2 and 2.35 ft./sec. are summarized in Table 2 and the results for all four experimental velocities are shown in comparison with the experimental data in Figure 10. In these calculations the standard drag coefficient for spheres was used to calculate the balancing velocity, the effects of any interparticle forces or of turbulence based on vessel dimensions being thus neglected.

VELOCITY DISSIPATION AND ENTRAINMENT BELOW T.D.H.

The curves drawn through the data of Figure 10 are based on an analogy with the velocity dissipation from gas jets. The curves are shown merely to illustrate the possibilities of this approach. The surface of the bed may be considered as a plane in which are located a number of nozzles which intermittently jet gas into the space above. The nozzles represent gas bubbles bursting at the bed surface. As a first approximation it was suggested that the distance required to dissipate continuous gas jets into space be considered as analogous. Koestel et al. (6) presented the results of such a study using ventilating ducts. Their data correlated as

$$\frac{V_x}{V_0} = 7 \frac{\sqrt{A_e}}{X} \quad (20)$$

Equation (20) applies to a situation in which the jet velocity dissipates into essentially infinite space and V_x approaches zero. In the case of bubble-velocity dissipation above a fluidized bed V_x , or in this instance V_{se} , approaches v_g . Therefore, in order to converge to a finite value Equation (20) may be modified to read

$$\frac{V_x - v_g}{V_0} = \frac{(\text{constant}) \cdot \xi(D_B)}{X} \quad (21)$$

when the cross-sectional area of the orifice, A_e , is considered proportional to some function of the emerging bubble diameter.

Equation (21) is plotted in Figure 11 as V_x/V_0 for the case where $v_g = 1.0$ ft./sec. and $V_0 = 12$ ft./sec. The plotted points refer to the coordinates V_{se}/V_g vs. (height above bed)/T.D.H. and represent the velocity dissipation function derived from the data points of Figure 10. The curve in Figure 11, in conjunction with the correlation presented in Figure 5,

TABLE 1. ENTRAINMENT OF TYPICAL FLUID CATALYTIC CRACKING CATALYST (FIGURE 9) FROM AN AIR FLUIDIZED BED 2 IN. X 24 IN. IN CROSS-SECTION (FIGURE 8)

Height above bed, in.	$v_g = 1.0$ ft./sec.	$v_g = 1.5$ ft./sec.	$v_g = 2.0$ ft./sec.	$v_g = 2.35$ ft./sec.
	Entrainment lb./cu. ft.	Height above bed, in.	Entrainment lb./cu. ft.	Height above bed, in.
105	0.0150	100	0.040	95
104	0.0160	91	0.049	86
96	0.0138	83	0.061	77
88	0.0152	75	0.072	69
82	0.0163	69	0.085	61
75	0.0205	60	0.082	57
68	0.0205	50	0.137	39
67	0.0184	39	0.15	30
58	0.0225	31	0.18	21
50	0.0265	24	0.26	14
42	0.0280	14	0.68	1.60
35	0.035			
26	0.075			
19	0.122			
11	0.34			
9	0.39			
4	1.5			

TABLE 2. ILLUSTRATION OF ENTRAINMENT TRANSPORT CALCULATION

From Fig. 9	Cale'd. wgt. terminal	50% point	Calculated Entrainment $e = (W/V_{ch}) \sum f$				
D_f in.	fract., velocity ft./sec.	$D_{avg.}$ ins.	V_{ch}	$\frac{V_{ch}^2}{gD_f^2}$	From Fig. 5	$W/V_{ch}P_0$	lb./cu. ft.
0.00045	0.01	0.0226					
0.00066	.01	0.0485					
0.00084	.03	0.0799					
0.0011	.05	0.138					
0.00137	.10	0.216					
0.00168	.10	0.320					
0.00194	.10	0.421					
0.00218	.10	0.507					
0.00246	.10	0.628					
0.0028	.10	0.799					
0.00318	.10	0.99					
0.0037	.10	1.25					
0.00435	.05	1.596					
0.0051	.03	1.99					
0.0066	.02	2.83					
tube blown clear		3.25					
			0.002	1.0	0.0154	0.16	0.0095
			0.00215	1.5	0.0321	0.55	.04
			0.0022	2.0	0.0560	1.7	.126
			0.0023	2.35	0.0735	2.8	.213

was used to calculate the curves drawn through the original data in Figure 10.

The analogy to velocity dissipation from jets as represented by Equation (21) and Figure 11 is referred to here merely as an illustration of the relatively reasonable nature of such an approach. A far better procedure would be to

develop the velocity dissipation function from experimental entrainment data using the theoretical approach through Equations (6) and (8). For significant results a larger variety of entrainment data such as shown in Figure 10 must be obtained for various particle sizes and densities.

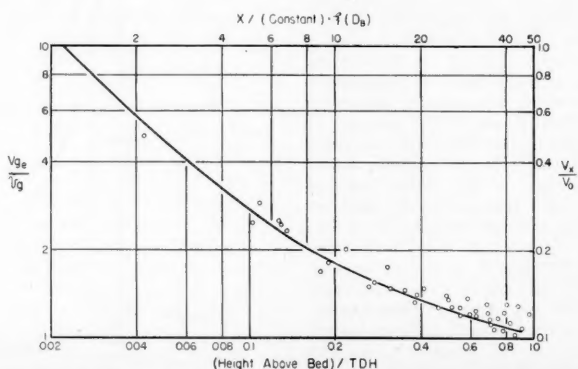


Fig. 11. Comparison between the bubble velocity dissipation function derived from entrainment data and the modified jet velocity dissipation function [Equation (21)].

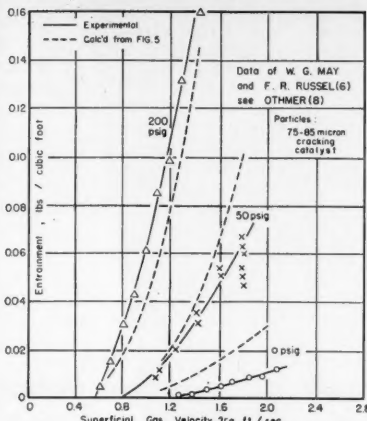


Fig. 12. Comparison between calculated and experimental entrainment at various fluidizing gas-pressure levels.

It is interesting to note that the analogy of Figure 11 indicates probable bubble velocities at the bed surface of about ten times the superficial velocity.

EFFECT OF HIGH-PRESSURE OPERATION

May and Russel (7) discussed the results of studies of the effect of high pressures on entrainment from beds of narrow- and wide-cut samples of FCC catalyst. Their data on a narrow-cut sample are given in Figure 12 as presented by Gohr (9). The solid curves are based on the experimental points; the dashed curves were computed from Figure 5. The agreement is not exceptional, but it does show rather well the proper order of the pressure effect. There is, of course, no assurance that any or all the experimental data were taken at distances above the bed greater than the transport disengaging height. It is also probable that the narrow diameter of the test vessel (2 in.) may have reduced its efficiency as a solids feeder particularly at low pressures where approach to slugging conditions may have occurred.

CONCLUSIONS

A mechanism of entrainment based on an effective bubble-velocity dissipation from the bed surface to the superficial velocity, at the transport disengaging height, has been developed. It has been shown to give fair agreement with representative entrainment data when correlated empirically and to yield curves of the form corresponding to experimental measurements when treated theoretically through a summation of force balances on the individual particles comprising the bed. Entrainment data from a minimum size experimental apparatus, represented as giving results which may be extrapolated to larger scale plants, have been presented for a typical fluid cracking catalyst, fluidized with atmospheric air. Published data at pressures up to 200 lb./sq. in. gauge are also shown in relatively good agreement

with the proposed mechanism of entrainment. It is expected that with sufficient data application of the theory will permit deriving a velocity dissipation function, which in conjunction with particle force balances will predict the entrainment curves for any system.

NOTATION

A	= effective particle cross-sectional area
A_e	= cross-sectional area of jet nozzle at outlet
C	= defined in text as $4\rho D^2/3 \mu$
C_R	= coefficient of drag resistance
D	= effective particle diameter
D_B	= diameter of gas bubbles
D_T	= tube or vessel diameter
E	= entrainment, number of particles per unit volume of gas
e	= entrainment, weight of particles per unit volume of gas
F	= drag force
f	= weight fraction of each component particle size in a mixture
g	= gravitational constant
h	= height above bed
h_{max}	= maximum height of rise of particle above bed
K	= entrainment multiplication or correction factor; ratio of true to calculated relative entrainment
k	= particle shape factor (depends also on flow field)
m	= particle mass
N	= total number of particles thrown up from bed per unit bed cross-sectional area
n	= number of particles of a given size thrown up from the bed per unit cross-sectional area
\bar{n}	= number or weight percentage of a given particle size in total spectrum
R	= resistance of particle in motion
t	= time
t^*	= time taken to reach maximum height of rise
τ	= particle residence time above a given elevation
T.D.H.	= transport disengaging height, height above bed at which entrainment equals saturation carrying capacity of gas stream
V_B	= velocity of rise of gas bubbles
V_{ch}	= superficial gas velocity taken at solids rate W_{ch} and voidage ϵ_s ; or minimum gas velocity capable of carrying solids at rate W_{ch} in vertical upflow
V_{ge}	= effective superficial gas velocity below T.D.H.
V_c	= center-line gas velocity issuing from orifice
V_s	= minimum gas velocity capable of carrying solids at rate W in horizontal flow
V_z	= center-line gas velocity at distance Z from orifice
V_{ch}	= superficial gas velocity taken

at particle inventory of $(1 - \epsilon_s)$ but with zero net flow of particles, for example, $W = 0$; or balancing velocity for suspension of voidage ϵ_s .

v	= particle velocity
v_g	= superficial gas velocity
v_m	= particle balancing velocity
v_0	= particle velocity leaving bed surface
W	= solids net flow rate per unit of tube cross-sectional area
W_{ch}	= weight rate of upflow of total blend of particle size per unit of vessel cross-sectional area at the saturation voidage ϵ_s .
w_{ch}	= uniform particle weight rate of upflow per unit of vessel cross-sectional area at the saturation voidage ϵ_s .
X	= distance from gas jet measured along center line normal to plane of the orifice

Greek Letters

ϵ_s	= tube fractional voidage at saturation solids upflow rate
ρ	= particle density
ρ_0	= fluid density
μ	= fluid viscosity
ξ	= arbitrary function

LITERATURE CITED

1. Ambrose, H. H., Ph.D. thesis, Univ. Iowa (1952); see also reference (7).
2. Blatch, N. S., *Trans. Am. Soc. Civil Engrs.*, **LVII**, 400 (1906).
3. Bond, R. K., *Chem. Eng.*, **64**, No. 10, 249 (1957).
4. Gregory, W. B., *Mech. Eng.*, **49**, 609 (1947).
5. Howard, G. W., *Proc. Am. Soc. Civil Engrs.*, **64**, 1377 (1938).
6. Koestel, A. E., P. Hermann, Tuve, G. L., *Heating, Piping Air Conditioning*, **22**, 113 (1950).
7. May, W. G., and F. R. Russel, paper presented at the North Jersey section of the A.C.S. (Jan. 25, 1954).
8. McNown, J. S., and M. C. Boyer, Proc. of the Fifth Hydraulics Conference, State Univ. Iowa Studies in Eng. Bull., **34** (1952).
9. Othmer, D. F., "Fluidization," Reinhold Pub. Co., N. Y. (1956).
10. Settle, J. J., R. Parkins, I.C.I. Ltd., General Chemicals Division, private communication (1951); see reference (12).
11. Smith, R. A., G. A. Carruthers, I.C.I. Ltd., Billingham Division, private communication (1951); see reference (12).
12. Spells, K. E., *Trans. Inst. Chem. Engrs. (London)*, **33**, No. 2, 79 (1955).
13. Thomas, D. G., Doc. 7540, Tech. Info. Div. U. S. Atomic Energy Comm., Oak Ridge, Tenn.
14. Yufin, A. P., *Izvest. U-Ser. Tekh. Nauk.*, No. 8, 1146 (1949).
15. Zenz, F. A., *Ind. Eng. Chem.*, **41**, 2801 (1949); see also reference (9).
16. Zenz, F. A., *Petroleum Refiner*, **36**, No. 6, 141 (1957).

Manuscript received August 18, 1957; revision received December 20, 1957; accepted January 6, 1958.

Density: Reduced-State Correlations for the Inert Gases

CHARLES E. HAMRIN, JR., and GEORGE THODOS

The Technological Institute, Northwestern University, Evanston, Illinois

The principle of corresponding states has been adopted to the correlation of densities and found to be applicable for nonpolar substances when the critical compressibility factor is introduced as an independent parameter. For the inert gases, densities available in the literature for the gaseous and liquid states have been referred to their critical densities to produce reduced-state correlations which are identical only when their corresponding critical compressibility factors are the same. As a result, a consolidated reduced density correlation for $z_c = 0.291$ has been developed from experimental data for argon, krypton, and xenon. Although the z_c values for helium and neon are essentially alike, different reduced-state correlations for these substances were found to exist. This behavior is expected in view of the radical nature of helium, which can be accounted for by its excessive quantum deviation. Therefore the reduced density correlation for neon ($z_c = 0.307$) is selected as representative of that class of substances having similar z_c values.

The validity of both correlations has been extended beyond the monatomic gases to include substances having comparable critical compressibility factors. With the generalized chart for $z_c = 0.291$ gaseous densities at elevated temperatures and pressures have been calculated for nitrogen, oxygen, carbon monoxide, and methane to produce an average deviation of 1.4% from reported values in the literature. For these substances the average deviation becomes 1.5% for densities in the liquid state. With the reduced density chart for neon ($z_c = 0.307$) densities calculated for hydrogen ($z_c = 0.305$) in the gaseous region produced an average deviation of 2.5% and covered pressures in excess of 500 atm. and temperatures as high as 500°C.

Several equations of state have been proposed for the calculation of densities of gases. In this connection the van der Waals' equation represents the initial attempt to account for nonideal behavior of real gases. Several investigators have proposed equations of state (4, 9, 42, 58) that are capable of representing experimental results accurately; however in some cases their application requires as many as twelve arbitrary constants which ordinarily are not available. In addition the use of these equations is unwieldy and impractical for conventional engineering calculations. Edmister (20) obtains fair agreement with experimental values for hydrocarbons by introducing the residual volume

not compatible with those resulting from a compressibility-factor correlation for gases. In addition, both compressibility- (53) and expansion-factor (65) plots are limited up to pressures of $P_R = 40$ $P_R = 5$, respectively.

The introduction of the critical compressibility factor as a necessary parameter for the correlation of fluid properties has been used by Meissner and Seferian (47) for the correlation of exacting gas-compressibility factors. Brock and Bird (13) extend this approach for the generalized correlation of surface tension, and Lydersen, Greenkorn, and Hougen (41) utilize z_c for the correlation of thermodynamic properties of eighty-two substances. The adaptability of z_c for the

$$\alpha = \frac{RT}{P} - V \quad (1)$$

The calculation of densities in the gaseous state by using compressibility-factor charts is limited in accuracy, particularly near the critical-point region. Furthermore the direct evaluation of liquid densities with the expansion-factor correlation of Watson (65) under isobaric conditions produces values that are

establishment of the saturated compressibility-factor envelope is presented by Hobson and Weber (25). These investigators show that a unique saturation envelope results from substances having similar z_c values. Their conclusions are well demonstrated for a number of substances having z_c values ranging from 0.220 for methanol to 0.291 for nitrogen.

The present investigation considers the development of reduced-state correlations capable of predicting densities in the gaseous and liquid regions. Such a correlation eliminates the discontinuities of density resulting from existing compressibility-factor charts for gases and the expansion-factor correlation for liquids. The inert gases have been arbitrarily selected for study because of their molecular simplicity and consequent adaptability to kinetic-theory considerations.

REDUCED DENSITY CORRELATIONS

An exhaustive literature search was conducted to compile experimental density data for helium, neon, argon, krypton, and xenon. In this search experimental densities for the liquid and gaseous states were considered, including the critical region. The critical constants presented in Table 1 were used to develop the reduced-state corre-

TABLE 1. CRITICAL CONSTANTS OF THE INERT GASES

	M	$T_c, ^\circ\text{K.}$	$P_c, \text{ atm.}$	$\rho_c, \text{ g./cc.}$	z_c
Helium	4.003	5.206 (10)	2.26 (33)	0.0693 (40)	0.306
Neon	20.183	44.45 (17)	26.86 (37)	0.484 (44)	0.307
Argon	39.944	151.2 (40)	48.00 (18)	0.531 (37)	0.291
Krypton	83.80	209.4 (46)	54.18 (46)	0.908 (40)	0.292
Xenon	131.3	289.75 (21)	57.64 (21)	1.099 (21)	0.290

$$0^\circ\text{C.} = 273.16^\circ\text{K.} \quad R = 82.055 (\text{cc.})(\text{atm.})/(\text{g. mole})(^\circ\text{K.})$$

lations
of a
ments
experi-
of the
density
this in
the fo
inert g

He
Ne
Ar
Kr
Xe

Helium
in the
32, 34,
as the
Overla
were a
consider
this fig
critica
critica
mende
were u
g./cc.
was se
densit
constr
of Be
satura
Onnes
Keeso

The
availa
Their
 $P_R =$
use o

lations of this study. With the exception of a limited number of density measurements (3, 5, 21) nearly all available experimental data are reported in terms of the relative quantities: the amagat density and the amagat unit. To convert this information into conventional units the following reference densities of the inert gases have been used:

Density, g./cc.	
(0°C. and 1 atm.)	
Helium	0.00017847 (36)
Neon	0.00089990 (2)
Argon	0.0017839 (6)
Krypton	0.003745 (2)
Xenon	0.0058989 (50)

In addition to these amagat quantities a number of investigators (3, 5, 23, 67, 68, 69) fit their data to virial type equations. The application of equations of this type becomes too laborious for ordinary use and can prove practical only with the use of high speed computers.

Helium ($z_c = 0.306$)

The density data for helium presented in the literature (10, 11, 26, 28, 30, 31, 32, 34, 38, 39, 52, 56, 62, 63, 70) were used as the basis to construct Figure 1. Overlapping points from different sources were carefully examined, and only those considered most reliable are presented in this figure. To develop Figure 1 the actual critical temperature $T_c = 5.206^\circ\text{K}$. and critical pressure $P_c = 2.26$ atm. recommended by Berman and Swenson (10) were used; the critical density $\rho_c = 0.0693$ g./cc. presented by Kobe and Lynn (40) was selected for the calculation of reduced densities. The saturation envelope was constructed from the vapor density data of Berman and Swenson (10) and the saturated liquid data of Kamerlingh Onnes and Boks (34) and Keesom and Keesom (38).

The experimental data of helium are available only for restricted regions. Their extension to cover the region to $P_R = 0.2$ was made possible through the use of the Nelson-Obert compressibility

TABLE 2. COMPARISON OF EXPERIMENTAL REDUCED DENSITIES FOR SEVERAL NON-INERT GASES WITH VALUES OBTAINED FROM FIGURE 4.

Gas	z_c	ρ_c , g./cc.	T_R	P_R	Range Investigated*		% Deviation
					Experimental Points	Maximum	
Oxygen	0.290	0.430	0.6-0.9 1.0-3.0	saturated 0.5-2.0	4	2.3	1.9
					23	3.6	1.2
Nitrogen	0.291	0.311	0.6-1.0 1.0-1.5	saturated-40 0.4-40	16	3.1	1.6
					32	2.9	1.1
Carbon Monoxide	0.294	0.301	0.6-0.95 2.0-7.5	saturated 1.2-2.9	4	3.9	1.7
					11	3.8	1.9
Methane	0.290	0.162	0.5-0.6 1.1-4.8	saturated 1.2-45	4	0.8	0.6
					16	7.1	1.8

*Values in upper line refer to the liquid state while those in lower line refer to the gaseous state only.

factor chart (53) and the relationship

$$\frac{\rho_R}{\rho_{R_1}} = \frac{z_1}{z} \frac{P_R}{P_{R_1}} \frac{T_{R_1}}{T_R} \quad (2)$$

For the case when $P_R = P_{R_1}$, Equation (2) enables the extension of an isobar from a single experimental density measurement. On the other hand, when experimental data are completely lacking in a region, isobars can be constructed by use of the density values of the nearest available isobar, and for conditions of constant temperature $T_R = T_{R_1}$. By using this dual approach and an extension of the isobars of the liquid region to properly join the corresponding isobars of the gaseous region, the reduced density correlation of helium presented in Figure 1 was developed. The isobars calculated in this manner are shown in Figure 1 as dashed lines. The availability of future experimental density data for these regions should prove valuable in definitely establishing the calculated portions of these constant pressure lines. The rather insignificant density change with temperature of helium in the saturated and supercompressed liquid region is unique to this substance, since values below $T_R = 1.0$ correspond to absolute temperatures of less than 5.2°K .

Neon ($z_c = 0.307$)

The experimental density data of

Crommelin, Martinez, and Kamerlingh Onnes (18), Holborn and Otto (27, 29), and Michels and Gibson (48) for gaseous neon and those of Mathias, Crommelin, and Kamerlingh Onnes (44) for the saturated envelope were utilized to construct the reduced density correlation presented in Figure 2. By following the procedure used to extend the isobars for gaseous helium the Nelson-Obert compressibility factor chart (53) in conjunction with Equation (2) made possible the extension of the isobars for neon into regions where no data were available. As in the case for helium these regions are indicated by dashed lines. The effect of pressure on the available saturated liquid data for neon was accounted for through the use of ω and the density data of Benedict (7, 8) for liquid nitrogen. The density data of Benedict made possible the extension of the ω -factor plot of Watson (65) up to reduced pressures of $P_R = 40$. Consequent transformations to account for the effect of pressure were based on the relationship

$$\frac{\rho}{\rho_s} = \frac{\omega}{\omega_s} \quad (3)$$

By following this procedure isobars for pressures up to $P_R = 40$ were calculated for the liquid region and were extended to the corresponding isobar of neon in the gaseous state; these regions are also expressed with dashed lines. The resulting reduced-state correlation for neon presented in Figure 2 covers temperatures as high as $T_R = 20$ and pressures ranging from $P_R = 0.3$ to $P_R = 40$. For these conditions of temperature and pressure the reduced density varies from $\rho_R = 0.1$ to $\rho_R = 3.00$. Comparison of the reduced-state density correlation for helium and neon indicates that no direct correspondence exists between them despite the fact that their values of z_c are almost identical. This difference is anticipated owing to the unusual behavior of helium which can be associated in terms of excessive quantum deviations that can be quantitatively expressed in terms of the quantum mechanical parameter, Λ^* , proposed by de Boer and Bird (19).

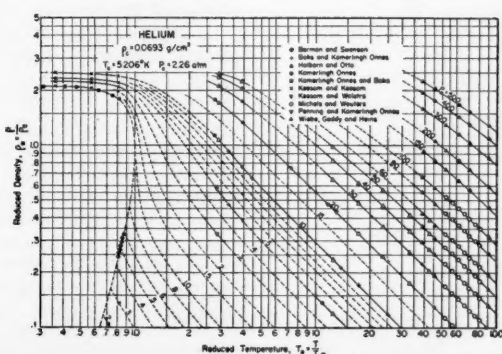


Fig. 1. Reduced density correlation for helium.

Argon ($z_c = 0.291$)

The available density data for argon are presented in Figure 3. The experimental density data of Crommelin (16) and Herz (22) define quite adequately the saturated envelope. Furthermore the data of Kamerlingh Onnes and Crommelin (35) and the calculated values of the National Bureau of Standards (23) cover the region included below a pressure of $P_R = 2.0$. The high pressure data above $P_R = 15$ of Bridgman (12) and those of Michels, Wijker, and Wijker (51) are consistent and define the region extending up to $P_R = 300$ for temperatures ranging up to $T_R = 3.0$. The region between $P_R = 2.0$ and $P_R = 15$ is also established from the data of Michels, Wijker, and Wijker (51) over the limited temperature range of $1.8 \leq T_R \leq 2.8$. As a result the region immediately near the critical point between $P_R = 2.0$ and $P_R = 15$ cannot be accounted for directly from argon density data.

Krypton ($z_c = 0.292$)

Density data for krypton were reported only by Beattie, Brierley, and Barriault (5) and Mathias, Crommelin, and Meihuizen (45). The data of Mathias, Crommelin, and Meihuizen are restricted to conditions representing the saturated envelope, whereas those of Beattie et al. extend up to temperatures of $T_R = 2.75$ and pressures as high as $P_R = 8.0$. These data are also presented in their reduced state in Figure 3 along with those of argon and xenon.

Xenon ($z_c = 0.290$)

Despite the fact that experimental values for xenon are available only from a few sources, these data are sufficient to define the saturated envelope and the region covering pressures up to $P_R = 40$ and temperatures up to $T_R = 2.0$. The data of Patterson, Cripps, and Gray (55)

are restricted to conditions representing the saturated envelope, while those of Beattie, Barriault, and Brierley (3) and Michels, Wassenaar, and Louwerse (50) cover the gaseous region. The experimental data of Habgood and Schneider (21) are limited to the critical region and vary from 15.590 to 16.620°C. Consequently these data were used only to define the critical temperature, pressure, and density for xenon. The density values from these sources are presented in their reduced state in Figure 3 along with those of argon and krypton. In particular the data of Michels et al. have proved helpful in establishing the shape of isobars in the critical region.

GENERALIZED REDUCED DENSITY CORRELATION

The consolidated reduced-density values for argon, krypton, and xenon are

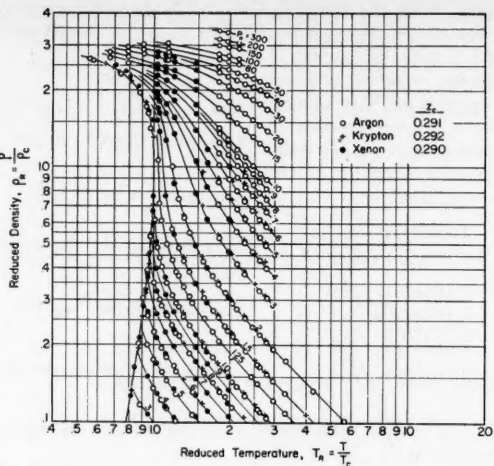


Fig. 3. Composite reduced density correlation for argon, krypton, and xenon.

presented in Figure 3. For these inert gases the critical compressibility factors are 0.291, 0.292, and 0.290, respectively. In Figure 3 it will be noted that the saturated envelope of these inert gases almost superimpose each other. A slight inconsistency is noted for the saturated liquid line of xenon. Aside from this small discrepancy the remaining data follow a corresponding states' behavior and thus permit the establishment of isobars based on experimental data up to pressures of $P_R = 300$ and temperatures up to $T_R = 3$. The isobars of Figure 3 were extended up to temperatures of $T_R = 30$ by using the same technique adopted for helium and neon. The final correlation presented in Figure 4 represents the density behavior for nonpolar substances having a critical compressibility factor $z_c = 0.291$. From the results of these studies it is apparent that the proposals of Meissner and Seferian (47) are valid, since the density data of argon, krypton, and xenon are found to follow a corresponding states' behavior. The reduced-state correlation presented in Figure 2 is based on data for neon but should be applicable to substances having a critical compressibility factor of $z_c = 0.307$. On the other hand the reduced-state correlation of Figure 1 is specific to helium ($z_c = 0.306$); its use should be restricted to this substance, since it differs so markedly from the corresponding correlation for neon ($z_c = 0.307$). This different behavior can be explained from statistical quantum considerations for these two substances. Excessive quantum deviations found to exist for helium are responsible for the unusual behavior of this substance. A measure of these quantum deviations is accounted for by de Boer and Bird (19) in their dimensionless quantum mechanical parameter

$$\Lambda^* = \frac{h}{\sigma \sqrt{m\epsilon}} \quad (4)$$

Fig. 2. Reduced density correlation for gases and liquids ($z_c = 0.307$).

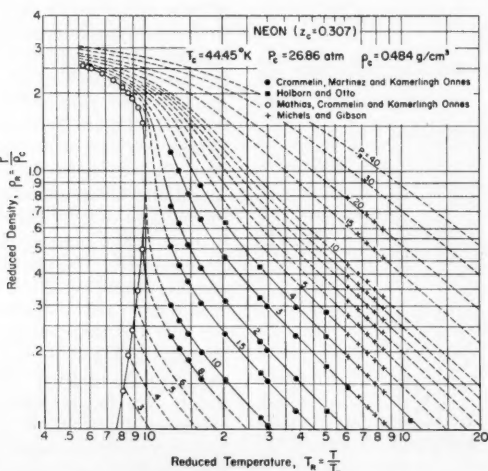


TABLE 3. COMPARISON OF EXPERIMENTAL REDUCED DENSITIES FOR ARGON WITH VALUES CALCULATED FROM SEVERAL REDUCED-STATE CORRELATIONS

		P _R Reduced Density Values				
T _R	P _R	From Experimental Values	Meissner and Seferian (47)	Maslan and Littman (48)*	Nelson and Obert (53)	This Investigation (Figure 4)
1.054	1.0	0.441	0.445	0.394	0.445	0.443
1.136	40.0	2.64	—	—	2.73	2.66
1.972	5.0	0.760	0.754	0.802	0.754	0.760
1.972	90.0	2.64	—	3.05	—	2.65
2.47	40.0	2.00	1.96	2.28	2.02	2.04

*For these reduced densities the pseudocritical values recommended by Maslan and Littman (48) $T_c = 143.7^\circ\text{K}$. and $P_c = 50.5 \text{ atm}$. have been used.

To present orders of magnitude the quantum mechanical parameter has been calculated for the inert gases from the Lennard-Jones force constants ϵ and σ and the corresponding atomic weight. The values used for these calculations were obtained from Hirschfelder, Curtiss, and Bird (24) and are presented below:

	ϵ, erg	$\sigma, \text{cm.}$	Λ^*
Helium	14.11×10^{-16}	2.576×10^{-8}	2.74
Neon	49.28	2.789	0.58
Argon	117.18	3.418	0.182
Krypton	262.29	3.61	0.096
Xenon	316.13	4.055	0.062

The calculated value for helium $\Lambda^* = 2.74$ represents the most excessive quantum deviation possible for the elements. Next in line is that of hydrogen which has a value of $\Lambda^* = 1.80$ followed by a value of $\Lambda^* = 0.58$ for neon. For argon, krypton, and xenon the calculated Λ^* values are 0.182, 0.096, and 0.062 and approach the limiting condition of zero for the idealized case. In view of these comparisons it is reasonable to expect helium to follow a pattern of behavior that is specific to it, since this is the only substance having a quantum mechanical parameter of the highest order of magnitude. Extending this line of reasoning it is expected that the reduced-state correlation of neon may be somewhat limited to this substance, since its quantum mechanical parameter cannot be completely neglected.

COMPARISON OF RESULTS

The reduced-state correlations of Figures 1 and 2 were based on the available experimental data for helium and neon; therefore for these substances the ability to read these charts establishes their accuracy. The validity of the regions where generalized approaches were utilized to complete these charts can only be established for accuracy with the introduction of new data specific to these regions.

Figure 1 cannot be used for any substance other than helium, despite the fact that the z_c values for helium (0.306), neon (0.307), and hydrogen (0.305) are essentially the same. The reasons underlying this pattern of behavior have

already been explained by the quantum mechanical parameter.

An attempt was made to utilize Figure 2 for the prediction of hydrogen densities. Twenty-three experimental density values for hydrogen were checked in the temperature range of $T_R = 2.0$ to $T_R = 15.0$ and the pressure range of $P_R = 0.8$ to $P_R = 40$. Figure 2 was found to agree with these values within 1.8% for pressures below $P_R = 10$. For higher pressures the average deviation increased to 4.2%. This behavior is not unexpected in view of the fact that the quantum mechanical parameters of neon and hydrogen are significant and different from each other. Because of the unusual nature of hydrogen, as characterized by its value $z_c = 0.305$ and $\Lambda^* = 1.80$, it is essential that a density correlation specific to this substance be treated separately (60).

Figure 4 is applicable to nonpolar substances having values of z_c about 0.290. Since the greatest quantum deviations are exhibited by helium, hydrogen, and neon, the quantum mechanical parameter of other substances becomes unimportant. Therefore only the z_c values need be considered in the application of reduced-state correlations for substances other than helium, hydrogen, and neon. Experimental densities for the

gaseous and liquid states of oxygen ($z_c = 0.290$), nitrogen ($z_c = 0.291$), carbon monoxide ($z_c = 0.294$), and methane ($z_c = 0.290$) were compared with those resulting from Figure 4 to produce the deviations presented in Table 2. The weighted average deviation of 1.5% for the gaseous and liquid regions of these substances suggests that the third parameter z_c is a valid criterion for the application of reduced-state correlations to nonpolar substances. No comparisons have been carried out with the original data for argon, krypton, and xenon to test the validity of Figure 4, since the densities of these substances superimpose each other satisfactorily (Figure 3).

Five arbitrarily selected values for argon were used to produce reduced densities for the experimental conditions presented in Table 3. For these conditions of temperature and pressure, reduced densities obtained directly from Figure 4 were compared with the corresponding values resulting from the experimental data. Additional reduced densities were calculated from several compressibility factor charts available in the literature (43, 47, 53). These results are presented in Table 3; they indicate, for the limited conditions investigated, that next to Figure 4 the Nelson-Obert compressibility chart offers a correlation capable of predicting adequately densities in the gaseous state.

Values from the Lydersen, Greenkorn, and Hougen (41) studies and also those of Pitzer (57) were not included in Table 3, since the ranges of temperature and pressure reported by them are limited and do not cover the majority of conditions presented in Table 3.

The results of these studies indicate the justification of using z_c in reduced-state correlations as a third correlating parameter for nonpolar substances as long as the quantum deviations of these substances can be ignored.

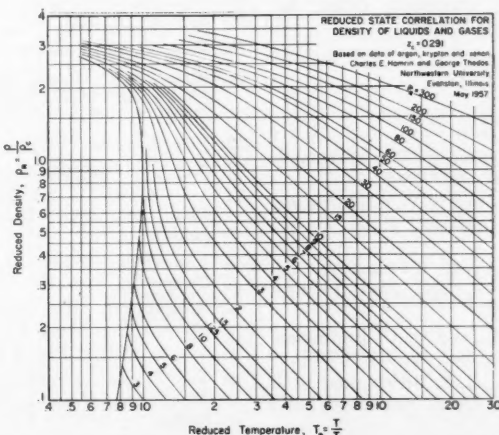


Fig. 4. Reduced density correlation for gases and liquids ($z_c = 0.291$).

NOTATION

$A.U.$ = amagat unit, PV/P_0V_0
 d_A = amagat density, ρ/ρ_0
 h = Planck's constant, 6.624×10^{-27} erg. sec.
 m = mass of molecule, g.
 M = molecular weight, g./g. mole
 P = pressure, atm.
 P_c = critical pressure, atm.
 P_0 = reference pressure, 1 atm. or 1 m. Hg
 P_R = reduced pressure, P/P_c
 P_{R_1} = reduced pressure for experimental density value
 R = gas constant, 82.055 (cc.)(atm.)/(g. mole)(°K.)
 T = absolute temperature, °K.
 T_c = critical temperature, °K.
 T_R = reduced temperature, T/T_c
 T_{R_1} = reduced temperature for experimental density value
 V = molar volume, cc./g. mole
 V_c = critical molar volume, cc./g. mole
 V_0 = reference molar volume at 0°C. and reference pressure, cc./g. mole
 z = compressibility factor, PV/RT
 z_1 = compressibility factor at P_{R_1} , and
 T_{R_1}
 z_c = critical compressibility factor, $P_c V_c / RT_c$

Greek Letters

α = residual volume, cc./g. mole
 ϵ = maximum energy of attraction for Lennard-Jones potential, erg.
 Λ^* = quantum mechanical parameter, dimensionless
 ρ = density, g./cc.
 ρ_c = critical density, g./cc.
 ρ_0 = density at 0°C. and 1 atm.
 ρ_R = reduced density, ρ/ρ_0
 ρ_{R_1} = experimental reduced density at conditions T_{R_1} and P_{R_1}
 ρ_s = saturated liquid density, g./cc.
 σ = collision diameter for Lennard-Jones potential, cm.
 ω = Watson expansion factor for liquids
 ω_s = Watson expansion factor for saturated liquids

LITERATURE CITED

1. Baly, C. C., and F. G. Donnan, *J. Chem. Soc.*, **81**, 907 (1902).
2. Baxter, G. P., and H. W. Starkweather, *Proc. Nat. Acad. Sci. U. S.*, **15**, 441 (1929).
3. Beattie, J. A., R. J. Barriault, and J. S. Brierly, *J. Chem. Phys.*, **19**, 1219 (1951).
4. Beattie, J. A., and O. C. Bridgeman, *J. Am. Chem. Soc.*, **50**, 3133 (1928).
5. Beattie, J. A., J. S. Brierly, and R. J. Barriault, *J. Chem. Phys.*, **20**, 1613 (1952).
6. Beattie, J. A., and H. P. Julien, *Ind. Eng. Chem.*, **46**, 1668 (1954).
7. Benedict, Manson, *J. Am. Chem. Soc.*, **59**, 2224 (1937).
8. *Ibid.*, p. 2233.
9. Benedict, Manson, G. B. Webb, and L. C. Rubin, *J. Chem. Phys.*, **8**, 334 (1940).
10. Berman, R., and C. A. Swenson, *Phys. Rev.*, **95**, 311 (1954).
11. Boks, J. D. A., and H. Kamerlingh Onnes, *Communs. Phys. Lab. Univ. Leiden*, No. 170a (1924).
12. Bridgeman, P. W., *Proc. Am. Acad. Arts. Sci.*, **70**, 1, (1935).
13. Brock, J. R., and R. B. Bird, *A.I.Ch.E. Journal*, **1**, 174, (1955).
14. Cath, P. G., and H. Kamerlingh Onnes, *Communs. Phys. Lab. Univ. Leiden*, No. 152b (1921).
15. Clark, A. M., F. Din, J. Robb, A. Michels, T. Wassenaar, and T. N. Zwietiering, *Physica*, **17**, 876 (1951).
16. Crommelin, C. A., *Communs. Phys. Lab. Univ. Leiden*, No. 118a (1910).
17. *Ibid.*, No. 162a (1923).
18. ———, J. P. Martinez, and H. Kamerlingh Onnes, *ibid.*, No. 154a (1914).
19. de Boer, J., and R. B. Bird, *Phys. Rev.*, **83**, 1259 (1951).
20. Edmister, W. C., *Ind. Eng. Chem.*, **30**, 352 (1938).
21. Habgood, H. W., and W. G. Schneider, *Can. J. Chem.*, **32**, 98 (1954).
22. Herz, W., *Z. Elektrochem.*, **33**, 348 (1927).
23. Hilsenrath, Joseph, C. W. Beckett, W. S. Benedict, Lilla Fano, H. J. Hoge, J. F. Masi, R. L. Nuttall, Y. S. Touloukian, and H. W. Woolley, "Tables of Thermal Properties of Gases," 75, National Bureau of Standards Circular No. 564, U. S. Department of Commerce (1955).
24. Hirschfelder, J. O., C. F. Curtiss, and R. B. Bird, "Molecular Theory of Gases and Liquids," 1110, John Wiley and Sons, Inc., New York (1954).
25. Hobson, Merk, and James H. Weber, *A.I.Ch.E. Journal*, **2**, 354 (1956).
26. Holborn, L. and J. Otto, *Z. Physik*, **10**, 367 (1922).
27. *Ibid.*, **23**, 77 (1924).
28. *Ibid.*, **30**, 320 (1924).
29. *Ibid.*, **33**, 1 (1925).
30. *Ibid.*, **38**, 359 (1926).
31. Kamerlingh Onnes, H., *Communs. Phys. Lab. Univ. Leiden*, No. 102a (1908).
32. *Ibid.*, No. 102c (1908).
33. *Ibid.*, No. 124b (1911).
34. ———, and J. D. A. Boks, *Communs. Phys. Lab. Univ. Leiden*, No. 170b (1924).
35. Kamerlingh Onnes, H., and C. A. Crommelin, *ibid.*, No. 118b (1910).
36. Keesom, W. H., "Helium," p. 27, Elsevier Publishing Company (1942).
37. ———, *Physik. Ber.*, **4**, 613 (1923).
38. ———, and A. P. Keesom, *Communs. Phys. Lab. Univ. Leiden*, No. 224d (1933).
39. Keesom, W. H., and W. K. Walstra, *Physica*, **7**, 985 (1940).
40. Kobe, K. A., and R. E. Lynn, Jr., *Chem. Revs.*, **52**, 117 (1953).
41. Lydersen, A. L., R. A. Greenkorn, and O. A. Hogen, Report No. 4, Engineering Experiment Station, Univ. of Wisconsin, Madison (1955).
42. Martin, J. J., and Y. C. Hou, *A.I.Ch.E. Journal*, **1**, 142 (1955).
43. Maslan, F. D., and T. M. Littman, *Ind. Eng. Chem.*, **45**, 1566 (1953).
44. Mathias, E., C. A. Crommelin, and H. Kamerlingh Onnes, *Communs. Phys. Lab. Univ. Leiden*, No. 162b (1923).
45. Mathias, E., C. A. Crommelin, and J. J. Meihuizen, *ibid.*, No. 248b (1937).
46. Meihuizen, J. J., and C. A. Crommelin, *ibid.*, No. 245c (1937).
47. Meissner, H. P., and Ralph Seferian, *Chem. Eng. Progr.*, **47**, 579 (1951).
48. Michels, A., and R. O. Gibson, *Ann. Physik*, **87**, 850 (1928).
49. Michels, A., and T. Wassenaar, *Physica*, **16**, 253 (1950).
50. Michels, A., T. Wassenaar, and P. Louwerse, *ibid.*, **20**, 99 (1954).
51. Michels, A., Hub. Wijker, and Hk. Wijker, *ibid.*, **15**, 627 (1949).
52. Michels, A., and H. Wouters, *ibid.*, **8**, 923 (1941).
53. Nelson, L. C., and E. F. Obert, *Trans. Am. Soc. Mech. Engrs.*, **76**, 1057 (1954).
54. Nicholson, G. A., and W. G. Schneider, *Can. J. Chem.*, **33**, 589 (1955).
55. Patterson, H. S., R. S. Cripps, and R. W. Gray, *Proc. Roy. Soc. (London)* **A86**, 579 (1912).
56. Penning, F. M., and H. Kamerlingh Onnes, *Communs. Phys. Lab. Univ. Leiden*, No. 165c (1923).
57. Pitzer, K. S., D. Z. Lippmann, R. F. Curl, Jr., C. M. Huggins, and D. E. Petersen, *J. Am. Chem. Soc.*, **77**, 3433 (1955).
58. Redlich, Otto, and J. N. S. Kwong, *Chem. Revs.*, **44**, 233 (1949).
59. Rudenko, N. S., *Physik. Z. Sowjetunion*, **6**, 470 (1934).
60. Schaefer, C. A., M.S. thesis, Northwestern University, Evanston (1957).
61. Schmidt, G., and W. H. Keesom, *Physica*, **4**, 971 (1937).
62. Schneider, W. G., *Can. J. Research*, **27B**, 339 (1949).
63. ———, and J. A. H. Duffie, *J. Chem. Phys.*, **17**, 751 (1949).
64. Uhlir, A., Jr., *ibid.*, **20**, 463 (1952).
65. Watson, K. M., *Ind. Eng. Chem.*, **35**, 398 (1943).
66. Weinberger, M. A., and W. G. Schneider, *Can. J. Chem.*, **30**, 422 (1952).
67. Whalley, E., Y. Lupien, and W. G. Schneider, *ibid.*, **31**, 722 (1953).
68. *Ibid.*, **33**, 633 (1955).
69. Whalley, E., and W. G. Schneider, *Trans. Am. Soc. Mech. Engrs.*, **76**, 1001 (1954).
70. Wiebe, Richard, V. L. Gaddy, and Conrad Heins, Jr., *J. Am. Chem. Soc.*, **53**, 1721 (1931).

Manuscript received March 14, 1958; revision received May 19, 1958; paper accepted May 20, 1958.

Flow Patterns of Liquids in Agitated Vessels

SHUICHI AIBA

University of Tokyo, Tokyo, Japan

In this paper flow patterns of liquids in an agitated vessel of 11 1/2-in. I.D. were measured with the radioisotope of cobalt as a means of measurement. Flow patterns of representative types of impellers, namely paddle, turbine, and propeller, were studied. Water and glycerine solutions were used as liquids the viscosity of which ranged from 1 to 108 cp. Effects of geometrical factors of agitated systems on flow patterns were investigated, in particular those of baffles.

Experimental results obtained were analyzed, and a curve showing the relation between flow patterns and power consumption by the agitation was made.

Generally agitation in miscellaneous chemical processes is concerned with blending such systems as solid-liquid, liquid-liquid, and liquid-gas with the objectives of increasing mass and heat transfer rates, of increasing physical and chemical reaction rates, of securing homogeneous mixtures, etc.

Many papers on agitation have been published over the past twenty years (1); for example, rather detailed information is now available on such problems as how to obtain homogeneous solid suspensions in liquids by using various types of impellers. However it can be seen that this information is not yet comprehensive enough to solve all kinds of problems because agitation itself is complex and because the basic principles have not yet been established. Another reason for this situation is that flow patterns of liquids, which are a fundamental of agitation, yet remain to be studied more thoroughly and quantitatively.

Several years ago the author devised a tiny mechanical instrument to determine flow patterns in an agitated vessel of pilot-plant scale (2). Flow patterns were qualitatively measured, and an explanation of the relation between flow patterns and the power requirements of agitation was tentatively made.

Recently Rushton published a paper on flow patterns in an agitated vessel (4) in which he measured flow patterns by optical means and determined liquid velocities in the vessel, particularly around the impeller of a flat-blade turbine, photographically. He correlated the pumping capacity of the impeller with these data.

More recently Yamamoto presented a paper on flow patterns and tried to get quantitative analyses from the theory of turbulence also photographically (5).

EQUIPMENT AND PROCEDURE

Figure 1 shows the principal parts of the device used to measure flow patterns. A miniature Geiger-Müller (GM) tube of about 25/64 in. in diameter and 1 3/16 in. in length, shielded by an aluminum tube,

was hung one on side. On the other side a steel ball of about 11/64-in. diameter, into which an appropriate amount of a radioisotope of cobalt-60 (metal form) was buried, was hung by a platinum wire of 30 μ diameter; both elements were immersed.

The intensity of gamma rays was markedly affected by changing the distance between the detector and the radiation source; that is, the intensity of radiation measured by the detector was greatly influenced by the geometrical configurations of the system. The effects of geometrical factors on the measurements of radiation are important in the application of radioisotope techniques.

In the case in which both the detector and the radiation source are immersed in liquids it is difficult to compute the radiation intensity detected by the counter solely on the basis of the geometrical configurations of the system because the multiple scattering phenomenon becomes predominant.

However in the special case in which the distance between the elements is not too large and the radiation source is located centrally along the length of the GM tube, the interrelation between the radiation intensity N_0 counts/min. and the distance could be calibrated, as shown in Figure 2.

When one uses such a calibration curve, the measurement of N_0 leads to the determination of l rather easily and accurately when the latter is unknown. When the liquid is in motion, the radiation source P is transpositioned to P' as a result of the balance of moment around A with liquid velocity head (Figure 3). Then the following equation of balance is obtained, in which the resistance of the platinum wire is negli-

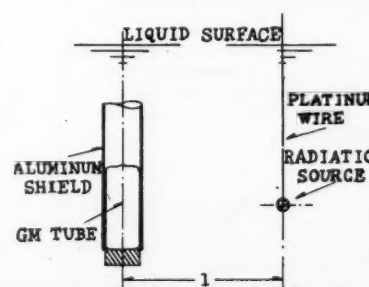


Fig. 1. Principal part of a device to measure flow velocity.

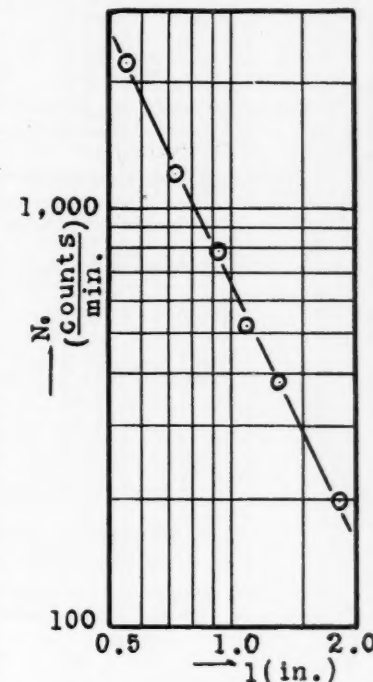


Fig. 2. Example of calibration curve.

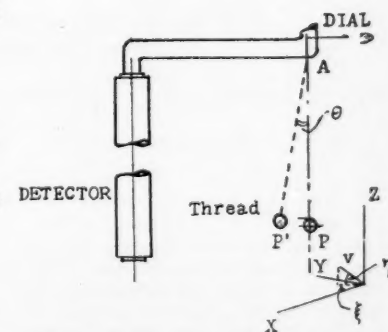


Fig. 3. Balance of moment with liquid velocity.

TABLE 1. REPRESENTATIVE DIMENSIONS OF IMPELLERS USED

	<i>L</i> , in.	<i>W</i> , in.	Number of blades
Paddle	4 46/64	5/8	2
Flat blade	3 15/16	25/32	6
turbine (4)			
Marine propeller	2 61/64	19 32/32*	3

*Mean along the radius.

TABLE 2. AN EXAMPLE OF CALCULATED RESULTS

	ω	C^{**}	C^*	Re^*
Paddle	7.35	3.93	12.6	1.47×10^4
Flat blade	10.2	3.28	10.6	2.08×10^4
turbine (4)	12.5	3.07	9.90	2.50×10^4
Marine propeller	15.7	2.96	9.50	3.13×10^4
	21.0	2.60	8.35	4.20×10^4

Paddle ($L = 4-46/64$, $W = \frac{5}{8}$ in., unbaffled, liquid, water).

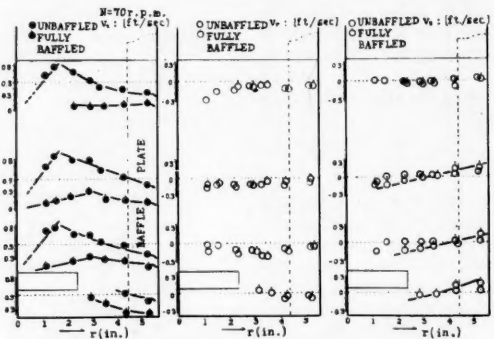


Fig. 4. Example of flow patterns (water)
 $N = 70$ rev./min. (unbaffled and fully baffled paddle surface at which flow velocity was measured).

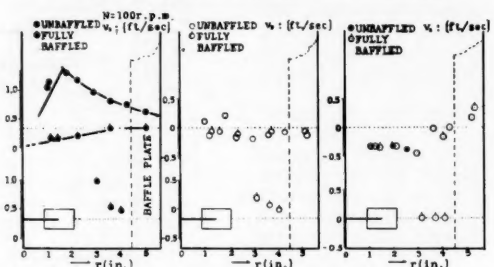


Fig. 5. Example of flow patterns (water)
 $N = 100$ rev./min. (unbaffled and fully baffled turbine).

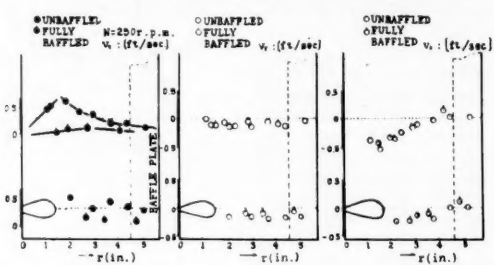


Fig. 6. Example of flow patterns (water)
 $N = 250$ rev./min. (unbaffled and fully baffled propeller).

gible, compared with that of the steel ball.

$$\left(\frac{\pi}{6}\right) \cdot D_P^3 \cdot (\rho_s - \rho) g \cdot \sin \theta = C \left(\frac{\rho}{2}\right) \cdot v^2 \cdot \left(\frac{\pi}{4}\right) \cdot D_P^2 \cdot \cos(\theta \mp \eta) \quad (1)$$

The term $\sin \theta$ in Equation (1) was calculated from the transposition of the ball from P to P' by determining the radiation intensity N_0 in such a way that the axis of the GM tube was vertical and lay in the same plane as point A and the radiation source P' (Figure 3).

Moreover, by measuring η in Equation (1) through a procedure which will be described later, the following equation was obtained relating to each experimental condition:

$$C \cdot v^2 = \text{const.} \quad (2)$$

For each experimental determination all factors on the right-hand side of Equation (2) were known, and for this determination this side is a constant.

The liquid velocity v at each point in the vessel was easily determined by trial and error from this equation, with the

help of the drag-coefficient data of the ball. The liquid velocity thus obtained is considered to be the average for the period of time of each experiment.

A cylindrical glass vessel about $11\frac{1}{2}$ in. in diameter and 14 in. high was used as the agitation vessel throughout this series of experiments. Glycerine and water were used as liquids. In most cases the vessel was filled to the depth of 11 in. Three representative types of impeller, that is, paddle, turbine, and marine propeller, were used. Each impeller was placed concentrically about $1\frac{13}{64}$ in. above the bottom of the vessel. Representative dimensions of these impellers are shown in Table 1. In each case flow patterns were measured under unbaffled and fully baffled* conditions. Four baffle plates, each $1\frac{13}{64}$ and 12 in. in width and length, respectively, were attached to a cage, which could be removed from the vessel for unbaffled operation.

To measure liquid velocity the device shown in Figure 3 was fixed at a certain radial position for each depth under the liquid surface. Varying the location of the device determined flow patterns throughout the vessel except in the immediate vicinity of each impeller.

Under fully baffled conditions, with the expectation that the velocity distribution might be changed depending on the radial direction along which the measuring instrument was fixed, experiments were made to determine the velocity distribution along several radial directions between the baffle plates. No difference was apparent among them. Then experiments were made, under fully baffled conditions, exclusively along the radius just midway between two baffle plates. This excludes of course the situation immediately behind or in front of each baffle plate, which cannot be studied by the instrument. For unbaffled conditions the effect was assumed to be negligible because of the symmetry of the flow, radially as well as peripherally.

When one compares the dimension of this device with the dimensions of the vessel, the effect of disturbances caused by the device on the flow patterns was assumed to be negligible, as far as this series of experiments was concerned. In Equation (1) η was determined as follows: The vertical distance between the tip of a tiny string ($1\frac{13}{64}$ in. long) attached to the ball and an imaginary horizontal line drawn through the center of the ball was measured by a cathetometer from outside the vessel.

The angle ξ subtended by the xy projection of the velocity vector and the x axis was measured during the determination of $\sin \theta$ with the help of a dial placed horizontally around the shaft (Figure 3). In this case the radial direction was arbitrarily chosen as the y axis.

When the determination of low velocity was necessary, an acryl-resin ball of about $7/64$ -in. diameter, containing an appropriate amount of cobalt-60, was used as the radiation source. It was determined by preliminary experiments that the flow resistance of the platinum wire which suspended the ball was not an appreciable source of error. It was also determined that

*Fully baffled conventionally means that the peripheral flow is completely impeded by a certain number of baffle plates causing vertical flow components. Usually four baffle plates are used.

the wind flow.
 Cons
 assure
 miniatur
 as sh
 each ex
 the wh
 It was
 error in
 3%.

Simp
 concer
 velocity
 transpor
 Liquid
 into ve
 paring
 Alon
 tions th
 was a
 were t
 chrono
 Reynol
 of exp
 turbula
 region

EXPERI
 Flow Pa
 Types o
 The C
 Flow
 and a
 5, and
 used a
 obtained
 baffled
 ease o
 and i
 individ
 figures
 repres
 of the

The
 shown
 and 8.
 Figure
 (11 in
 indep
 tank,
 determ
 fied in
 show
 lines
 measu
 each e

Wh
 follow
 the ca
 tive o
 region
 periph
 region
 vessel
 whole
 forced
 found
 wall,
 cylind

Wh
 than 1

Vol.

ball.
1
period

2 in.
and
series
were
vessel
three
is,
were
center
tom
as of
the 1.
asured
ndi-
and
rely,
ll be
ffed
vive
tain
the
out
nity

the
dition
radial
struc-
e to
long
the
rent
ade,
vely
two
the
front
be
ffed
the
be
ffed
the
the
essel,
ed
to
peri-
(1)
n
tical
ring
and
ough
by a
pro-
the x
tion
aced
(3).
arbi-
city
about
ariate
the
by
flow
which
able
that
the
certain
com-

the wire did not bend, owing to the liquid flow.

Constant precautions were taken to assure the calibration stability of the miniature GM tube, and a calibration curve as shown in Figure 2 was prepared before each experiment to check the reliability of the whole circuit, including the GM tube. It was estimated that the experimental error inherent in the circuit was about 2 to 3%.

Simple geometrical corrections were made concerning the position at which the liquid velocity was measured because of the transposition of the ball from P to P' . Liquid velocity thus measured was resolved into vectors v_t , v_r , and v_z for ease of comparing experimental results.

Along with the flow pattern determinations the power consumption of the agitators was also measured. The dynamometer used was a spring type, the deflections of which were transmitted by a pair of self-synchronous motors. Judging from the modified Reynolds number, one sees that this series of experiments was made covering the turbulent region as well as the transition region from turbulent to laminar flow.

EXPERIMENTAL RESULTS

Flow Patterns of Representative Types of Impellers

The Case of Unbaffled Operations (Water)

Flow patterns of a paddle, a turbine, and a propeller are shown in Figures 4, 5, and 6, respectively, when water was used as the liquid. In each figure data obtained under unbaffled and fully baffled conditions are superimposed for ease of comparison. Peripheral, radial, and vertical components are shown individually from left to right in these figures. The abscissa of each figure represents the distance from the center of the vessel.

The liquid level at a standstill is shown in Figure 4. (See also Figures 7 and 8.) Though the level is not clear in Figures 5 and 6, it was described before (11 in.). Moreover, since the velocity is independent of the depth within the tank, as is apparent in Figure 4, the determination of the velocity was simplified in Figures 5 and 6. The data points show the actual elevations. The dotted lines indicate the depth to which the measuring instrument was immersed in each experiment.

When one refers to these figures, the following facts seem to be apparent. In the case of unbaffled agitation, irrespective of the type of impeller, two flow regions existed in the vessel relating to the peripheral velocity component. In the region found around the center of the vessel the liquid seemed to rotate as a whole, as if it were a solid (cylindrical forced vortex). In the other region, found between the former and the vessel wall, the liquid rotated along with the cylindrical vortex (free vortex).

When many experimental results other than those shown in Figures 4, 5, and 6

were reviewed, it was found that the radius of the cylindrical vortex was constant, irrespective of the rotational speed of the impeller as well as of its location inside the vessel. It is presumed that r_p is influenced mainly by the geometrical conditions of the agitation system and the physical properties of

the liquid, in particular by the viscosity. The latter effect will be described later.

Outside the cylindrical vortex, tangential velocity was experimentally found to be

$$v_t = C_s r^{-n} \quad (3)$$

Inspection of many experimental results shows that

$$n_0 = 1 \sim 0$$

Furthermore, it was found that n_0 approached unity as the location of the velocity measurement approached the liquid surface; therefore liquid velocity becomes more averaged owing to fluctuations or turbulence in the vicinity of each impeller. In the case of the paddle, in particular, it was found that radial as well as vertical velocity components were nearly independent of r except for the region adjacent to the impeller.

When one considers the radial component, the negative direction is that toward the tank center. In each figure the positive direction is not always apparent; however the positive direction of flow, namely, the radial flow toward the tank wall, should exist, as may be deduced from the simple concept of a material balance. It is assumed that such flows might exist in the region just adjacent to the impeller or to the tank wall when the positive direction is not apparent. Study of such a region is beyond the scope of this investigation.

The small-scale circulation, radially or vertically, could not be determined, owing to the geometry of the measuring instrument. If stress is placed on such details, other appropriate procedure should be adopted, say for example, optical means. Moreover the data obtained experimentally are not refined enough to define local swirls or small eddies. The fact that positive radial flow vectors or reasonable vertical components could not be found because of the difficulty of their determination does not indicate that the data which were obtained are in error. In the case of turbine and propeller types of impellers radial discharge and suction flow were more apparent, even in the case of unbaffled condition. Generally it can be seen that the flow patterns of the paddle, turbine, and propeller types of impellers are characterized by peripheral, radial, and axial flows, respectively, when unbaffled conditions are in effect.

The Case of Fully Baffled Operation

In the case of fully baffled operation the flow pattern is characterized by a marked decrease in the tangential velocity component, irrespective of the impeller type. The radial component remains almost unchanged. Moreover the tangential velocity decreased as the location at which the velocity was measured approached the liquid surface (Figure 4). For each impeller, when one refers to the

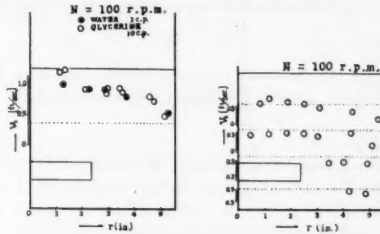


Fig. 7. Flow patterns of glycerine solution (unbaffled paddle).

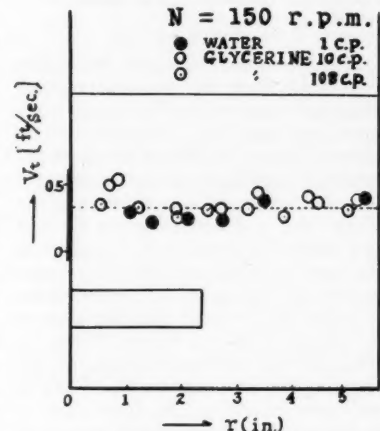


Fig. 8. Flow patterns of glycerine solution (fully baffled paddle).

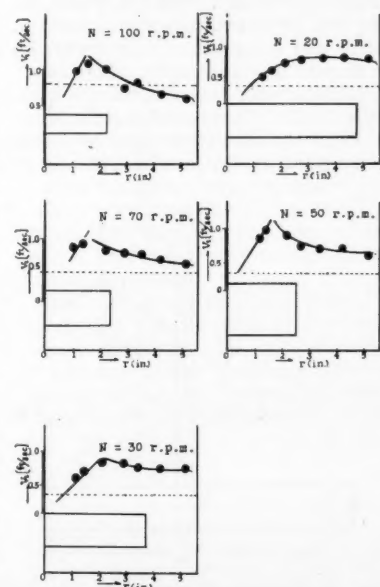


Fig. 9. Effect of geometrical dissimilarity (unbaffled paddle, liquid: water).

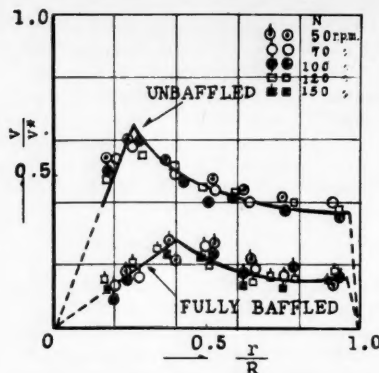


Fig. 10. Review on flow patterns (paddle).

other figures obtained, there were certain cases in which the so-called "cylindrical" vortex was found rather distinctly. However the radius of the cylindrical vortex was larger than that observed in the case of unbaffled condition. Even in the case of paddle type of impellers, upward and downward flow became apparent.

Effect of Viscosity.

The effect of liquid viscosity on flow patterns is shown in the case of the paddle type of impeller for unbaffled and fully baffled conditions in Figures 7 and 8, respectively. In these figures only the tangential velocity component is shown. From Figure 7 it is to be noted that tangential velocity does not decrease markedly along liquid depth even in the case of the viscous liquid (viscosity = 108 centipoises). In the unbaffled case, as liquid viscosity increased, the boundary between forced and free vortex became more vague, and the region of forced cylindrical vortex became narrowed down around the center of the vessel. Such a tendency can also be seen in the case of fully baffled conditions. However it is seen that the difference of flow patterns relating to unbaffled and fully baffled conditions is not so great as that noted when water was used. The effect of liquid viscosity will be considered again in the discussion of experimental results.

Effect of Impeller Geometry

Since the effect of geometry on flow patterns can be most distinctly seen in the tangential velocity component for each impeller under unbaffled conditions, experimental data for the paddle type of impeller, with water used as the liquid, are presented in Figure 9 as an example. Figure 9 is based upon the total tangential velocity gradient along the radius. Different speeds were chosen mainly for convenience in experimenting. However, by referring to Figure 10, which will be described later (unbaffled case, tangential velocity predominant), one can see that the flow pattern under any revolitional speed is represented by

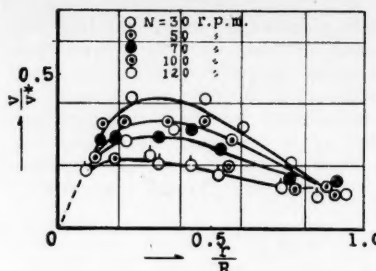


Fig. 11. Review on flow patterns (unbaffled paddle, glycerine solution 108 centipoises).

the gradient of tangential velocity. It is to be noted from these figures that impeller span is more effective than width in decreasing the velocity gradient in the free vortex region.

DISCUSSION OF EXPERIMENTAL RESULTS

Summary of Flow-Pattern Behavior

In this summary the data for paddle type of impellers for the case in which water was used as liquid are considered, based on many data other than those shown in Figure 4; Figure 10 shows the results. In this figure the ordinate is the ratio of the liquid velocity at a given depth from the liquid surface (in this case about 7 in.) to the tip velocity of the impeller. The abscissa is the ratio of the distance from the vessel center at which the velocity was measured to the vessel radius. In Figure 10 parameters are the rotational speeds of the impeller. It is seen that the flow patterns are independent of N . This fact is significant because it constitutes one of the clues with which to judge whether or not the flow is turbulent. If v/v_L were to be used as the ordinate in Figure 10, the flow patterns which are independent of N and dependent of r/R would be obtained. In the so-called "turbulent" region the same fact was found experimentally for other types of impellers also.

Figure 11 shows the effect of liquid viscosity. It can be seen from this figure

that liquid viscosity has a significant influence on the flow patterns as indicated by increased slip between the liquid and the impeller surface as the impeller speed increases. Thus the effect of viscosity is not negligible, as would be suspected from a consideration of the Reynolds number.

The Correlation Between Flow Patterns and Power Consumption

For simplicity the correlation between flow patterns and power consumption will be considered first for the case of the paddle type of impeller. Schematically the flow pattern relating in particular to tangential velocity components is drawn in Figure 12.

It is assumed that liquid viscosity is negligible, as far as flow patterns in the turbulent region and in the steady state are concerned. It is further assumed that Helmholtz's theory of conservation of vorticity is applicable to the vortex tube which was found experimentally to exist in the vessel. This tube is assumed to extend from the liquid surface to the vessel bottom, just encompassing the impeller. The vorticity of a cross section of this tube is $2\omega_0$, and its circulation is $2\pi r_F^2 \omega_0$. Vorticity around the impeller is assumed to be $2\pi r_0 \omega'$.

$$\omega' = \left(\frac{r_F}{r_0} \right)^2 \cdot \omega_0 \quad (4)$$

The torque with length, width, and angular velocity of L , W , and ω , respectively, is calculated by the following equation:

$$T = \int dT = \int C' \frac{\rho(v_i - v_t)^2}{2g_e} \cdot W \cdot r \cdot dr \quad (5)$$

$$\left. \begin{aligned} v_L &= r \cdot \omega \\ v_t &= r \cdot \omega' \\ W/r_0 &= \alpha \end{aligned} \right\} \quad (6)$$

When one substitutes Equation (6) into Equation (5) and postulates C^* as an average of C' covering the integration range from $r = 0$ to $r = r_0$,

$$\begin{aligned} T &= \frac{C^* \cdot \rho \cdot \alpha \cdot r_0 (\omega - \omega')^2}{2g_e} \int_{r=0}^{r=r_0} r^3 dr \\ &= \frac{C^* \cdot \rho \cdot \alpha \cdot (\omega - \omega')^2}{8g_e} \cdot r_0^5 \end{aligned} \quad (7)$$

The power consumption of agitation becomes

$$\begin{aligned} P_0 &= T \cdot \omega = \frac{C^* \cdot \rho \cdot \alpha \cdot \omega \cdot (\omega - \omega')^2}{8g_e} \cdot r_0^5 \\ &= \frac{C^* \cdot \rho \cdot \alpha \cdot \omega \cdot (\omega - \omega')^2 \cdot L^5}{(8)(32)g_e} \end{aligned} \quad (8)$$

Also

$$C^* \cdot \omega \cdot (\omega - \omega')^2 = C^{**} \cdot \omega^3 \quad (9)$$

By introducing C^{**} defined by Equation

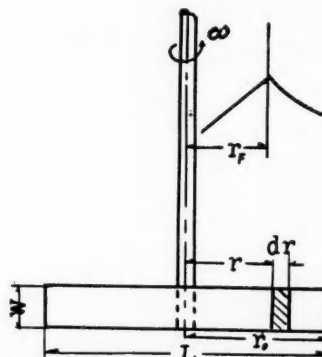


Fig. 12. Schematic diagram of the relation between flow pattern and power consumption of agitation.

(9),
Equa
And
a'
Accor
Fo
from
agit
tions
betw
sump
for
geom
calcul
flow
values
relati
surfa
from
mina
exam
(L =
wate
Tabl
Such
patte
were
dime
baffe
13.
It
spite
ment
baffe

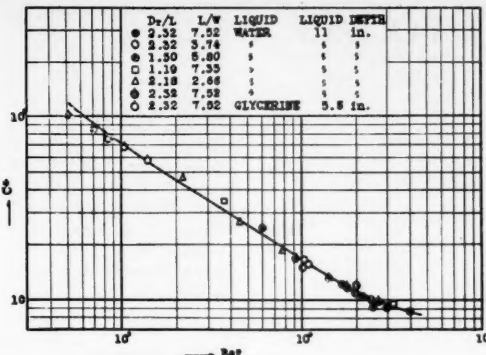


Fig. 13. Correlation between C^* and Re^* .

(9), Equation (10) is obtained from Equations (8) and (9).

$$P_0 = \frac{C^{**} \cdot \rho \cdot \alpha \cdot \omega^3 \cdot L^5}{(8)(32)g_c} \quad (8)(32)g_c$$

$$= \frac{C^{**} \cdot \rho \cdot \alpha \cdot (2\pi n)^3 \cdot L^5}{(8)(32)g_c}$$

$$= \frac{C^{**} \cdot \rho \cdot \alpha' \cdot n^3 \cdot L^5}{g_c} \quad (10)$$

And

$$\alpha' = \frac{(2\pi)^3 \cdot \alpha}{(8)(32)} = (0.966) \cdot \alpha \quad (10a)$$

Accordingly the power number is

$$N_P = \frac{P_0 \cdot g_c}{n^3 L^5 \rho} = \alpha' \cdot C^{**} \quad (11)$$

For the region around the impeller, from which the energy required for agitation disseminates into liquid, Equations (9) and (11) show the interrelation between flow patterns and power consumption of agitation. Using the data for power consumption for a given geometrical agitation system, one can calculate C^{**} from Equation (10). From flow-pattern measurements numerical values of (r_p, ω_0) can be found. Then the relative angular velocity of liquid on the surface of the impeller may be estimated from Equation (4), followed by the determination of C^* from Equation (9). For example, for a paddle type of impeller ($L = 4.46/64$ in., $W = 5/8$ in., liquid: water) calculated results are shown in Table 2, in which Re^* is defined as

$$Re^* = \frac{r_0^2 \cdot \omega \cdot (1 - \omega'/\omega) \cdot \rho}{\mu}$$

Such calculations, based on data for flow patterns as well as power determinations, were made for other paddles of various dimensions, both unbaffled and fully baffled. The results are shown in Figure 13.

It is noted from this figure that, in spite of a rather wide range of experimental conditions and irrespective of baffled and unbaffled conditions, the

relation between Re^* and C^* is rather simple. For the other types of impellers, in particular flat blade turbines, correlation curves which coincide with that of Figure 13 were obtained by similar calculations (3). For propeller type of impellers, in which drag due to lift cannot be neglected, a similar relation was found by introducing a correction factor which is a function of the drag coefficient, lift coefficient, and the angle between the blade and the plane of rotation (3).

It is to be noted that local velocity information, in particular the radius of the forced-vortex region within the tank, is necessary for the prediction of power consumption by use of Figure 13.

CONCLUSIONS

1. A means of measuring flow patterns in an agitation vessel was devised by applying radioisotope techniques.

2. Flow patterns of representative types of impellers, namely paddles, turbines, and propellers, were measured by this procedure.

3. Effects of geometrical factors on flow patterns were investigated. In particular, effects of baffle plates on flow patterns were studied.

4. It was found that flow patterns for a given agitation system are independent of the impeller speed in the turbulent region. This does not hold true for the case of viscous liquids, when agitation is far from turbulent.

5. Based on several assumptions, a correlation between flow patterns and power consumption was made. A rather simple and unique curve was obtained between Re^* and C^* , covering the whole range of this experimentation.

ACKNOWLEDGMENT

The author wishes to express his cordial thanks to Professor Y. Ohyama of the Tokyo Institute of Technology for his constant guidance throughout this work. He is also indebted to Professor J. L. York of the University of Michigan for his encouragement to publish this paper.

NOTATION

C_0 = experimental constant
 C = drag coefficient of ball
 C' = drag coefficient
 C^* = drag coefficient of impeller
 C^{**} = drag coefficient of impeller
 D_p = ball diameter, in., ft.
 D_T = vessel diameter, in., ft.
 g = acceleration due to gravity, ft./sec.²
 g_c = conversion factor, (lb.-mass)(ft.)/(lb.-wt.)(sec.²)
 l = distance between the radiation source and the detector, in.
 L = impeller diameter, in., ft.
 n = revolutionary speed of impeller, rev./sec.
 N = revolutionary speed of impeller, rev./min.
 N_0 = number of gamma quantum per unit time detected by the GM counter
 N_P = power number
 P_0 = power consumption of agitation, (lb.-wt.)(ft.)
 r = distance from the vessel center, in., ft.
 r_0 = half of impeller length, in., ft.
 r_p = radius of a cylindrical vortex which rotates as if it were solid, in.
 R = vessel radius, in.
 Re = Reynolds number, ft. of impeller
 T = torque imposed on impeller, (lb.-wt.)(ft.)/sec.
 v = liquid velocity ft./sec.
 v^* = tip velocity of impeller, ft./sec.
 v_L = tangential velocity of a point on the impeller, ft./sec.
 v_t = tangential velocity component, ft./sec.
 v_r = radial velocity component, ft./sec.
 v_z = vertical velocity component, ft./sec.
 W = impeller width, in., ft.

Greek Letters
 ρ = liquid density, lb./cu. ft.
 ρ_s = ball density, lb./cu. ft.
 μ = liquid viscosity, lb./(ft.)(sec.)
 ω_0 = half of vorticity, radian/sec.
 ω = angular velocity of impeller, radian/sec.
 ω' = angular velocity of liquid on the surface of impeller, radian/sec.

LITERATURE CITED

1. Aiba, Shuichi, *Chem. Eng. (Japan)*, **15**, 354 (1951).
2. —, *J. Sci. Research Inst., Tokyo*, No. 1286 (1952).
3. —, *Chem. Eng. Japan*, **20**, 290, 298, 571 (1956).
4. Rushton, J. H., *Chem. Eng. Progr.*, **50**, 597 (1954).
5. Yamamoto, Kazuo, *Chem. Eng. Japan*, **20**, 685 (1956).

Manuscript received October 31, 1957; revision received December 19, 1957; paper accepted May 19, 1958.

INDEX TO VOLUME 4

Authors

A	Hottel, H. C. 3 Howard, Katherine S. 362 Howkins, J. E. 324 Hsu, Y. Y. 58 Hyman, Seymour C. 33	I	Sikchi, K. G. 27 Simkin, O. J. 493 Slattery, John C. 137 Smith, G. C. 180 Smith, Julian C. 330 Smith, P. L., Jr. 266 Stein, Ralph P. 127 Storow, J. Anderson. 305 Strom, J. R. 153 Stuart, Edward B. 383 Suckling, R. D. 114
B	Isaac, Nadine. 498 Isbin, H. S. 81	J	
Babb, A. L. 143 Baddour, R. F. 90, 223 Baer, Eric. 218 Baird, R. M. 460 Balekjian, Garen. 43 Banchero, J. T. 102 Bankoff, S. G. 24 Baumeister, Ernest B. 69 Beckmann, R. B. 180 Begell, William. 127 Bennett, C. O. 69 Bennett, J. A. R. 418 Bird, R. Byron. 137 Bondi, A. 493 Boylan, D. R. 175 Braulick, C. J. 465 Bretton, R. H. 367 Brewer, Jerome. 317 Brian, P. L. T. 223 Brier, J. C. 453	K	Johanson, L. N. 445 Johnson, Homer F. 273 Joseph, Leon. 33	
C	Katz, Donald L. 43 Kay, Webster B. 293, 296 Kern, Donald Q. 157 Kintner, R. C. 153 Knudsen, J. G. 332 Kohn, James P. 211 Kottwitz, F. A. 175 Kurata, Fred. 211, 317	L	Lake, W. C. 403 Lama, R. F. 497 Lance, R. P. 75 Lemlich, Robert. 376 Lenoir, J. M. 263 Lermond, David S. 330 Lewis, J. B. 418 Lightfoot, E. N. 499 Lind, John E., Jr. 330 Longwell, P. A. 53
D	Madonna, L. A. 497 Malloy, John B. 6J Marchello, J. M. 97 Maruyama, T. 245 McAllister, R. A. 282, 362 McKelvey, James M. 218 Mesler, Russell B. 102 Metzner, A. B. 393 Myers, J. E. 75	M	Walker, Charles A. 413 Walker, J. E. 240 Warzel, F. Morgan. 296 Weil, N. A. 472 Wendel, M. M. 249 Wender, Leonard. 15 Westwater, J. W. 58 Whan, G. A. 240 White, R. R. 161 Wilhelm, R. H. 423
E	Ebach, E. A. 161 Eckstrom, H. C. 403	N	Yang, H. H. 453 Yasui, George. 445
F	Fatt, Irving. 49 Flint, Daune L. 132 Forman, J. Charles. 356 Foss, Alan S. 231 Friend, W. L. 393 Frisch, Herbert A. 293 Frye, C. G. 403 Fujinawa, K. 245	P	Zennik, Herbert E. 37 Zenz, F. A. 472
G	Garner, F. H. 114 Geddes, R. L. 389 Gerster, J. A. 231 Gilliland, E. R. 90, 223 Glaser, Marvin B. 63 Gruber, Alan K. 33 Gunn, R. D. 430, 494	R	
H	Hamrin, Charles E., Jr. 480 Hanratty, Thomas J. 132, 495 Happel, John. 197 Hayes, W. B., III. 346 Hellums, J. D. 465 Hesson, James C. 207 Himmelblau, D. M. 143 Hoelscher, H. E. 300 Holland, C. D. 346	S	
		S	
		T	
		V	
		W	
		Y	
		Z	

Subject Index

A

Absorption, gas-phase, accompanied by a liquid-phase chemical reaction.	223
into an accelerating film.	382
of nitrogen tetroxide in water.	249
phase equilibrium at the gas-liquid interface during.	439
Absorption, steady state of a sparingly soluble gas in an agitated tank with simultaneous irreversible first-order reaction.	499
Acetone-water, liquid viscosities of, up to normal boiling point.	362
Adsorption equilibria, liquid-phase.	383
Agitated vessels, flow patterns of liquids in.	485
Ammonia-n-butane, phase relations for.	293
Ammonia-isooctane system, phase relations for.	296
Analyses, film penetration model for mass and heat transfer.	97
Analyses, electrical models for steady state flow.	49
Analogy between momentum transfer and heat or mass transfer for a	

homogeneous isotropic turbulent field.....	495	Convergence Pressures for Close-Boiling Nonideal Systems.....	263	Estimation of the Stage Efficiency of Simple Agitated Vessels Used in Mixer-Settler Extractors.....	202
Aqueous liquids, dissolution rates of solids in mercury and.....	418	Correlation of Local Velocities in Tubes, Annuli, and Parallel Plates.....	240	Extraction of Sugar from Beets.....	453
Axial dispersion of mass in packed beds.....	13M, 14M, 161, 367	Countercurrent column for the zirconium-hafnium separation.....	498	Extraction, estimation of efficiency of, in agitated mixer-settler vessels	202
Axial Dispersion of Mass in Flow Through Fixed Beds.....	367	Countercurrent gas-liquid flow, correlation of loading in packed towers.....	324	of immiscible liquid accompanied by chemical reaction.....	245
Axial Dispersion and Void-Cell Mixing Efficiency in Fluid Flow in Fixed Beds.....	13M	Critical locus for binary azeotropes, ammonia- <i>n</i> -butane.....	293	F	
B					
Baffled heat exchangers, local shell-side heat transfer coefficients.....	332	ammonia-isooctane.....	296	Film, accelerating, absorption into...	382
Ball flow meters.....	380	close-boiling nonideal systems.....	263	Film Boiling From Vertical Tubes...	58
Beds, fluidized, characteristics of gas pockets in.....	445	Critical Temperatures and Pressures of Hydrocarbons.....	356	Film coefficients, individual, for immiscible-liquid mass transfer.....	180
mechanism of particle entrainment from.....	472	D	324	Film condensation, heat transfer coefficients for.....	218
surface dynamics of, and quality of fluidization.....	423	Density: Reduced-State Correlations for the Inert Gases.....	480	Film-Penetration Model for Mass and Heat Transfer.....	97
packed, radial porosity variations in.....	453	Derivation of an Equation for Predicting Minimum Spouting Velocity.....	497	Film thickness distributed, reactor design for.....	300
Beets, extraction of sugar from.....	263	Diffusion in a Pore of Varying Cross Section.....	343	Filtration, effect of porosity upon variable rate-variable pressure	170
Binary systems, nonideal close-boiling, critical locus for.....	293	Diffusion coefficients of dilute gases and self-diffusion coefficients of dense gases.....	137	prediction of cake resistance in constant pressure.....	175
Boiling, film, on vertical tubes.....	58	Discharge Coefficients through Perforated Plates at Reynolds Numbers of 400 to 3,000.....	497	First-order reaction, steady state absorption of a sparingly soluble gas in an agitated tank with simultaneous irreversible.....	499
nucleate, effect of high pressure on organic liquids.....	102	Dispersion of immiscible liquids by orifice mixers.....	346	Flow of Two-Phase Carbon Dioxide Through Orifices.....	207
local coefficients for horizontal tubes.....	75	Dissolution Rates of Solids in Mercury and Aqueous Liquids: the Development of a New Type of Rotating Dissolution Cell.....	300	Flow distribution in mixing headers...	33
Boundary layer, reactor design for distributed thickness.....	300	Dissolution cell, rotating.....	266	Flow measurements with ball flow meters.....	380
Bubble trays, effect of liquid mixing upon efficiency.....	231	Distillation, effect of liquid mixing upon bubble tray efficiency	418	Flow Patterns of Liquids in Agitated Vessels.....	485
pulsed operation of.....	282	fractional, for hydrocarbon mixtures.....	418	Fluid flow	
C					
Cake resistance, prediction of, in constant-pressure filtration.....	175	pulsations on sieve and bubble trays.....	231	analogue for nonsteady state one-dimensional packed beds.....	49
Calculation of the Diffusion Coefficient of Dilute Gases and of the Self-diffusion Coefficient of Dense Gases.....	137	Distribution of Eddy Viscosity and Mixing Length in Smooth Tubes.	389	correlation of local velocities in tubes, annuli, and parallel plates.....	240
Carbonation reaction, kinetic studies of.....	143	Distributions, Poisson, some properties of.....	282	distribution of eddy viscosity and mixing length in smooth tubes	27
Carbon dioxide, two-phase flow through orifices.....	207	Drainage of Packed Beds in Gravitational and Centrifugal-Force Fields.....	27	theoretical development of velocity profiles for fully developed isotropic turbulence in pipes	495
Centrifugal extraction, theory of cake drainage.....	305	Drop Formation in Liquid-Liquid Systems from Single Nozzles.....	290	two-phase, of carbon dioxide through orifices.....	207
Characteristics of Gas Pockets in Fluidized Beds.....	445	Drops, wall effect upon terminal velocity of, in liquid-liquid systems.....	153	Fluidization, quality of, and surface dynamics of fluidized beds.....	423
Chlorine-ferrous chloride system in study of absorption with chemical reaction.....	223	Dynamics, surface, of fluidized beds, and quality of fluidization.....	423	Fluidized beds, characteristics of gas pockets in	445
Combined Laminar Free-and Forced-Convection Heat Transfer in External Flows.....	285	E	190	correlation of heat transfer coefficients to boundary surfaces.....	15
Condensation, film heat transfer coefficients.....	218	Eddy diffusion, momentum and mass transfer in wetted-wall columns.....	27	heat transfer in	376
Condensation of Vapor in the Presence of Noncondensing Gas.....	413	Eddy viscosity and Prandtl mixing length in smooth tubes.....	102	surface dynamics of, and quality of fluidization	423
Condensers, mathematical development of tube loading.....	157	Effect of Liquid Mixing on the Performance of Bubble Trays.....	493	theoretical-empirical approach to the mechanism of particle entrainment from	472
Conductive heat transfer, shape factors for.....	330	Effect of Superatmospheric Pressures on Nucleate Boiling of Organic Liquids.....	102	Fluid-particle heat transfer in packed beds.....	63, 69
Constants, pseudocritical from volumetric data for gas mixtures....	493	Electric analogues, for nonsteady state fluid flow	49	Forced-convection heat transfer with internal heat generation.....	319
Control of Flow Distribution by Headers.....	33	Electrolytic Methods for Measuring Water Velocities.....	338	Formation of Interfacial Area in Immiscible Liquids by Orifice Mixers, The.....	346
Convection, natural, for fluids in maximum density region.....	81	Entrainment, particle, a theoretical-empirical approach to the mechanism of, from fluidized beds	472	Fractional distillation, a general index of power for hydrocarbon mixtures	389
Convective heat transfer, combined laminar free and forced in external flows.....	285	Entrapment of Gas in the Spreading of a Liquid Over a Rough Surface	24	Freezing of liquids, graphical methods for	53
Convective Heat Transfer from High-Temperature Air Inside a Tube.	37	Equilibria, liquid-phase adsorption	383	Freezing Points of Binary Mixtures of Methane.....	317
		Equilibrium, phase, at the gas-liquid interface during absorption	439	Furnace design, radiant heat transfer in nonisothermal gas fields	3

Gas, sparingly soluble in an agitated tank with simultaneous irreversible first-order reaction.....	499	the Methane-Hydrogen Sulfide System.....	211	Loading in Horizontal Condensers.....	157
Gas Absorption Accompanied by a Liquid-Phase Chemical Reaction.....	223	Homogeneous isotropic turbulent field.....	495	Mechanism of particle entrainment from fluidized beds, a theoretical-empirical approach to.....	472
Gas flow rates, through microporous solids.....	90	Horizontal tubes, local boiling coefficients for.....	75	Mercury dissolution rates of solids in, and aqueous liquids.....	418
Gas-liquids interface during absorption, on phase equilibrium at the Gas-liquid solutions, regular solution theory.....	439	Hydrocarbon mixtures, a general index of fractional distillation power for.....	389	Methane, freezing points of binary mixtures containing.....	317
Gas-Solid Contacting with Ozone Decomposition Reaction.....	269	Hydrocarbons, estimation of critical temperature and pressure.....	356	Methane-hydrogen sulfide, heterogeneous phase equilibrium.....	211
Gaseous mixtures, nonpolar, volumetric properties of.....	403	Hydrogenation of propylene on nickel catalyst.....	351	Minimum sputtering velocity, derivation of an equation for predicting	497
Generalized Correlation for Loading in Packed Towers with Counter-current Gas-Liquid Flow.....	430	I		Mixing, axial, of fluids in flow through packed beds.....	13M, 14M, 161, 367
Generalized properties, critical temperatures and pressures of hydrocarbons.....	324	Immiscible liquid systems, area formation by orifice mixers.....	346	effect of liquid mixing upon bubble-tray efficiency.....	231
reduced-state correlations of viscosity of inert gases.....	356	drop formation in.....	273	formation of interfacial area in immiscible liquids for orifices.....	346
Schmidt numbers and diffusion coefficients of isotropic dense gases.....	257	Improved Experimental Reactor for Applied Kinetic-Studies, An.....	351	Mixing of Fluids Flowing Through Beds of Packed Solids.....	161
Graphical Method for Solution of Freezing Problems, A.....	53	Individual Film Coefficients of Mass Transfer in Liquid-Liquid Extraction.....	180	Mixtures, nonpolar gaseous, volumetric properties of.....	430
		Inert gases, reduced-state correlations for density of.....	480	Momentum and Mass Transfer by Eddy Diffusion in a Wetted-Wall Channel.....	190
		Interface, gas-liquid, phase equilibrium at, during absorption.....	439	Momentum, mass, and heat transfer, analogy among.....	393
		Isotropic turbulent field.....	495	Momentum transfer, analogy between heat or mass transfer for a homogeneous isotropic turbulent field.....	495
		K		by gases in packed beds.....	63, 69
Heat and Momentum Transfer in the Flow of Gases Through Packed Beds.....	69	Kinetic Studies of Carbonation Reactions Using Radioactive Tracers.....	143	N	
Heat, mass, and momentum transfer, analogy among.....	393	Kinetics of Nitrogen Tetroxide Absorption in Water.....	249	Natural-Convection Heat Transfer in Regions of Maximum Fluid Density.....	81
Heats of Vaporization of Hydrogen Bonded Substances (Erratum).....	493	diffusion in a pore of varying cross section.....	343	New Electric Analogue Model for Nonsteady State Flow Problems, A.....	49
Heat Transfer Between Fluidized Solids Beds and Boundary Surfaces-Correlation of Data.....	15	interpretation of flow kinetic data, recirculating reactor for applied research.....	246	Newton terminal-velocity equation, correlation for single-drop liquid-liquid systems.....	153
Heat Transfer from Superheated Vapors to a Horizontal Tube.....	43	L			
Heat Transfer in Film Condensation.....	218	Laminar external flow, combined free and forced convection in.....	285	New Type of Countercurrent Column for the Zirconium-Hafnium Separation, A.....	498
Heat Transfer in Forced convection with Internal Heat Generation.....	319	Liquid-Liquid Extraction Accompanied by Chemical Reaction.....	245	Nitrogen tetroxide, kinetics of absorption in water.....	249
Heat Transfer to a Liquid Fluidized Bed.....	376	Liquid-liquid extraction, film coefficients for.....	180	Noncondensing gas, condensation of vapor in the presence of.....	413
Heat Transfer to Water in Turbulent Flow in Internally Heated Annuli.....	127	Liquid-Phase Adsorption Equilibria.....	383	Nonpolar gaseous mixtures, volumetric properties of.....	430
Heat transfer, annuli, internally heated, coefficients for.....	127	Liquid-vapor phase equilibrium, convergence pressures for close-boiling nonideal systems.....	263	Note on the Analogy Between Momentum Transfer and Heat or Mass Transfer for a Homogeneous Isotropic Turbulent Field.....	495
conductive, shape factors for.....	319	regular solution theory for gas-liquid systems.....	485	Note on Kinetics Data, A.....	246
convection, forced with internal heat generation.....	81	Liquids, flow patterns of, in agitated vessels.....	324	Nuclear reactors, heat transfer coefficients from fuel elements.....	127
in maximum fluid-density region.....	285	Loading of packed towers, generalized correlations for gas-liquid countercurrent flow.....	75	orificing in mixing headers.....	33
convective, combined laminar free and forced, in external flow.....	37	Local Boiling Coefficients on a Horizontal Tube.....		O	
convective from high-temperature air in a tube.....	58	Local Shell-side Heat Transfer Coefficients in Baffled Tubular Heat Exchangers.....	332	On Phase Equilibrium at the Gas-Liquid Interface During Absorption.....	439
film boiling in vertical tubes.....	218	Longitudinal Dispersion in a Packed Bed.....	14M	Organic liquids, effect of pressure upon nucleate boiling of.....	102
film condensation.....	97	M			
film-penetration model.....	15	Mass, momentum, and heat transfer, analogy among.....	393	Orifice mixers, formation of interfacial area by immiscible liquids.....	346
fluidized beds, correlation to boundary surfaces.....	376	Mass transfer, by eddy diffusion in wetted-wall columns.....	190	Orifices, two-phase fluid flow of carbon dioxide through.....	207
liquid.....	75	individual film-coefficients in liquid-liquid.....	97	Ozone decomposition reaction, gas-solid contacting with.....	403
local boiling coefficients on horizontal tubes.....	63, 69	Mass Transfer from a Soluble Solid Sphere.....	180	P	
packed beds, gases in.....	102	Mathematical Development of Tube		Packed beds, axial mixing by fluid flow through.....	13M, 14M, 161, 367
pressure boiling, nucleate effect of in organic liquids.....	3				
radiant exchange in a nonuniform gas field.....	330				
shape factors for solids.....	332				
shell-side coefficients for baffled exchangers, local.....	332				
superheated vapors to a horizontal tube.....	43				
tube loading in horizontal condensers.....	157				
Heterogeneous Phase Equilibrium of					

drain
tria
heat
gas
radi
rates
sol
visco
Packed
wit
flow
Penetrat
film
trai
Perfora
De
Permea
sol
Phase
dri
Phase
int
Phase
Th
and
Physica
fici
estim
and
visco
Plates
fici
Poisson
of
Pore d
erod
Porosit
tio
Porosit
be
Prandtl
cos
Predict
Pr
Pseudo
me
Pulsati
Ca
Radial
Be
Radian
Fil
Radioa
ics
Rates
So
Reacto
Pr
La
Recirc
exp
Reduc
inc
Regula
Lie
Reside
Role o
Par
Rotatin
of
Sedime
reg
Separat
a
col

drainage in gravitational and centrifugal-force fields.....	305	Shape Factors for Conductive Heat Transfer.....	330	Turbulence, velocity profiles for fully developed flow in pipes.....	495
heat and momentum transfer from gases.....	63, 69	Shell-side heat transfer coefficients in baffled tubular heat exchangers.....	332	Turbulent field, homogeneous isotropic.....	494
radial porosity variations in.....	460	Sieve trays, discharge coefficients through.....	266	Turbulent Heat Transfer Inside Tubes and the Analogy Between Heat, Mass, and Momentum Transfer.....	393
rates of flow through microporous solids.....	90	pulsed operation of.....	282		
viscous flow in.....	197	Solids, dissolution rates of, in mercury and aqueous liquids.....	418	V	
Packed towers, correlation for loading with countercurrent gas-liquid flow.....	324	Solution theory modified for gas-liquid equilibria.....	269	Vapor, condensation of, in the presence of noncondensing gas.....	413
Penetration theory combined with film theory for heat and mass transfer.....	97	Some Properties of the Poisson Distribution.....	290	Variables, design and operating effect of on perforated-plate efficiency.....	465
Perforated-Plate Efficiency—Effect of Design and Operating Variables.	465	Spheres, mass transfer from soluble solid.....	114	Velocity, correlation of local, for tubes, annuli, and plates.....	240
Permeabilities of packed microporous solids.....	90	Spouting velocity, the derivation of an equation for predicting minimum.....	497	electrolytic methods for measurement in water.....	338
Phase equilibria of the methane-hydrogen sulfide system.....	211	Spreading of liquids over surfaces, gas entrainment by.....	24	minimum spouting.....	497
Phase equilibrium at the gas-liquid interface during absorption.....	439	Steady State Absorption of a Sparingly Soluble Gas in an Agitated Tank with Simultaneous Irreversible First-Order Reaction.....	499	Velocity Profiles for Fully Developed Turbulent Flow in A Pipe.....	495
Phase Relations of Binary Systems That Form Azeotropes Parts I and II.....	293	Stirred tanks, estimation of efficiency for mixer-settler operation.....	202	Vessels, agitated, flow patterns of liquids in.....	485
Physical properties, diffusion coefficients for gases.....	137	Sugar, extraction of, from beets.....	453	Viscosity of Acetone-Water Solutions up to Their Normal Boiling Points.....	362
estimation of critical temperature and pressure in hydrocarbons.....		Superheated vapors, heat transfer to in tubes.....	43	Viscosity: Reduced-State Correlation for Inert Gases.....	257
viscosity of inert gases.....		Surface Dynamics of Fluidized Beds and Quality of Fluidization.....	423	Viscous Flow in Multiparticle Systems: Slow Motion of Fluids Relative to Beds of Spherical Particles.....	197
Plates, perforated, discharge coefficients through.....	266			Volumetric data for gas mixtures.....	494
Poisson distribution, some properties of.....	290	T		Volumetric Properties of Nonpolar Gaseous Mixtures.....	430
Pore diffusion, in holes of varying cross section.....	343	Tank, agitated, steady state absorption of a sparingly soluble gas in an.....	499	W	
Porosity of cake, effect upon filtration rate.....	170	Theoretical-Empirical Approach to the Mechanism of Particle Entrainment from Fluidized Beds.....	472	Wall Effect for the Fall of Single Liquid Drops.....	153
Porosity, radial variations in packed beds.....	460	Transfer, turbulent heat, inside tubes	393	Wetted walls, momentum and mass transfer by eddy diffusion.....	190
Prandtl mixing lengths and eddy viscosity in smooth tubes.....	27	Tube loading in horizontal condensers, mathematical development of.....	157	Z	
Prediction of Resistance in Constant-Pressure Cake Filtration.....	175			Zirconium-hafnium separation.....	498
Pseudocritical Constants from Volumetric Data for Gas Mixtures...	494				
Pulsations in Sieve-Tray and Bubble-Cap Distillation Towers.....	282				

R

Radial Porosity Variations in Packed Beds.....	460
Radiant Heat Exchange in a Gas-Filled Enclosure.....	3
Radioactive tracer technique, kinetics of carbonation reaction by...	143
Rates of Flow Through Microporous Solids.....	90
Reactor-Design Equation Based on a Proposed Distributed Boundary-Layer Thickness.....	300
Recirculating reactors, an improved experimental kinetic research technique.....	351
Reduced-state correlations for the inert gases.....	480
Regular Solution Theory for Gas-Liquid Solutions.....	269
Residence times in flow reactors.....	246
Role of Porosity in Filtration, The: Part III.....	170
Rotating dissolution cell, development of a new type of.....	418

S

Sedimentation in the viscous-flow region.....	197
Separation of zirconium-hafnium by a new type of countercurrent column.....	498

ERRATUM

Heats of Vaporization of Hydrogen Bonded Substances

A. Bondi and D. J. Simkin

The data given in Table 1 of the above paper have been taken erroneously from the vapor-pressure calculation without compensation for vapor-phase association. Use of the directly measured heats of vaporization of methanol and ethanol given by Flock *et al.* (1) and appropriate correction of the *n*-propanol data yields the corrected values of the hydrogen bond increment $\delta(OH)$ shown on Table 1. These data appreciably reduce the previously apparent trend of $\delta(OH)$ with molecular weight.

TABLE 1. HYDROGEN BOND INCREMENTS OF THE HEAT OF VAPORIZATION OF LOWER PRIMARY *n*-ALIPHATIC ALCOHOLS

Alcohol/T°C.	0	30	60	90	120	150
Methyl	5.5	5.35	5.2	4.9	4.5	3.85
Ethyl	5.6	5.45	5.2	4.8	4.4	3.85
Propyl	5.9	5.6	5.2	4.9	4.3	3.8

LITERATURE CITED

1. Flock, E. F., Ginnings, D. C., and Holton, W. B., *J. Res. Nat. Bur. Standards* **6**, 881 (1931).

This article appeared on page 473 of the December, 1957, issue of the Journal.

COMMUNICATIONS TO THE EDITOR

Pseudocritical Constants from Volumetric Data for Gas Mixtures

J. M. PRAUSNITZ and R. D. GUNN

University of California, Berkeley, California

As a result of recent correlations based on an extended theorem of corresponding states (2, 3), it is now possible to estimate the volumetric properties of pure, non-polar or slightly polar fluids with an accuracy of about 2% or better. In an effort to extend the correlation of Pitzer and co-workers (3) for the estimation of the properties of gas mixtures by means of pseudocritical parameters, it became necessary to decide on a suitable method of determining pseudocritical constants from volumetric data. Such a method is described.

There are four pseudocritical parameters for any mixture at constant composition: the pseudocritical temperature, pressure, and volume, and the acentric factor of the mixture. Of these four only three are independent. At reduced temperatures of unity or above, the effect of the acentric factor, is not very large, and it was therefore arbitrarily decided to define the acentric factor of the mixture by the linear relationship

$$\omega_m = \sum_i y_i \omega_i \quad (1)$$

The pseudocritical temperature and pressure can then be determined conveniently from volumetric data in the following manner. From the generalized compressibility tables (3) a table is prepared which gives the value of the minimum compressibility factor with respect to the reduced temperature and the acentric factor. For a given value of the acentric factor the minimum compressibility factor uniquely determines the pseudocritical temperature. From volumetric data the minimum compressibility factor for a mixture at a particular temperature is selected. The reduced temperature corresponding to this minimum compressibility factor and to the acentric factor of the gaseous mixture is found from the table. Both the absolute and the reduced temperatures are known; hence the pseudocritical temperature for the mixture can be found. The minimum compressibility factor is relatively insensitive to the reduced pressure; therefore the pseudocritical pressure is best calculated from an experimental com-

pressibility factor at as high a pressure as possible. At high pressures the compressibility factors are sensitive to the reduced pressure but relatively insensitive to errors in the reduced temperature. Once the pseudocritical temperature is known, the pseudocritical pressure can be calculated from a compressibility factor for the mixture at a high pressure by use of the Pitzer compressibility tables. The same value of the compressibility factor is located in the generalized compressibility-factor tables at the same reduced temperature and acentric factor as those of the mixture, and the reduced pressure corresponding to this compressibility factor is obtained. Once the reduced and absolute pressures are known, the pseudocritical pressure is found.

The pseudocritical temperatures and pressures were determined in the manner described for a number of mixtures, including the systems methane-decane, methane-n-heptane, methane-n-pentane, propane-benzene, hydrogen sulfide-decane, carbon dioxide-nitrogen, nitrogen-ethane, carbon dioxide-n-butane, and carbon dioxide-ethane. With these pseudocritical constants it was possible to calculate the compressibility factors for the respective mixtures to within 2 or 3%, even near the critical region. It was found that the pseudocritical temperature and pressure are complicated functions of the composition which cannot be predicted accurately by simple rules. The pseudocritical volume, however, appears to be a much simpler function of the composition and is calculated from the pseudocritical pressure and temperature by the equation

$$V_{cm} = \frac{z_{cm} RT_{cm}}{P_{cm}} \quad (2)$$

According to the Pitzer compressibility tables the compressibility factor at the critical point is related to the acentric factor by a linear relationship; the arbitrary mixing rule for the acentric factor [Equation (1)] implies therefore that

$$z_{cm} = \sum_i y_i z_{ci} \quad (3)$$

For all systems studied it was found that the pseudocritical volume could be predicted by a quadratic function of the mole fractions

$$V_{cm} = \sum_{ij} y_i y_j V_{c_{ij}} \quad (4)$$

It was also found that, when the ratio of the critical volumes of the pure components is less than about 3, the pseudocritical volume is a linear function of the composition; this result has also been reported by Haselden and coworkers (1). For such cases, therefore, Equation (4) still holds, with the additional relation

$$V_{c_{ij}} = \frac{1}{2}(V_{ci} + V_{cj}) \quad (5)$$

In that case Equation (4) becomes

$$V_{cm} = \sum_i y_i V_{ci} \quad (4a)$$

A more detailed discussion of the application of corresponding states theory to mixtures is given elsewhere (4).

NOTATION

- P = pressure
- R = gas constant
- T = absolute temperature
- V = volume
- y = mole fraction
- z = compressibility factor
- z_c = compressibility factor at critical point
- ω = acentric factor

Subscripts

- i, j = components
- c = critical (or pseudocritical)
- m = mixture

LITERATURE CITED

1. Haselden, G. G., et al., *Proc. Royal Soc. (London)* **A240**, 1 (1957).
2. Lydersen, A. L., R. A. Greenkorn, and O. A. Hougen, *Univ. Wis. Eng. Exp. Sta. Rept.* 4 (October, 1955).
3. Pitzer, K. S., et al., *J. Am. Chem. Soc.*, **77**, 3427 (1955).
4. Prausnitz, J. M., and R. D. Gunn, *A.I.Ch.E. Journal*, **4**, No. 4, 430 (1958).

Note on the Analogy Between Momentum Transfer and Heat or Mass Transfer for a Homogeneous Isotropic Turbulent Field

THOMAS J. HANRATTY

University of Illinois, Urbana, Illinois

One of the chief difficulties in the description of turbulent transport is that all real turbulent fields are nonhomogeneous; the properties of the turbulence vary with position in the field.

The examination of the effect of these nonhomogeneities on the transport process has been conditioned by knowledge that has been gained concerning the description of molecular transport. Equations of the same form as Fick's Law have been used to describe turbulent transport of heat or mass:

$$q = \left(\frac{k}{\rho C_p} + \epsilon_c \right) \frac{d(\rho C_p T)}{dx} \quad (1)$$

One might think that a variation in ϵ_c reflects entirely the nonhomogeneities in the turbulence. This need not be so; as a matter of fact, a homogeneous isotropic turbulent field can exhibit large variations in the coefficient ϵ_c defined by Equation (1). Therefore this equation is probably not the best basis from which to examine the effect of the turbulence nonhomogeneities on the transport process. A correct description of turbulent diffusion from a point source in a homogeneous isotropic field as been given by G. I. Taylor (1). In two previous papers by the author (2, 3), Taylor's description has been applied to situations involving wall-transfer processes.

One of the situations considered was the transfer of heat from a hot wall of a channel to the opposite cold wall of a channel. Air was flowing turbulently between the channel walls. Far enough along the channel there was no further change in the temperature of the air, and the temperature profile was fully developed. For a nonturbulent flow in which heat is transferred by molecular conduction a linear temperature profile would be obtained; Equation (1) would suggest the line shown in Figure 1 for a homogeneous turbulent field, if constancy of ϵ_c is assumed to be the criterion for homogeneous turbulence. Experimental data of Page, Corcoran, Schlinger, and Sage (4) are also presented in Figure 1. The deviation of the data from a straight line near the wall cannot be attributed entirely to nonhomogeneities. The temperature profile for a homogeneous isotropic turbulence can be calculated by using Taylor's description of point-source diffusion by summing the effects of an infinite number of sources of heat along the hot wall and an infinite number of sinks of heat along the cold

wall (2). Figure 2 presents the results of such a calculation. A similar deviation from a straight line as is indicated by experimental data is obtained; however the data differ from the calculated profile near the wall, as would be expected, since the assumption of a homogeneous field would not be valid in this region.

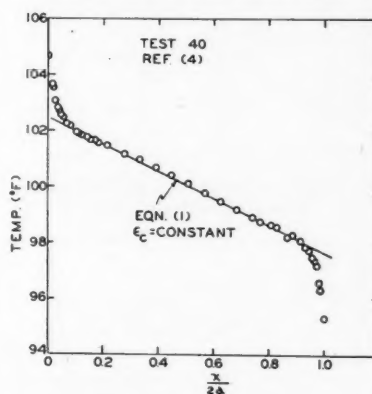


Fig. 1. Data on turbulent heat transfer between two plane walls.

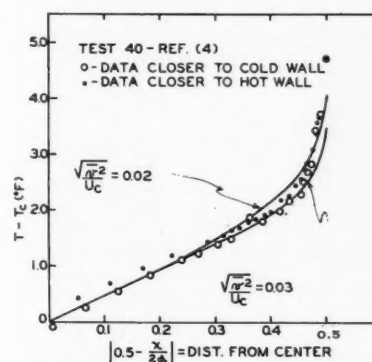


Fig. 2. Heat transfer between two plane walls for a homogeneous isotropic turbulence. $\bar{v}^2 \tau = 0.005$ sq. ft./sec.

The description of turbulent velocity fields has usually been based on an analogy between momentum transfer and mass or heat transfer. Far enough from the entry of a pipe or channel the velocity profile reaches a fully developed condition in which it is not changing. There is no net flow in the radial direction, and momentum transfer is associated with the radial movement of the eddies, as are turbulent heat transfer and mass transfer. An equation of the same form as

Equation (1) is often used to describe turbulent momentum transfer:

$$g_c S = \left(\frac{\mu}{\rho} + \epsilon_m \right) \frac{d(\rho U)}{dx} \quad (2)$$

If ϵ_m is constant, a plot of $U_e - U$ vs. the square of the distance from the channel or pipe center would yield a straight line. On the basis of the calculations on turbulent heat transfer, it is to be expected that variations in ϵ_m or deviations of a plot of $U_e - U$ from linearity should not be due entirely to nonhomogeneities in the turbulence.

In the June, 1958, issue of the *A.I.Ch.E. Journal* (3) an expression was derived for the fully developed velocity profile in a pipe by using Taylor's statistical description of turbulent diffusion for a homogeneous isotropic field as the basis of an analogy between momentum transfer and mass or heat transfer. A velocity profile calculated on the basis of this derivation is presented in Figure 3 and compared with data obtained by Deissler (5). Details of this calculation are in a Ph.D. thesis by D. L. Flint (6). Equations (20) and (43) presented in reference 3 were used for this calculation:

$$U + C_2 = - \int_0^\infty \frac{2S_0}{a} \quad (3)$$

$$+ \sum_{s=1}^{\infty} \exp(-\alpha_s^2 K(t-t')) \frac{J_0(\alpha_s r)}{J_0(\alpha_s a)} dt'$$

$$K(t-t') = \bar{v}^2 \tau(t-t') - \bar{v}^2 \tau^2$$

$$+ \bar{v}^2 \tau^2 \exp\left(-\frac{(t-t')}{\tau}\right) + \frac{\mu}{\rho} (t-t') \quad (4)$$

The factor C_2 is a constant of integration. In the paper it was suggested that C_2 be evaluated from the condition that the velocity is zero at the wall. Since this condition is based on experimental observation, and since a homogeneous isotropic field cannot be realized experimentally, it would be fortuitous if this condition were applicable. Therefore in the calculations presented in Figure 3 the constant C_2 is evaluated from the velocity at time zero:

$$C_2 = U_{avg} \quad (5)$$

The values of the parameters $(\bar{v}^2)^{1/2}$ and τ used in the calculations were obtained from measurements of turbulent diffusion of hydrogen from a small tube in a turbulent pipe flow (6). The calculated profile does not agree with experimental data. A calculation of the velocity profile for a Reynolds Number of 30,000 was presented in Figure 4 of reference 3. It has been found that these calculations are in error and that the agreement between the calculated velocity profile and experimental data are much worse than

indicated in Figure 4 of reference 3. The disagreement could to a large extent be due to a poor choice of the turbulence parameters, $(\bar{v}^2)^{1/2}$ and τ .

To examine further the analogy as formulated in reference 3, calculations have been made of the velocity profile for the conditions prevalent in test 40 of the experiments of Page, Corcoran, Schlinger, and Sage (4). The temperature measurements in test 40 are presented in Figure 2 along with calculated profiles based on the development presented in reference 2

$$T - T_c = \int_0^\infty \frac{q dt'}{\sqrt{\pi \rho C_p} [\phi(t - t')]} \cdot \left\{ \sum_{n=-\infty}^{n=\infty} \exp \left(-\frac{(2na + x)^2}{4\phi(t - t')} \right) \right\} \quad (6)$$

However a term for molecular exchange [as is suggested in the footnote on the bottom of page 44 of reference (2)] has been included in the expression for $\phi(t - t')$, and \bar{X}^2_0 has been dropped from the expression

$$\phi(t - t') = \bar{v}^2 \tau (t - t') - \bar{v}^2 \tau^2 + \bar{v}^2 \tau^2 \cdot \exp \left\{ -\frac{(t - t')}{\tau} \right\} + \frac{k}{\rho C_p} (t - t') \quad (7)$$

The two calculated curves used a value of $\bar{v}^2 \tau$ equal to an average value of ϵ_c for the data in the center portion of the channel. A value of $(\bar{v}^2)^{1/2}/U_c = 0.03$ gives a good fit to the experimental data in the center of the channel, where the turbulence is approximately homogeneous. This value of the turbulence intensity agrees with hot-wire anemometer measurements. The curve based on a value of $(\bar{v}^2)^{1/2}/U_c = 0.02$ gives a closer approximation to the wall temperature but a poorer fit to the experimental data in the regions closer to the channel center. From the heat transfer data it appears that values of $\bar{v}^2 \tau = 0.005$ sq. ft./sec., and $(\bar{v}^2)^{1/2}/U_c = 0.03$ represent the properties of the turbulence in the center of the channel.

An analogy between heat transfer and momentum transfer based on Taylor's statistical description of point-source diffusion may be employed to calculate the velocity profile for this case. The equations for a channel may be developed in the same manner as done for a circular pipe in reference 3, and the following expression results:

$$U - U_{avg} = \frac{g_e S_0}{\rho a} \cdot \int_0^\infty dt' \left[1 - \frac{a}{\sqrt{\pi} [K(t - t')]} \right] \cdot \sum_{n=-\infty}^{n=\infty} \exp \left(-\frac{(2na + x)^2}{4K(t - t')} \right) \quad (8)$$

*For this reason much of the discussion in reference 3 pertaining to Figure 4 should be disregarded.

Use of values of $\bar{v}^2 \tau = 0.005$ sq. ft./sec. and $(\bar{v}^2)^{1/2}/U_c = 0.03$ give a poor fit to the velocity measurements of Page, et al. However values of $\bar{v}^2 \tau = 0.80 \times 0.005$ sq. ft./sec. and $(\bar{v}^2)^{1/2}/U_c = 0.03$ give a good fit to the experimental data as shown in Figure 4. This value of $\bar{v}^2 \tau$

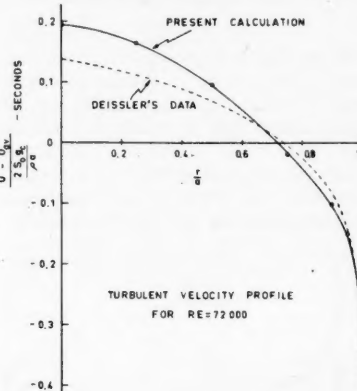


Fig. 3. Velocity profile in a pipe for isotropic homogeneous turbulence.

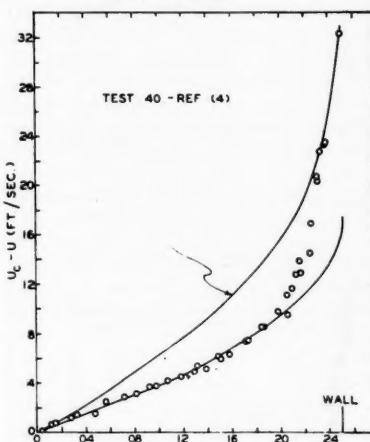


Fig. 4. Velocity profile in a channel for isotropic homogeneous turbulence. $\bar{v}^2 \tau = 0.004$ sq. ft./sec. and $\sqrt{\bar{v}^2 \tau} = 0.01$ for upper curve. $\bar{v}^2 \tau = 0.004$ sq. ft./sec. and $(0.5 - X/2d)\sqrt{\bar{v}^2 \tau}/U_c = 0.03$ for lower curve.

equals the average value of ϵ_m for the velocity data in the center of the channel. The profile calculated from the analogy by use of these values for the turbulence parameters deviates from a straight line near the wall, as do the experimental data. However the calculated values of $U_c - U$ based on a homogeneous isotropic field are smaller than the measurements near the wall. This would mean that the analogy predicts a finite velocity at the wall for a completely homogeneous field. A velocity profile has also been calculated for $(\bar{v}^2)^{1/2}/U_c = 0.01$ and $\bar{v}^2 \tau = 0.004$ sq. ft./sec. Although the value of $U_c - U$ at the wall agrees with measurement, the calculated profile gives

a poor fit to experimental data in the center of the channel.

From the calculations presented it appears that the analogy as formulated in reference 3 fits velocity data in the center of a channel, and therefore until a more exact theoretical treatment of turbulent velocity fields is available, an analogy based on Taylor's description of point-source diffusion might supply a proper basis from which to examine the effect of nonhomogeneities on the velocity field. However the analogy is open to the same criticism as the analogy based on Equations (1) and (2) in that values of τ different from those obtained from the diffusion of heat or mass must be used to calculate velocity fields.

ACKNOWLEDGMENT

The author is grateful for the support of the Office of Ordnance Research.

NOTATION

a	= half width of the channel, pipe radius
C_p	= heat capacity
k	= thermal conductivity
q	= rate of heat transfer per unit area
r	= radial distance
S	= shear stress at r
S_0	= shear stress at the wall
t	= time
t'	= time at which diffusing material entered the turbulent field
T	= temperature
T_c	= temperature at the center of the channel
U	= velocity
U_c	= velocity at center of the channel or pipe
U_{AV}	= average velocity
$(\bar{v}^2)^{1/2}$	= root-mean-square turbulent velocity in the x or in the r direction
x	= distance from the wall

Greek Letters

α_s	= root of $J_0'(\alpha_s a) = 0$
ϵ_c	= eddy conductivity analogous to molecular thermal diffusivity
ϵ_m	= eddy viscosity analogous to molecular viscosity
μ	= molecular viscosity
ρ	= density
τ	= Lagrangian time scale

LITERATURE CITED

1. Taylor, G. I., *Proc. Roy. Soc. (London)*, **151A**, 421 (1935).
2. Hanratty, T. J., *A.I.Ch.E. Journal*, **2**, 42 (1956).
3. —, and D. L. Flint, *ibid.*, **4**, 132 (1958).
4. Page, F., W. H. Corcoran, W. G. Schlinger, and B. H. Sage, *Ind. Eng. Chem.*, **44**, 419 (1952).
5. Deissler, R. G., *Natl. Advisory Comm. Aeronaut., Tech. Note 2138* (1950).
6. Flint, D. L., Ph.D. thesis, Univ. Illinois, Urbana (1958).

A New Type of Countercurrent Column for the Zirconium-hafnium Separation

NADINE ISAAC and R. L. DE WITTE

Centre d'Etudes pour les Applications de l'Energie Nucléaire, Brussels, Belgium

The vibrating column, an apparatus which assures an intimate contact between two nonmiscible or very slightly miscible liquids circulating countercurrently, is especially useful for liquid-liquid extraction processes in a continuous system. Simple in construction and very efficient, as described below, it is an excellent instrument for laboratory-scale and pilot plant.

As is well known, the primary requisite for efficient extraction is to realize the equilibrium state in the shortest possible plate height, which may be done by increasing the contact surface and the contact time between the two phases. The main problem in liquid-liquid extraction is to realize such a system while maintaining the countercurrent circulation.

Two interesting solutions have already been proposed: the pulse column (1) and the multistage column (2). The principal disadvantages of the pulse column are, first, the high price of pulse pumps or a pulsating system and, second, the limitations on the pulse frequency, which is the factor most favorable to good mixing. The multistage column is characterized by a complicated internal construction, as adequate mixing and separation require a very precisely disposed suc-

sion of baffles. This fact makes it a less suitable instrument to operate in a laboratory; moreover, the high number of baffles inside the column will exercise a resistance which will limit the total throughput.

The column that we are proposing consists of a simple cylindrical tube, in which moves a coaxial rod to which several perforated plates are securely attached (Figure 1). A simple electromagnetic device or a mechanical vibrating system makes this central rod vibrate at 3,000 cycles/min. with an amplitude of $1/25$ in. The countercurrent liquid movement is assured through the holes of the plates and through the annular space between these plates and the wall of the column. The particular shape of the holes (semispherical chamfer) increases the contact time between the two phases at each plate level by creating a secondary local countercurrent (Figure 2).

A column of this type has been constructed to study the problem of zirconium-hafnium separation. The aqueous phase of the system contains zirconium-hafnium nitrates in nitric acid. The organic phase is a mixture of 60% TBP and 40% white spirit (specific gravity, 0.74; boiling point, between 140° and 160°C.). The average separation factor in this system is equal to roughly 13 (3).

The value obtained for 1 H.T.U. is 10 in. The experimental conditions are a Pyrex-glass column 2.4 in. in diameter, a Plexiglass rod, an amplitude frequency value of 120 in./min., and a flow rate of 10 liters/hr. for both phases.

Further details on the working of this column will be published later together with curves of H.T.U. against frequency and amplitude as well as curves of total throughput against the product of amplitude and frequency.

LITERATURE CITED

1. Van Dyck, W. J. D. U. S. Patent 2,011,186 (Feb. 16, 1934).
2. Fenske, M. R., and R. B. Long, U. S. Patent 2,667,407 (Jan. 26, 1954).
3. Hure, Jacques, and R. Saint-James-Schonberg, French Patent, provisional number 665,494 (March 17, 1954).

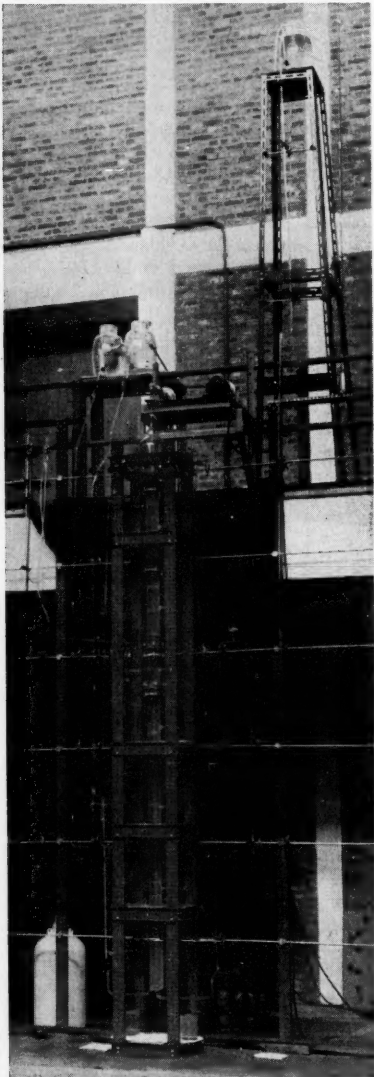


Fig. 1. Vibrating column.

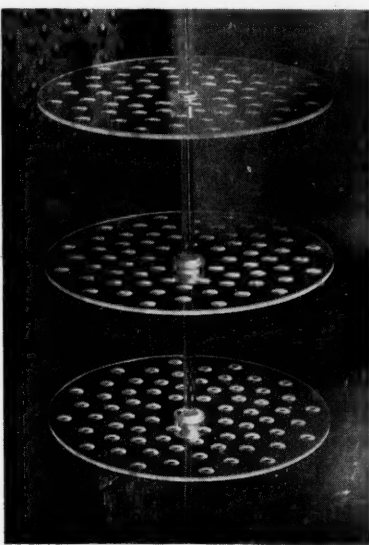


Fig. 2. Perforated plates.

Steady State Absorption of a Sparingly Soluble Gas in an Agitated Tank with Simultaneous Irreversible First-order Reaction

E. N. LIGHTFOOT

University of Wisconsin, Madison, Wisconsin

It is common practice to estimate volumetric mass transfer coefficients in gassed agitated tanks from the rates of absorption into liquids reacting chemically with the dissolving gas, for example the absorption of O_2 by aqueous sodium sulfite solutions containing a copper catalyst (1, 2, 3). The mass transfer coefficients are calculated by assuming steady state physical absorption into a liquid containing no dissolved gas. This calculation is reliable only if the chemical reaction is fast enough to maintain the concentration of dissolved gas near zero in the bulk of the solution but slow enough not to affect appreciably the concentration near the surfaces of dissolving gas bubbles.

No exact analysis of this situation is yet possible because of the complexity of the gas-absorption process; however a clearer understanding of the conditions required for the validity of this calculation method may be obtained by analysis of relatively simple model systems. This is done for first-order removal of dissolved gas and for two common models: absorption according to the penetration theory of Higbie (4) into bubbles with internal gas circulation and absorption through a hypothetical stagnant film of definite thickness completely surrounding the bubble. In each case it will be assumed that gas bubbles of reasonably uniform size and composition are evenly distributed about the tank and that no important gross variations in solution concentration or bubble velocity relative to the liquid occur. It will further be assumed that the gas is sparingly soluble, so that diffusion in the liquid obeys Fick's Law and interfacial concentration of gas is constant. Finally the system as a whole will be assumed to be at steady state, that is that the liquid in the tank is being maintained at constant over-all composition, or that the effect of rate of change of this composition is negligible. The latter will generally be true if the concentration of dissolved reactant is very large compared with the concentration of dissolving gas—a common situation.

CIRCULATING BUBBLES AND THE PENETRATION THEORY

Here the absorption is assumed to be to elements of liquid moving around the bubble from front to rear in accordance

with Higbie's model (4) and maintaining their identity for a distance into the fluid greater than the effective penetration of dissolving gas during the time required for this journey. The differential equation and boundary conditions governing the rate of absorption are then

$$\mathfrak{D} \frac{\partial^2 c}{\partial x^2} = kc + \frac{\partial c}{\partial t} \quad (1)$$

$$\text{at } x = 0, c = c_i \text{ for } t > 0 \quad (1a)$$

$$\text{at } t = 0, c = c_0 \text{ for all positive } x \quad (1b)$$

$$\text{at } x = \infty, c = c_0 e^{-kt} \text{ for } t \geq 0 \quad (1c)$$

at any instant

$$-\mathfrak{D} \iint_A \left(\frac{\partial c}{\partial x} \right)_{x=0} dA = \iiint_V kc dV \quad (1d)$$

where

A = total bubble surface area in tank, lb^2

c = concentration of dissolved gas, m.l./b

c_i = concentration at the gas-liquid interface, assumed constant

c_0 = concentration of dissolved gas in a liquid element meeting the gas phase at the front of a bubble, that is, at the start of its journey around the bubble

\mathfrak{D} = diffusivity of dissolved gas through the liquid, assumed constant, lb^2/t

$$\frac{c_0}{c_i} = \frac{\operatorname{erf}(\tau_0)^{1/2} + \frac{1}{2} \left\{ e^{\xi_0} \operatorname{erfc} \left[\frac{\xi_0}{2\sqrt{\tau_0}} + \tau_0^{1/2} \right] - e^{-\xi_0} \operatorname{erfc} \left[\frac{\xi_0}{2\sqrt{\tau_0}} - \tau_0^{1/2} \right] \right\}}{\xi_0 \left[1 - e^{-\tau_0} \operatorname{erf} \left[\frac{\xi_0}{2\sqrt{\tau_0}} \right] \right] - \tau_0^{1/2} e^{-\tau_0} \left(\frac{2}{\pi^{1/2}} \right) [e^{-(\xi_0^2/4\tau_0)} - 1]} \quad (4)$$

k = first-order reaction rate constant for removal of dissolved gas, t^{-1}

t = time measured for any liquid element from the time it first contacts a bubble

V = total volume of liquid in tank, lb

x = distance measured outward from and normal to the bubble surface

Boundary condition [Equation (1d)] is a statement of steady state for the tank as a whole; its exact application requires a detailed knowledge of the flow pattern in the tank. Here an orderly flow

liquid around each bubble and complete mixing between bubbles will be assumed. Then Equation (1d) becomes

$$\int_0^{V/A} c(t_0, x) dx = \frac{V}{A} c_0 \quad (2)$$

where t_0 = time required for a liquid element to move completely around the bubble. Following the original suggestion of Higbie one can assume that

$$t_0 = D/v_t$$

where

D = diameter of bubble

v_t = bubble velocity relative to the fluid

With the aid of the first three boundary conditions Equation (1) may be integrated to give [see, for example, Equations 20(4) and 21(9) (5).]

$$\frac{c}{c_i} = \frac{1}{2} \left\{ e^{-\xi} \operatorname{erfc} \left[\frac{\xi}{2\sqrt{\tau}} - \tau^{1/2} \right] + e^{\xi} \operatorname{erfc} \left[\frac{\xi}{2\sqrt{\tau}} + \tau^{1/2} \right] \right\} + \left(\frac{c_0}{c_i} \right) e^{-\tau} \operatorname{erf} \left[\frac{\xi}{2\sqrt{\tau}} \right] \quad (3)$$

where for convenience the dimensionless variables $\xi = x(\mathfrak{D}/V)^{1/2}$ and $\tau = kt$ have been introduced.

Equations (2) and (3) can be combined to give an expression for c_0 :

Here

$$\xi_0 = (k/\mathfrak{D})^{1/2}(V/A)$$

$$\tau_0 = kD/v_t$$

Since the gas is sparingly soluble, the flux of gas at any point on the bubble surface is

$$N_A = -\mathfrak{D} \frac{\partial c}{\partial x} \Big|_{x=0}$$

where N_A = moles of gas per area per unit time through interface and the average flux over the bubble surface

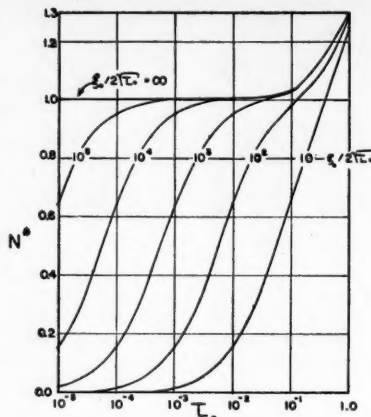


Fig. 1. Higbie model.

$$(N_G)_{avg} = \frac{1}{t_0} \int_0^{\tau_0} N_G dt \quad (5)$$

Then from Equations (3) and (5)

$$(N_G)_{avg} = \frac{c_i(k\mathfrak{D})^{1/2}}{\tau_0} \left\{ \left(\tau_0 + \frac{1}{2} - \frac{c_0}{c_i} \right) \cdot \text{erf}(\tau_0^{1/2}) + \frac{\tau_0^{1/2}}{\pi^{1/2}} e^{-\tau_0} \right\} \quad (6)$$

or

$$N^* = \frac{1}{2} e^{-\tau_0} + \left(\tau_0 + \frac{1}{2} - \frac{c_0}{c_i} \right) \frac{\pi^{1/2}}{4\mathfrak{D}} \cdot \text{erf}(\tau_0^{1/2}) \quad (7)$$

where

$$N^* = \frac{(N_G)_{avg}}{c_i} \left(\frac{\pi \tau_0}{4\mathfrak{D}} \right)^{1/2} \quad (8)$$

Here N^* is the ratio of absorption rate in the presence of chemical reaction to the rate of physical absorption when the tank contains no dissolved gas. Thus this method of estimating mass transfer coefficients is valid only where N^* is one.

Figure 1 shows values of N^* for a wide range of values of $[\xi_0/2t_0]^{1/2}$ and t_0 . It can be seen that for high enough values of $[\xi_0/2t_0]^{1/2}$ there is a plateau region, as suggested by Bernard, in which N^* is very nearly unity and independent of the chemical rate constant over a wide range. Such a situation would occur, for example, when (V/A) is large. However if the gas bubbles are concentrated in a small region of the tank, as from a single fine-bubble sparger, for example, Figure 1 could be misleading in that even distribution of bubbles has been assumed in this development.

STATIC FILM MODEL

It is assumed here that the gas bubbles are surrounded by static films, thin compared with the diameter of the bubbles, in which all the resistance to mass transfer is assumed to be concentrated and in which steady state is

rapidly established. Film curvature and unsteady state may be taken into account if desired (6). Here

$$D \frac{\partial^2 c}{\partial x^2} = kc \quad (8)$$

$$\text{at } x = 0 \quad c = c_i \quad (8a)$$

$$\text{at } x = \delta \quad c = c_l \quad (8b)$$

where δ is the film thickness. Then

$$\frac{c_l}{c_i} = \frac{(c_l/c_i) \sinh \xi + \sinh(\delta(k/\mathfrak{D})^{1/2} - \xi)}{\sinh(\delta(k/\mathfrak{D})^{1/2})} \quad (9)$$

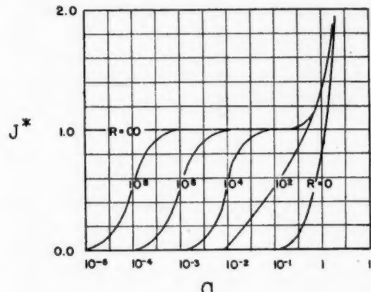


Fig. 2. Film model.

When one determines fluxes through the bubble-solution interface and outer film boundary and equates the rate of absorption through the outer film boundary with the rate of reaction in the bulk of the solution,

$$J^* = \frac{a}{\sinh a} \left[\cosh a - \frac{1}{\cosh a + aR \sinh a} \right] \quad (9)$$

where

J^* = ratio of rate of absorption to rate of physical absorption to tank containing no dissolved gas

$$a = \delta(k/\mathfrak{D})^{1/2}$$

$R = V - A\delta/A\delta$ = ratio of volume of solution outside film to that inside film

In Figure 2 J^* is shown as a function of a and R . The behavior here is seen to be qualitatively similar to that for penetration theory model.

LITERATURE CITED

1. Cooper, C. M., G. A. Fernstrom, and S. A. Miller, *Ind. Eng. Chem.* **36**, 504 (1944).
2. Bernard, R. A., *A.I.Ch.E. meeting*, Chicago, 1957.
3. "Annual Agitation Reviews," presented in *Ind. Eng. Chem.* (March).
4. Higbie, Ralph, *Trans. Am. Inst. Chem. Engrs.*, **31**, 365 (1935).
5. Carslaw, H. S. and J. C. Jaeger, "Conduction of Heat in Solids," Oxford University Press, New York (1947).
6. Carslaw, H. S., and J. C. Jaeger, *ibid.*, p. 208.

BOOKS

The Properties of Gases and Liquids: Their Estimation and Correlation, Robert C. Reid and Thomas K. Sherwood, McGraw-Hill Book Company, Inc., New York (1958). 386 pages. \$10.00.

This excellent book represents the investment of an immense quantity of work which has yielded excellent results. Reid and Sherwood's book is a critical summary of contemporary (1956) methods of calculating the common thermodynamic and transport properties of liquids and gases needed in design. The format of the book will appeal to the design engineer: the basic problems involved in calculating each property are outlined at the beginning of each chapter, then clear and concise descriptions of the selected methods are presented, and finally the best relations for various situations are recommended. In addition numerous sample calculations demonstrate the use of the equations, and an index of best methods for all properties covered is placed most advantageously at the beginning of the book. Thus it is easy to find, to understand, and to use the correlation sought.

The quality of this work stems from the authors' lucid understanding of the subject matter. Although not intended as a treatise upon aspects of physical chemistry, the text gives the reader an understandable, if abbreviated, description of the concepts involved. Hence the blunders which frequently appear in "plug-in" calculations are minimized. Since the decision to use a particular correlation rests upon the accuracy obtained for a given amount of work, statements of the expected accuracy are consistently given. These critical evaluations are based upon a vast body of calculations made by Reid and Sherwood in addition to the trials made by the various original authors. In particular, the authors stress the pitfalls of improper extrapolation of usage. Careful judgment is shown in the methods selected, most calculations being empirical but based upon theoretical considerations. The limitations of the empirical methods presented are emphasized, and tedious and often impractical theoretical methods are wisely avoided. When possible, tables and graphs of parameters appearing in these functions are located adjacent to their description. Thus most methods yield answers from a reasonably short calculation effort.

Reid and Sherwood have covered a vast field in surprisingly few pages, and hence omissions will appear to experts in the various fields covered (particularly the chapter on vapor-liquid equilibria). These limitations are more than compensated for by the general utility of the book; it is a must for design engineers and a necessary reference for students of applied physical chemistry and thermodynamics. The extensive documentation will appeal to researchers, as papers and reviews of particular merit are emphasized. Although the authors state that continued fundamental research and publication of physical properties will make their book needless, this reviewer

(Continued on page 10D)

VAPOR-LIQUID EQUILIBRIUM

By E. HALA, J. PICK, V. FRIED and O. VILIM, Technical University, Prague

This book is intended for workers in the chemical industry who have to deal with problems of distillation and rectification. It should help them in design, development and the rational operation of distillation equipment by showing how to obtain the necessary equilibrium data and numerical results.

\$14.00



CHEMICAL REACTION ENGINEERING

Edited by Dr. K. RIETEMA, Secretary, European Federation of Chemical Engineers

This volume contains the thirteen papers presented at a symposium held in Amsterdam under the auspices of the European Federation of Chemical Engineers, which was attended by over 200 participants from all over Europe. Each paper is preceded by an abstract in English, French and German. Topics covered are flow phenomena, mass and heat transfer, and reaction kinetics—and their relation and interaction.

\$12.50



PHYSICAL CHEMISTRY

By E. A. MOELWYN-HUGHES, D.Sc. (Liverpool), D. Phil. (Oxon), Sc.D. (Cantab), University Lecturer in Physical Chemistry, Cambridge, England

This carefully planned, critical and scholarly work covers the whole of physical chemistry, first from the experimental angle and next from the standpoint of the partition function. Equal emphasis is placed on experiment and theory, and the notation is uniform throughout. The book, containing 1,200 pages of text and numerous diagrams, is based on the author's lectures at Cambridge, and although primarily written to meet the needs of students taking Part II of the Natural Sciences Tripos at this University, will also be most useful to research workers, teachers and all who desire to be conversant with modern mid-century physical chemistry.

\$15.00



CHEMICAL ENGINEERING in the COAL INDUSTRY

Edited by Dr. FORBES W. SHARPLEY

This volume contains the papers presented at the symposium held at the National Coal Board Research Establishment. The subjects covered were: Controlled oxidation of coal; Fluidized oxidation of coal; Investigations into carbonization of briquettes in Germany; Hot briquetting; Semicarbonization in a fluidized bed; Study of tars obtained in fluidized carbonization; Industrial treatment of tar obtained by low-temperature carbonization. Also included is a review of the conference by Dr. J. Bronowski.

\$8.50



SURFACE PHENOMENA IN CHEMISTRY AND BIOLOGY

Edited by J. F. DANIELLI, Professor of Zoology, King's College, London, K. G. A. PANK-HURST, British Leather Manufacturers' Association and Dr. A. C. RIDDIFORD, University of Southampton

This is a collection of essays and articles on surface phenomena in chemistry and biology, written by active workers in the field from many countries, compiled as a tribute to Professor N. K. ADAM on his retirement from the Chair of Chemistry at the University of Southampton, in appreciation of his contributions to the study of surface phenomena.

\$10.00

In preparation



SOME PROBLEMS OF CHEMICAL KINETICS AND REACTIVITY

Vol. 1

By Academician N. N. SEMENOV, Institute of Chemical Physics, Academy of Sciences of the U.S.S.R. Translated by Dr. J. S. BRADLEY

Revised and expanded, and incorporating several new chapters specially written by the author for this authorized English edition and received in March, 1958.

Volume II in preparation



PERGAMON PRESS

New York • London • Paris • Los Angeles

122 East 55th Street, New York 22, N. Y.
P.O. Box No. 47715, Los Angeles 47, California



(Continued from page 500)

hopes that the success of this work will continue in future (and necessary) editions.

J. H. OLSON

Chemical Reaction Engineering, International Series of Monographs on Chemical Engineering, Vol. I, K. Rietema, editor. Pergamon Press, New York (1957). 200 pages. \$12.50.

This volume contains papers presented at the First European Symposium on Chemical Engineering held in Amsterdam in May, 1957, under the auspices of the European Federation of Chemical Engineering. It provides a comprehensive survey of the problems encountered in applying the fundamental concepts of chemical kinetics, heat and mass transfer, and fluid dynamics, especially degree of mixing, to the design of industrial chemical reactors. The papers are predominantly theoretical in nature and all are by authors prominent in the field of applied reaction kinetics. There are a total of thirteen papers, which are divided into five groups: Introductory Papers, Transport Phenomena in Heterogeneous Reactions, Nonuniform Concentration Distributions, Reactor Efficiency and Stability, and Reactor Development.

The first group of papers presents (1) a classification of the various types of chemical-reaction systems and the multitude of reactors in which they are being conducted and (2) brief summaries of classical chemical reaction kinetics and of the treatment of the physical factors present in any practical reactor design.

The second group of papers includes a summary of the general principles of mass transfer through films and within porous solids. Rate data involving both absorption and chemical reaction in a stirred vessel and in a wetted-wall column are presented and analyzed in terms of the separate chemical and physical rate processes.

The third group of papers treats the nature of mixing in continuous agitated vessels from the standpoint of both the scale of mixing and the residence-time distribution. The point is stressed that the performance of continuous tank reactors can be predicted from batch-reaction data and the estimated residence-time distribution only for a first-order reaction unless the mixing is perfect on a molecular scale. The behavior of heterogeneous liquid systems in various types of staged reactor vessels involving both concurrent and countercurrent flow is discussed, and applications to the nitration of benzene and the production of furfural from xylose are shown.

The fourth group of papers considers the problem of (1) obtaining the maximum yield of a desired product of a complex reaction system by proper control of the temperature gradient and (2) analyzing the performance of autothermal processes, where the exothermic heat of reaction serves to maintain the reaction temperature. A simple and very useful means of establishing the possibility of stable operation of an autothermal system is presented by Dr. van Heerden. The performance of a commercial ammonia oxidation reactor is used to illustrate the principles of treating auto-thermal processes.

The last group of papers is concerned primarily with the application to commercial reactor design of the principles enumerated earlier, with special emphasis being placed upon the utilization of pilot plant data.

A valuable addition to the literature in chemical-reactor design has been provided by this work though it is not recommended for the uninitiated. An increased amount of research in this important area should result from the ideas presented. The appeal of the book to American engineers is reduced somewhat by the fact that one of the papers is written in French and four of them are written in German.

JOHN M. WOODS

Elements of Water Supply and Waste-Water Disposal. G. M. Fair and J. C. Geyer. John Wiley and Sons, New York (1958). 615 pages. \$8.95.

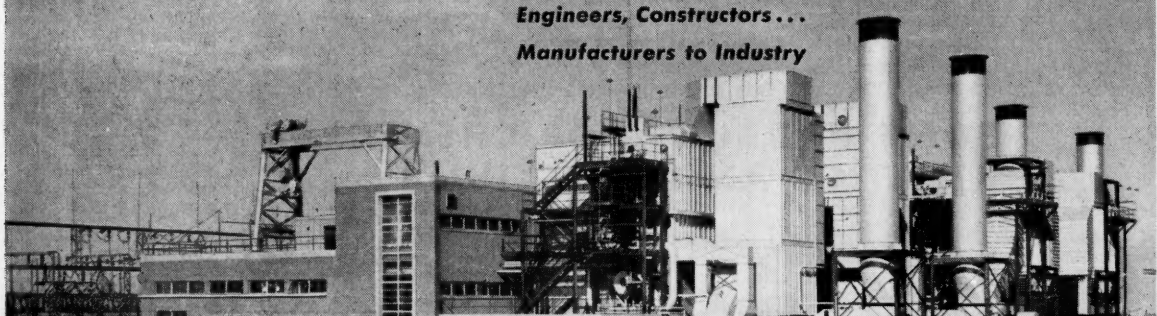
This book, like its predecessor, "Water Supply and Waste-Water Disposal" (Wiley, 1954), is directed to students of civil and sanitary engineering. In this reviewer's opinion, many chemical engineers must be or should be within this category, because of the well-recognized importance of water as a raw material and waste product of the process industries. The two books are essentially similar, but the present edition has been greatly abridged in order to meet the time and financial limitations of undergraduate students (twenty chapters in 615 pages instead of thirty in 973; \$8.95 instead of \$16.00).

(Continued on page 11D)

...point of production

When the design, the engineering and the construction work are completed, Stearns-Roger delivers a complete project. The plant is at the point of production to run far into the future, efficiently, economically.

Engineers, Constructors...
Manufacturers to Industry



Stearns-Roger
THE STEARNS-ROGER MFG. CO. DENVER, COLORADO

DENVER • HOUSTON • EL PASO
SALT LAKE CITY
Stearns-Roger Engineering Co., Ltd. Calgary

(Continued from page 10D)

The first ten chapters of the "Elements" deal with civil engineering aspects of water utilization. Such topics as rainfall, run off, and the population growth of cities are of slight interest to the average chemical engineer, but other sections like the chapters on water distribution and waste-water collection are valuable. The first half of this book provides good reference material for chemical and process engineers.

The second ten chapters relate to the processing of water for use or after use and cover a field of considerable interest to the chemical engineer. A joint discussion of water and wastes is possible because the authors have based their work on principles rather than practice. The latter, however, has not been ignored, and the book is a useful reference for the practicing engineer. The significance of test methods and test results is described adequately, without detailed outlining of the procedures.

The authors describe "unit operations" of water and sewage treatment; this term is not used in the conventional chemical engineering manner but includes also chemical and biological processing. Screening, sedimentation, flotation, and filtration (sand filters) receive detailed consideration, as do chemical- and biological-treatment methods. This half of the book should be particularly useful to chemical engineers. The section on industrial water and industrial wastes is brief, but perhaps it is felt that this field belongs particularly to the chemical engineer and that adequate reference books are already available.

Fair and Geyer have done an excellent writing job on the civil and sanitary aspects of water, and one or the other of their two books is recommended to all chemical engineers concerned with water and waste.

C. FRED GURNHAM

Applied Mathematics in Chemical Engineering,
2 ed., Harold S. Mickley, Thomas K. Sherwood, and Charles E. Reed. McGraw-Hill Book Company, Inc., New York (1957). 413 pages. \$9.00.

About twenty years ago Sherwood and Reed, recognizing that most advanced mathematics texts for engineers had the example problems divided among several fields of engineering, directed the first edition of this book specifically toward problems in chemical engineering. These included reaction kinetics, and unsteady state mass balances, heat transfer fluid flow, and diffusion. Now the authors, in this second edition, have reorganized the book and added new topics which reflect advances in the profession. The primary objective of the text continues to be the formulation and solution of problems which involve differential equations, but also included are chapters on the treatment and interpretation of engineering data, which serve as a natural introduction to the primary objective. Since the mathematics presented in this text is considered as a tool for the solution of problems, much of the rigor found in texts written for mathematicians has been omitted or simplified.

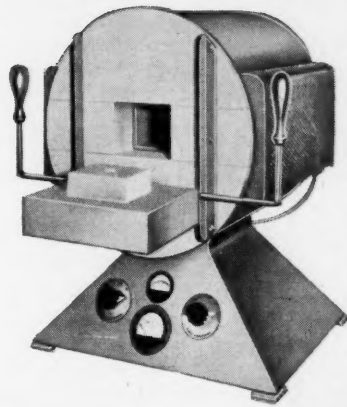
The second edition may be divided roughly into three sections: treatment and interpretation of engineering data, ordi-

(Continued on page 12D)



Hevi-Duty "G-07-PT" FURNACE temperatures to 2600° F.

This furnace is designed for high-temperature work where accurate control and uniformity are important. Controls, which provide 48 temperature gradients, and an indicating pyrometer are located in the pyramid base. For greatest uniformity in the heating chamber, three heating elements are installed over and three are beneath the refractory muffle.



Write for Bulletin 957 for full details.

Type	Watts	Chamber			Price
		W.	L.	H.	
G-07-PT	3500	4"	7"	2 3/4"	\$585.00

*Operating voltage either 115 or 230 A.C. only.

FOR GENERAL AND SPECIALIZED LABORATORY APPLICATIONS

HEVI-DUTY "Multiple Unit" TUBE TYPE COMBUSTION FURNACES in Two Temperature Ranges, 1850° F. or 2200° F.

Hevi-Duty Combustion Tube Furnaces are available in either the split* (illustrated) or solid type and can be used horizontally or modified for vertical operation. Long-life "Multiple Unit" brand heating units offer fast heat-up because the heat is radiated directly into the heating chamber. The heated length may be divided for zone temperature control which gives greater temperature uniformity over a specified length. A few of the standard furnaces are shown below. Many sizes are in stock. Special sizes with diameters up to 16 inches can be built to your specifications.

*5-in. and smaller diameters are hinged.



TYPE	CHAMBER		RATING WATTS	SHIPPING WEIGHT	PRICE
	DIA.	LENGTH			
70	1 1/4"	12"	750	35	\$ 75.00
M-2012	2 3/8"	12"	1400	90	\$ 165.00
M-3024	3"	24"	3400	135	\$ 250.00
M-5036	5"	36"	7500	325	\$ 650.00
M-8040	8"	40"	14500	520	\$1180.00

Write for Bulletin 552
for complete details.



• LABORATORY FURNACES

TRADE
MULTIPLE UNIT
MARK

• ELECTRIC EXCLUSIVE

(Continued from page 11D)

nary differential-equations problems, and partial-differential-equations problems.

The chapter on the treatment of engineering data extends the applications of elementary calculus to other topics from the first edition. However, the discussion of types of graph paper, alignment charts, enthalpy-concentration diagrams, and Ponchon-Savart method has been eliminated. Those few graphical methods which are retained in this edition, such as the Schmitt method for conduction, are presented in more concise form in the appropriate chapters on numerical solutions. Dimensional analysis is still omitted.

The authors have incorporated some of the topics previously described as theory of errors and precision of measurements into a chapter on interpretation of data. This chapter, which is largely statistics, includes new topics such as factorial design of experiments, statistics of variance, and confidence levels for the Gaussian distribution of small samples.

Prefacing the solution of differential equations is a discussion of methods of transferring the physical problem into terms of differential equations. Some discussion of kinetics is omitted in this second edition. The section on solution of ordinary differential equations is essentially the same as in the first edition except that the presentation of infinite series is rewritten and includes the Frobenius method and more detail on the general form of Bessel's equation.

The section on partial differentiation has undergone substantial change. An introduction to vector analysis including line and surface intervals has been added. New chapters include the Laplace transform and other topics in operational calculus, the calculus of finite differences for use in stage processes, and substantial stress on numerical methods in a form suitable for use of high-speed digital computers. The relaxation method has been added, but few graphical methods have been retained. Missing is the discussion of Jacobians for deriving thermodynamic relationships.

Mathematical topics are introduced directly into the sections where they are first required. Derivations are held to a minimum. As a result, the limitations of the mathematical methods are often touched lightly, and if the reader wishes to understand some of the mathematical concepts better, he should refer to more rigorous advanced-calculus texts. The authors have recognized these limitations and in this second edition have placed suitable bibliographies at the end of every chapter.

Nevertheless, the notable shortcoming of this text is due to its lack of rigor, especially in the first topics of advanced calculus. However, this disadvantage is also a virtue. Because of the simplified mathematical development, the material is in more readily available form for both undergraduates and practicing engineers.

This text continues to be outstanding and unique in the field of chemical engineering. Furthermore, this new edition is a welcome revision containing substantial improvements in organization and coverage and is highly recommended both as a text and a reference.

JOHN A. TALLMADGE, JR.

*Translation of an important work
by a famous Soviet scientist*

SOME PROBLEMS IN CHEMICAL KINETICS AND REACTIVITY, Vol. I

BY N. N. SEMENOV

Director, Institute of Chemical Physics of the U.S.S.R.

A translation, by Michel Boudart, of an introductory paper presented to a Symposium on Chemical Kinetics and Reactivity held in Moscow in 1954, which has been enlarged and revised by the author, who is originator of the idea of branched chain reactions and winner of the Nobel Prize for Chemistry in 1956. Volume I covers a wide range of important work, and includes a survey of radical and chain reactions, and discussions of chemical changes, direct mono- and bi-molecular processes, ionic reactions, heterogeneous catalysis, initiation, and destruction of radical chains on solid surfaces.

Volume I, 250 pages. \$4.50

Volume II is in preparation

Order from your bookstore, or

PRINCETON UNIVERSITY PRESS
Princeton, New Jersey

INDEX OF ADVERTISERS

Atlas Powder Company	5D
Eimco Corporation, The	4D
Electronic Associates, Inc.	6D
Grace & Co., W. R. Davison Chemical Div.	8D
Hevi-Duty Electric Company	11D
Hunt Machine Co., Rodney ..Inside Back Cover	
Mixing Equipment Company Outside Back Cover	
Pergamon Press	9D
Princeton University Press	12D
Stearns Roger Mfg. Company	10D
York Co. Inc., Otto H.Inside Front Cover	

Advertising Offices

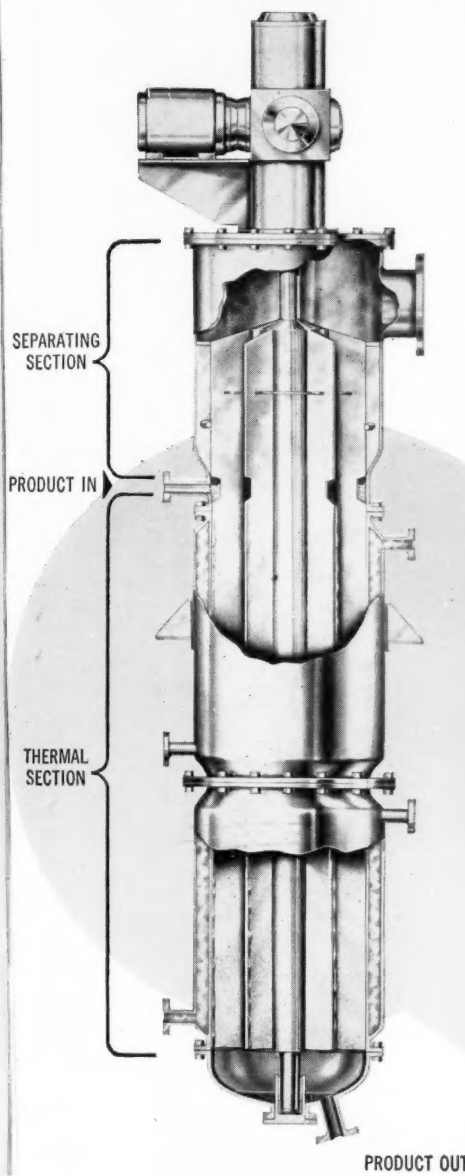
New York 36—Lansing T. Dupree, Adv. Mgr.; John M. Gaede, Asst. Adv. Mgr.; Paul A. Jolcuvac, Dist. Mgr.; Donald J. Stroop, Dist. Mgr.; 25 W. 45th St., Columbus 5-7330.
Chicago 4—Martin J. Crowley, Jr., Dist. Mgr.; Robert Klesch, Dist. Mgr.; 53 W. Jackson Blvd. Harrison 7-0382.
Cleveland 15—Harry L. Gabauer, Dist. Mgr., 434 Bulkley Bldg., Superior 1-3315.
Pasadena 1—Richard P. McKey, Dist. Mgr., 465 East Union St., Ryan 1-8779.
Dallas 18—Richard E. Hoierman, Dist. Mgr., 9006 Capri Drive, Diamond 8-1229.
Birmingham 9, Ala.—Fred W. Smith, Dist. Mgr., 1201 Forest View Lane—Vesthaven, Tremont 1-5762.

Solve Difficult Liquid Processing Problems

with the New

RODNEY
HUNT

TURBA-FILM® MARK II PROCESSOR



When viscous fluid processing is "bugged" by complex procedures, time-at-temperature-sensitive materials, sluggish control of product quality ... look to the new Rodney Hunt Turba-Film Mark II Processor to simplify your problems.

Utilizing a turbulent thin-film technique, the patented Turba-Film Mark II Processor provides mechanically aided heat and mass transfer *in one pass, continuously and rapidly*, for a wide range of viscous fluids and slurries. It delivers controlled uniformity of product in

**concentration ... deodorization ...
dehydration ... evaporation ...
heat transfer ... reaction ...
stripping ... and other processes.**

Short-time exposure and minimum hold-up of the process fluid in the thermal section assures uniform heat and mass transfer, even at high temperature. Foaming is controlled by a mechanical separator and the formation of crust is minimized permitting continuous operation for long periods.

A large number of installations have proved conclusively the superiority of the Turba-Film Processor for processing chemicals, pharmaceuticals, latices, solvents, foods and many other products.

An Invitation

Rodney Hunt will be happy to work with you, utilizing its engineering, laboratory and pilot plant facilities. Portable units are available for process evaluation in your laboratory. Address your inquiry to the Process Equipment Division or write for Catalog 117.



**RODNEY HUNT MACHINE CO.
PROCESS EQUIPMENT DIVISION
630 VALE STREET, ORANGE, MASSACHUSETTS, U. S. A.**

SERVING THE PROCESS INDUSTRIES WITH EQUIPMENT AND ENGINEERING



Ideas explode here... but nothing else can

This new MIXCO laboratory is designed for studying the mixing of hazardous fluids.

If you are working with such materials, these facilities can help you explore—safely—the merits of continuous *versus* batch processing, and many related questions involving single-stage and multi-stage mixing.

For example, we can now pilot-plant the following operations for you, on a continuous or batch basis, with as much as 600 gallons in process at a time:

- gas-liquid contacting
- solid-liquid contacting
- liquid-liquid extraction
- homogeneous reactions

One versatile tool in the new laboratory is a continuous multi-stage contactor designed for pilot plant work. (MIXCO produces full scale sizes for commercial processing.) The pilot LIGHTNIN CMContactor, as it is called, is convertible to any number of stages from 5 to 20. It permits wide variation of mixing impeller speeds and diameters, stage opening sizes, and flow rates.

The Hazardous Materials Laboratory also has a selection of variable-speed mixer drives mounted as dynamometers. These permit accurate measurement of impeller power consumption to provide reliable mixer scale-up data.

7870

An elaborate ventilation system allows individual venting of any equipment in use. All electrical equipment is U/L approved. Safety flooring is used throughout.

We invite you to consider this test adjunct to the existing MIXCO laboratories as part of your research and pilot plant facilities. For a description of the complete system now available to help you solve mixing problems, write us requesting Bulletin B-516.

Lightnin Mixers

MIXCO fluid mixing specialists

MIXING EQUIPMENT Co., Inc., 161-n Mt. Read Blvd., Rochester 3, N.Y.

In Canada: Greely Mixing Equipment, Ltd., 100 Miranda Ave., Toronto 19, Ont.

C 37

0585
1326
2563
3326
4283
5582
6688 7228

0585
1326
2563
3326
4283
5582
6688 7228

tion system
g of any eq
ical equipm
ety floorin

nsider this
existing M
of your
nt facilitie
plete se
you solve
te us requ

Mixers
ng specialis